Nuclear Fusion Project Annual Report of the Association Forschungszentrum Karlsruhe/EURATOM

October 1996 – September 1997

Projekt Kernfusion

Forschungszentrum Karlsruhe

Technik und Umwelt

Wissenschaftliche Berichte

FZKA 6050
EUR 18156 EN

Nuclear Fusion Project
Annual Report of the
Association Forschungszentrum Karlsruhe/
EURATOM
October 1996 - September 1997

compiled by G. Kast
Projekt Kernfusion

Contents   Page

Long-Term Technology Programme

Blanket Development Programme

WP B 7 Demonstration of Blanket Reliability

WP B 8 Development of Ceramic Pebbles

WP B 9 Behaviour of Beryllium Pebbles under Irradiation

Long Term Materials Programme

Neutron Source

Nuclear Data Base

Long Term Safety Programme

Socio-Economics

Next Step Technology Programme

The Association FZK-EURATOM contributes to various fields of the European Next Step Fusion Technology Programme. The work is strongly focused on the ITER Engineering Design Activity. Development of superconducting magnets and microwave heating systems are equally important for the stellerator programme Wendelstein 7X.

FZK has upgraded the TOSKA magnet test facility to be able to test, successively, the prototype coil for W7X (from mid 1998 on) and the ITER toroidal field model coil (after 1999). Preparatory steps were qualification of the LCT background field coil for a field strength of 10 Tesla at superfluid helium temperatures, adaptation of the data acquisition system and operation of the cryogenic system including separate loops for 1.8 K and 4.5 K cooling circuits for the background field coil and the test coil, respectively. Conductor- and flat coil tests are in progress for the W7X-conductor, paralleling the industrial fabrication of the prototype coil.

Major modifications are being made to the power supplies and the fast switching system in view of high current (80 kA), fast discharge operation of the ITER model coil.

Forces on the coils (W7X and ITER) as expected in full machine operation shall be simulated in the TOSKA experiments. Finite element calculations are improved to describe stresses and displacements under load. Studies for ITER-EDA include magnet safety aspects and the mechanical behaviour of low temperature structural materials.

An extended engineering design activity for ITER leaves time for improvements on the microwave heating system. More power per generator unit, higher power efficiency and more flexibility in choosing the wavelength are development goals of the FZK gyrotron activity. Work splits into development of a coaxial gyrotron (1,5 to 2 MW power at 170 GHz) and of suitable high power windows. New materials as CVD diamond are qualified for use as water cooled disk windows that cope with up to 2 MW of transmitted power.

In the field of Vacuum Technology and Fuel Cycle two important contributions are being made to the development and testing of prototypical components for the ITER machine. Concerning vacuum it has been demonstrated that cryopumping can cope with all requirements for the vacuum system of ITER including very short pumping/regeneration cycles to assure the set limit for tritium accumulation on the panels. A half-scale prototypical cryopump is being manufactured under an industrial contract and will be extensively tested at FZK. Work is under way to provide the necessary infrastructure.

The broad programme to demonstrate a technical process for tritium recycling from the plasma exhaust with a decontamination factor in the 10^7 range is well under way in the Karlsruhe Tritium Laboratory (TLK). After the different conversion and separation steps have all shown excellent performance, a technical facility is being erected the specifications of which have been adopted for the ITER Tritium Plant. Modelling has been continued on a limited scale for tritium behaviour in the environment.

A small number of individual activities, based on available expertise and testing facilities, has been ongoing for ITER contributing to the field of Plasma Facing Components. They cover three different aspects of First Wall behaviour under the impact of the plasma: tritium uptake, plasma erosion and cyclic heat load.

MCOI ITER-TF Model Coil Development

Subtask 1: Monitoring Manufacture of the Toroidal Field Model Coil (TFMC)

The aim of the subtask is the support of the NET Team in the design and fabrication of the ITER TF model coil.

The fabrication of the ITER TFMC is running in the European industry consortium AGAN (ACCEL, Germany, GEC Alsthom, France, Ansaldo, Italy, Noell, Germany). FZK participated in the „TFMC Project Progress–, TFMC Technical– and TFMC Review Meetings" . FZK contributed to the following items:

a) Analyses and optimization of the mechanical support structure (see also ERB 5000 CT 95 00064 [NET 95 – 384]) for the TFMC test configuration.

b) Contribution to the design work and test facility related items (instrumentation, cryogenic and electrical supply, superconducting busbars gravitational support, TFMC test program)

Instrumentation: Proposals for the voltage tap arrangement for the winding and the instrumentation of the thermohydraulical circuits was elaborated which were needed for diagnostic, quench protection and operation control.

Cryogenic and electrical supply system: It was tested that the 2 kW refrigerator was not capable for stable operation at temperature levels > 5 K. It was proposed to use injected heated gaseous helium slugs for measuring the current sharing temperature and for quenching the coil.

Different discharge time constants were requested for investigation of the eddy current heating of the shear plates and the impact of heat diffusion to the conductor during fast discharge of the coil. Possible discharge time constants are given Table 1 limited by the load limit integral of the TCMC conductor of $1.3*10^{10}$ A^2 s or the maximum energy capacity of the dump resistor unit of 20 MJ. The dump resistor consists of 5 units.

Superconducting busbars : The extrapolated losses for the operation of the 80 kA current leads installed in horizontal position derived from the results of the 1.8 K test of the LCT coil (see MTOS 1) were outside the capability of the cryogenic system. Therefore vertical installation of the 80 kA current leads required a proposal for a new busbar system.

Gravitational support : A conceptual design of the gravitational support carrying the LCT coil and the TFMC in the intercoil structure was elaborated giving guiding interfaces for the TFMC test configuration design. The support design was based on the principles used for the LCT coil support.

Test program : A proposal for a test program was elaborated and presented at the 3rd TFMC Project Review Meeting. The goal of the test program is the verification of the overall engineering design for the magnetic, thermohydraulic, mechanical and electrical insulation properties. The TFMC has to be equipped by a suitable instrumentation and preparing work for making codes available giving guidelines for drafting the test procedure (see also NET Contract : ERB 5004 CT 96 0050) and the later evaluation of the test results.

Subtask 3: Basic Development of High Voltage Technique for Components used in the Model Coil and Test Facility (Feedthroughs, Insulation Breaks, Current leads) and High Voltage Measuring Technique

The aim of the subtask is the transfer of the know-how in the development of high voltage components and high voltage measuring technique gained in the POLO project to the ITER model coils.

In collaboration with IEH of the University of Karlsruhe the special shear plate design of the TFMC was assessed with respect to the investigation of the electrical insulation properties by the partial discharge (PD) diagnostic. Giving all shear plates the same potential the winding of the coil can be considered for ns pulses like they occur for PD as a coiled coaxial cable. Therefore the PD measuring technique can be applied like for coaxial power transmission cables. This offers the possibility for having a nondestructive method for the assessment of the electrical winding insulation during the life time of the magnet. The joint regions of the magnet disturb the coaxial symmetry. Investigation are runnig for calculating and making simulation experiments for the estimation of the impact on the PD signals. First PD measurements on a TFMC fullsize shear plate section (< 1 m) showed at relevant voltage levels (conductor / shear plate: 1 kV_{pp}, respectively 2 kV_{pp} assuming the max. possible voltage if one end of the pancake is shorted with the shear plate; shear plate/ shear plate: 2 kV_{pp}, respectively 3 kV_{pp}) no PD activity above the noise level of 0.3 pC.

Staff:

K. Bauer
S. Fink (Subtask 3)
G. Friesinger
I. Meyer
U. Padligur

A. Ulbricht (Subtask 1)
F. Wüchner
G. Zahn
V. Zwecker

Table 1: Possible resistors combinations and time constants for discharging the TFMC (R : Dump resistor, τ : Dump time constant, E_n : Nominal stored energy, I_n : Nominal current, I_{max} : Maximum allowable current by dump resistor capacity, I_{limit} : Current limit by load limit integral shadowed areas)

Resistor Combin.	R [mΩ]	τ [s]	E [MJ]	E / E_n [%]	I/I_n [%]	I_{max} [kA]	$\int I^2$ dt [10^{10} * A^2 s]	I_{limit} [kA]
5 Series	6.7	4.0	100	100	100	80	1.3	----------
4 „	5.36	5.0	80	80	89	71.2	1.3	----------
3 „	4.02	6.7	60	60	77	61.2	1.3	----------
2 „	2.68	10.1	40	40	63	50.4	1.3	----------
1 „	1.34	20.1	20	20	44	35.0	1.3	----------
2 Parall.	0.67	40	40	40	63	50.4	5.1	25.3
4 „	0.335	80	80	80	89	71.2	20.2	17.9
5 „	0.268	100	100	100	100	80	32.0	16
2 Ser. a then Par.	1.34	20.1	80	80	89	71.2	5.1	35.6

M 12 (N 11 TT 19)
Preparation of the ITER TF-Model Coil Test Facility

Subtask 1: Preparation of the TOSKA Facility for the Test of the ITER TF Model Coil (TFMC)

The fabrication of the ITER TF model coil is running in the European industry. The task is performed by a consortium called AGAN (ACCEL, Germany; GEC Alsthom, France; Ansaldo, Italy; Noell, Germany). The accompanying work which is being performed by FZK for the TFMC is reported in subtask MCOI 1.

1. Upgrading of the TOSKA Facility

A second test of the LCT coil at 1.8 K was performed in beginning 1997 to test improvements of the facility (cold gas return at the cold end of the current leads for improving the adjustment of operation parameters; data acquisition, visualisation and control; quench protection circuit).

Also the impact of fringing fields of the LCT coil in the experimental area on components of the cryogenic and electrical supply system as well as of the control system were investigated. Table 1 gives a comparision of the number of Ampere turns which are direct proportional for different coils and coil configurations to the fringing fields in the experimental area. The operation of the LCT coil at 19.5 kA generate nearly equivalent fringing fields in the surrounding like for the next test configuration (LCT + W 7-X). This is about 60 % of the fringing fields of the TFMC configuration.

The operation of the different components like helium pumps, control units of power supplies and dump circuits, programmable logic controllers as well as current measuring devices were investigated and a field mapping were performed for having suitable scaling laws for future installation of components. Results are reported in the following sections.

1.1 The Cryogenic Supply System

The installation of a cold gas return path at the cold end of the current leads of the LCT coil improved the adjustment of the operation parameters remarkably. The minus currrent lead showed at lower currents an instable operation behaviour. No explanation was found for this phenomen from the evaluation of the operation parameters.

A piston-, a centrifugal- and a thermomechanical pump, respectively, were tested at 1.8 K operation. Piston pump, centrifugal and thermomechanical pump achieved their expected parameters. No impact of magnetic fringing fields were found on the operation up to field levels of < 7 mT (19 kA LCT coil current) for the piston and centrifugal pump.

Dumps up to 300 MJ of stored energy were easily handled by the cryogenic system without any helium gas release to the atmosphere. Each of the three pumps were able to recool the

LCT coil and its reinforcement structure in 2 hours.

1.2 The Electrical Supply System

The electrical supply system (power supply and dump circuit of the LCT coil) worked well. In the fringing fields of the LCT coil the POLO dump circuit was operated together with the 30 kA power supply and a copper coil. The current level of the LCT coil was increased in steps and the function of the electrical system was tested. First faults were observed in the control circuits of the POLO dump circuit at current levels of 8 kA to 13 kA with a big hysteresis corresponding to field levels in the cabinets of about 3 mT. A Reed relais was identified causing the fault. Changing of the orientation of the relais with respect to the magnetic fringing field direction solved the problem. At 16 kA current level the current transformer of the 30 kA power started to saturate which led to emergency switch off of the power supply (fringing field level about 5.5 mT in this area). An iron plate shield surrounding the transformer result in a shielding of about 50% which was sufficient for fault free operation up to 19 kA LCT coil current level corresponding a fringing field level of about 6.5 mT [1]. Iron cored current transformers showed no impact from fringing fields up to levels of < 20 mT.

Table 1 and results achieved allow predictions for the testing of the TFMC configuration to assure the proper function of the components of the TOSKA facility.

1.3 Instrumentation and Data Acquisition

After the first test many improvements were implemented in hard- and software and tested in the second test.

A progammmable logic controller (PLC) (product: Siemens Simatic S5-135) was prepared in hard- and software for being tested in the surrounding of magnetic fringing fields. The PLC was tested in a magnetic field up to 22 mT (vertical 20 mT, horizontal 9 mT) and remained operable in all its components [2].

1.4 The 80 kA Current Lead

A water cooled flexible busbar was successfully tested at 80 kA steady state current (Fig. 1). A current density of 45 A/mm^2 was achieved in the copper braids with stable operation parameters (Fig. 2). The busbar allows a space saving joint to the warm end of the current lead and balancing of displacements between the rigid aluminium busbar and the warm end of the current lead.

A new high current density strand material was applied for the Nb$_3$Sn inserts. The outer tin enriched bronze matrix showed in short sample measurements not well defined current transition properties between strand and the embedding copper. Samples with about 1 m length are being prepared to repeat the measurements.

Table 1: The number of Ampere turns of different and coil configurations which have been tested and will be tested in the TOSKA facility (Axis positon: Vacuum vessel axis and coil axis).

Coil, Coil, Configuration	Conductor Current	Ampere turns	Axis Position
LCT	10.0 kA	5.88 MA	⊥
POLO	22.5 kA	1.25 MA	∥
LCT	19.5 kA	11.5 MA	⊥
LCT + W 7-X	LCT: 14 kA + W 7-X: 18.7 kA	10.5 MA	⊥
LCT + ITER TFMC	LCT: 16 kA + TFMC: 80 kA	17.25 MA	⊥
ITER TFMC	80.0 kA		
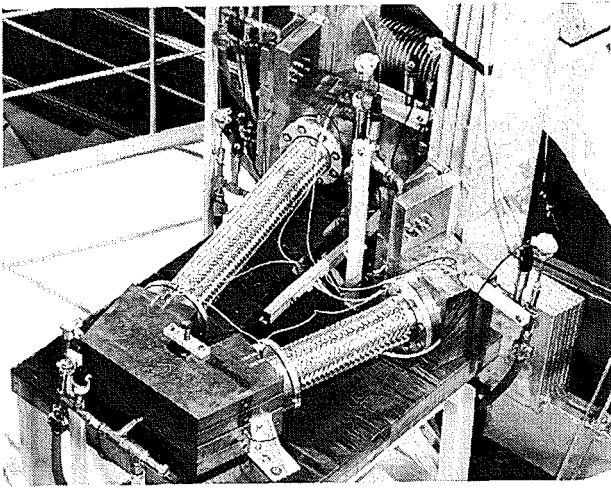
Fig. 1: Two water cooled flexible busbar short circuited by a water cooled copper busbar are connected to the Al busbars of the 50 kA power supply.

Refrigeration capacity vs. liquefaction capacity at the control cryostat B250

Fig. 3: The working diagram of the cryogenic system shows the upscaled requirements for operation of the 80 kA/70 kA current leads in horizontal installation position which is outside the capability of the cryogenic system. Operation points for 2,5 nΩ and 5 nΩ joint resistance are given.

Fig. 2: Temperature (in- and outlet) and current profiles during operation of the flexible water cooled busbars.

The unexpected high losses of the LCT coil currrent leads in horizontal installation position required an action for the 80 kA current leads. Scaling up of the measured losses for the operation of the 80kA current led to a cryogenic power which would have exceeded the capability of the cryogenic system (Fig. 3). The change from the horizontal installation position to the vertical one is the only solution to come to predictible current lead losses without starting new developments. A conceptual design for installing the current leads in a horizontal position was elaborated. The superconducting busbars consist of two pieces now, whereby each busbar has a joint in the vacuum vessel. This solution releases also the space limitations in the vacuum vessel because the relative large busbar terminal is now outside vacuum vessel volume.

Literature:

[1] J. Zimmmermann, A. Ulbricht , F. Wüchner, Streufelder beim Betrieb der LCT-Spule, Interner Bericht, Juli 1997, Forschungszentrum Karlsruhe

[2] J. Zimmmermann, M. Süßer, F. Wüchner, Test einer Siemens Simatic S5-135 im statischen Magnetfeld, Interner Bericht, August 1997, Forschungszentrum Karlsruhe

Staff:

A. Augenstein	W. Maurer
H. Barthel	I. Meyer
S. Darweschsad	G. Nöther
G. Dittrich	U. Padligur
P. Duelli	K. Rietzschel
S. Fink	G. Schleinkofer
F. Frankrone	T. Schneider
G. Friesinger	K. Schweikert
A. Götz	E. Specht
P.Gruber	H.-J. Spiegel
A. Grünhagen	H. Stiefel
R. Heller	M. Süßer
W. Herz	A. Ulbricht (1 and 1.2)
H. Kathol (till 31.12.96)	D. Weigert
R. Kaufmann	F. Wüchner
A. Kienzler	G. Würz (till 30.08.96)
P. Rohr	G. Zahn (1.1, 1.3, 1.4)
L. Lang	H.P. Zinecker
O. Langhans	V. Zwecker
W. Lehmann	

M 27 (N 11 TT 45)
Critical Current vs Strain Tests on EU Strands and Sub-Size CICC's with Stainless Steel and Incoloy Jackets

The aim of this task is to investigate the effect of different cross sections of stainless steel, ss, and Incoloy jacketed subsize "Cable in Conduit Conductors", CICC's, on the critical current, I_c, versus axial strain, ε, characteristics. Furthermore, the application of different fabricated basic Nb_3Sn strands and the effect of low temperature strain cycling will be studied.

The CICC samples investigated consists of an outer conduit and an inner cable of 3x3x4 Nb_3Sn strands. Thin (0.34 mm) and thick (1.25 mm) walled ss 316 L and thick walled Incoloy 908 conduits (1.25 mm) have been used. ID = 6.0 mm of all samples, resulting to a helium void fraction of v_f = 34 %. Nb_3Sn strands (d = 0.81 mm) from Vacuumschmelze (VAC) and Europa Metalli (LMI) have been used, fabricated by the bronze route and the internal tin process, respectively. The samples have been fabricated by SMI, heat treated by CEA and measured in the FBI test facility of FZK/ITP. The tests have been finished in Sept. 97 and the final report is in progress.

First results about the difference between thin and thick walled ss 316 L jacketed conductors with VAC cable were shown in the last annual report. The most important result is presented in Fig. 1, which compares the strain dependence of critical current of thick walled ss 316 L (CV6) and Incoloy 908 (CV7) jacketed CICC's with VAC strands. The numbers attached to the CV6 curve indicate the sequence of testing in stressed and unstressed condition of the sample. The prestrain, ε_m, results mainly from the difference in thermal contraction between conduit and Nb_3Sn during cooling from reaction to LHe temperature. This degrades the critical current from the max. value, I_{cm}, to the initial value of I_{co} at ε = 0. For the 316 L and Incoloy samples ε_m amounts to 0.76 % and 0.34 % and the corresponding degradation of I_c, I_{co}/I_{cm}, amounts to 0.50 and 0.86, respectively. The drastic increase of the critical current of the Incoloy sample is due to its about a factor of two lower thermal contraction with respect to that of steel. Both I_c vs ε curves behave reversible up to the measured strain, ε_{irr}. I_c measured without stress (sample CV6: numbers 10, 13, 16, 29, 22 and 25) indicate the plastic deformation of the sample. These values at the Incoloy sample are small ($\varepsilon \approx 0.05$ %, no numbers) due to high yield strength Incoloy.

In Fig. 2 the influence of cycling on the I_c vs ε curves of thick walled ss 316 L (CV5) and Incoloy 908 (CV8) jacketed conductors is presented in comparison to the corresponding uncycled samples (CV 6,7). First, I_{co} (ε = 0) has been measured, then 1000 cycles, 0 - 0.2 % strain, 0.2 Hz at 4.2 K and 13 T applied and after that the tests of I_c completed under statically straining in stressed and unstressed state of the samples. Note, that, after cycling and in stressed condition the I_c vs ε curve of the steel sample has been shifted slightly (decrease of ε_m, increase of I_{co}) while the Incoloy conductor is not effected. But I_c increases clearly after cycling within the unstressed state at both conductors (clear symbols). This could mean that after cycling further stress on the Nb_3Sn has been removed and/or a change of the current distribution within the cable has been occured. One can conclude that 1000 strain cycles have no negative effect on the I_c vs ε behaviour. But with respect to the foreseen 50.000 cycles of the ITER magnet system these investigations should be extended to higher cycling rates.
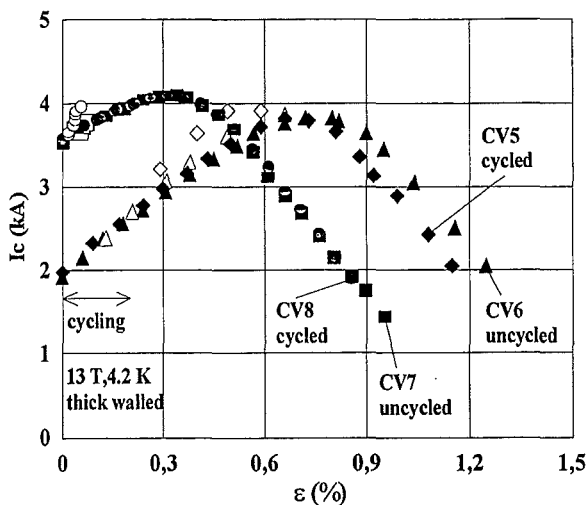
Fig. 2: Effect of cycling on I_c vs ε of thick walled 316 L (CV5) and Incoloy 908 (CV8) jacketed conductors with VAC cable.
CV5, 8: 1000 cycles, 0 - 0.2 % strain, 0.2 Hz.
CV6, 7: uncycled reference

Comparable results as for the CICC's with VAC strands have been obtained at samples with LMI wires [1]. The critical current of the internal tin processed LMI wires is about 23 % higher than I_c of the bronze route fabricated ones of VAC (at 13 T). However, the degradation of I_c due to prestrain is stronger at the LMI conductors. This is demonstrated in Fig. 3, where the normalized critical current, I_c/I_{co}, as a function of the intrinsic strain, $\varepsilon_0 = \varepsilon - \varepsilon_m$, is plotted for both thick walled CICC's with VAC (CV6) and LMI cable (CLI) including their corresponding strands (VAC 2 - 5, LMI 003). The stronger decline of the LMI samples in the most interesting range of negative values of ε_0 results from the lower upper magnetic field, B_{c2}, with respect to B_{c2} derived at the VAC samples [1].

Literature:

[1] W. Specking, J.L. Duchateau and P. Decool, "First Results of Strain Effects on Critical Current of Incoloy Jacketed Nb_3Sn CICC's", Proc. MT-15, Peking, China, Oct. 20 - 24, 1997.

Staff:

H. Kiesel
W. Specking

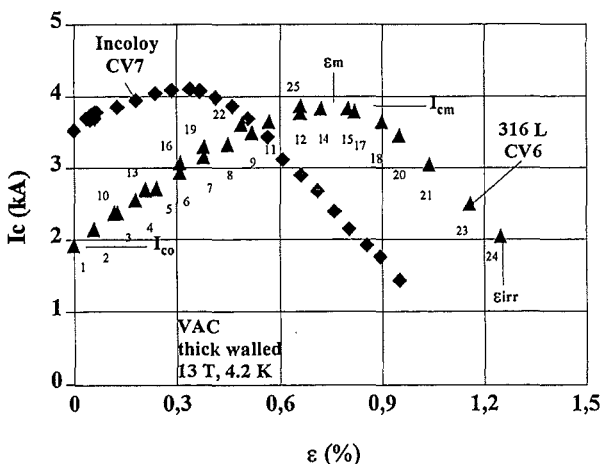

Fig. 1: Critical current versus applied strain of stainless steel 316 L and Incoloy 908 jacketed CICC's with VAC strands.

Fig. 3: Normalized critical current versus intrinsic strain of thick
walled 316 L jacketed CICC's with both VAC (CV6) and
LMI cable (CLI) and their basic strand (VAC 2 - 5, LMI
003).

M 31
Development of 60 kA Current Leads Using High Temperature Superconductors

Introduction

The aim of the task is to develop a 60 kA current lead for the ITER Toroidal Field Coil system using high temperature superconductors (HTSc) in the temperature range between 4 K and 77 K to reduce the steady state heat load at the 4 K level. The task is being done in collaboration with the Fusion Technology Division of the Centre de Recherches en Physique des Plasmas of the Ecole Polytechnique Fédérale de Lausanne (CRPP-EPFL).

The development program is subdivided into three stages:

A-1 Test of different materials and concepts in 1 kA modules

A-2 Test of a 10 kA HTSc binary current lead using the material selected in stage A-1

B Design and test of a 20 kA HTSc binary current lead to prove modularity and scalability of the design

C After completion of stage B, a 60 kA current lead could be designed to replace an existing 80 kA current lead in the TOSKA facility. This stage is an option, the decision will be made after completion of stage B

Test results of 1 kA modules

During stage A-1, four current leads with different materials resp. concepts were constructed and tested at a test facility of the CRPP-EPFL, i.e.,

1. Bi-2212 (tubes) bulk material made by Hoechst AG, Germany,

2. Bi-2223 tapes with Ag3%Au sheath in a straight stacked configuration made by AmericanSuperconductor Corp. (ASC), USA,

3. Bi-2223 tapes with Ag8%Au sheath in an axially twisted configuration fabricated at ITP-FZK, and

4. rods (bulk material) made by INFP-FZK.

The tests at CRPP cover the steady state behaviour, i.e., temperature profile, heat load at 4 K and He mass flow rate of Cu heat exchanger to fix the temperature of the upper end of the HTSc part to 70 K, as well as transient behaviour, i.e., performance of the leads during loss of He mass flow rate while the current is kept constant.

For version 3, Bi-2223 tapes with Ag/Au sheath were fabricated. The tapes consist of seven filaments embedded in a sheath of Ag8%Au. The critical current of the tape in self field at 77 K was in the range of 6.5 - 8.5 A (critical current density of j_c = 7.5 - 10 kA/cm^2). It should be mentioned that the tapes were not well optimized with respect to critical current because of the small number of filaments and the heat treatment process. The main aim was to demonstrate the capacity of such tapes. In the 1 kA module, the critical current was expected to be about 650 A taking into account the degradation due to the higher self field. Afterwards, the tapes were mounted in the 1 kA module with a twist pitch of twice the length of the module. Figure 1 shows a photography of the connection area of the 1 kA module. After the completion of the module, the critical current at 77 K and self field was measured at CRPP. A critical current of 282 A was measured which has to be compared to the expected

critical current of 650 A, i.e., a degradation of about 60 % was observed.

Fig. 1: Photography of part of the HTSc module fabricated at FZK including copper connector

The reason for this large degradation is the large stress sensititvity of the AgAu sheathed tapes at room temperature which could be demonstrated in a stress experiment. This will be discussed lateron.

Nevertheless, the degradated 1 kA module was installed in the test facility at CRPP an tested up to 500 A. The test demonstrated the expected performance in both DC as well as in transient operation.

For version 4, Y-123 rods fabricated by INFP have to be contacted, i.e., a low resitive high current density contact has to be developed. First trials to sputter Ag onto the surface o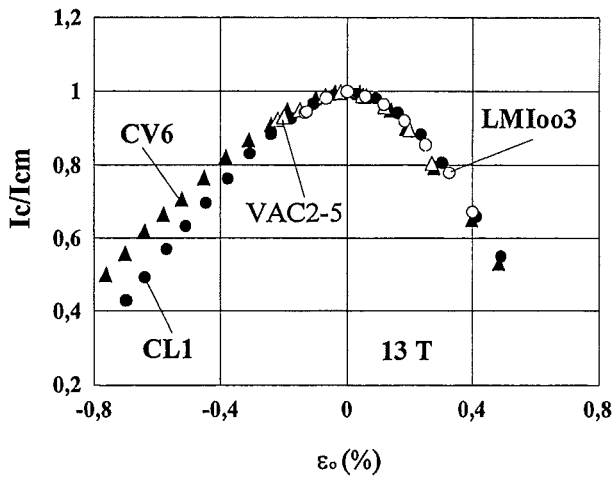f the HTSc failed. The possibility of using Ag filled epoxy which has to be burnt onto the surface of the HTSc was also investigated. Up to now no large area high current contact is successfully fabricated. So it was decided not to proceed with this version because of lack of technical ability for current leads.

Table 1: Main results for steady state and transient operation

I [kA]	Mass flow [g/s]	$P_{e,hex}$ [W]	Q [W]	$P_{e,htsc}$ [W]	$P_{e,tot}$ [W]
Bi-2212 (tube) - Hoechst					
0	0.045	56.5	0.101	7.1	63.6
1	0.080	100.4	0.111	7.8	108.2
1.5	0.101	126.8	0.124	8.7	135.5
2	0.156	195.8	0.141	9.9	20.6
Bi-2223 (tape) - ASC					
0	0.055	69.0	0.365	25.6	94.6
1	0.080	100.4	0.408	28.6	129
1.2	0.100	125.5	0.427	29.9	155.4
Bi-2223 (tape) - FZK					
0	-		0.370	25.9	-
0.407	0.0496	62.2	0.372	26.0	88.2
0.457	0.0550	69.0	0.373	26.1	95.1
0.509	0.0526	66.0	0.373	26.1	92.1

Module	I [kA]	Δt(0 - 100 mV) [s]	Δt(0 - 100 mV) [s]
Bi-2212 (tube) - Hoechst	1	565	2
	1.5	309	1.1
Bi-2223 (tape) - ASC	1	600	19
	1.1	540	17
	1.2	430	15
Bi-2223 (tape) - FZK	0.407	2257+	726+
	0.509	1648	400

+ = extrapolated from 66 mV to 100 mV

Table 1 contains the main results of the test of the 1 kA modules of versions 1 to 3 in steady state and transient operation.

Figures 2 and 3 show the 60-K He mass flow rate resp. the heat load at 4 K as a function of current for the three versions. In Figure 4, the time difference between loss of He mass flow initiation until the current is switched off as a function of I^2/A_{tot}, i.e., proportional to the Joule heating per unit length. The time difference reaching 10 mV and 90 mV resistive voltage is also shown.
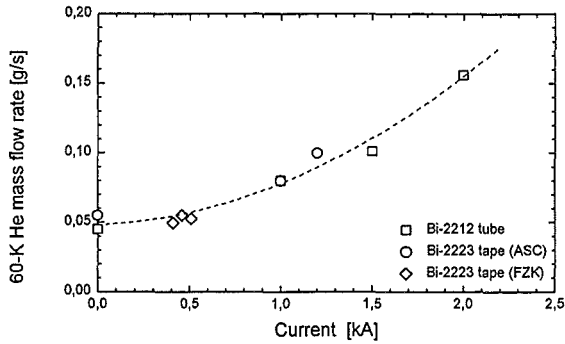
Fig. 2: 60-K He mass flow rate vs current for 3 versions of 1 kA modules
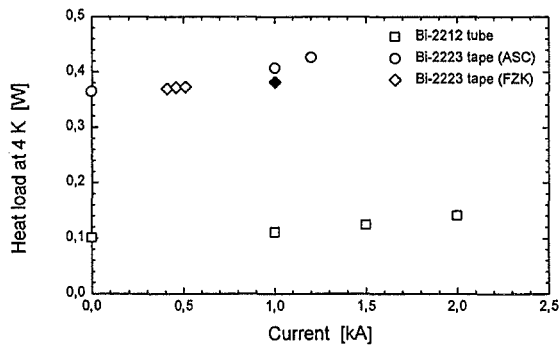
Fig. 3: Heat load at 4 K vs current for 3 versions of 1 kA modules
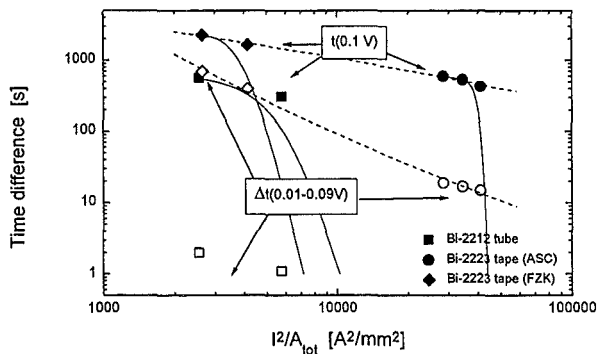
Fig. 4: Time difference vs I^2/A_{tot} vor 3 versions of 1 kA modules

The conclusions are as follows:

1. Comparing the three versions tested up to now, there is no difference in the 60-K He mass flow rate which is adjustded to fix the temperature of the upper end of the HTSc module to 70 K.

2. Looking to the heat load at 4 K, the bulk material has a much lower value than the stabilized tapes, i.e., about a factor of 4.

3. The contact resistances are comparable.

4. Comparing the transient behaviour, there is a clear distinction between bulk and stabilized tape material. Important for the safety margin during quench is the time duration between 10 and 90 mV which is much larger for the tapes. The stabilized tapes are more safe than the bulk material. The use of bulk material requires the design of an electrical by-pass which has to be highly resistive during normal operation but has a low current response time in case of a quench.

So it has been decided to proceed with task stage A-2, i.e., the construction and test of a 10 kA HTSc binary current lead. As material, it was decided to use stabilized tapes because of their larger safety margin than bulk material.

The large degradation of the Bi-2223 tapes fabricated at ITP was explained by a large stress sensitivity of the tapes even at room temperature. It was decided to develop mechanically reinforced tapes with an interior Ag8%Au matrix and an hardened Ag-alloy outer sheath. For this, 37 filamentary tapes were produced in an industrial technique of bundling monocores. The critical current density achieved was 10 - 11.5 kA/cm^2. The mechanical properties of the reinforced tapes were measured and compared to the numbers of the AgAu tapes used in the 1 kA module. At room temperature, The tolerable stress values for the AgAu stabilized tapes are about 20 MPa whereas for the reinforcded AgAu/Ag-alloy tapes they are between 90 and 170 MPa depending on optimization. Figure 5 shows the normalized critical current as a function of stress for both AgAu and AgAu/Au-alloy tapes. The tapes were thermally cycled between 77 K and room temperature. Figure 6 shows the critical current as a function of the cycling number. Up to about 180 cycles, almost no dramatic degradation was observed. Even the use of a heater fan during warming up results in no dramatic current degradation. This also demonstrates the high mechanically stability of the tapes.

It is forseen to built a second 1 kA module and test it at CRPP. The production of the tapes has been started. The characterization of the tapes, i.e., the measurements of $I_c = f(T)$ resp. $I_c = f(B)$ is currently under investigation. The results of these measurements are important for the design of a 10 kA module.

Status of 10 kA HTSc current lead

The test of the 10 kA HTSc binary current lead in conjunction with a conventional bath cooled copper lead will be done at CRPP. The design of the test facility is completed, the cryostat will be available at the beginning of next year. The conventional copper lead is completed, the construction of the 10 kA HTSc binary current lead has been started. Because the Bi-2223 tapes of ASC are up to now the best material, a call for tender to ASC has been started.
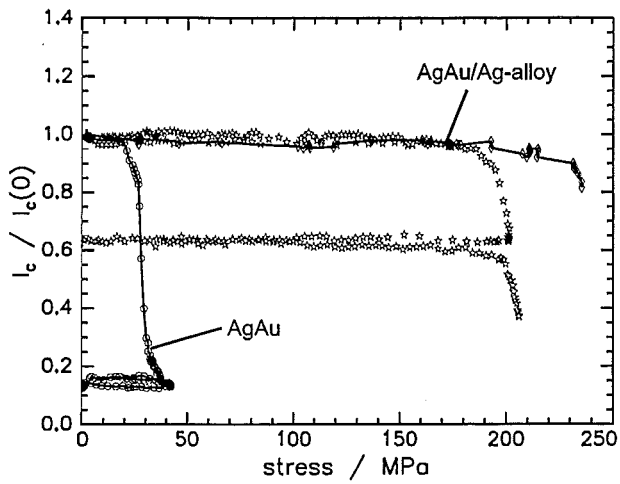
Fig. 5: Normalized critical current vs stress for AgAu and AgAu/Ag-alloy tapes
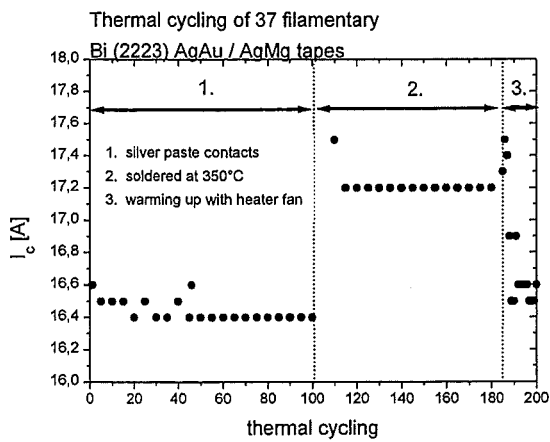
Fig. 6: Critical current vs number of thermal cycles

Literature:

W. Goldacker, B. Ullmann, A. Gäbler, R. Heller, "Properties of Bi(2223)/AgAu Multifilamentary Tapes for Current Leads", presented at EUCAS 97, Eindhoven, Netherlands, June 29th - July 3rd, 1997

Staff:

K. Bauer
G. Friesinger
R. Bußjäger
W. Goldacker
R. Heller
H. Kathol (until 31.12.96)
H. Orschulko
M. Quilitz
B. Ullmann
S. Zimmer

Gyrotron Development
(includes ITER Tasks T24, T245/6 and T360)

1. Introduction

The FZK gyrotron development programme is based on the conventional cylindrical cavity gyrotron and the coaxial cavity gyrotron. Conventional cylindrical cavity gyrotrons at frequencies around 140 GHz are limited in output power to about 1 MW due to ohmic wall loading, mode competition, and limited beam current. These limiting factors can be considerably reduced with the use of coaxial cavities, which offer the possibility of operation in high order volume modes with reduced mode competition problems. Furthermore, the presence of the inner conductor practically eliminates the restrictions of voltage depression and limiting current. Therefore, gyrotrons with coaxial cavities have the potential to generate, in CW operation, rf-output powers in excess of 1 MW at frequencies above 140 GHz.

Important development goals of a 1 MW, 140 GHz cylindrical cavity gyrotron operated in CW as required for W7-X, such as the depressed collector technology, the advanced built-in quasi-optical (q.o.) mode converter and the window concept are also prerequirements for the coaxial cavity gyrotron development and therefore in these areas the development of a cylindrical cavity 1 MW gyrotron will provide an important input for the development of the coaxial 2 MW gyrotron for ITER.

2. Coaxial Gyrotron at 140 GHz

A gyrotron designed for operation at 140 GHz in the $TE_{-28,16}$ mode and at 165 GHz in the $TE_{-31,17}$ mode with an rf output power of 1.5 MW is under investigation in collaboration between the FZK and the IAP, Nizhny Novgorod. The development has been planned to be performed in two steps. In a first step which has already been completed, a coaxial gyrotron equipped with an axial waveguide output has been designed, built and operated. At both frequencies an rf-output power close to 1.2 MW with an efficiency of about 27 % was measured [1,2].

In the second step a $TE_{-28,16}$ coaxial cavity gyrotron with lateral rf-output was designed, built and tested. For the first time the generated rf-power was split in two parts and coupled out through two rf output windows in order to reduce the power loading of the windows. The q.o. rf-output system is based on a two-step mode conversion scheme, $TE_{-28,16} \Rightarrow TE_{+76,2} \Rightarrow TEM_{00}$, which generates two narrow rf-output wave beams with an azimuthal divergence of $\approx 60°$ at the launcher. Especially, the first step, converting the cavity mode into its degenerate whispering gallery mode, is strictly limited to the design mode. Therefore, such a scheme is not suitable for step frequency operation.

The gyrotron is equipped with a single-stage depressed collector in order to enhance the total efficiency and to reduce the power loading and x-ray generation at the collector surface. A view of the fully assembled tube is given in Fig. 1.

First results with the gyrotron were reported in [3,4]. A maximum rf output power of P_{out} = 0.95 MW with an output efficiency of 20 % was measured [5]. Fig.2 gives as an example the measured rf-output power P_{out} as function of the beam current.
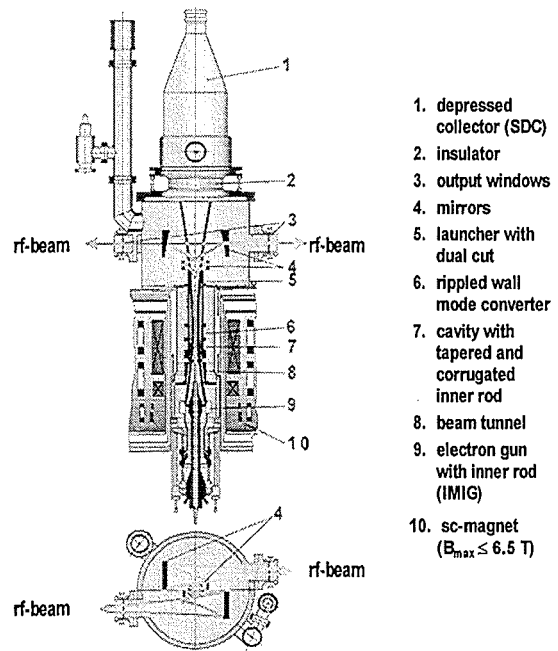
Fig. 1: Schematic layout of the coaxial cavity gyrotron with dual rf-beam output.

1. depressed collector (SDC)
2. insulator
3. output windows
4. mirrors
5. launcher with dual cut
6. rippled wall mode converter
7. cavity with tapered and corrugated inner rod
8. beam tunnel
9. electron gun with inner rod (IMIG)
10. sc-magnet ($B_{max} \leq 6.5$ T)
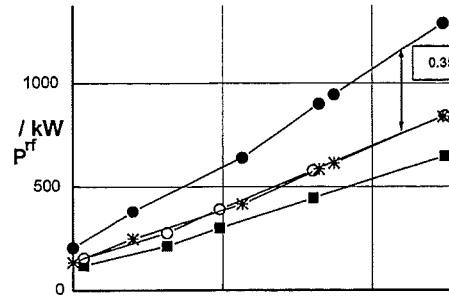
Fig. 2: RF-power versus the beam current. B_{cav} = 5.637 T, U_c = 80 to 90 kV, U_c optimized for maximum P_{out}. The meaning of the symbols: (— ■ —) P_{out} ; (— O —) P_{out} + P_{capt} + $P\Omega$; (— ● —) P_{th} ; (— · —) $0.65*P_{th}$

The single-stage depressed collector raised the efficiency from 20 % to 29 %. According to numerical calculation an rf-power above 1.5 MW is expected to be generated in the cavity. Even if all losses are added to the experimentally measured output power, a discrepancy between experiment and calculations remains. The power deficit seems to be partly caused by the influence of stray radiation captured inside the tube. As a main reason, however, a large energy spread of the electron beam, caused by trapped electrons, is suspected. In order to improve the quality of the electron beam the LaB_6-emitter ring, which was exposed to air for many times, will be replaced by a new one before the next experiment. A wide single-mode operating range has been found in good agreement with the theoretical expectations. Beam instabilities limited the operation at a magnetic field distribution delivering a velocity ratio $\alpha \cong 1.4$ at the design parameters. The instabilities are enhanced due to the captured rf-radiation. It is suspected that the appearance of the instablities is also related to the poor beam quality and trapped electrons.
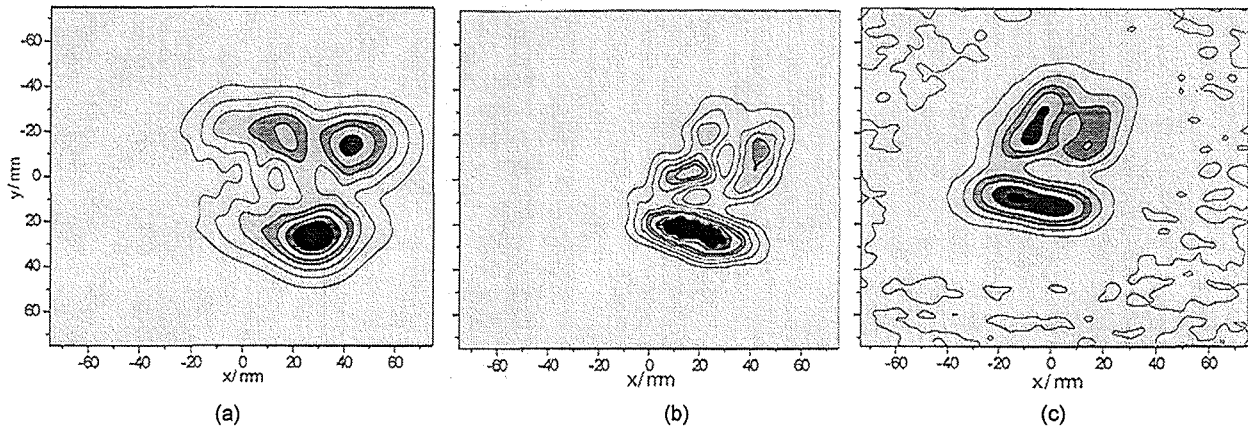
Fig. 3: The distribution of the rf-power 37 cm outside the window. (a) calculation, (b) cold measurement, (c) hot measurement.

3. Quasi-Optical Mode Converter for Coaxial Gyrotrons

In order to optimize the power output coupling of the q.o. system the position of the launcher and the mirrors had been adjusted in cold measurements [6,7]. The obtained flattened beam image shown in Fig. 3b was measured 37 cm outside the window and is in good agreement with the hot measurement as shown in Fig. 3c. The results of calculations (Fig. 3a) are in qualitative agreement with the experiment.

The diffraction losses have been estimated to be about 6 %. For some unkown reasons the measured losses are somewhat higher, resulting in an efficiency of the rf-output system of approximately 86 %. Due to a modification of the rippled wall mode converter the efficiency even decreased to $\cong$ 80 % only.

4. Conventional Cylindrical Cavity Gyrotron

In order to demonstrate the usability of gyrotron oscillators as frequency step tunable high-power millimeter-wave sources, experiments on a 1 MW, 140 GHz, $TE_{22,6}$ gyrotron with a built-in q.o. mode converter have been performed.

A maximum output power of 1.35 MW (I_b = 51A) with nearly 30 % efficiency was measured at 140 GHz. To increase the efficiency a single-stage depressed collector has been used. In Fig. 4 the output power and efficiency as function of the retarding collector voltage is given.
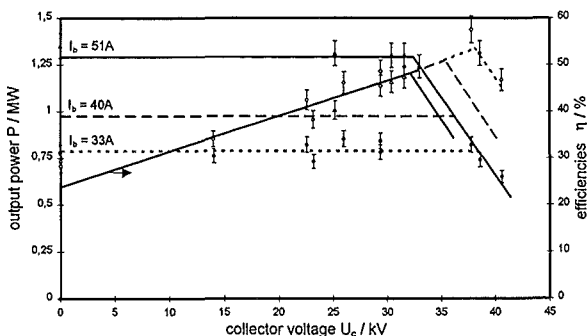
Fig. 4: Power efficiency as function of the retarding collector voltage.

With I_b = 51A an output power of 1.3 MW at nearly 50 % efficiency was reached, with I_b = 40 A the output power was 1 MW with 52 % efficiency and with I_b = 33A the output power was 0.8 MW at 57.4 % efficiency [8,9].

By varying the operating parameters of the tube a series of oscillations in the frequency range from 114 GHz to 166 GHz were excited. To avoid reflections, caused by the required vacuum barrier window, the gyrotron was equipped with a Brewster window. The significant influence on the mode spectrum can be seen in Fig. 5. Practically all modes are coupled out with the same intensity. Only at frequencies where the radial mode indices change (see Fig. 6), the power levels are slightly reduced. To be able to compare the gyrotron cavity internal field levels for corresponding modes, the values measured with a conventional single-disk window are corrected for the window reflection: $P_{cor} = P_{out}/(1-r^2)$. The results are summarized in Fig. 6. Only for vanishing window reflections the same results were achieved. Whereas modes located at high reflections are coupled out even less than that expected by the correction. These results indicate that even by using a q.o. mode converter, window reflections cannot be neglected.

o   without reflections (Brewster window)

■   with reflections (conventional window)
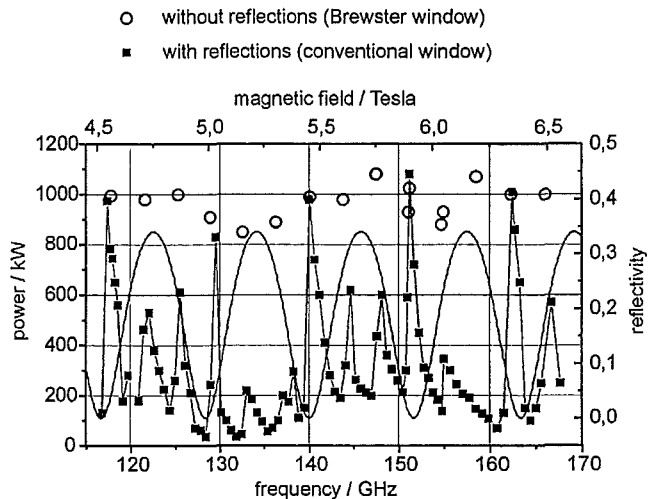
Fig. 5: Reflectivity of the conventional single-disk window versus frequency and calorimetrically measured output power versus magnetic field.

A 0.5 MW, 118 GHz, $TE_{22,6}$ Gyrotron (planned for operation up to 210 s pulse length) with cryogenically-edge-cooled single-disk sapphire window was developed and tested in collaboration with CEA Cadarache, CRPP Lausanne and Thomson Tubes Electroniques [10]. Up to now, 0.53 MW pulses with a duration of 5 s have been achieved at an efficiency of 32 % without depressed collector.
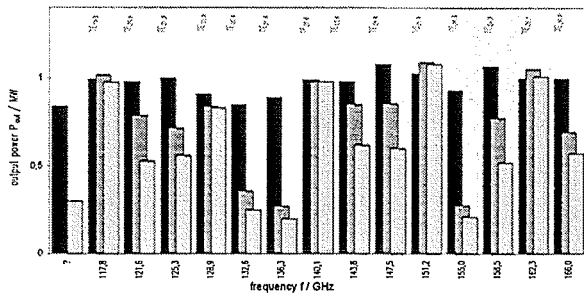
Fig. 6: Output power at different frequencies for
a) Brewster window (dark bars)
b) conventional window (light bars) and values
corrected for reflections (gray bars).

Literature:

[1] B. Piosczyk, O. Braz, G. Dammertz, C.T. Iatrou, S. Kern, M. Kuntze, A. Möbius, M. Thumm, V.A. Flyagin, V.I. Khishnyak, V.I. Malygin, A.B. Pavelyev, V.E. Zapevalov, IEEE Transactions on Plasma Science 25(3), 1997, 460-469.

[2] C.T. Iatrou, O. Braz, G. Dammertz, S. Kern, M. Kuntze, B. Piosczyk, M. Thumm, IEEE Transactions on Plasma Science 25(3), 1997, 470-479.

[3] B. Piosczyk, O. Braz, G. Dammertz, C.T. Iatrou, S. Kern, M. Kuntze, G. Michel, A. Möbius, M. Thumm, V.A. Flyagin, V.I. Khishnyak, A.B. Pavelyev, V.E. Zapevalov, Proc. 10th Workshop on ECE & ECRH, Ameland, Netherland, 1997.

[4] M. Thumm, O. Braz, G. Dammertz, C.T. Iatrou, S. Kern, M. Kuntze, G. Michel, A. Möbius, B. Piosczyk, Proc. MIOP97, Sindelfingen, 1997, 96.

[5] B. Piosczyk, O. Braz, G. Dammertz, C.T. Iatrou, S. Kern, M. Kuntze, G. Michel, A. Möbius, M. Thumm, V.A. Flyagin, V.I. Khishniyak, A.B. Pavelyev, V.E. Zapevalov, Conf. Dig. 22nd Int. Conf. Infrared and Millimeter Waves, Wintergreen, Virginia, USA, 1997, 114-115.

[6] O. Braz, A. Arnold, M. Losert, A. Möbius, M. Pereyaslavets, M. Thumm, Conf. Dig. 21th Int. Conf. Infrared and Millimeter Waves, Berlin, 1996, ATh6, ISBN 3-00-000800-4.

[7] O. Braz, A. Arnold, H. Kunkel, M. Thumm, Conf. Dig. 22nd Int. Conf. Infrared and Millimeter Waves, Wintergreen, Virginia, USA, 1997, 21-22.

[8] G. Dammertz, O. Braz, M. Kuntze, B. Piosczyk, M. Thumm, Conf. Dig. 22nd Int. Conf. Infrared and Millimeter Waves, Wintergreen, Virginia, USA, 1997, 150-151.

[9] O. Braz, G. Dammertz, M. Kuntze, M. Thumm, Conf. Dig. 22nd Int. Conf. Infrared and Millimeter Waves, Wintergreen, Virginia, USA, 1997, 148-149.

[10] E. Giguet, P. Thouvenin, C. Tran, P. Garin, M. Pain, S. Alberti, M.Q. Tran, M. Thumm, Conf. Dig. 22nd Int. Conf. Infrared and Millimeter Waves, Wintergreen, Virginia, USA, 1997, 104-105.

Staff:

J. Anderer (from 1.10.96, Uni Karlsruhe)
H. Baumgärtner
E. Borie
O. Braz (Uni Karlsruhe)
H. Budig
A.K. Chopra (1.4.-30.6.97, guest scientist)
G. Dammertz
C. DelRio (from 1.4.97, guest scientist)
P. Grundel
S. Henry (from 1.10.96, guest scientist)
C. Iatrou (to 31.12.96, guest scientist)
S. Illy
H. Kunkel
K. Koppenburg (from 1.1.97, Uni Karlsruhe)
M. Kuntze
W. Leonhardt
G. Michel (Uni Karlsruhe)
A. Möbius
N. Münch
B. Piosczyk
J. Szczesny
M. Thumm
R. Vincon

High Power ECH Windows
(includes ITER Tasks T25, T245/6, T360, D321 and D351)

1. Introduction

High unit power, in excess of 1 MW, and high-efficiency gyrotrons significantly lower the cost of Electron Cyclotron Wave (ECW) systems by reducing the size of the auxiliary support equipment (power supplies, cooling system, number of sc magnets, ...). CW operation is required for some of the anticipated ITER applications: 3 s for start-up, 100 s for heating to ignition and 100-1000 s for current drive. In order for the ECW systems to perform these functions a window has to be developed to serve as both the tritium containment barrier on the torus and as the output window on the tube. The former application is technically more demanding as the torus window must also serve as a high pressure barrier during off-normal events (0.5 MPa overpressure capability), should not use FC-cooling liquid, must not degrade unacceptably under modest neutron and γ irradiation (and x-rays), and, in the case of cryo-cooling, must be prevented by a cold trap from cryo-pumping.

Starting from the previously examined concept [1] of a liquid nitrogen edge cooled sapphire single-disk window at FZK, a number of alternative concepts have been considered in additional field studies related to the coolant (LNe, 27K; H_2O, 293 K) window material (diamond, silicon) and the window geometry (circular, elliptical, rectangular), by which concepts the potential could be enhanced of achieving 1 MW transmission power. Furthermore, the frequency (140 GHz, 170 GHz) and the power profile (Gaussian, flat, annular) have been taken into account as sub-parameters. A very promising material is Chemical Vapor Deposition (CVD)-diamond which nowadays can be manufactured in window disks of up to 100 mm diameter and 2.5 mm thickness. A water-cooled diamond window would provide the two very important advantages, namely employing a cheap and simple as well as effective coolant.

2. CVD-Diamond Window

Diamond is attractive due to its good mechanical properties, modest dielectric constant, relatively low loss and excellent thermal conductivity. The last point (the thermal conductivity of diamond is at least 40 times higher than that of sapphire) will allow a 2 MW CW transmission through a single-disk water-edge-cooled window at room temperature.

The temperature dependence of the loss tangent of CVD-diamond (DeBeers, diameter = 40 mm, thickness = 1.1 mm) at 145 GHz is presented in Fig. 1 together with sapphire (HEMEX grade) and Au-doped HR-silicon.

Current CVD capabilities have allowed for tests with diamond disks of up to 100 mm diameter and 2.5 mm thickness. In the temperature range 200-370 K the loss tangent and the permittivity of diamond are practically constant [2]. This is not the case for sapphire and silicon. The frequency dependence of the loss tangent of sapphire, diamond and silicon is proportional to f, $1/f^{1/2}$ and 1/f, so that the absorbed power is proportional to f^2, $f^{1/2}$ and constant, respectively. The loss tangent values of the large diameter CVD-diamond disks are approximately $5 \cdot 10^{-5}$ with tendency to decrease, so that we consider a value of around $2 \cdot 10^{-5}$ as feasible. Manufacturers (DeBeers) claim that they also can produce disks with up to 160 mm diameter which could be used as Brewster windows [3].

In order to validate the low-power loss tangent measurements on large-size CVD-diamond disks, a first series of experiments using a 170 GHz, 0.2 MW, 10 s JAERI/Toshiba gyrotron was

performed [4]. The dielectric loss tangent has been determined to be $tan\delta = 1.3 \cdot 10^{-4}$ which is in good agreement with
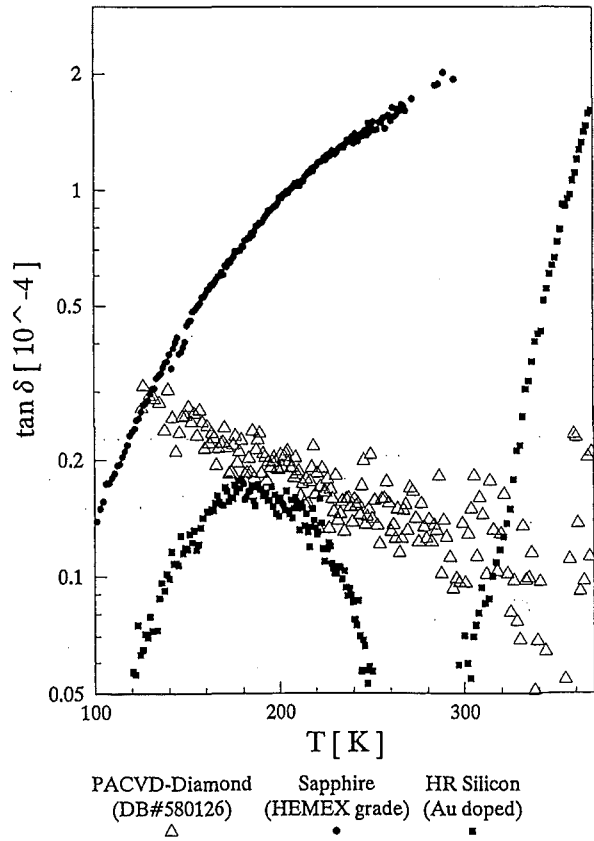
Fig. 1: Temperature dependence of $tan\delta$ at 145 GHz [2].

the low power value. By comparing the experimental results with numerical simulations the thermal conductivity was estimated to be about $k \approx 1800$ W/mK. Finite element calculations showed that the peak temperatures for CVD-diamond disks with a wide range of $tan\delta$ and ratio of window aperture to disk diameter are acceptable (central temperature below 300°C). The window disk in corrugated HE_{11} waveguide with 57.5 mm inner diameter should have an outer diameter of approximately 85-90 mm. In collaboration with DeBeers Company, FZK is successfully performing metallization and brazing tests on cheap (gray) diamond samples with up to 100 mm diameter and 1 mm thickness (Fig. 2).

Thermomechanic cycling at temperatures up to 450 °C did not lead to diffusion degradation of the brazing and no leaks occured. Finite element stress calculations including brazing/bonding stress show that the maximum principal stress is located at the window brazing (205 MPa) and is always present. During a 0.5 MPa overpressure event the max. stress increases to 290 MPa and the transmission of 1 MW microwave power finally increases the max. stress to 300 MPa. All these stress values are upper limits since a rigid connection between brazing collar and window disk was assumed. Because the ultimate bending strength of CVD diamond is 600-900 MPa all stresses are well below the admissible limits.
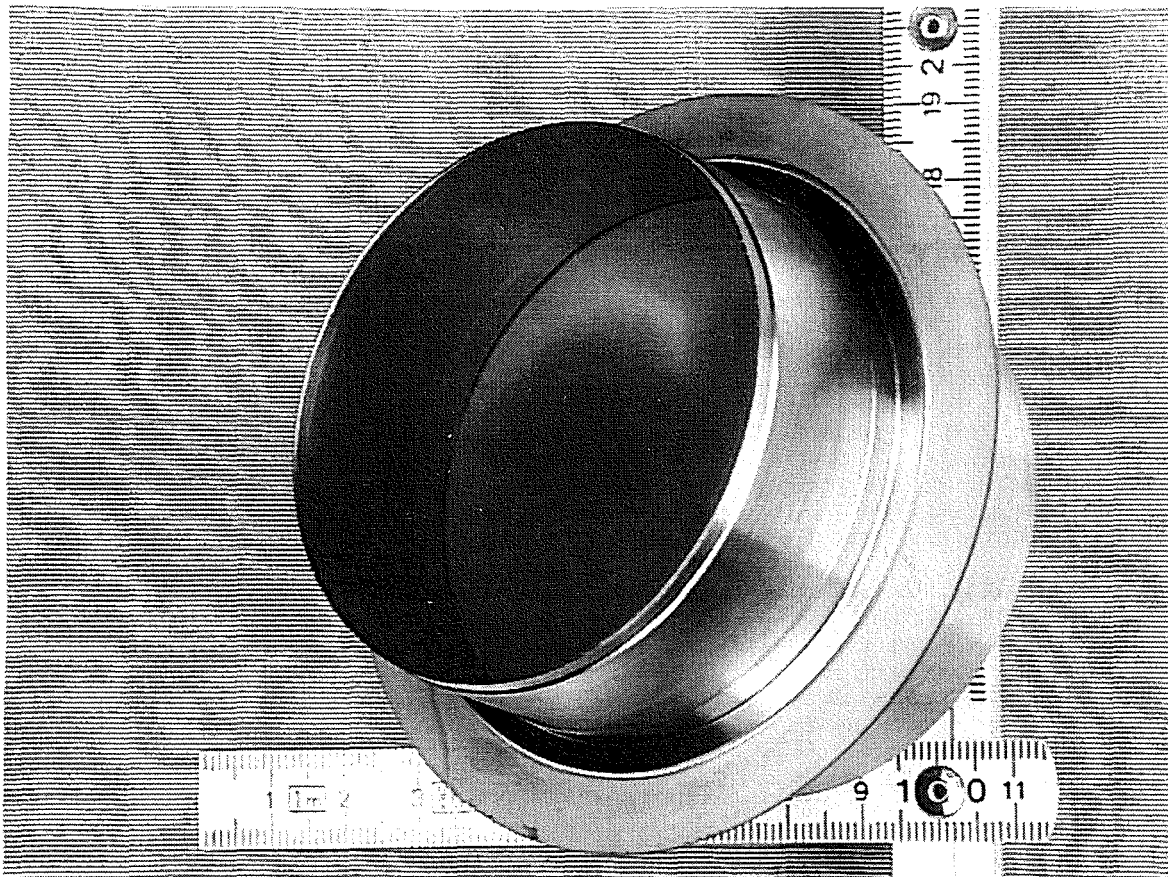
Fig. 2: Photography of a 100 mm diameter, single-diskdiamond window.

4. Design of the ITER Window Block

The proposed ITER window block consists of a flat array of window assemblies together with the maintenance and the isolation vacuum valves [5]. We are considering one major option that can easily carry 1 MW CW power at 170 GHz: Edge-cooled (Water, 293 K) twin CVD-diamond window in a corrugated HE_{11} waveguide with 57.7 mm inner diameter. Through the use of a double window, window failures can be easily detected (as on the JET LH and ICRH system) [Fig.3].

A very high vacuum ($\approx 10^{-7}$ Pa) can be achieved within the interspace between the two window disks. Since the total volume is small, vacuum pumping can be done with only one Vac-Ion pump. Any failure of either window is detectable as a pressure rise on the ion pump even in the case in which a lower grade vacuum ($\approx 10^{-3}$ Pa) is present on the opposing surfaces. Bandwidth calculations show, that the disk distance should be e.g. 52.9 mm = 30 λ. Up to now there exist no measruments of tritium permeation through CVD diamond.

For a loss tangent of $1.815 \cdot 10^{-5}$ the rf-power absorption in one window disk is approximately 400 W. With a heat transfer coefficient of 12 kW/m^2K to the cooling water (flow velocity = 3 m/s) the central window temperature will not be higher than approx. 327 K and the edge temperature is about 298 K. The pre-design of the window assembly and general assumptions, classifications, guidelines and procedures for the maintenance have been done.

Design considerations for a window block employing LNe (30 K) edge-cooled single-disk sapphire windows were carried out [5]. This much more complicated option is kept as back-up solution.
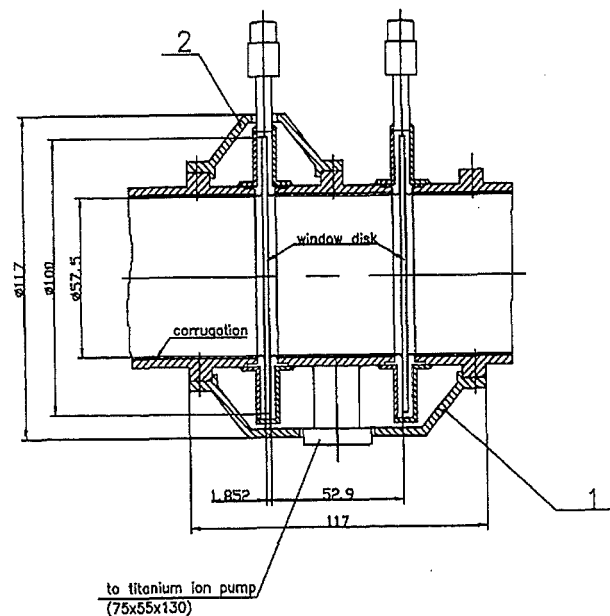
Fig. 3: Water-edge-cooled, double-disk diamond window unit.

A broadband ECH system employing step-tunable gyrotrons is being developed for the start-up system and a similar system could also be considered for heating and current drive. Two possible solutions for multi-frequency high-power millimeter

wave diamond windows are considered: multipass-band window and Brewster window. First successful experiments at FZK with a conventional cavity gyrotron equipped with a fused quartz Brewster window (pulse duration 1 ms) gave 1 MW output power for all operating mode series in the frequency range from 114 to 166 GHz (frequency tuning in 3.7 GHz steps) by variation of the magnetic field in the cavity) [6].

Literature:

[1] M. Thumm, O. Braz, H.E. Häfner, R. Heidinger, A. Möbius, P. Norajitra, G. Soudée, FZKA Report 5808, Karlsruhe, 1996.

[2] R. Heidinger, R. Schwab, R. Spörl, M. Thumm, Conf. Dig. 22nd Int. Conf. Infrared and Millimeter Waves, Wintergreen, Virginia, USA, 1997, 142-143.

[3] O. Braz, M. Thumm, A. Kasugai, K. Sakamoto, K. Takahashi, M. Tsuneoka, T. Imai, Conf. Dig. 22nd Int. Conf. Infrared and Millimeter Waves, Wintergreen, Virginia, USA, 1997, 144-145

[4] O. Braz, G. Dammertz, M. Kuntze, M. Thumm, 1997, D-Band Frequency Step-Tuning of a 1 MW Gyrotron using a Brewster Output Window, Int. Journal of Infrared and Millimeter Waves, 18, 1465-1477

[5] M. Thumm, O. Braz, R. Heidinger, S. Henry, A. Hofmann, M. Makowski, G. Soudée, FZK Report 5909, Karlsruhe, 1997.

[6] O. Braz, T. Imai, K. Kasugai, K. Sakamoto, K. Takahashi, M. Thumm, M. Tsuneoka, 1997, High power millimeter wave transmission though CVD diamond, Int. Journal of Infrared and Millimeter Waves, 18, 1495 - 1503

Staff:

O. Braz
R. Heidinger
S. Henry (from 1.10.96, guest scientist)
A. Hofmann
N. Münch
B. Schulz
R. Spörl
R. Schwab
M. Thumm

T 246 (G 55 TT 01)
Ceramics for Heating and Current Drive and Diagnostic Systems

The mm-wave investigations of radiation effects on insulator materials covered the candidate materials for high power window materials for electron cyclotron (EC) systems as well as for transmission windows for EC emission spectroscopy. The major part of the dielectric property studies were performed at 145 GHz in the ambient and cryogenic temperature ranges. Steps were successfully taken to install measurement systems for studies at 90 GHz and 180 GHz at room temperature.

The work for the mm-wave data base related to the cryogenically cooled Sapphire window was concluded by a coherent measurement series of the specimen set from the previous GKSS (pool temperature) and Petten (LN2 temperature) irradiations [1]. The lack of any evident difference between the loss of Sapphire irradiated at 2 - $4 \cdot 10^{16}$ n/cm^2 at Petten to the loss curves obtained for fluences up to $1 \cdot 10^{17}$ n/cm^2 at GKSS thus consolidated the conservative estimates to the tolerable fluence limits at the torus window.

The progress in CVD diamond growth which was accompanied by mechanical, thermal and mm-wave property measurements has made available first discs for high power transmission experiments [2]. In the frame of the ITER cooperation, spatially resolved dielectric loss measurements on windows grown for JAERI and FZK were performed and marked inhomogeneities in mm-wave absorption were put to evidence [3,4]. The feed-back to the producer has led to discs with improved homogeneities. The first neutron irradiation to 10^{16} n/m^2 on CVD diamond specimens for dielectric property measurements showed for advanced discs no significant modification of the low loss behaviour (cf Fig. 1) [1]. Another neutron irradiation to 10^{17} n/cm^2 is prepared for which a disc from the window with optimized homogeneity could be purchased.

In parallel to the study on CVD diamond, the neutron irradiation to 10^{16} n/cm^2 served to investigate the behaviour of doped Silicon, which is maintained in the programme for a fall-back window concept. It could be shown that the lattice damage produced at this fluence level did not deteriorate the ultralow loss properties of this special material. Even the lattice damage was effective in the undoped material to produce the reduction in dielectric loss to the same extent as it is realized by the gold doping procedure [5,6].

Single crystalline quartz was studied for its use in transmission windows for EC emission spectroscopy. Following the previous comparison between unirradiated specimens and those from the cryogenic irradiation, a direct comparison to material from the GKSS irradiation at pool temperature was performed. While there is an early onset of radiation increased mm-wave loss, the specimen from the cryogenic irradiation again perfectly fits into the ranking defined by the irradiation at pool temperature (cf. Fig. 2) [1].

Finally, a specimen geometry was established for alumina discs which is suited for electron irradiations to induce the RIED effect and in which mechanical strength can be assessed without significant contributions from surface damage. The comparison between electron irradiated discs at CIEMAT, Madrid, and unirradiated control specimen produced in ball-to-ring tests mechanical strength data which cannot be differentiated within the scatter band of Weibull statistics.
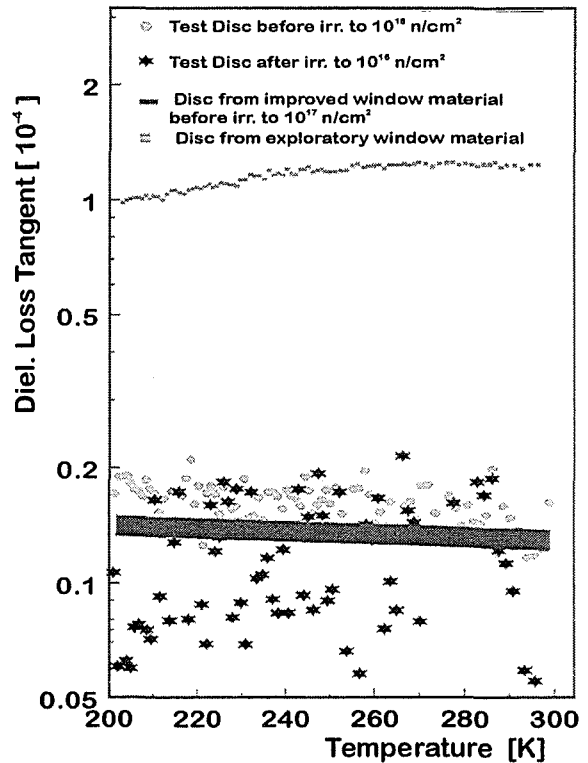
Fig. 1: The dielectric loss measured at 145 GHz for advanced CVD diamond grades to assess the radiation effect of a first neutron irradiation 10^{16} n/cm^2 and to prepare a second irradiation to 10^{17} n/cm^2.
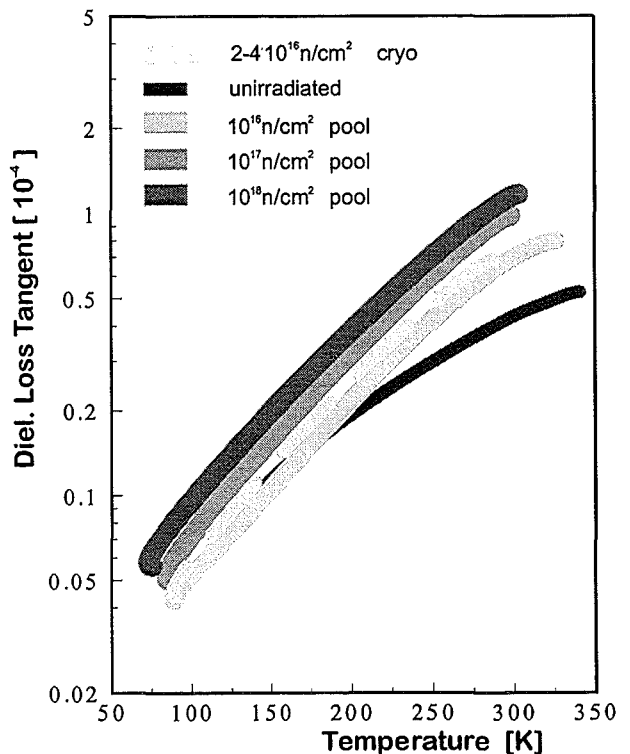
Fig. 2: Radiation-increased dielectric loss in neutron irradiated single crystal quartz (ordinary ray) measured at 145 GHz.

— 17 —

Literature:

[1] R. Heidinger, A. Ibarra, J. Molla, Pre- and post-irradiation studies on mm-wave losses in reference window materials for electron wave systems. Accepted contribution to 8th Int. Conf. on Fusion Reactor Materials (ICFRM-8), Sendai (J), 26-31/10/97

[2] A. Ibarra, R. Heidinger, J. Molla, CVD diamond for high power rf applications in nuclear fusion reactors. Proc. 5th Int. Symposium on Diamond Materials, Paris (F), August 1997

[3] R. Heidinger, R. Schwab, R. Spörl, M. Thumm, Dielectric loss measurements in CVD diamond windows for gyrotrons. Proc. 22nd Int. Conf. on Infrared and MM-Waves (IR+MM22), Wintergreen (USA), 20-25/7/1997

[4] R. Spörl, R. Schwab, R. Heidinger, Dielectric loss measurements in CVD diamond windows for gyrotrons. Proc. 9th Joint Russian-German Workshop on ECRH and Gyrotrons, Karlsruhe/Stuttgart/München, 22-27/6/1997

[5] V.V. Parshin, R. Heidinger, B. Schulz, New results on the mm-wave dielectric properties of pure and doped silicon. Proc. 9th Joint Russian-German Workshop on ECRH and Gyrotrons, Karlsruhe/Stuttgart/München, 22-27/6/1997

[6] J. Molla, R. Vila, R. Heidinger, A. Ibarra, Radiation effects on dielectric loss of Au-doped silicon. Accepted contribution to 8th Int. Conf. on Fusion Reactor Materials (ICFRM-8), Sendai (J), 26-31/10/97

Staff:

M. Blumhofer
R. Heidinger
P. Severloh
H. Zimmermann

The determination of the thermal conductivity of Sapphire irradiated at 4.2 K has been started and will be finished this year.

The investigation of fusion ceramics (SiC, AlN, Al_2O_3) irradiated to higher doses except irradiated Li_4SiO_4 has been finished.

Staff:

G. Haase
M. Mangai
B. Schulz
G. Ziegler

Thermophysical Properties of Ceramic Isolating Materials

Samples of Si single crystal and Au-doted Si-single crystal BeO and CVD diamond were irradiated ($10^{20} n/m^2$) and investigated with the laserflash method to detect potential reduction of thermal conductivity. The relevant results are given in the table.

Thermal conductivity of irradiated and non-irradiated potential window materials (irradiation temperature 300 K for Si, diamond and 573 K for BeO)			
Material	Temperature	Thermal conductivity non-irradiated	Thermal conductivity irradiated
Si-EK	300 K	145 W/mK	unchanged
	400 K	106 W/mK	unchanged
Si-EK (Au-dotiert)	300 K	140 W/mK	unchanged
	400 K	106 W/mK	unchanged
BeO	300 K	201 W/mK	
	400 K	160 W/mK	unchanged
CVD Diamond	300 K	1800 W/mK	400 W/mK

Only the diamond shows a reduced thermal conductivity. The reason is the very high Debye temperature of diamond (2000 K), which makes its irradiation temperature of 300 K comparable to a temperature of 100 K for the other materials.

T 221 (G 17 TT 13)
Plasma Facing Armour Materials (2)

This task was started recently by studying - in the frame of a JET task - tritium release from JET graphite tiles exposed to a D-T plasma. Samples were prepared from the tiles by drilling a 7.6 mm $\varnothing$ cylinder and cutting the cylinder into ~1 mm thick disks. The samples were purged with 10 cm^3/min He + 0.1% H_2 and heated up to 1100 °C with ~16 °C/min. The tritium release rate as function of time, i.e. temperature, is determined from the tritium concentration of the purge gas downstream of the sample as measured with a highly sensitive proportional counter.

Only the disks which were in contact with the plasma showed a significant tritium release of ~1.1 10^5 Bq/g, for all other disks the release was below the detection limit. This is in agreement with the results obtained by combustion and liquid scintillation counting [1]. The release starts at ~700 °C and reaches a maximum at ~850 °C. At still higher temperatures the release decreases rapidly. Concerning detritiation of the tiles, these results indicate that temperatures well above 700 °C are necessary to liberate the tritium by purging with He + 0.1% H_2.

The investigation will be continued by studying tritium inventory and release kinetics of co-deposited (graphite) layers ("flakes"), removed from the surface of the JET inner wall. In addition, a collaboration with the Russian Academy of Science concerning retention of deuterium in co-deposited D-Be layers is in preparation.

Literature:

[1] R. Penzhorn, private communication

Staff:

E. Damm
R. Penzhorn
R. Rolli
H. Werle
H. Ziegler

T 226 b (G 17 TT 25)
Plasma Disruption Simulation

During the period to be reported here the main activities were on further improvement, on validation and application of the 2D radiation magnetohydrodynamic (R-MHD) code FOREV-2 for analysis of disruption erosion under realistic ITER conditions [1]. Moreover the conditions for enhanced erosion were clarified, a detailed analysis of electric fields and ExB drifts in cold plasma / hot plasma interactions was done [2, 3] and an analytical model for the modulation of erosion in case of tilted targets was developed [4].

FOREV-2 is now operable with a time step size of 10^{-9} s and with an improved forward reverse scheme for the 2D radiation transport which takes into account the angular dependence of the radiation flux in a simplified manner by using averaged cosines [1]. Fully consistent 2D R-MHD calculations for the ITER slot divertor with up to 10000 meshes, 24 frequency groups and physical time up to 1 ms now can be completed within 25 hours of CPU time on a RS-6000 workstation.

FOREV-2 results for typical ITER conditions are shown in Figs. 1 - 4 for tilted targets, two different power densities of the incoming hot plasma, realistic unsymmetrical power density profiles across the SOL and the different orientations (1) and (2) of the inclined target relative to the power density profile. Power density profiles and corresponding target erosion profiles are shown in Figs. 1 and 2 for the two different target orientations (1) and (2). The differences in erosion at identical power density but different target orientations can be understood from Fig. 3 showing 2D density profiles in the plasma shield and side wall erosion. The density lines correspond to densities in the range 2.5×10^{17} to 4×10^{18} cm^{-3}. The target plasma is flowing along the tilted target downwards. In case of upstream separatrix strike point the downward flow results in a continuous depletion of target plasma at the strike point and thus in higher erosion. Fig. 3 also shows the erosion profile at side walls caused by radiation escaping laterally from the radiating plasma shield. Fig. 4 shows the time evolution of the peak target erosion. For the 1 MW/cm^2 case the peak erosion with upstream separatrix is larger than for the case with 10 MW/cm^2. The reason is upstream target erosion by radiation in the 10 MW/cm^2 case and subsequent downstream movement of the plasma shield providing increased shielding at the separatrix strike point for the 10 MW/cm^2 case.
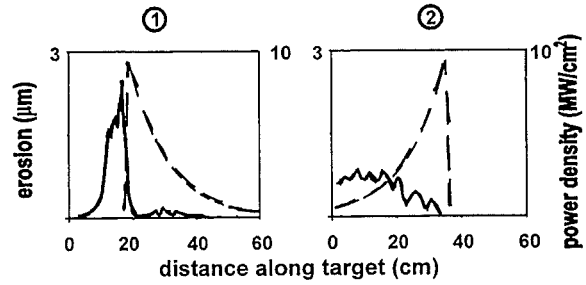
Fig. 2: Realistic power density profile and target erosion at 500 μs. Peak power density 10 MW/cm^2.
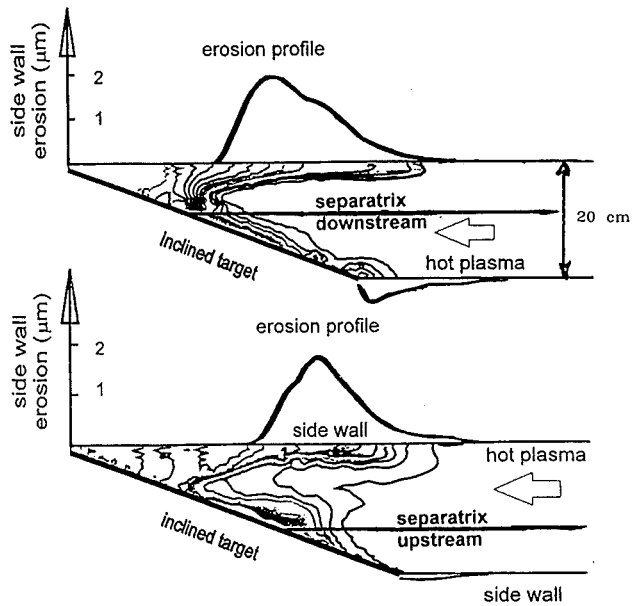
Fig. 3: 2D density distribution in the plasma shield and side wall erosion at 500 μs. Peak power density 10 MW/cm^2.
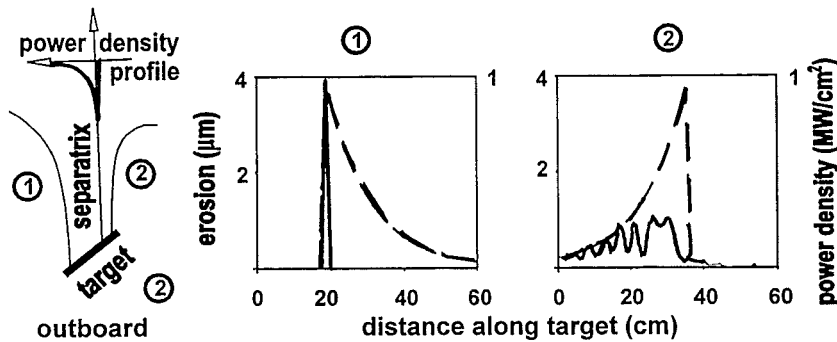
Fig. 1: ITER slot divertor outboard section schematically. Realistic power density profile across the SOL and erosion for the two different target inclinations at 500 μs. Peak power density 1 MW/cm^2.
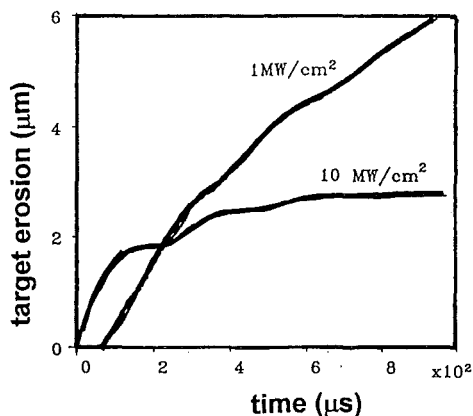
Fig. 4: Comparison of time evolution of peak target erosion.

Electric fields in the plasma shield hot plasma interaction region can result in ExB drifts of the plasma shield of the hot plasma or both which influence the plasma shield efficiency. For inclined impact of the magnetized hot plasma a nonstationary Vlasov Maxwell model was used for calculation of electric fields and an uncompensated current was assumed in toroidal direction [2, 3]. In the hot plasma region a significant potential drop occurs resulting in a lateral drift motion of the impacting hot plasma which is shown schematically in Fig. 5. The evolution of an additional magnetic field could result in a self compression of the plasma shield. The shock wave dynamics of this self compression, the dynamics of the ExB drift of the hot plasma and the consequences for the plasma shield stability and for erosion still need more detailed investigations.

Enhanced erosion by phase transitions inside of the material was analyzed. In the numerical model a third moving boundary was introduced describing the moving phase transition. This model was applied to experimental results as obtained from electron beam and plasma stream target experiments. In Fig. 6 a comparison of enhanced erosion of beryllium is shown for a 120 keV electron beam. Assuming a damage threshold energy of 55 kJ/gmol good agreement between calculated and measured values is achieved [5]. Melt layer erosion due to instabilities remains a still open question. This requires experimental results from disruption simulation experiments with power densities of the impacting plasma stream well below 1 MW/cm^2.

[5] V.T. Astrelin, A. Burdakov, P. Chebotaev, V. Filipov, V. Koidan, H. Würz, "Hot electron target interaction experiments at the GOL-3 facility", submitted and accepted for publication in Nucl. Fusion.
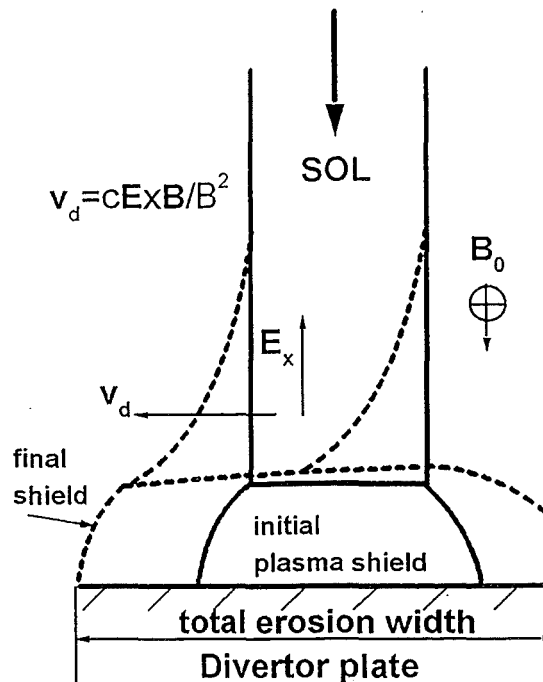
Fig. 5: ExB drift of impacting hot plasma due to electric field in the cold/hot plasma interaction region schematically.
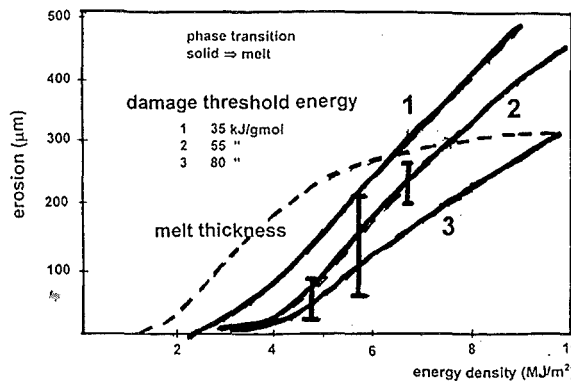
Fig. 6: Comparison of calculated and measured erosion for Beryllium under irradiation with electrons of 120 keV and time duration 5 ms.

Literature:

[1] S. Pestchanyi, H. Würz, B. Bazylev, F. Kappler, I. Landman, "Results from 2D radiation magneto-hydrodynamics calculations of the interaction of ITER disruptive plasma with the slot divertor", 24th EPS Conf. on Controlled Fusion and Plasma Physics, Berchtesgaden, June 9 - 13, 1997.

[2] I. Landman, H. Würz, "Electric stopping in hot plasma wall interactions", 24th EPS Conf. on Controlled Fusion and Plasma Physics, Berchtesgaden, June 9 - 13, 1997.

[3] I. Landman, H. Würz, "Electric fields and ExB drifts in hot plasma cold plasma interactions", submitted for publication in Physics of Plasmas.

[4] H. Würz, B. Bazylev, F. Kappler, I. Landman, S. Pestchanyi, G. Piazza, "The plasma shield in ITER plasma wall interactions", Fusion Technology 1996, Vol. I, 1997, p. 191

Staff:

B. Bazylev
F. Kappler
L. Landman
S. Pestchanyi
H. Würz

T 227 (G 17 TT 25)
Tritium Permeation and Inventory

**Subtask 2:   H/T Retention Studies in Neutron Irradiated
                    Graphites, CFCs and Doped C Composites**

Carbon—based materials and beryllium are candidates for protective layers on plasma-facing components of fusion reactors. In contact with the D-T-plasma these materials absorb tritium and it is anticipated that tritium retention increases with neutron damage due to neutron-induced traps, leading eventually to tritium inventories which represent a safety problem. Previous investigations indeed show that for carbon-based materials tritium retention increases with neutron damage in the range ≤ 0.1 dpa by two to three orders of magnitude [1, 2]. A similar effect, i.e. a 10 to 20 times larger tritium inventory in irradiated (~ 1.6 dpa) compared to unirradiated samples has been observed recently also for beryllium [3] and has been discussed in the previous Annual Report. In the reporting period ITER-representative CFC (carbon fibre composites) have been studied.

Tritum retention and its dependence on neutron damage is studied by loading unirradiated and irradiated samples at elevated temperatures in a H_2+5 ppm T_2 atmosphere (2 bar, 1000 °C, 6 h) and determining the tritium uptake by annealing (1100 °C, several h, purging with He+0.1 % H_2).

Three types of CFC were studied: 2-d type CX2002 U (Japan), 3-d type N112 (SEP Bordeaux) and 2-d type A05 (Carbon Lorraine). The samples were irradiated in the tests CERAM and MACIF at temperatures between ~ 400 and 1000 °C to a fast neutron fluence corresponding to a damage between 0.4 and 1.8 dpa.

The tritium retention in material A05 was observed to be about a factor three higher than that of the other materials. For all three materials the tritium retention of the irradiated samples was found to be about a factor ten higher than that of the unirradiated samples (Fig. 1).

Literature:

[1] H. Kwast, H. Werle, C.H. Wu, Physica Scripta T 64 (1996) 41.

[2] C.H. Wu et al., "EU Results of Neutron Effects of PFC Materials" ISFNT-4, Tokyo, April 6 - 11, 1997.

[3] R. Rolli, S. Rübel, H. Werle, C.H. Wu, "Influence of Neutron Irradiation on the Tritium Retention in Beryllium", Third IEA Int. Workshop on Beryllium Technology for Fusion, Mito City, Japan, Oct. 22 - 24, 1997.

Staff:

E. Damm
R. Rolli
H. Werle
H. Ziegler

T 216 (C 16 TT 76)
Shield Blanket Fabrication and Testing

Four small scale first wall mock-ups had been specified before for the ITER task WP4.1. They should be capable of long-term thermal fatigue testing the Cu/SS joints in the first wall (FW) area by making use of the FIWATKA test facility. The mock-ups were designed to have a 250 by 110 mm heated FW surface and to be 80 mm thick without an Be protection layer. The mock-ups should differ concerning the type of CU (DS-Cu and PH-Cu), the joining technique (solid HIP and powder HIP), and the manufacturer (NNC and Framatome).

During the report period the FIWATKA facility was up-graded for performing the long term thermal fatigue tests with four small scale mock-ups in parallel. The mock-ups were originally scheduled to be available for testing early in 1997; according to recent plans they will be supplied by the NET Team in September 1997.

Staff:

E. Eggert
G. Hofmann

T 218 (G 17 TT 82)
Shielding Neutronics Experiments

The experimental validation of the nuclear performance of the shielding system is one of the tasks in the Engineering Design Activities for ITER. In a joint Japanese/US effort the outboard blanket is studied, whereas experiments dealing with the inboard shield are carried out by European and Russian groups [1].

The inboard shield mock-up includes first wall, blanket, vacuum vessel and toroidal field coils and was assembled at the Frascati Neutron Generator [2]. TU Dresden contributed to the joint programme with measurements of neutron and gamma flux spectra inside the mock-up and FZK by computational analyses. The reliable knowledge of the spectra is important in order to understand neutron and gamma transport inside the assembly; furthermore they are the basic weighting functions for integral quantities such as reaction rates, nuclear heating, gas production and radiation damage.
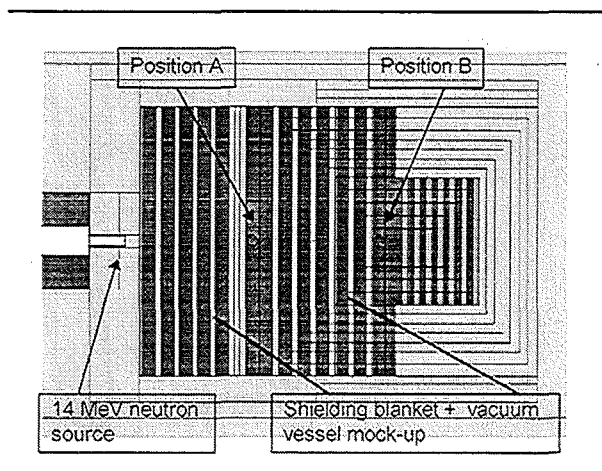
Fig. 1: MCNP model of the ITER shield mock-up assembly

The measurements were carried out on the central axis of the assembly at the two positions A and B (Fig. 1). Position A corresponds to the back plate of the shield blanket. Position B is located near the boundary of the vacuum vessel to the coil. The measured flux spectra were presented and compared with calculated spectral fluxes in the previous Annual Report [3].

More detailed calculational analyses have been performed to compare calculated and measured integral neutron and photon fluxes and arrive at C/E - (calculation over experiment) values that provide safety margins for ITER design calculations. Tables 1 - 4 show the results obtained with detailed three-dimensional MCNP-calculations and nuclear cross-sections from the EFF-2, -3 (European Fusion File), FENDL-1 (Fusion Evaluated Nuclear Data Library) and JENDL-FF (Japanese Fusion File) data libraries. There are included associated uncertainties from the experiment (systematics) and the calculation (statistical errors). Main result from the comparison is that the neutron flux is underestimated in the calculations by about 10 % at the back of the shielding blanket and by up to 30% in the region of the vacuum vessel. For the photon flux there is better agreement with an underestimation of no more than 10% at the back of the vacuum vessel.

In order to check the consistency of experimental results obtained for the mock-up with different methods, reaction rates which have been measured by groups of CEA [4] and ENEA [5] were calculated utilising the measured spectral neutron fluxes. The cross sections of these reactions were taken from the International Reactor Dosimetry File (IRDF-90) [6]. All of the

deduced reaction rates agreed with the measured integral values within the uncertainty intervals.

Nuclear heating in SS316 of the mock-up is dominated by gamma interaction processes [7]. With the measured gamma flux spectra and KERMA data (heating numbers) from FENDL-1 [8] it was calculated and compared with TLD measurements of the ENEA group [5]. Agreement was found within the uncertainty range for these data, too.

The good consistency of measured reaction and heating rates with the values derived from the measured flux spectra suggests to determine also the nuclear design parameters gas production and radiation damage on the basis of the experimental spectra. Tables 5 and 6 show for positions A and B, respectively, helium production, hydrogen production, and displacement rates in SS316 calculated with the measured neutron flux spectrum. The values are normalised to one source neutron and 10^{24} atoms of SS316. For comparison with ITER-relevant neutron fluences, the responses were also normalised to a fluence of 1.0 MWa/m^2 corresponding to 1.33*10^{25} source neutrons of 14.8 MeV energy. Due to the unavoidable use of a point neutron source in the experiment, the corresponding values at the same locations in the ITER torus will be higher [9]. Corresponding results of MCNP-calculations for the ITER torus with the proper plasma volume source and blanket/shield configuration are included in tables 5 and 6. The given responses have been calculated for the inboard shield system of ITER (at torus mid-plane) at the locations corresponding to the positions A and B in the mock-up. As compared to the responses derived from the experimental spectra, the actual ITER values are higher by a factor 2 at position A (back plate of the shielding blanket) and between a factor 4 (dpa) and 6 (gas production) at position B (back of the vacuum vessel).

New data evaluated within the framework of an IAEA Co-ordinated Research Programme [10] were used for the α-production cross section on ^{56}Fe. The participants estimate the uncertainty with 5% and conclude that the total uncertainty for SS316 should also not exceed 5% if the cross sections for the less abundant isotopes of Fe and for Cr and Ni nuclides from libraries such as ENDF/B-VI (adopted for FENDL-1) are used. Together with the flux uncertainties for E > 1MeV, the total uncertainty of the α-production should be less than 10%. For the (n,p) and (n,np) reactions on Fe, Cr and Ni nuclides data of the FENDL-1 library were used. The European Damage Cross Sections in IRDF-90 for Fe, Cr and Ni in steel were applied for the determination of the displacement rates.

Literature:

[1] P. Batistoni et al., Neutronics shield experiment for ITER at the Frascati neutron generator FNG, Proc. 19th Symposium on Fusion Technology, Lisbon, 1996, page 233.

[2] M. Martone, M. Angelone and M. Pillon, The 14 MeV Frascati neutron generator, Journal of Nuclear Materials, 212 (1994) 1661-1664.

[3] Nuclear Fusion Project, Annual Report of the Association Forschungszentrum Karlsruhe/EURATOM, comp. G. Kast, FZKA5858, EUR17512EN, page 44.

[4] L. Benmansour, A. Santamarina, B. Camous and H. Philibert, Neutronic measurement results of the ITER prototypical blanket shield experiment at FNG, Report CEA NT-SPRC-LEPH-96/207, Cadarache (July 1996).

[5] P. Batistoni, M. Angelone, L. Petrizzi, M. Pillon and M. Gallina, Nuclear heating measurements and analysis in the Bulk Shield Experiment, Report ENEA Frascati and EFF-Doc-492 (June 1996).

[6] N. P. Kocherov and P. K. McLaughlin, The international reactor dosimetry file (IRDF-90), Report IAEA-NDS-141, Vienna (October 1993).

[7] H. Freiesleben et al., Methods for nuclear heating mesurements in an ITER shield-blanket mock-up, Proc. 19th Symposium on Fusion Technology, Lisbon, 1996, page 1567.

[8] S. Ganesan and P. K. McLaughlin, FENDL/E - evaluated nuclear data library of neutron interaction cross-sections and photon production cross-sections and photon-atom interaction cross-sections for fusion applications, version 1.0, Report IAEA-NDS-128, Vienna (May 1994).

[9] U. Fischer, P. Batistoni, M. Pillon, Three-dimensional neutronics analyses of the ITER bulk shield experiment, Fusion Technology 1996: Proc. of the 19th Symp. on Fusion Technology, Lisbon, Portugal, 16-20 Sept. 1996, Vol. 2, p.1563-1566, Elsevier 1997

[10] A. B. Pashchenko (ed.), Improvement of measurements, theoretical computations and evaluations of neutron induced helium production cross sections, Report INDC(NDS)-358, IAEA Vienna (December 1996).

Staff:

U. Fischer
H. Freiesleben
W. Hansen
D. Richter
K. Seidel
S. Unholzer
Y. Wu

Table 1: Comparison of calculated and measured neutron fluxes at position A in the ITER bulk shield mock-up.

Energy interval [MeV]	TUD measurement	C/E				Statistical error [%]
		EFF-3	EFF-2	FENDL-1	JENDL-FF	
0.1 - 1	$(2.76\pm0.28)\cdot10^{-6}$	0.90	0.91	0.86	0.89	0.6
1 - 5	$(1.43\pm0.08)\cdot10^{-6}$	0.95	0.99	0.91	0.89	0.8
5- 10	$(2.47\pm0.13)\cdot10^{-7}$	1.02	1.02	1.04	0.97	1.0
E > 10	$(5.42\pm0.14)\cdot10^{-7}$	0.99	0.98	0.99	1.00	0.9
E > 0.1	$5.74\cdot10^{-6}\pm6.1\%$	0.94	0.94	0.88	0.91	0.4

Table 2: Comparison of calculated and measured neutron fluxes at position B in the ITER bulk shield mock-up.

Energy interval [MeV]	TUD experiment	C/E				Statistical error [%]
		EFF-3	EFF-2	FENDL-1	JENDL-FF	
0.1 - 1	$(8.78\pm0.89)\cdot10^{-9}$	0.73	0.74	0.68	0.73	0.8
1 - 5	$(2.37\pm0.13)\cdot10^{-9}$	0.84	0.86	0.77	0.78	0.9
5- 10	$(2.69\pm0.14)\cdot10^{-10}$	1.07	1.07	0.99	0.97	1.5
E > 10	$(5.79\pm0.15)\cdot10^{-10}$	0.87	0.87	0.81	0.83	1.5
E > 0.1	$1.20\cdot10^{-8}\pm7.5\%$	0.77	0.77	0.72	0.77	0.7

Table 3: Comparison of calculated and measured photon fluxes at position A in the ITER bulk shield mock-up.

Energy interval [MeV]	TUD experiment	C/E				Statistical error [%]
		EFF-3	EFF-2	FENDL-1	JENDL-FF	
0.4 - 1	$3.18\cdot10^{-6}$	1.15	1.05	0.99	1.04	0.6
1 - 10.5	$4.29\cdot10^{-6}$	1.19	1.08	1.05	1.12	0.6
E > 0.4 MeV	$7.47\cdot10^{-6}\pm2.5\%$	1.17	1.07	1.02	1.09	0.5

Table 4: Comparison of calculated and measured photon fluxes at position B in the ITER bulk shield mock-up.

Energy interval [MeV]	TUD experiment	EFF-3	EFF-2	FENDL-1	JENDL-FF	Statistical error [%]
		C/E				
0.4 - 1	$4.50 \cdot 10^{-8}$	1.06	0.96	0.89	0.96	1.0
1 - 10.5	$6.20 \cdot 10^{-8}$	1.05	0.98	0.90	0.99	0.9
E > 0.4	$1.07 \cdot 10^{-7} \pm 2.8\%$	1.06	0.97	0.89	0.98	0.8

Table 5: Comparison of gas production and radiation damage for Fe, Cr, Ni and SS-316 as derived from the measured neutron flux spectrum of mock-up position A and calculated for the ITER torus at the corresponding location of the inboard shield system.

Position A (back plate of shielding blanket)	Fe	Cr	Ni	SS-316
α-particles / $(sn^{-1} \cdot 10^{24} at)$	$1.77 \cdot 10^{-8}$	$0.35 \cdot 10^{-8}$	$0.83 \cdot 10^{-8}$	$2.95 \cdot 10^{-8}$
He production / (appm) for 1.0 MWa/m²				
Mock-up (experimental spectra)	0.236	0.046	0.110	0.392
ITER (calculated spectra)	0.380	0.08	0.273	0.733
Protons / $(sn^{-1} \cdot 10^{24} at)$	$8.49 \cdot 10^{-8}$	$1.75 \cdot 10^{-8}$	$5.77 \cdot 10^{-8}$	$1.60 \cdot 10^{-7}$
H production / (appm) for 1.0 MWa/m²				
Mock-up (experimental spectra)	1.13	0.23	0.77	2.13
ITER (calculated spectra)	1.89	0.37	1.84	4.10
Displacements / $(sn^{-1} \cdot 10^{24} at)$	$2.62 \cdot 10^{-3}$	$0.81 \cdot 10^{-3}$	$0.46 \cdot 10^{-3}$	$3.89 \cdot 10^{-3}$
Damage / (dpa) for 1.0 MWa/m²				
Mock-up (experimental spectra)	$3.48 \cdot 10^{-2}$	$1.08 \cdot 10^{-2}$	$0.61 \cdot 10^{-2}$	$5.17 \cdot 10^{-2}$
ITER (calculated spectra)	$6.62 \cdot 10^{-2}$	$1.86 \cdot 10^{-2}$	$1.47 \cdot 10^{-2}$	$9.95 \cdot 10^{-2}$

Table 6: Comparison of gas production and radiation damage for Fe, Cr, Ni and SS-316 as derived from the measured neutron flux spectrum of mock-up position B and calculated for the ITER torus at the corresponding location of the inboard shield system.

Position B (back of vacuum vessel)	Fe	Cr	Ni	SS-316
α-particles / $(sn^{-1} \cdot 10^{24} at)$	$1.86 \cdot 10^{-11}$	$0.37 \cdot 10^{-11}$	$0.90 \cdot 10^{-11}$	$3.13 \cdot 10^{-11}$
He production / (appm) for 1.0 MWa/m²				
Mock-up (experimental spectra)	$2.48 \cdot 10^{-4}$	$0.49 \cdot 10^{-4}$	$1.20 \cdot 10^{-4}$	$4.16 \cdot 10^{-4}$
ITER (calculated spectra)	$1.34 \cdot 10^{-3}$	$2.85 \cdot 10^{-4}$	$1.01 \cdot 10^{-3}$	$2.63 \cdot 10^{-3}$
Protons / $(sn^{-1} \cdot 10^{24} at)$	$8.92 \cdot 10^{-11}$	$1.83 \cdot 10^{-11}$	$6.33 \cdot 10^{-11}$	$1.71 \cdot 10^{-10}$
H production / (appm) for 1.0 MWa/m²				
Mock-up (experimental spectra)	$1.19 \cdot 10^{-3}$	$0.24 \cdot 10^{-3}$	$0.84 \cdot 10^{-3}$	$2.27 \cdot 10^{-3}$
ITER (calculated spectra)	$6.65 \cdot 10^{-3}$	$1.29 \cdot 10^{-3}$	$6.65 \cdot 10^{-3}$	$1.46 \cdot 10^{-2}$
Displacements / $(sn^{-1} \cdot 10^{24} at)$	$4.32 \cdot 10^{-6}$	$1.33 \cdot 10^{-6}$	$0.77 \cdot 10^{-6}$	$6.42 \cdot 10^{-6}$
Damage / (dpa) for 1.0 MWa/m²				
Mock-up (experimental spectra)	$5.75 \cdot 10^{-5}$	$1.77 \cdot 10^{-5}$	$1.02 \cdot 10^{-5}$	$8.54 \cdot 10^{-5}$
ITER (calculated spectra)	$2.33 \cdot 10^{-4}$	$6.72 \cdot 10^{-5}$	$5.30 \cdot 10^{-5}$	$3.53 \cdot 10^{-4}$

T 228 (G 18 TT 22)
Cryopump Development

1. TIMO-Test Facility

1.1 Introduction

The ITER primary vacuum pump shall be tested in the TIMO-facility (Test facility for ITER model pump). The TIMO-facility will be able to supply the 1:2 scaled down model pump with cryogenic fluids and process gas during the pumping modes required for the ITER operation.

1.2 Status of 1:2 Model Pump

An order for manufacturing the 1:2 model pump was given by a NET-contract to an industrial company. The PID-schemes have been defined. The calculations for the cryogenic system have been finished. General arrangement drawings and detailed drawings are ready. The pumping panels are manufactured and delivered to FZK for coating. The cryogenic valves have been ordered. The work is well in time.

1.3 Test Facility for ITER Model Pump (TIMO)

The ITER model pump will be tested at HIT in the TIMO facility, which is an upgrade of the former HELITEX facility. The basic part of the TIMO facility (Fig. 1) is the test vessel, in which the model pump is installed. The test vessel is designed according to the PNEUROP standard for vacuum pump testing. Due to safety reasons caused by the handling of protium and deuterium, the test vessel is designed to withstand an overpressure of 7 bar. In addition, the test vessel can be heated up to a temperature of 475 K to simulate the temperature of the divertor duct walls.

The main parts of the TIMO facility are the components for the cryogenic supply of the model pump. An overview of the cryogenic performance of the TIMO facility is given in Table 1.

The available cryogenic system is based on a 600 W helium refrigerator at 4.4 K. It supplies a cryostat with a maximum Joule Thomson flow rate of 30 g/s or in liquefaction mode 150 l/h.

The cryostat is used as a buffer volume for the surplus of liquid helium from the helium refrigerator during pumping and non pumping operation of the cryopump. The buffered liquid helium in the cryostat is used for the peak loads during cooling down of the cryopanels from 90 K to 4.5 K. Besides, the liquid helium bath is used as a thermostat for the SCHe loop.

In the existing (HELITEX) cryostat, cold blowers for SCHe are installed in the cryostat which allow mass flow rates of 50 g/s. With this available SCHe supply system acceptance tests of the model pump will be performed. For tests under ITER relevant conditions this presently existing 850 l cryostat is being upgraded by a new cryostat:

The new cryostat contains a cold blower for SCHe which allows a mass flow of 250 g/s at 4 bar to achieve the required temperature gradients of < 0.7 K along the cryopanels. In order to have more cold helium at disposal as the helium refrigerator delivers during the fast cooling down of the cryopanels (< 75 s), the new cryostat contains an additional helium buffer volume at a pressure of about 19 bar. About 50 operating cycles per day will be possible with the 1:2 model pump.
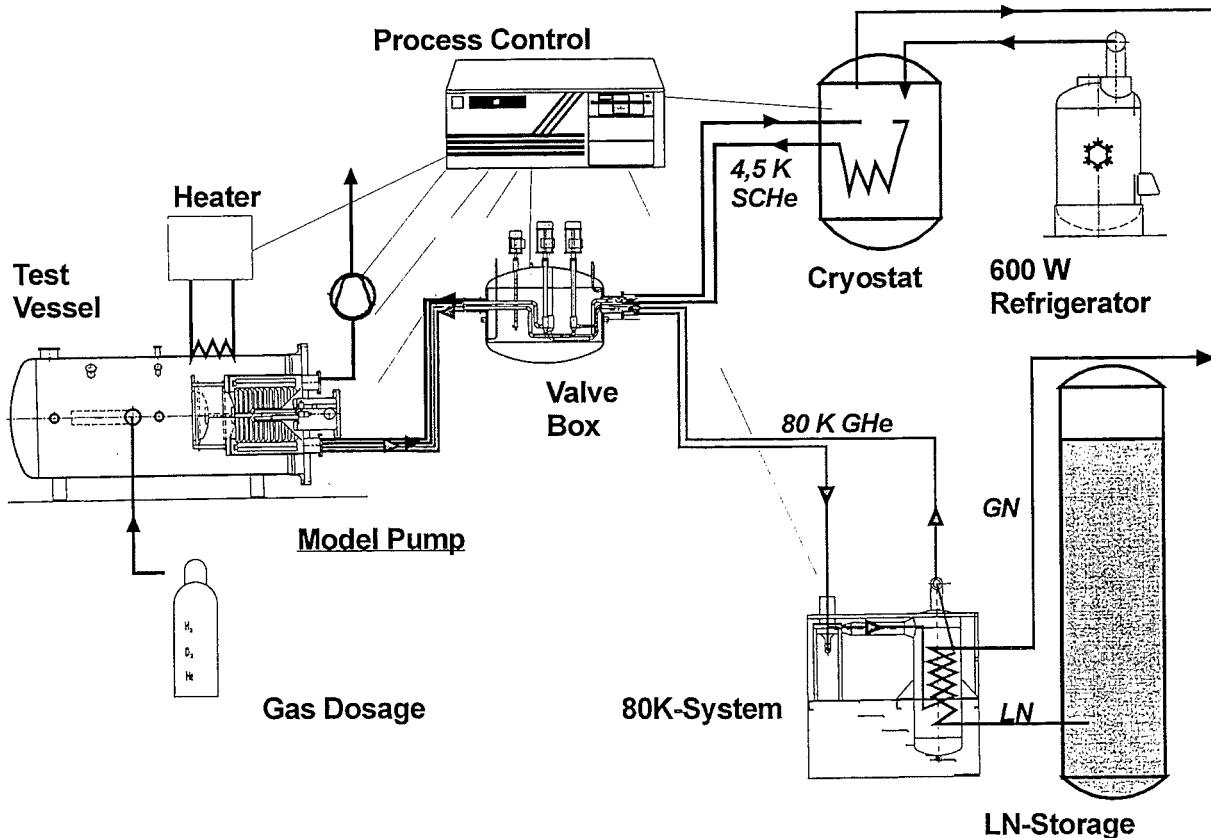

Fig. 1: Test facility for ITER Model Pump

The new cryostat can be upgraded for tests with a 1:1 ITER prototype cryopump by the installation of a bigger cold helium blower.

Due to periodically very high heat loads on the 80 K temperature components of the model pump (baffle and shields) and in accordance with the ITER cryogenic requirements a closed loop of cooled 80 K GHe is selected for the 80 K cooling stage. For that purpose a 80 K LN_2-GHe heat exchanger facility (called „80 K-system") is presently purchased. The 80 K-system is designed for a heat exchange power of up to 30 kW and is operated with a cold blower (Barber Nicols BN Hep-13) of 200 g s-1 of GHe. This high mass flow is needed to maintain a homogeneous temperature across baffle and shields.

The supply and return streams of the cryogenics will be controled by a cold valve box. The process control system is located in the TIMO-terminal box including process operation system, COROS process desktop visualisation system and a data acquisition system which is capable of collecting data from 200 different measurement devices (temperature, pressure, mass flow etc.) with a frequency of up to 10 Hz. In addition to the main parts of the TIMO facility described above, several smaller items are needed. Important minor components of the TIMO facility, for example, are explosion safe mechanical vacuum pumps which are needed for the conditioning of the test vessel and for pumping down the model pump.

Due to the risk of oxyhydrogen explosions, the operation of the TIMO facility must be licensed for these scenarios.

Table 1: Cryogenic performance of TIMO facility

Temp. stage	Pressure	Mass flow rate	Cooling power	Pressure drop
4.5 K	4 bar	50 g s^{-1} (250 g s^{-1})	600 W	0.2 bar
80 K	15 bar	200 g s^{-1}	15 kW	1.2 bar
300 K	15 bar	50 g s^{-1}	--	--

2. Component Tests

In parallel to the development of the model pump component tests have been continued which deliver results for the design and operation of the cryopump.

2.1 Experimental Determination of Pumping Characteristics for Quilted Cryosorption Panels

The pumping speed of a cryosorption pump depends in a very complex manner on the arrival rate of the gas, the capture probability, the cold surface, the type of sorbent used, the temperature and the gas load. The speed for a gas mixture may not only depend on the total amount of previously pumped gas, but also on the loading history (i.e. the time scale and the sequence with which the gases have been admitted into the pump). Consequently, in order to assess the suitability of the recommended cryopanel design, an experimental testing programme at the TITAN facility has been performed and just been completed. The key scaling parameter involved in the transfer from component test results to the ITER pump is the pumping speed (related to the cryopanel surface of 3500 cm^2) of about 1 l/(s·cm^2) at a maximum specific gas load of about 0.23 (Pa·m^3)/cm^2, corresponding to 900 s pumping time, except for pure helium, where the operation times are limited.

As the cryosorption process is due to two totally different, but interdependent physical pumping mechanisms (sorption and condensation), the main objective of the test campaign was not only to measure the pumping speed performance for different gas compositions, but also to determine and separate the major factors affecting cryopump performance and to check the mutual influences of sorption and condensation.

2.1.1 Pumping Speed Results Overview

The whole test series has been performed in the upgraded TITAN facility with an electrically heatable panel, which has been described in last year's annual report. The gas mixing facility, which has been developed and constructed at FZK, allowed for a quick and short-term production of the required gas mixtures and has turned out to be a reliable tool within the whole test programme. The investigated mixtures were designed to stand as model gases for the fusion exhaust produced in the various plasma operation modes of ITER. In the DDD, their composition is specified to contain up to 5 mol-% inert gases, up to 6 % impurities and up to 10 % helium besides the hydrogens as major component. For that reason, we defined a pre-mixed base-mixture consisting of 96 % D_2 or H_2 (remainder impurities), denoted H_2-Base and D_2-Base, respectively, and produced pseudobinaries and -ternaries with nitrogen or one of the noble gases He, Ne and Ar in composition steps of approx. 5 %. The compositions listed in Table 2 were investigated for both base-mixtures. We reduced the experimental work to a minimum number of tests with the strongest evidence to draw the right conclusions.

The experiments yield the relationship between pumping speed, gas load and pressure during pumping. To also obtain additional information about cryosorption equilibrium, the experiments were performed in an intermittent mode, like usual.

Table 2: Investigated gas mixture compositions

Approx. Comp. in mol-%	95/5	90/10	85/15	80/20
Base/He	✓	✓		✓
Base/Ne	✓		✓	
Base/Ar	✓	✓		
Base/N_2	✓	✓		
Base/Ne/He=75/15/10				

Some results for the D_2-Base/He system are shown in Fig. 2 The gas load was built up by flowrates, which were stepwise increased, starting at 0.16 (Pa·m^3)/s up to 1.7 (Pa·m^3)/s. The measured increase in pumping speed for the helium-free D_2-Base is due to the pressure during pumping, which rises from 10^{-2} to 1 Pa within the experiment and corresponds to transition flow regime. This effect is overcompensated, if helium is present in the gas mixture; the decrease in pumping speed varies more than linearly with the increasing helium content.

The results of the tests can be summarized as follows:

- The saturation limit of the charcoal is not reached, except if helium is being pumped.

- Maximum helium capacity at the LHe-cooled panel is about 0.6 (Pa·m^3)/cm^2.

- The deteriorating influence of the inert gases Ar, Ne and N_2 on the overall pumping speed is significant, but not critical.

- No additional trapping effects have been observed.

- Pumping speed requirements can very well be met by the recommended panel design including a considerable safety margin, which allows for the 20 % excursion mentioned in the DDD.
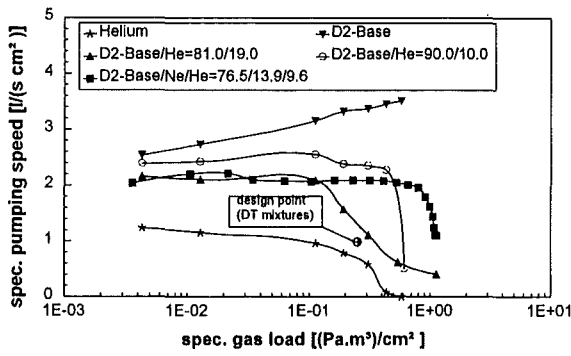
Fig. 2: Comparison of pumping speed curves for helium, deuterium and their mixtures at the LHe-cooled panel.

- The most critical composition is a combination of high protium and high helium contents. Already small percentages (some mol-%) of helium reduce the H_2 pumping speed to almost the pure helium level. This is due to a competitive sorption situation, which is the responsible pumping mechanism for both helium and protium [1].

- For helium pumping and H_2 shot operation mode, it is favourable to make both panel sides coated.

- The strong interaction of the various gas species does not permit to predict mixture pumping from pure gas data only [1].

The pumping speed results will also be used for comparison with theoretical calculations based on a Monte-Carlo simulation for the TITAN geometry (see section 2.2).

2.1.2 Mass Spectrometric Monitoring of Selectivity Effects in Pumping of Mixtures

The measurement results derived from the integral pumping speed tests revealed that the cryosorption process is predominantly influenced by a competition between the gases helium, protium and partly deuterium for the active sorption sites. So as to investigate that effect in more detail, we made use of a high resolution gas mass spectrometric system, with which we could monitor the composition changes during pumping.

The mass spectrometer has been especially developed for the separation of helium and deuterium peaks and procured from BALZERS, Liechtenstein. Besides standard operation, the mass analysing system can be operated in a high resolution mode, which has the resolution increased by factor 45. A cross-beam ion-source with tungsten cathode is used. The mass filter is a 16 mm molybdenum rod system with the length of 300 mm. The standard mass range is 1-128 amu, the mass range according to high resolution operation is 1-22 amu. The detector is a 90° secondary electron multiplier. The sensitivity reached is about 10^{-7} A/mbar in the high resolution mode and $8 \cdot 10^{-4}$ A/mbar in the normal resolution mode. To always achieve the optimum pressure of 10^{-4} Pa in the analyser chamber, an automatic gas inlet system was developed. It comprises a direct inlet via throttling orifice for pressures less than 10 Pa and a batch sampling line, where the sample pressure is tuned to the analyser pressure by stepwise pressure reduction. The data acquisition system is equipped with software tools which allow for a quantitative evaluation of the mass scans to obtain exact composition data. The performance of the mass spectrometer (repeatability, calibration stability, relative resolution) for the comparably rough conditions at the TITAN facility was very good. It can be used for sample pressures down to about 10^{-2} Pa, still achieving a base line separation between deuterium

and helium. The set-up of the mass spectrometric device has been presented in full detail elsewhere [2].

By now, the mass spectrometric device is completely integrated in the standard evaluation procedure for TITAN tests. A library of control software modules has been developed to be able to adapt the automated mass spectrometer operation quickly and easily to the scheme of the individual TITAN test run. The analyser will be an indispensable tool for the poisoning tests which have been started in late 97 (see below).

A typical result is highlighted in Fig. 3, which shows the concentration shifts during pumping of the pseudoternary system D_2-Base/Ne/He. The measurements indicate some increase in the common He/D_2 concentration and some decrease in the neon concentration. This is due to the fact that neon has the highest pumping probability of all gases present [1]. The bottom part depicts the high resolution separation of the He/D_2 peak. It is now revealed that the composition ratio of He and D_2 changes drastically: There is a strong relative enrichment of helium during pumping. Taking into account the relatively poor pumping speed of pure helium, this explains very well the measured strong decrease in pumping speed even at moderate nominal helium concentrations in the mixture to be pumped. However, increase in He concentration becomes significant only after pumping periods which are considerably longer than those proposed for ITER.
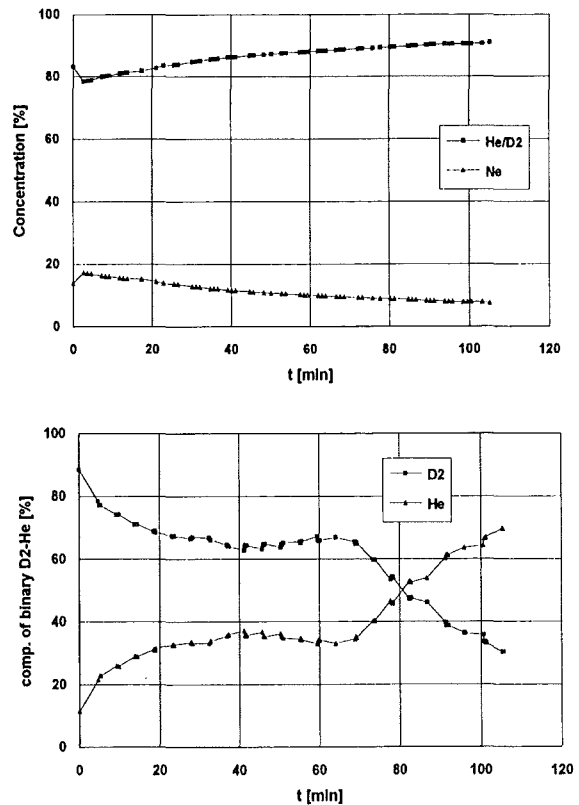
Fig. 3: Composition changes during cryopumping of a mixture containing nominally 76.5 % D_2-Base, 13.9 % Neon and 9.6 % Helium. The data in the upper part are recorded in the normal resolution mode, the data below in the high resolution mode.

2.1.3 Dynamic Loading Effects: Influence of Time Scale

A great part of the tests listed in Table 2 were repeated according to different loading scenarios, such as:

- longer dosage steps at smaller flow rates with equilibration breaks,

- shorter steps of higher flow rates (ITER typical) with equilibration breaks, or

- continuous dosage, without equilibration breaks.

These tests were done to investigate if the time range for cryosorption has a significant impact on the overall pumping behaviour [3]. The breaks in between the dosage steps give time for further molecule migration into the charcoal and, thus, provide new active sites for sorption at the surface. Our tests could validate such an influence, but not with predominant significance. All pumping speed results obtained with different loading programs are identical within the bounds of ± 15 %. However, it was noted that the overall pumping performance of a cryopump does not depend on a specific parameter only but on the entire pumping history.

The tests demonstrated, that there is a temperature level for each gas species, which has to be exceeded to achieve increased mobility. We determined this critical temperature for different pure gases in heating experiments at pre-loaded panels. This temperature was observed to be about 25 K for deuterium, 12 to 13 K for protium and about 9 K for helium. The mobility effect can be used to disperse the sorbed molecules faster into the charcoal pores and thus reverse the typical decrease in speed with accumulated gas on the surface. However, for ITER, the gas load is limited by maximum tritium inventory, not by achieving saturation capacity.

2.1.4 Preparation of the Poisoning Test Campaign

As we have found that the cryosorption pumping is predominantly ruled by the competitive sorption mechanism, potential sorbent poisoning effects within the partial regeneration cycles might deteriorate the pumping performance drastically. Such effects may be caused by clogging of the pores due to accumulation of residual gas which is not thermally released within the partial regeneration steps.

The value of the upper temperature limit for partial regeneration is not fixed yet and has to reconcile two contrary demands: on the one hand the temperature should be sufficiently high to release the pumped gas almost completely, on the other hand the cryogen consumption needed for the subsequent cool-down of the panel should be minimized for economic reasons. Therefore, in a first step, the required temperature limit must be specified very carefully. As the partial regeneration is based on fast heating (less than 75 s), the desorption equilibrium condition is not fulfilled and, thus, predictive theoretical methods are not applicable. Consequently, thermal desorption tests were performed so as to obtain the appropriate dynamic data needed. In these tests, the panel was loaded and afterwards heated according to a pre-defined temperature program; the pressure evolution curve can be used for derivation of the dynamic desorption characteristics. A first set of thermal desorption tests has already been performed. They indicate a required temperature range between 80 and 85 K to release the hydrogens from the charcoal surface. However, some more tests have to be done until a final decision can be made as to what temperature should be chosen for the poisoning test series.

Within the poisoning test campaign, the pumping behaviour of a certain gas mixture shall be monitored during a series of up to 10 ITER-relevant pumping cycles with only partial regeneration after each cycle. A change of pumping speed over the different pumping cycles would be a definite hint at potential poisoning effects. The measurements of the achieved pressures before dosage, during pumping and after the regeneration, coupled with a mass balance, will yield information about the effectiveness of thermal gas release within the regeneration process and thus also indicate a possible sorbent poisoning. Selectivity phenomena and enrichment effects will be revealed by on-line mass spectrometric gas analysis.

2.2 Monte Carlo Analysis of the TITAN Test Facility and its Pumping Characteristics

The TITAN test facility was extensively analysed using the Monte Carlo method, in order to quantify the geometry impact on the measured pumping speed in the molecular flow regime. For this purpose the general Monte Carlo code MOVAK3D was employed and a series of calculations was carried out with the following objectives:

- to determine the conductance (through the estimation of the transmission probability) of the entire TITAN vacuum structure, including the PNEUROP dome, the chevron baffle, the panel in the circular as well as in the quilted geometry form and the 80 K volume

- to estimate the capture probability in dependence of the panel pumping characteristics

- to check the dependence of the capture probability on a panel position, changed by rotation around the horizontal symmetry axis of the panel

- to gain an insight into the relative pressure variation within the structure

- to derive from the experimental results for different gases the sticking coefficients of the panel coated with activated charcoal sorbent material, employing the calculated transmission and capture probabilities in the evaluation procedure

- to investigate the saturation point of the helium pumping

Three most important integral characteristics of the TITAN pumping system: the transmission probability, the capture probability and the back-scattering coefficient were delivered by the MOVAK3D code. The transmission probability of the TITAN structure amounts to 0.1. The maximum capture probability is equal to 0.092 for the structure with the quilted panel, whereas for the structure with the circular panel the capture probability is equal to 0.085. The backscattering coefficient can be obtained subtracting from one the transmission or the capture probability, respectively.

Moreover, basing on the MOVAK3D results, it can be stated that:

- The cause of the strong decrease of the measured pumping speed as compared to the panel pumping speed is the poor conductance of the other TITAN components.

- The capture probability strongly depends on the sticking coefficient of the sorbent material. Fig. 4 illustrates this dependence in case of the structure with the quilted panel.

- The contribution from two different quilted panel surfaces (front and back) to the overall capture probability vary with the panel position as a result of different exposure to the flow.

- The pressure in the pump above the panel reduces by one decade relatively to the pressure in the PNEUROP dome.

- The discrepancies, which occurred between the measured specific pumping speed for the circular panel and the measured specific pumping speed for the quilted panel can

be attributed to a significant increase (by a factor 2.95) of the panel surface area and a relatively small increase of the measured pumping speed.

Additionally, the analytical formula, describing the dependence of the capture probability on both the sticking coefficient and the transmission probability was derived. On this base the method to calculate the sticking coefficients from the measured quantities was developed. The sticking coefficients obtained for helium are plotted in Fig. 5.
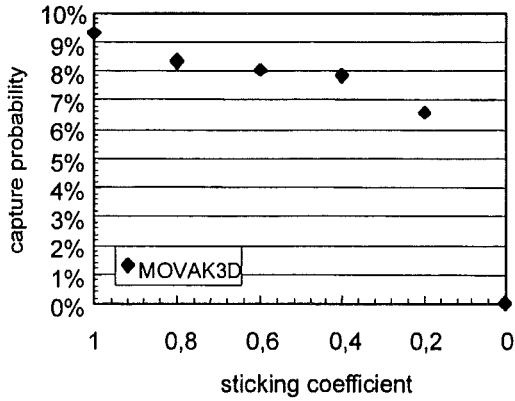
Fig. 4: Capture probability of the entire TITAN vacuum structure with the quilted panel versus the sticking coefficient
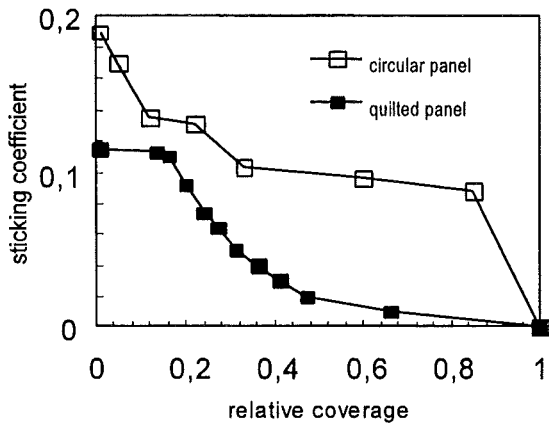
Fig. 5: Sticking coefficient for helium calculated from the measured pumping speed plotted versus the relative coverage of the panel

2.3 Fast Heating and Cooling Tests in HELITEX

Because of the maximum allowable Tritium inventory within the ITER primary pump system the cool down from 90 K to 5 K is limited to 60 s. Within the framework of the preliminary tests with flat panels it could be demonstrated that cooling down times within $\leq$ 60 s could be achieved.

The objective of the tests described here was to demonstrate that cooling down times of less than 60 s can be achieved with pumping panels in quilted design as used in the ITER pump.

2.3.1 Test Arrangement

The tests were performed with panels in ITER relevant dimensions 150 x 1000 mm (Fig. 6).
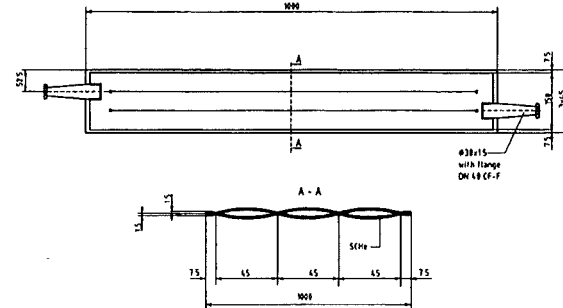
Fig. 6: Design of ITER panel

In the first test campaign a bare panel was used in the second a coated panel.

The surface temperatures of the test panel were recorded by nine cernox sensors of the type „CX-1050-SD" and diodes delivered from Lake Shore.

The test panels were installed in the HELITEX vacuum test vessel ($\varnothing \approx 2$ m, H ≈ 2 m).

To simulate the 80 K shielding of the cryopump LN cooled shields were arranged on both sides of the test panels (Fig. 7).
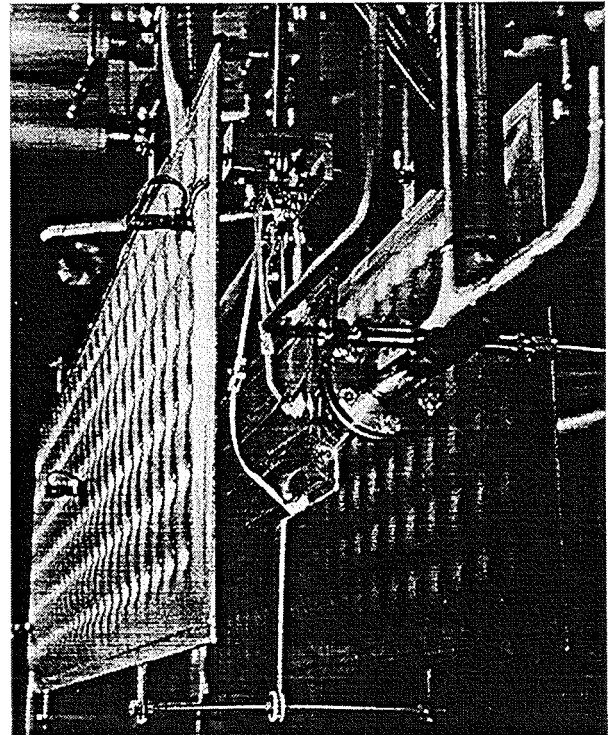
Fig. 7: View of the upper part of the HELITEX test cryostat with the panel and the LN shields.

The gas pressure inside the vessel was measured within the range $10^{-2} - 10^{-10}$ mbar. For measuring the mass flow of SCHe three venturi tubes for 10, 20 and 30 g/s were installed.

For heating up the panel the facility was supplied with 300 K GHe at a maximum flow rate of 50 g/s and a pressure of 15 bar.

2.3.2 Test Programme

During the heating/cooling tests, the SCHe mass flow applied for cooling the test panel installed was set to 10, 20 and 30 g/s, respectively. After the planned SCHe mass flow, e.g. 10 g/s, has been reached, the pressure of the test cryostat was set to the required level of 10^{-4}, 10^{-3}, 10^{-2} or 10^{-1} mbar. For this purpose, GHe (6.0) was metered into the test cryostat via the gas dosage system.

For heating the test panel from the operating temperature to $\approx$ 100 K, 300 K hot GHe is supplied by the Linde facility at a mass flow of $\approx$ 25 g/s and a pressure of 15 bar. During the cooling phase, the test panel was cooled from starting temperatures of $\approx$ 100 K to operating temperature using SCHe.

Following the tests at a certain mass flow (e.g. 10 g/s) and all pressure levels, the panel has to be conditioned for subsequent studies. For this purpose, the panel is heated to T $\approx$ 280 K using hot GHe. As a result, the bound GHe is released. Then, the test cryostat is evacuated to a pressure of < 10^{-5} mbar and the test panels are cooled to temperatures of < 5 K again.

2.3.3 Test Results

The fast heating/cooling tests were performed both with a plain and with an activated-carbon coated test panel. The central temperature measuring point TIR 411 which is located in the central flow channel was applied for the evaluation of the heating and cooling times.

The heating times are represented as a function of the GHe mass flow related to the panel surface (Fig. 8). In addition to the results obtained at the HELITEX facility, the test results of the TITAN facility, where also panels of quilted design were tested, are plotted. Due to the high GHe mass flow, heating times of < 10 sec could be measured at the HELITEX facility.
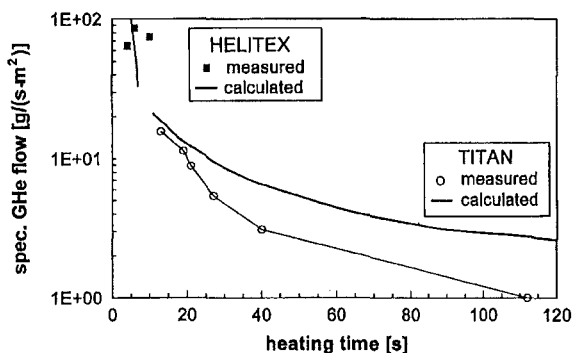
Fig. 8: Panel heating time versus GHe flowrate

The cooling times related to the panel surface are represented in Fig. 9. It can be noted that a panel of quilted design can be cooled twice as fast as the fin panels studied in the preliminary test. While the cooling time of a fin panel is 75 - 100 sec, the quilted panel reaches the temperature of < 10 K required within a period of 34 sec only. These shorter cooling times have to be attributed to the larger heat exchange surfaces and the reduced wall thickness of the quilted panel [2].
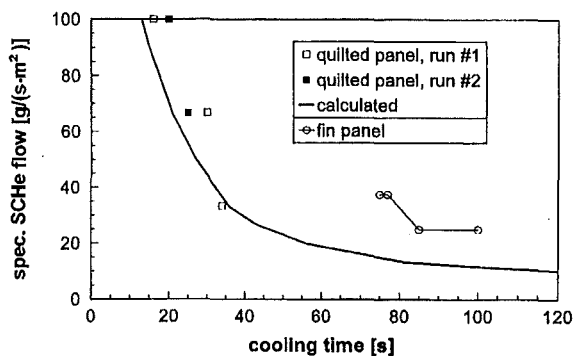
Fig. 9: Specific panel cooling time

2.4 Cycling Tests

The pumping panels to be used in the ITER primary vacuum pump must be designed to withstand the temperature cycling between ~ 4 K and 90 K for partial regeneration and ~ 4 K and 300 K for total regeneration. A number of 220 000 cycles is expected for the partial regeneration and 20 000 cycles for the total regeneration during the lifetime of the reactor.

Both the number of cycles in the machine lifetime and the rate of temperature increase/decrease are much more demanding than in similiar pumps in other applications. Therefore it was decided to perform a systematic study including theoretical stress analysis and experimental validation.

The stress analysis uses a two dimensional Finite Element code for the cryopanel which consists of three layers, namely a metal (SS) substrate, an inorganic bonding agent and the activated charcoal fixed on the bonding agent.

A two layer model was generated to apply the FE-code. The first layer is the stainless steel substrate the second layer is the bonding material, Thermoguss 2000. The bonding layer has direct contact to the steel. The charcoal particles do not carry any mechanical stress.

The strains and stresses for thermal deformations and varying internal gas pressures were analysed for each kind of stress and superposed.

The main stress is caused by the internal pressure change of the panels during pumping and heating. Helium gas with 15 bar / 300 K is circulated through the refrigerant channels during heating and SCHe with 4 bar / 5 K during pumping.

The results with the available material data show that the stainless steel will not fail within the number of cycles of the ITER-operation. Because of missing material data for the bonding agent no theoretical statement could be made concerning the failure.

To find out whether the panel will fail tests within the most critical temperature range of 300 K to 80 K were performed.

2.4.1 Test arrangement for 300 K ↔ 80 K Cycles

The test bench shown in Fig. 10 consists of a vacuum chamber, the assembly of three adsorbent panels, supply and exhaust lines of nitrogen, process controller. Three panels in quilted design with LxW 500x107 mm were installed in parallel in the test chamber.
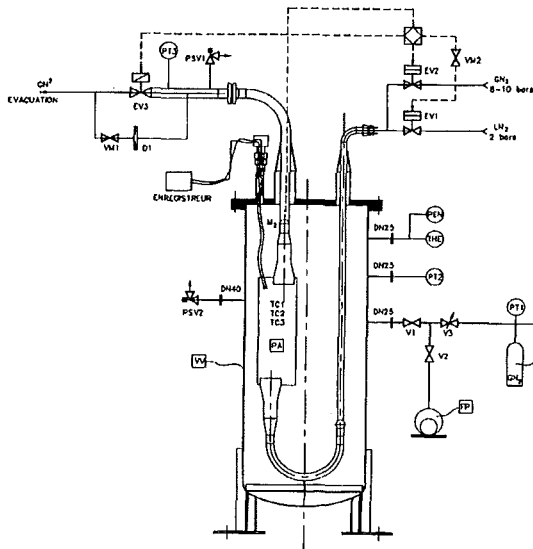
Fig. 10: Test arrangement for 300 K ↔ 80 K cycling tests.

Three thermocouples, one per panel were attached on the surface. The vacuum in the test chamber was measured by a Penning gange.

2.4.2 Test Programme for 300 K ↔ 80 K Cycles

The test consists of 10 000 thermal cycles. Each thermal cycle performed under vacuum includes two minutes of LN_2 injection and 3 minutes of GN_2 injection. The pressure inside the panel varied between ≈ 9 bar during heating and 1 – 2 bar during cooling down. The lowest temperature is between 138 K and 123 K, the highest temperature between 258 K ± 3 K. After 10, 100, 1000, 2000, 4000, 6000, 8000, 10000 cycles an evaluation of the N_2-adsorption behaviour, a visual examination and collecting and weighing of the particle fallen down from the panel surface was performed.

2.4.3 Test Results

The total loss of activated charcoal particles at the end of the 10 000 cycles was 0.89 g. Compared with the total activated charcoal mass of 180 g on the panel surface the measured loss values are no problem for the ITER-operation.

The N_2-adsorption didn't decrease as a function of cycle number.

The optical inspection showed no degradation of the panel surface.

3. Tritium Exposure Tests

For tritium exposure tests at ARZAMAS 16 (RF) 118 activated carbon coated test panels were manufactured at FZK.

For fixation of the sorbent material on the specimens of 80 x 15 x 1 mm in size, the two-component bonding material „THERMOGUSS 2000" was applied. Chemviron SC II activated carbon granules were sprayed onto one side of 112 test platelets. The remaining six specimens were coated with the activated carbon powder Chemviron GFF 30.

Selected specimens were not only subjected to the helium loading tests, but also to cycling tests at temperatures between 300 K and 80 K. Both helium and tritium were used as exposure gas. During investigation at ARZAMAS 16, no change of the macrostructure of the bonding/sorbent layer, no detachment of

the bonding layer and no activated carbon losses were observed [5].

Literature:

[1] Day, Chr. and A. Mack: Investigation into pumping characteristics of ITER cryopumps. ISFNT-4, Tokyo, 1997.

[2] Day, Chr.: The use of a high-resolution quadrupole gas mass spectrometer system for selective detection of helium and deuterium. Proc. 2nd Int. Workshop Vacuum Science, Magdeburg, 1997. To be published in 'Vacuum'.

[3] Day, Chr., B. Kammerer and A. Mack: Pumping performance of cryopanels coated with activated carbon. CEC/ICMC, Portland, Oregon, 1997. To be published in 'Adv. Cryogen. Engng.'

[4] H. Haas, Chr. Day, A. Mack: Component test on fast heating and cooling with cryopanels for use in the ITER primary vacuum system. ISFNT 1997, Tokyo.

[5] A.I. Vedeneev: Experimental Investigation of effect on cryosorption panel Mock-ups for ITER vacuum pump. ISFNT 1997, Tokyo.

Staff:

Chr. Day
E. Diegele
A. Edinger
H. Haas
T. Höhn
W. Höhn
M. Jäger
B. Kammerer
U. Kirchhof
H. Knauß
S. Kraegermann
J. Laier
A. Mack
N. Petersohn
A. Schwenk-Ferrero
R. Simon
D. Stern
U. Tamm
J. Weinhold
D. Zimmerlin

T 332 B
Plasma Exhaust Processing (2)

Subtask 1: PETRA Experiment

The front-end permeator battery of the ITER exhaust processing system recovers elemental hydrogen isotopes from the exhaust gas and produces a stream suitable for direct recycling into the Torus Fuel Supply System. According to the current fuel clean-up concept CAPER, the separation of hydrogen isotopes from the impurities is carried out by permeation through palladium/silver alloy membranes, which are uniquely permeable to hydrogen. During the course of the separation it is conceivable that β-rays emitted by tritium induce radiochemical reactions to occur, particularly when the specific activity of tritium is high. Furthermore, the palladium/silver surface of the membranes that separate impurities from the hydrogen isotopes could catalytically promote chemical reactions. During the past months a considerable effort has therefore been invested into the investigation of radiochemical reactions taking place in various sections of the facility PETRA employing a variety of experimental conditions. The PETRA facility comprises a 10 l primary system with an integrated permeator of 0.12 m^2 permeation area and a gas cell having sapphire optical windows. In the present investigation the cell was used to follow the kinetics of the reaction between hydrogen isotopes and carbon oxides using an infrared spectrophotometer from Perkin Elmer (Mekos spectrometer). The instrument is self-calibrating and designed for the quantitative measurement of methane, carbon monoxide and carbon dioxide.

The experiments were carried out using either protium or a 1:1 deuterium/tritium mixture containing small concentrations helium (3 %) and either carbon monoxide (3 %) or carbon dioxide (3 %). The protium was selected to account for the fact that the Mekos spectrophotometer is designed for the measurement of CH_4 and the 1:1 mixture to simulate the conditions encountered in the Tritium Plant of a fusion reactor. With protium only it is possible to assess the catalytic effect of the palladium/silver surface. By comparing the radiation-induced reaction rate in the infrared cell with the rate measured in the complete primary system when the gas mixture is passed through the permeator kept at its operation temperature, i.e. 350

°C, it is possible to obtain the synergistic effect of the beta radiation and the noble metal surface on the reaction rate.

At room temperature hydrogen does not react with carbon oxides. However, when a hydrogen/carbon monoxide mixture is recirculated through a heated permeator carbon monoxide undergoes a slow reaction yielding methane, water, and other products, possibly higher hydrocarbons. CO, CO_2 and CH_4 were identified by infra red absorption and the other products by additional analytical techniques. Fig. 1 shows the time evolution of the reaction products and a carbon material balance, which suggests that besides methane other carbon containing products such as carbon or higher hydrocarbons are also formed in small yield.

When protium is replaced by a 1:1 deuterium/tritium mixture a beta radiation-induced reaction is observed at room temperature in the infra red cell causing a consumption of carbon monoxide and a rise and fall of the carbon dioxide partial pressure. Gas chromatographic analysis indicates that in addition polytritiated methane and other higher hydrocarbons (ethane) as well as water (detected with a hygrometer) are also produced. The rate of this reaction is further enhanced by the hot palladium/silver membrane of the permeator. The reaction rate of carbon monoxide with the deuterium/tritium mixture shows a direct dependence from total pressure, i.e. the higher the total pressure of a given gas mixture the faster the reaction rate. Under conditions of excess DT this is consistent with an ion pair production rate being directly proportional to the partial pressure of carbon dioxide. Work in progress will provide the data needed for a quantitative evaluation of these results.

A comparison between the reaction rate of deuterium and of a 1:1 deuterium /tritium with carbon dioxide on the surface of a palladium/silver membrane is depicted in Fig. 2. The measurements were carried out with a permeator whose secondary side was closed (this explains the somewhat higher initial concentration of carbon dioxide). From the data it is apparent that the beta radiation of tritium brings about a considerable enhancement of the reaction rate. One consequence could be a deterioration of the achievable decontamination factor at the front end permeator level because of the partial conversion of molecular free hydrogen into non-permeable bonded hydrogen (methane).
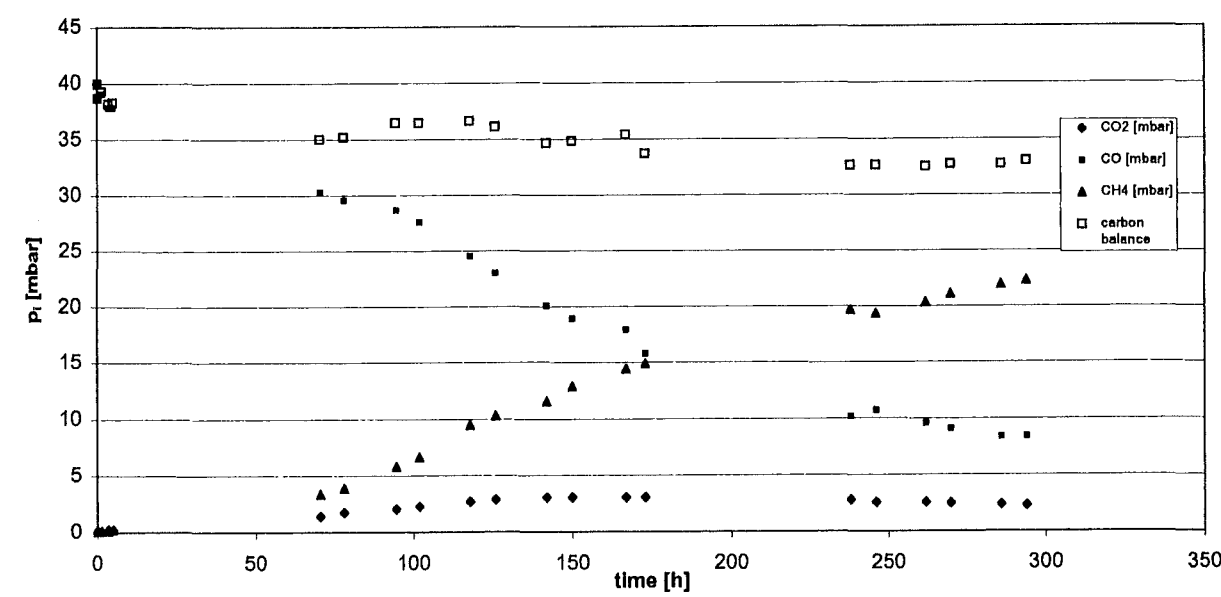
Fig. 1: Reaction of CO (3 %) with H_2 (94 %) in the presence of He (3 %) on the surface of a permeator held at 340°C
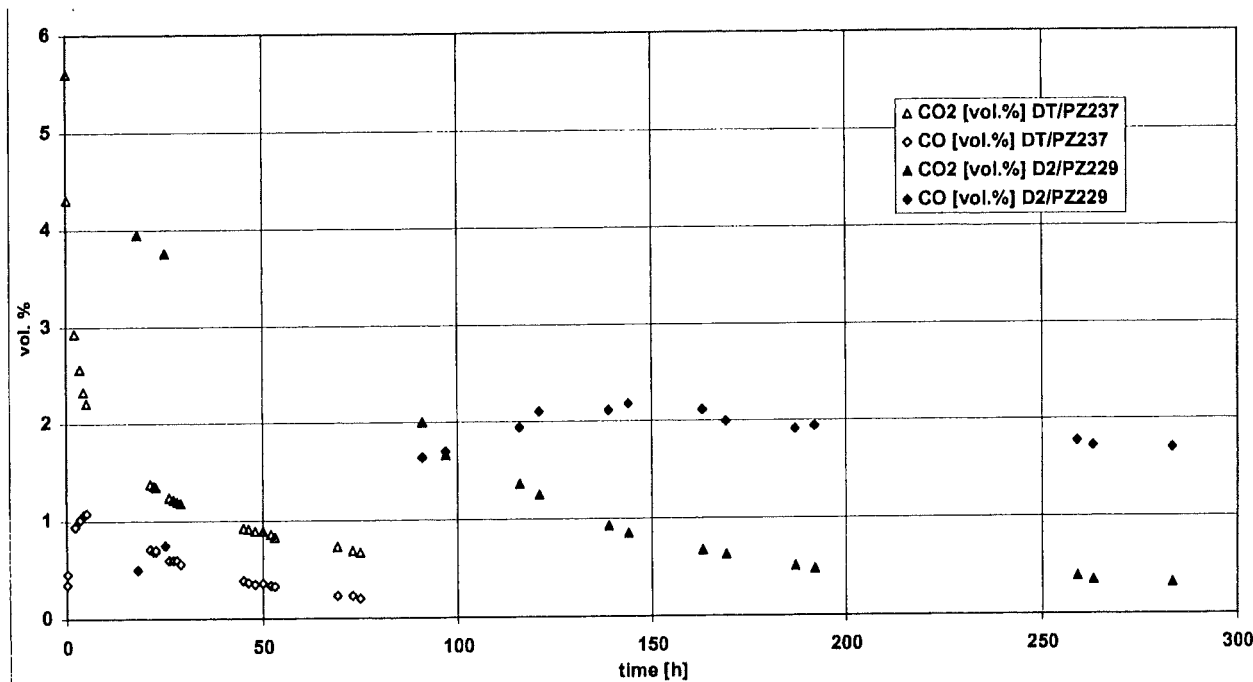
Fig. 2: Reaction of CO2 (3 vol.%) with either D2 (94 vol.%) closed symbols) or DT (94 vol.%) (open sympols) in presence of He (3 vol.%). Permeator at 350°C and gas recirculation 0.5 [l/min].%.

From the cumulative tests carried out so far it can be concluded that an exposure even for a period of weeks of a permeator to an equimolar deuterium/tritium mixture in the presence of carbon oxides has no detrimental effect on the permeator. Neither the mechanical integrity of the permeator is impaired nor is its permeability significantly reduced. However, when palladium/silver is subjected to high partial pressures of carbon oxides in the presence of low partial pressures of the equimolar deuterium/tritium mixture a rather rapid poisoning of the permeator takes place. The rate is even faster than that observed previously with polytritiated methane. With respect to ITER it appears to be strongly recommendable on the basis of the performed experiments to avoid exposure of the permeator to hydrocarbons or carbon oxides when the partial pressure of hydrogen isotopes is low. Concerning the achievable ITER front end permeator decontamination factors it appears recommendable to assume conservative values.

Under all circumstances was it possible to regenerate completely a poisoned permeator by repeated treatment with moist laboratory air when the permeator was kept at its normal operation temperature., i.e. 350 °C.

After completion of nearly three years of semi continuous operation with the PETRA facility using equimolar deuterium/tritium mixtures in the presence of carbon oxides and hydrocarbons a large quantity of data concerning the qualification of large components, e.g. permeator, tritium storage bed, scroll pumps, and metal bellows pumps, etc. as well as small components, e.g. valves and sensors of various kinds, for use in tritium installations has accumulated (see Table I). The gained experience is deemed of value during the ITER licensing and construction phase.

In addition, the operational experience gained at the Tritium Laboratory Karlsruhe with tritium retention systems, the transfer of gases from one facility to another, with the calorimetric accountancy of tritium and the analytics of tritiated species will provide complementary basic data of value for ITER.

Staff:

U. Bernd
E. Kirste
R.-D. Penzhorn
J. Wendel

Table 1: Components tested over an extended period of time (> 2.5 years) mostly with an equimolar deuterium tritium mixture and fusion fuel cycle relevant impurities at the TLK facility PETRA	
Component	**Comments**
Palladium/silver permeator	Reliable performance. Completely reversible poisoning by polytritiated hydrocarbons observed. Frequent reactivation with laboratory air at 350 °C necessary.
ZrCo tritium storage bed	JET storage bed design shows permeation losses into the glove box through axial heater. ZrCo performed reproducibly and reliably. Reversible poisoning of ZrCo by carbon monoxide observed. The original properties (reaction rate with hydrogen isotopes) could be completely restituted by heating the getter to 400 °C for an hour.
18 m^3/h NORMETEX scroll pump PV12	Reliable performance, no leaks observed.
Two stage, double contained Siemens single metal bellows pump	Reliable performance, no leaks observed.
Tylan mass flow meters FM 830	Severe plugging of inlet screen observed with all three PETRA flow meters after approx. two years of operation (polymers, rust?). Cause is under investigation.
Mekos infrared spectrometer	Shown to be adequate as *on line* analytical instrument to follow long-term gas phase concentration changes of carbon monoxide, carbon dioxide and methane in a helium or hydrogen carrier gas. Suitable as a process control instrument. Particularly useful at low impurity pressure and approx. constant total pressure.
Spectran infrared spectrometer, Perkin Elmer	Shown to be adequate as *on line* analytical instrument to follow long-term gas phase concentration changes of carbon monoxide in a helium or hydrogen carrier gas. Suitable as a process control instrument. Particularly useful at low impurity pressures and approx. constant total pressure.
Edwards magnetic levitation turbomolecular pump 300 T	Reliable performance
Drystar pump DP40	Oil-free fore pump to turbo molecular pumps. First version showed strong rust formation by cooling water. Problem now solved. Loud.
Local process control system Simatic AG95 from Siemens	Reliable performance. Used to control safety relevant temperatures and pressures (including virtual temperatures and pressures) during attended and unattended operation of the facility. A trip leads to an automatic shut down of the experiment

Subtask 2: Catalytic Cracking Process

An integrated fuel clean-up concept, based on permeation of hydrogen isotopes through palladium/silver, heterogeneously catalyzed cracking or conversion reactions, and isotopic swamping has been developed to process torus exhaust gases specified for ITER. The concept designated by the acronym CAPER (CAPRICE/PERMCAT) is strongly based on experimental experience from operation of the technical facility CAPRICE (Catalytic Purification Experiment), which has been successfully used with up to 90 % tritium in deuterium along with mixtures of relevant tritiated and non tritiated impurities at the Tritium Laboratory Karlsruhe (TLK), and from tritium experiments with a permeator / catalyst combination (PERMCAT) for isotopic swamping.

The CAPRICE concept comprises only two process stages, that is a front-end permeator, followed by catalytic cracking and conversion reactions combined with selective permeation of hydrogen isotopes through palladium/silver. However, due to adsorption and desorption effects from tritium exposed pipe work, pumps and in particular from surface active materials such as catalysts or palladium/silver, the decontamination factor (DF) reasonably achievable with these two stages was limited to approximately 10^6. The PERMCAT unit, in which tritium contaminated parts are permanently segregated from non tritium contaminated parts, is needed as a final decontamination step to accomplish the very high overall decontamination factor of about 10^8, as currently required by ITER.

Hence the CAPER catalytic clean-up process for ITER comprises three process stages, that is a front-end permeator battery with an optional methane cracker and a front-end bleed permeator, an impurity processing loop and the final clean-up segment.

The different steps of the process have already been demonstrated with relevant concentrations of tritium and for the most also at a technical scale. The experimental results and the results from mathematical modelling have been utilized to form the basis of the detailed engineering and design of a full scale torus exhaust clean-up plant for ITER. Each stage of CAPER is not only optimized individually, but also considered with respect to the process as a whole. Trade off's within the stages of the torus exhaust clean-up plant for ITER as well as between them, and particularly incompatibilities between the stages, were analyzed in the engineering and design.

A process flowsheet (AutoCAD 13 format) including a mass balance and tritium inventories of vessels, and a pipe and instrumentation diagram (AutoCAD 13 format), along with contributions to the 'Design Description Document' (DDD) were provided to the Joint Central Team of ITER. One of the features of working with AutoCAD is that actual lists of components, instruments, heaters, valves and pipes, including their dimensions, can be extracted from the drawings. The result was a complete and consistent documentation package, which was also used as a basis to prepare general layout drawings and isometric views of that particular ITER tritium subsystem.

The CAPRICE impurity processing concept and the final clean-up step with the PERMCAT will be part of the DDD and of the 'Final Design Report' (FDR) of ITER.

In order to conduct integral experimental tests of the CAPER concept with tritium on a semitechnical scale the CAPRICE facility is currently modified according to the outline flow diagram shown in Figure 1. The new components (right hand side area in the diagram, within the dotted line), that are the technical PERMCAT, the combined catalyst bed, the five pumps, the two buffer vessels and the associated instrumentation and pipework, are to be installed in a new glovebox adjacent to the CAPRICE facility. This minimizes the modifications necessary

within CAPRICE and its tritium contaminated primary system. The modified facility is called 'CAPER at TLK'.

The primary loop permeator of CAPER (section 1) represents the front-end permeator battery and can now be operated under conditions that avoid coking of the permeation membranes by hydrocarbon cracking. The decontamination factor of the primary loop permeator is thereby intentionally limited to only about 10 to 20.

Depending on the ultimate layout of plasma facing components for ITER, hydrocarbons may significantly contribute to the impurity gas stream. Hence an optional catalytic hydrocarbon cracker is currently included into the flow sheets prepared for ITER to promote an instantaneous recovery of tritium and deuterium locked up in e.g. methane. This concept can be experimentally tested by using the methane cracker and the secondary loop permeator (section 2), the latter representing the so called front-end bleed permeator of ITER in this case. Both the methane cracker and the front-end bleed permeator will only be necessary, if an average flow rate for hydrocarbons of 2.5 Pa m³/sec or higher is finally approved by the designers of ITER.

In a closed loop with continuous feed and bleed streams a combined catalyst bed (section 2) and a permeator are employed to reduce the tritium concentration in the impurity gas stream to levels below 0.1 %. Downstream of this second stage the overall decontamination factor will be at least 5000.

The final clean-up in the third stage (section 3) is carried out by a combined permeator/catalyst reactor (PERMCAT) for isotopic swamping with protium. The PERMCAT takes advantage of the high efficiency of (isotopic) exchange flows in counter current systems and is operated in such a way that the impurity gas outlet of the PERMCAT does not become tritium contaminated. Memory effects are thereby reduced to an absolute minimum.

The exceedingly high efficiency of the PERMCAT was shown by mathematical modeling and was already experimentally demonstrated with tritium under a variety of conditions. Decontamination factors of 10^4 or higher were regularly measured. Recently the geometry of the component was further optimized in an experimental campaign with a single tube unit, carried out in collaboration with the Chalk River Laboratories, Chalk River, Canada. A helium carrier gas with 0.5 % HT and 0.25 % CH_2T_2 (50 % T, 50 % H) was employed to represent an impurity flow with a tritium concentration of approximately 15,000 Ci/m³. Specific results are depicted in Figure 2.
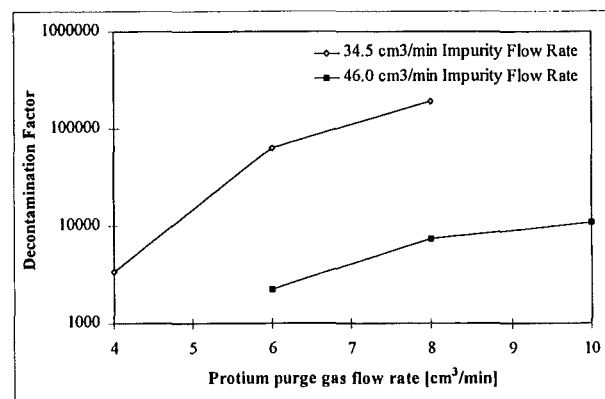
Fig. 2: Decontamination factors at different impurity flow rates versus protium flow rate

At an impurity flow rate of 34.5 cm³/min a protium purge flow rate of only 5 cm³/min is sufficient to achieve decontamination

factors above 10^4. For the given experimental inlet impurity composition of 0.5 % tritium (0.25 % in HT and 0.25 % in CH_2T_2) in helium, the tritium concentration in the waste gas drops below 0.1 Ci/m^3 at protium purge flow rates above 7.5 cm^3/min, and thus ITER specifications are met. An impurity flow rate of 46 cm^3/min demonstrates the capacity limit of the small laboratory scale unit. In this case a protium purge flow rate of about 10 cm^3/min yields decontamination factors above 10^4.

The tritium experiments also confirmed the understanding of the concentration profiles along the PERMCAT, as calculated by mathematical modelling. The CAPER facility at the TLK will be operated with a prototype of a multitube PERMCAT, manufactured at the main workshop of the Research Center Karlsruhe. The pure hydrogen isotope side of the prototype PERMCAT will be maintained at about 20 mbar by a positive displacement pump with ceramically coated cylinders and pistons from the french company SRTI. While pressures above ambient are chosen at the impurity side of the PERMCAT, the optimum pressure at the pure hydrogen isotope side is only about 20 mbar.

Even though the partial pressure of protium in the waste gas from the PERMCAT is therefore also only about 20 mbar, it would bring about a certain water load to the molecular sieves of the central detritiation system on a long term basis. Consequently another small so called off-gas permeator (section 3) is employed before the gas is finally exhausted.

Literature:

[1] M. Glugla, D.K. Murdoch, H. Geißler, P. Herrmann, R. Kraemer, T.L. Le, Design of a Catalytic Exhaust Clean-up Unit for ITER and Experimental Results, ISFNT-4, 1997

[2] M. Glugla, R.-D. Penzhorn, Tritiumlabor: Arbeiten zur Brennstoffrückgewinnung und Abgasreinigung für ITER, FZK-Nachrichten, Jahrgang 29, 1/97

[3] R.-D. Penzhorn, M. Glugla, Plasma Exhaust Gas Processing for Fusion Reactors: Developments and Problems, Proceedings of the International Tritium Workshop on Present Status and Prospect of Tritium - Material Interaction Studies, Eds. K. Watanabe, M. Matsuyama, Toyama University, Gofuku, Toyama, Japan, July 18-19, 1996

Staff:

M. Glugla
K. Günther
P. Herrmann (Ph.D. Student)
T.L. Le
W. Leifeld
R.-D. Penzhorn
K.H. Simon
D. Taylor (guest scientist)
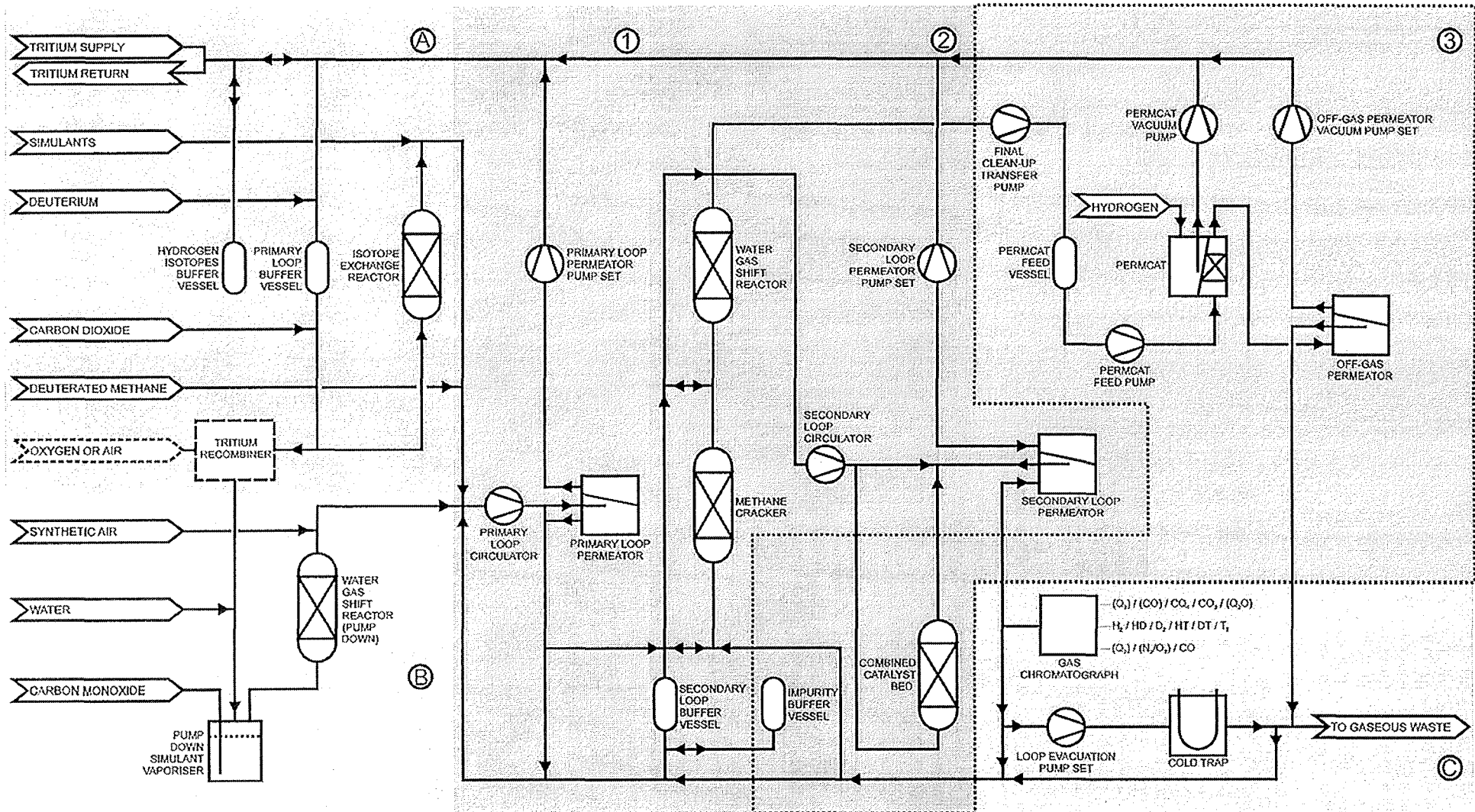
Fig. 1: Outline Flow Diagram of 'CAPER at TLK' (Tritium Laboratory Karlsruhe)

TEP 3 A
Tritium Storage

The intermetallic compound zirconium-cobalt has been selected by ITER as the reference material for the storage of hydrogen isotopes in the Tritium Plant because of its good gettering properties and non-nuclear character. On this account it is of great practical interest to continue the investigation of the properties of this material with the aim of obtaining a solid scientific data base.

Rechargeable hydriding alloys used under cyclic operating conditions may be subject to performance degradation of two types: interaction with gaseous impurities (extrinsic process) and alloy disproportionation (intrinsic process). While ZrCo is comparatively non-sensitive towards the reaction with gaseous impurities it does undergo disproportionation. Further careful examination of this latter property of ZrCo is therefore of importance.

From previous work it was established that the disproportionation of ZrCo is promoted by high hydrogen pressures, high temperatures and the number of adsorption/desorption cycles. Recent results indicate that a rather fast disproportionation commences at temperatures above 470 °C when the getter material is exposed to a pressure of approx. 1 bar. Thus, to evade conversion of ZrCo into $ZrCo_2$ and Zr, exposure of the getter material concomitantly to high temperature and high pressures should be avoided.

The results in Table 1 demonstrate that disproportionated material can be regenerated. When a small sample of ZrCo was loaded employing 805.8 torr of hydrogen at 30 °C the temperature of the sample rose to 115 °C due to the

exothermicity of the reaction. The achieved loading was $ZrCoH_x$ with x = 2.65 (max. x = 3). The sample was then heated under vacuum for 12.2 hours and after that loaded and deloaded several times. As apparent from the results, the sample could be carried through several loading/deloading cycles without a significant change in its hydrogen absorption properties. The same sample was then completely disproportionated to the point that the stoichiometric factor reached a value of only x = 0.95. A further loading/deloading cycle showed that the achievable stoichiometric factor, i.e. x = 2.43, was somewhat below that reached in previous loading/deloading cycles with an intact sample. A regeneration was therefore carried by evacuating the sample for an extended period of time, i.e. 20 hours. After this treatment the sample could again be loaded and deloaded yielding „normal" stoichiometric factors of x = 2.59. These experiments, which indicate that a regeneration of ZrCo is possible at temperatures of about 500 °C provided a good vacuum is maintained for an extended period of time, are in line with earlier results obtained at the Tritium Process Laboratory in Naka, Japan.

Further work aimed at determining quantitatively the kinetics and thermodynamics of the disproportionation/reproportionation characteristics of ZrCo are in progress.

<u>Staff:</u>

N. Bekris
U. Besserer
<u>R.-D. Penzhorn</u>
M. Sirch

Table 1: Disproportionation and regeneration of ZrCo

Treatment	Temp °C	Temp. Max. °C	P_{H2}^o [torr]	P_{H2}^{in} [torr]	P_{H2}^f	% degradation	x	% regeneration	Time [h]
Loading	35	115	805.8	760.7	641.1		2.65		0.17
Regeneration	500								12.2
Loading	30	110	811.6	766.2	649.7		2.58	97	
Deloading	510								2.75
Loading	30	115	803.5	758.5	640		2.62	99	
Deloading	500								1.67
Loading	30	110	814	768.4	650		2.62	99	
Deloading	510								2
Loading	30	110	806.2	761.1	642.1		2.63	99	
Regeneration	515								16
Loading	20	105	804.6	759.6	641		2.62	99	
Disproportionation	500			641/750	727	84	0.95		
Deloading	500								2.67
Loading	25	100	806	760.9	651		2.43	93	
Regeneration	510								20
Loading	20	105	830	783.5	667.7		2.56	98	
Deloading	510								2
Loading	25	105	817.1	771.4	654.4		2.59	99	
Disproportionation	500			654.4/763	741.3	84	0.92		65

SEA 3-2 (N 11 TD 72)
Reference Accident Sequences - Magnet Systems (2)

Subtask 2: Magnet System Safety

Within the subtask 3.2 FZK investigates the thermal behavior of magnet systems during accidents.

In the period reported code application and validation of MAGS have been major parts of the work.

Improvement of MAGS has been done mainly on the modules CRYOSTAT and SHORTARC. The application of CRYOSTAT with Nitrogen properties below its critical point indicated numerical instabilities in heat and mass flow, due to the small heat capacities of low pressure volumina. These problems have been solved by introduction of maximum heat fluxes and minimum gas content in the volumes. Another effort in improvement of CRYOSTAT was the introduction of water and steam properties.This allows now the analysis of steam flow. Mixtures, however, cannot yet be handled.

For module SHORTARC a more realistic power release within the mesh elements of the arc is modeled. While the old version cumulated all arc energy into one mesh element, the new distributes the arc energy to all mesh elements containing the arc. Ignition and extinction of arcs require sharp gradients in the resistivities of the electrical circuits. This leads for some cases to an unexpected interrupt of the analysis. To overcome these problems damping functions have been superimposed on the switching operations. Another point of criticism on the SHORTARC model is the high voltage calculated. It is caused by the growth of the arc length beyond realistic values, e.g. several tens of meters. Now a maximum arc length, e.g. 1m, can be specified by the user.

Investigation of arcs in the ITER coils have been continued. Especially the possibly large energy deposition in the PF 5 coil, reported last year, was of interest. The huge voltages calculated with the first version of SHORTARC initiated considerations on the realism of this model. One criticism has been that an arc in SHORTARC is fixed to a given location:

It was suspected that the magnet field will direct the plasma according the Lorentz force to one side and may cause a moving arc burning between adjacent turns. This would result in an arc of a fixed length, i.e. the distance between the adjacent conductors, and a relative low power. Simple estimates show that this would reduce the power released in the coil considerably. The travel distance of such an arc would be in the range of some meters. On the other hand there are also low field locations in a coil where practically no Lorentz force is excerted. Finally prior to use such an effect for safety arguments, experiments should demonstrate the effect.

A more general way to overcome the problem of long arc lengths is to consider the thick jacket of the conductor as a parallel current path to the arc. I.e. if the voltage along the arc is high enough to press the current through the jacket and the contact resistances between conductor and jacket, the current takes this path. Application of this model leads to low energy depositions in the PF coils, the contact resistances, however should be measured in an experiment.

A sensitivity study of the quench behavior on the quench location in the ITER coils showed, that the main spatial effect is the power released due to the local magnet field. Even dump delay of 10 seconds, assumed for the analysis, poses no problem for the coils. Typically a maximum temperature is reached between 50 K and 180 K and the quenched zone is convected along the conductor.

Application of CRYOSTAT on the accident sequence 'leak in the cryostat' indicates for large leaks, about $1 m^2$, a pressure reduction in the adjacent volume of 0.02 MPa. For small leaks the pressure in the cryostat is increased to 10 Pa and is then constant for hours, i.e. sufficient time to initiate mitigating actions.

The experiment to investigate transversal heat conduction and quench propagation Q3D, performed at and together with ITP at FZK has been successfully completed. The analysis of the data measured will start in near future.

Validation of MAGS has been continued recalculating some runs of the QUELL experiment (QUench Experiment on Long Length). The experiment used a subsized cable with a central hole, typical for the CS coil of ITER. The pressure calculated for the first 4 seconds shows a very good agreement, while for larger times the calculated pressure is too low (Fig. 1). The calculated jacket temperature is a little bit too high ($\Delta T = 3K$ to 15K) but the shape of the plot agrees well. Comparision of the quenched length shows a good quantitative agreement. However, while the experiment shows a progressive growth of the quenched length, the analysis shows a degressive one.

A sensitivity study, investigating 12 different parameters did indicate sensitivity of the results on magnet field, critical current density and thermal conductance. The shape function of the calculated quenched length was not to be changed with any of these parameters, meaning that some basic effect of conductors with a central hole is not yet well modelled.

Staff:

M. Biemüller
G. Bönisch
W. Kuhn
R. Meyder
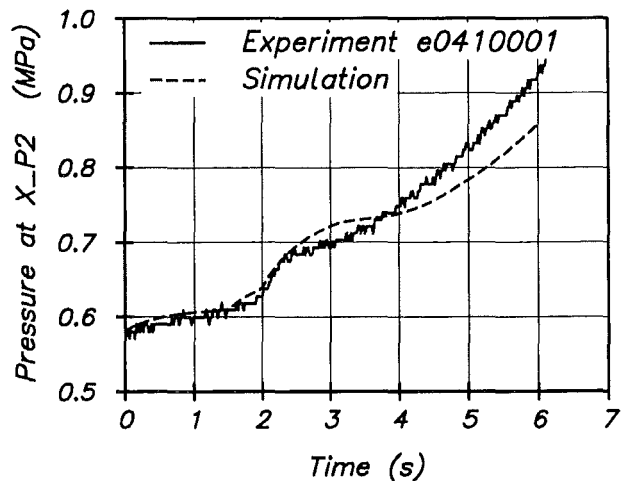
Fig. 1: Measured and calculated pressure history for the QUELL experiment e0410001

SEP 2
Environmental Impact

The computer code 'Plant-OBT' for describing the OBT formation and translocation in wheat plants has been further developed [1]. Comparative calculations performed with experimental data from 1995 and 1996 showed, however, that our present understanding of the processes seems to be not deep enough to describe the OBT formation in the seedlings of winter wheats using only a limited number of environmental parameters. In particular, the dynamics of the OBT formation could not reproduced in detail. The final OBT content at the time of harvest, however, could be predicted within a bandwith of a factor of two. The next step will be the modification of the present OBT model in UFOTRI, the accident consequence assessment code for tritium releases [2], based on the knowledge which has been gained by developing and testing 'Plant-OBT'.

Within BIOMOVS II (BIOsheric MOdel Validation Study - phase II) tritium models for accidental releases, including UFOTRI and Plant-OBT, have been tested using various scenarios. Both computer codes performed these tests successfully [3], [4]. After the completion of this study, the BIOMASS (BIOspheric Modelling and ASSessment) project was launched particularly with the goal to continue work started within BIOMOVS. Also the tritium working group continued, however the main emphasis is now directed towards normal operation questions. Mainly atmospheric dispersion and deposition following routine releases as well as transport and dispersion in ground water will be investigated in future.

For accidental and normal operation releases, dose assessments were performed in the frame of subtask SEP2 of the European Fusion Programme for the two sites of Greifswald, Germany, and Cadarache, France, which were potential sites for ITER at the time of the investigations. Probabilistic dose assessments for accidental atmospheric releases of various source terms which contain either tritium and/or activation products were carried out. No country specific rules were applied and the input parameters were adapted as far as possible to those used within former ITER studies to have a better comparison to site independent dose assessments performed in the frame of ITER. The present calculations were based on source terms which, for the first time, contain a combination of tritium and activation products. This allowed a better judgement of the contribution of the individual fusion relevant materials to the final dose. The results were compared to site independent dose limits defined in the frame of ITER. Source terms for two different categories, representing 'extremely unlikely events' (CAT-IV) and 'hypothetical sequences' (CAT-V), were investigated. In no cases, the release scenarios of category CAT-IV exceeded the ITER limits. However, early doses from the hypothetical scenarios of type CAT-V exceeded in several situations 10 mSv, but were still below 50 mSv or 100 mSv which are defined as the lower values for the initiation of evacuation in many potential home countries of ITER. Only the banning of food products was found to be a potential countermeasure affecting larger areas [5].

Literature:

[1] Raskob, W., Diabaté, S. and Strack, S., A New Approach for Modelling the Formation and Translocation of Organically Bound Tritium in Accident Consequence Assessment Codes, in: Proc. of the International Symposium on Ionising Radiation: 'Protection of the Environment', Stockholm, Sweden, May 20 - 24, 1996, pp.: 400 - 408, 1996

[2] Raskob, W., Description of the New Version 4.0 of the Tritium Model UFOTRI Including User Guide, Report KfK-5194, Kernforschungszentrum Karlsruhe (1993)

[3] BIOMOVS II, Tritium in the Food Chain: Intercomparison of Model Predictions of Contamination in Soil, Crops, Milk and Beef after a Short Term Exposure of Tritiated Water Vapour in Air, Technical Report No. 8 of the BIOMOVS II Working Group on Special Radionuclides, (1996)

[4] BIOMOVS II, Tritium in the Food Chain: Comparison of Prediction and Observed Behaviour A. Re-Emission from Soil and Vegetation B. Formation of Organically Bound Tritium in Grain of Spring Wheat, Technical Report No. 13 of the BIOMOVS II Working Group on Special Radionuclides, (1996)

[5] Raskob, W. and Hasemann, I., Dose Assessment for Greifswald and Cadarache with new source terms from ITER NSSR-1. Report FZKA-5960, Forschungszentrum Karlsruhe (1997)

Staff:

J. Ehrhardt
I. Hasemann
W. Raskob

ERB 5000 CT95 0064 (NET/95-384)
ITER Magnets and TFMC Stress Analysis

Under this contract finite element analyses for two subtasks are performed:

a) Stress analysis for the ITER Toroidal Field Model Coil (TFMC), the Intercoil Structure (ICS) and the LCT coil to test the TFMC in the background field of the LCT coil in the TOSKA cryostat in cooperation with the EU Home Team,

b) stress analysis for the ITER coils in cooperation with the ITER Joint Central Team.

This work, from which previous activities are reported in [1, 2], has been continued.

TFMC analysis

The finite element analyses of the TFMC test configuration performed so far [3] have shown that particular attention should be paid to stress concentrations arising inside the ICS and in particular in the side wedges.

To study the stress concentrations in more detail additional analyses using local models have been performed. Fig. 1 shows a FE model for a side wedge and a quarter part of the model coil. The Lorentz force loaded coil is kept in position in out-of-plane direction by the side wedges. With this model the stress distribution along the contact surfaces could be studied in more detail taking into account stress redistributions due to plastic deformations.
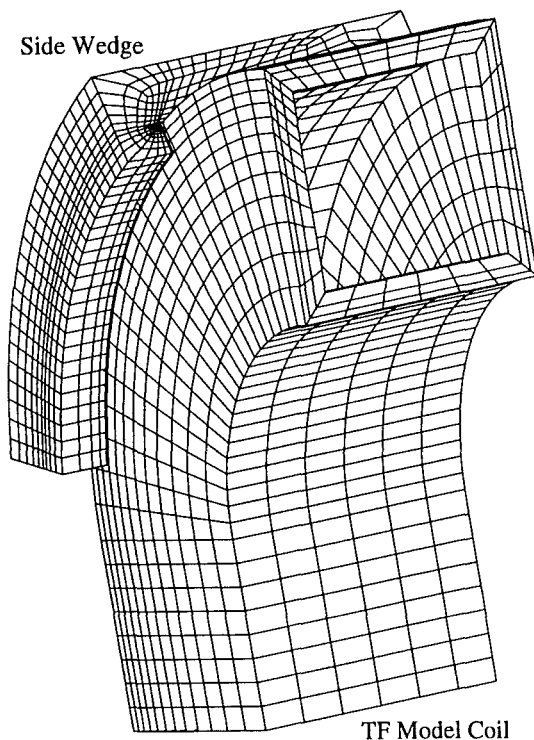
Fig. 1: TFM, Mesh of one side wedge and a quarter of the model coil

In a further activity using a simple beam-and-shell model the reasons for the stress concentrations and possible design modifications to avoid them have been studied. For instance, concerning the side wedges the stress peaks at the wedge ends can be reduced either by flexible edges (changed wedge design), by a sloped wedge surface (to control the contact behaviour) or by a softer interface layer (to redistribute the stresses by plastic deformation).

The results of these investigations and several proposals for design modifications are reported in [4,5]. Some proposals are now realized in the engineering design which is carried out by the industrial consortium AGAN.

A second major TFMC problem revealed also in [3] is the relative high deformation in the area of conductor joint boxes which lies at the straight leg of the race track form of the model coil. In order to find design modifications to reduce this deformations a study about the different reasons for this problem has been performed [6]. It was shown that the problem is mainly caused by the chosen race track form of the model coil (not D-shape as at the ITER TF coils) and that the potential for improvements using the chosen ICS concept is rather limited.

Therefore a proposal was made by NET to integrate the ICS into the coil casing (welding the ICS onto the casing) in order to stiffen the model coil and thus reduce the deformations. The results of the analysis for such a design are reported in [7]. However, this change would affect the model character of the coil. Meantime the decision was made by the JCT to use the original ICS design.

Our further activities will be to support and guide the engineering design being performed by AGAN. To prepare the tests in TOSKA we will plan the mechanical instrumentation of the test rig and develop a calculational model to predict and postprocess the mechanical test behaviour of the coil assembly.

ITER stress analysis

To continue the EU Home Team work for the ITER stress analysis the global model for the ITER coils established by C.Jong [8] was transferred and modified to take into account the new coil supporting of the BDPA-95 design. Fig. 2 shows the modified FE model. (The poloidal field coils and their supporting structures are not shown.) In comparison with the former design only minor changes of the global stress and deformation behaviour occurred.

Some detailed post processing was done to look for stress concentrations at the monorail/crown contact zones in order to search for parallels to the TFMC wedge behaviour. Some post processing for the joint area deformations has been carried out for similar reasons. It was shown that the D-form of the coil is less problematic than the race track form of the model coil concerning this item. An investigation on the potential of the TF coil weight reduction was done with a linearized model derived from the global model used above. The result was that about 10% reduction should be possible. Of course this has to be proven by a detailed analysis.

Meantime new design modifications (BDPA-97), which are supposed to be the final ones, have been established by the JCT. Our first activity for this final design is a study of some details of the radial plate behaviour aimed at the stresses at the radial plate/cover welding and the influence of the welding seem deepness on the welding stresses under different loadings given by the global model. Fig. 3 shows the details of the model for one conductor laying in the groove of the radial plate, closed by the welded cover. The 3D FE model for four such unit cells is shown in Fig. 4.
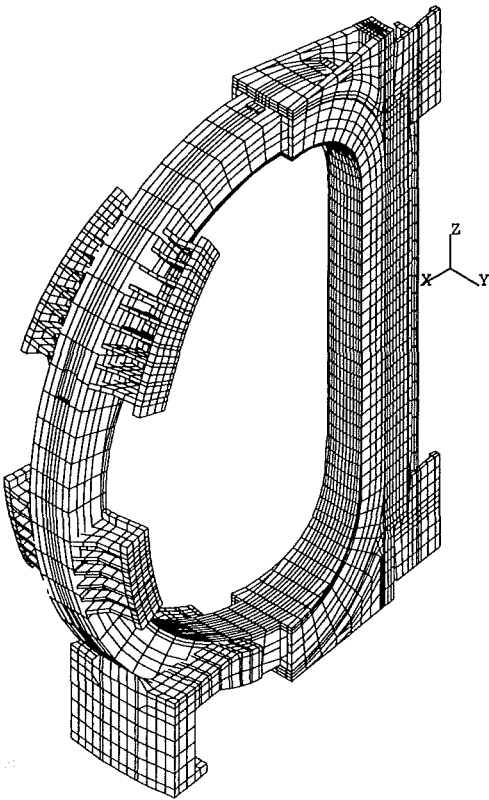
Fig. 2: ITER magnets global model

Fig. 3: Modelled details of one conductor unit cell

This and further activities will be performed in close cooperation with the JCT in the rather tight time schedule of the final EDA period.

Fig. 4: Local model of four conductor unit cells

Literature:

[1] 'Nuclear Fusion Project Annual Report of the Association Forschungszentrum Karlsruhe/EURATOM', October 1994 - September 1995, FZKA 5688, EUR 16749EN

[2] 'Nuclear Fusion Project Annual Report of the Association Forschungszentrum Karlsruhe/EURATOM', October 1995 - September 1996, FZKA 5858, EUR 17512EN

[3] EU Home Team 'ITER TF Model Coil - Finite Element Analysis of the Conceptual Design of the TFMC Test Configuration', June 1996

[4] P. Libeyre, P. Decool, B. Turck, B. Dolensky, R. Meyer, S. Raff 'Simulating the ITER TF magnet with the TF Model Coil adjacent to the LCT Coil', Proc. 19th SOFT, Sept. 16-19,1996,Lisbon

[5] EU Home Team 'ITER TF Model Coil - finite element analysis of modifying the intercoil structure - side wedge extension, - pads and horizontal plates reinforcement', June 1997

[6] EU Home Team 'ITER TF Model Coil - Influence of load components on the joint area elongation and design modifications to minimize it', June 1997

[7] EU Home Team 'ITER TF Model Coil - Finite element analysis of welding the case to the ICS', revised version, June 1997

[8] C.T.J. Jong 'Analysis of the Mechanical Behaviour of the ITER Magnet System', ECN-c--96-001

Staff:

B. Dolensky
R. Meyer
S. Raff

ERB 5004 CT 960050 (NET/96-405)
(Subtask of ITER Task MD9 for 1996)
Transient Voltage Behaviour for the ITER TF
Coil

The aim of the contract is the investigation oft he ITER toroidal field coil with respect to its behaviour under transient voltages like they occur during the operation of counteracting current switches for removal of the energy after a quench.

The final report with an addendum was submitted to NET and the ITER JCT at Naka site and accepted [1], [2].

In the addendum a detailed finite element model was developed to investigate the magnetic coupling of the turns of the ITER TF coil in the frequency and time domain [3]. The model was excited by a frequency independent current through a single cable. At higher frequencies currents in steel portion in which the cable is imbedded reduce the magnetic field and the coupling.

At each frequency the comparision of the induced currents in the neighbouring conductors with the currents which are induced if the steel is replaced results in mutual inductances related to its DC value. While low frequencies (below 100 Hz) currents in steel portion have almost no influence on the magnetic coupling, at 1 kHz the coupling is about 25 % of its DC value and at 10 KHz it is about 2.5 %

Transient analysis was performed with an exponentially time dependent current with time constants in the range of 250 μs to 10 ms. If the time constant is 250 μs the magnetic coupling at 0.2 ms is 20 % of its DC value. At 0.6 ms the coupling is 50 % converging to its DC value after 1 ms. For 10 ms time constant currents in steel portions are very small and do not signifcantly reduce the magnetic coupling.

If magnetic coupling is reduced the natural frequencies of oscillation are expected to increase. All magnetic coupling inductances were removed from the network model to perform worst case analysis. The lowest frequency of oscillations for the case where a small resistor (5 Ohms) is used for electrical connection to the conductor to the potential potential of the shear plates occurs at about 4 kHz (compared to 1.7 kHz if the DC value of magnetic coupling is applied). Although the result may slightly differ with different grounding conditions the lowest frequency of oscillation will be in any case far below 10 kHz.

The finite element model applied in the frequency domain can be used for improving the network model by introducing frequency dependent mutal inductances.

The TF model coil is the first shear plate coil built which can be experimentally investigated according to its transient behaviour for the validation of calculation models.

Literature:

[1] C. Sihler, A. Ulbricht , A. M. Miri, Transient voltage effects in the ITER TF coils (Subtask1 of ITER Task MD9 for 1996), Final Report, Forschungszentrum Karlsruhe, Interner Bericht , December 1996

[2] A. M. Miri, C. Sihler, A. Ulbricht, Reduction of electrical stresses in large superconducting magnet coils by optimizing grounding conditions, Proc. 10th Int. Symp. of High Voltage Engineering, Montreal ,Canada, 1997/08/25-29

[3] A. M. Miri, N. Riegel, C. Sihler, A. Ulbricht, Addendum to the Final Report: Transient voltage effects in the ITER TF coils (Subtask1 of ITER Task MD9 for 1996), Final Report, Forschungszentrum Karlsruhe, Interner Bericht, June 1997

Staff:

A. Ulbricht

ERB 5004 CT 960053 (NET/96-408)
Characterization of Jacket Materials

The aim of the contract is the characterization of conductor jacket materials for ITER. By introducing a novel measurement method, assured by means of existing standards, the characterization was performed through all actual fabrication stages. For 316LN and Incoloy 908 the characterization was successfully performed.

Background

This report refers to the final results with respect to materials characterization of the industrial manufactured jacket material, designed for the use as a conduit for the ITER CS-model coil. Type 316LN austenitic stainless steel and Incoloy 908, a γ'-precipitation hardened nickel base superalloy, are the principal candidate materials for the jackets of the ITER TF and CS model coils. Tensile, fracture toughness, and fatigue crack growth rate (FCGR) tests at 7 K were carried out to characterize the mechanical properties of both jacket materials and provide the data required for the engineering design and performance evaluation of the magnet structures.

The fracture toughness test standards demand the use of specimens whose dimensions are at the limit of the CS jacket section thickness whilst there is no test technique currently available for obtaining valid fracture toughness data for the thinner TF jacket. The existing ASTM elastic - plastic fracture mechanics test standards have therefore been critically assessed with respect to the measurements on 3 - 4 mm compact tension (CT) specimens; the uncertainties and possible sources of the scatter in the results obtained using the single specimen test method were evaluated and a new approach adopted for establishing the resistance (J - R) curves. In addition, a novel fracture toughness test method for small specimens has been developed and the validity of the results cross - checked, utilizing established data bases for several different materials.

Material and specimens

The 316LN austenitic steel and Incoloy 908 TF and CS jacket sections were provided by Ansaldo, Genoa. The austenitic steel TF jacket sections were produced initially as seamless tubes, 46 mm OD and 2 mm wall thickness; they were subsequently drawn to 40.5 mm OD and 1.6 mm wall thickness and orbital fusion welded by an autogenous technique. The extruded CS jackets were delivered in 400 mm long pieces, 51 mm square sections with a 38 mm diameter central hole. Transverse fusion welds had been made in the mid zones of each jacket length using a V - grooved joint and, with exception of the first pass, filler wires (ferrite content ~0) of similar compositions to the base materials. The welded sections had then been compacted, bent to a radius of 2,000 mm, and subsequently straightened to simulate the spooling procedure. Some of the TF and CS sections were finally aged at the reaction heat treatment

temperature of 650 C for 200 hours in vacuum and under clean condition (< 1 ppm oxygen, 10^{-3} Pa total pressure at temperature). The type and orientations of the specimens machined from the jacket sections for the tensile, fracture toughness and FCGR tests at 7 K are illustrated in Figure 1. The specimen dimensions were as follows:

CT: ASTM proportional 45 x 43 x ~ 4 mm.

EDM notched round bar: 30 - 65 mm long with a shaft diameter of 4 - 6 mm and a net diameter after notching around the girth of about one third of the shaft diameter.

Round smooth tensile: gauge diameters of 4 and 3 mm for specimens machined from the CS - jacket corner and mid wall positions respectively.

Double notched flat tensile: nominal and net section widths of 5 and 1.5 mm respectively.

Tensile test results

The results (average of two measurements) of the tensile tests on the non - aged and aged CS - jacket (corner position) sections and TF - jacket tubes performed at an initial strain rate of $2 \cdot 10^{-4}$ K are given in Table 1. The yield strengths of the specimens machined from the minimum wall thickness position of the CS sections are about 5 per cent lower than those for corner positions; this is attributed to the increased level of cold working at the corner positions compared to the mid - wall during manufacture. The results demonstrate that the aging treatment has little or no effect on the 7 K tensile properties of the 316LN austenitic steel but increases the yield and ultimate strengths of the Incoloy 908 as a result of the γ' precipitation. Furthermore, the strengths and ductilities of the aged CS 316LN steel welds are inferior to those of the base steel and the yield strength of the aged TF jacket steel is about 100 MPa lower than for the CS - jacket.

Fracture toughness tests and results

The standard single specimen test method, as recommended by ASTM E 813 - 88, was initially adopted for the fracture toughness tests at cryogenic temperatures. However, the limitations on the dimensions of the specimens which should be machined from the CS - and TF - jackets posed several problems which had to be solved before reliable assessments of the elastic - plastic J - values
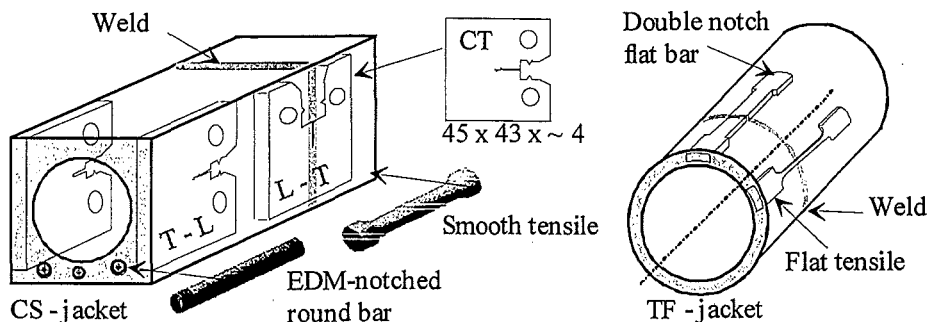
Fig. 1: Type and orientation of the specimens from CS and TF-model jacket structures

Table 1: Effects of aging on tensile properties at 7 K

Jacketing materials and position of the specimens in extrusion or tubing (L) - and transverse (T) - direction	Young's Modulus, E GPa	Yield strength, σ_Y MPa	Ultimate tensile strength, UTS MPa	Uniform Elongation %
CS - aged ~316LN corner (L)	207	1226	1673	~ 38
CS - aged ~316LN mid wall (L)	205	1167	--	--
CS - non aged ~316LN corner (L)	203	1232	1692	~ 40
CS - aged ~316LN, weld, corner (L)	197	1104	1467	~ 17
CS - aged ~316LN, weld, (T)	196	1030	1430	~ 18
TF - aged ~316LN (L)	202	1100	1606	~ 40
CS - aged Incoloy 908 corner (L)	175	1216	1706	~ 22
CS - aged Incoloy 908 mid wall (L)	177	1141	--	--
CS non aged Incoloy 908 corner (L)	180	625	1028	~ 52

that reliable data could be made. Thus, whilst the load - displacement curve for a welded and aged Type 316LN steel CS - jacket CT specimen of 4 mm thickness (Figure 2b) does not appear to show any unusual behavior, the evaluation of the data using the initial unloading compliance method (Figure 2a) reveals two significant features; these are the apparent negative crack extension and the large scatter of the J - R data despite the high precision of the measurements. Similar behavior was exhibited in the tests on the jacket base material but the scatter in the data was less than that of the weld metal. The negative extensions result from the crack lengths being estimated from the unloading compliance lines of the load - displacement records and the present standard does not make any recommendations as to how the data should be corrected. A new approach has consequently been developed to determine the "precise" corrections to be applied to the J - R plots and enable a reasonable assessment of the data to be made without violating the standard. This was accomplished using all of the data from the unloading lines and plotting the stiffness (rather than the initial compliance) versus the displacement at the onset of unloading. The open circles in Figure 2b are the „as-measured" experimental points; a second order least square regression analysis of the data was performed and a smooth function established (closed circles in Figure 2b). The maximum stiffness value is an important parameter and is the result of two opposing deformation processes. During the initial loading phase plastic deformation occurs and produces blunting at the crack tip whilst additional deformation takes place due to the plane stress constraints imposed by the opposite faces of the CT specimen. The stiffness increases gradually during the initial stage but microvoid coalescence occurs on further loading resulting in crack extension and decreases in stiffness (Figure 2b). This pattern of behavior has been confirmed in several tests in which the unloading/loading process was stopped at the point of maximum stiffness and the fracture surfaces of the CT specimens examined microscopically. Microvoid coalescence was observed in the majority of cases and it has consequently been concluded that crack initiation occurs at the point of

maximum stiffness. The crack extensions were therefore calculated taking the maximum and final stiffness points as corresponding to the initial and final crack lengths, the latter being measured after specimen fracture.

The J - R curve shown in Figure 2a was therefore established by shifting the J - value corresponding to the maximum stiffness position to the zero - offset blunting line, the subsequent crack lengths being calculated using a linear approximation determined with multi - specimen method. The provisional critical J values for the jacket and reference plate materials obtained by this procedure are listed in Table 2. However, the provisional J_Q values derived for the aged 316LN and Incoloy 908 CS - jackets using the 4 mm thick CT specimens are not valid according to the ASTM E 813 - 88 standard criteria; the size criterion (§9.4.1.1) was not fulfilled in every case whilst all the crack extension profiles showed a sharp triangular appearance, thereby violating the §9.4.1.6 criterion. The 15 mm thick CT specimen tests of the aged reference plate materials fulfilled the E 813 - 88 validity criteria. In addition, it was possible to test specimens of the aged commercial Type 316LN and 03Cr20Ni16Mn6N steel plates at 4 K using the ASTM E 399 standard because of their low fracture toughness. However, the low elastic plastic fracture toughness of the aged Type 316LN steel U - section (J_Q ~ 56 N/mm) at 7 K determined using 4 mm thick CT specimens implied could be obtained in this case with the E 813 - 88 standard using small size specimens; the crack tunneling was also considerably less pronounced, giving added confidence in the validity of the data. The J_Q of 295 N/mm at 4 K for the aged Incoloy 908 plate measured using the multi - specimen method (four 15 mm thick CT specimens) resulted in a fracture

(a)

(b)
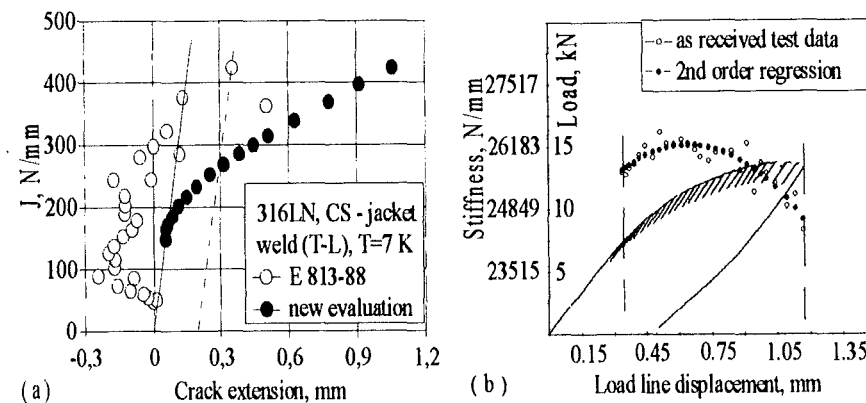
Fig. 2: Single specimen test results of a Type 316LN aged jacket weld material at 7 K. (a) according to unloading initial compliance function of E 813-88 standard (open circles) and the evaluated J - R curve (bold circles) using a new approach where the "exact" amount of shift was determined. (b) unloading loading record of the load versus load line displacement diagram and the corresponding stiffness at the unloading points (open circles).

Table 2: Elastic - plastic toughness at 7 K of aged jacket and reference materials determined using various test methods

Aged jacketing and reference materials	Provisional J_Q CT 4 and 15 N/mm	Critical J_c with flat double notch EDM N/mm	Critical J_c with round bar EDM N/mm	K_{Ic} at 4 K by E 399 MPa√m
316LN CS jacket base, CT- 4	165 - 270	180 - 208	175 - 239	
316LN CS jacket weld, CT- 4 compacted	230- 285	--	79 - 149	
316LN CS jacket weld, CT- 4 compacted / bent / straightened	175 - 190	--	63 - 176	
Incoloy 908 CS jacket base, CT- 4	305 - 365	--	191 - 237	
Incoloy 908 CS jacket weld, CT~ 4	135 - 170	--	70 - 74	
316LN TF jacket base	--	156 - 200	--	
316LN TF jacket weld	--	95 - 116	--	
Incoloy 908 TF jacket base	--	316	--	
Incoloy 908 TF jacket weld	--	91 - 101	--	
Incoloy 908 plate CT - 15	295	--	251	
03Cr20Ni16Mn6N plate CT - 15	69 - 90 (CT- 4 and 5)	--	53 - 69	109 - 113
316LN plate CT - 15		--	81 - 85	122 - 128
316LN A-410 U-section CT - 4	52 - 60	--	59 - 62	

toughness $K_{Ic}(J)$ of 230 MPa√m $[K_{Ic}(J)^2 = E \times J_{Ic}]$; however, the elastic - plastic critical J - integral values tend to overestimate the toughness even with 1.0 - 1.5 in. (25.4 - 38.1 mm) thick CT specimens and so the values of > 200 MPa√m measured with 15 mm thick samples should be treated with some caution.

Additional fracture toughness investigations were carried out using the newly developed technique in which round (4 or 6 mm diameter) bar specimens with circumferential EDM notches are tested at a slow stroke rate (~ 0.5 mm/min) at 7 K. The results of such tests (Table 2) on the aged commercial Type 316LN and 03Cr20Ni16Mn6N steel plate materials yielded mean critical J_c values of 83 and 61 N/mm respectively; these values are in good agreement with the results of the E 399 tests on these materials at 4 K (K_{Ic} = 126 and 112 MPa√m corresponding to J_{Ic} = 77 and 61 N/mm respectively). The results of the round bar tests at 7 K on the aged Type 316LN steel U - section also agree with the J_Q data obtained with the 4 mm thick CT specimens (see Table 2). Similar tests at 7 K on the TF - jacket materials (1.6 and 1.0 mm thick Type 316LN and Incoloy 908 respectively) were also performed using the double EDM notch flat specimens and the results are included in Table 2. In addition, the J_c data at 7 K obtained with the notched flat specimens of the aged Type 316LN steel CS - jacket material were similar to those for the round bar specimens machined from the same position of the CS - jacket section. The minimum fracture toughness values for both the aged Type 316LN steel and Incoloy 908 jacket base material measured in the tests to date on the round bar specimens are in excess of 185 MPa√m. The reduction in fracture toughness of the Type 316LN steel CS - jacket produced by the aging treatment is moderate as the previously measured values for this type of steel in the unaged condition ranges from 200 - 260 MPa√m depending on the fabrication (thermo - mechanical treatment) details.

Fatigue crack growth rate results

The base material and weld metal FCGR specimens were machined from the CS - jacket sections in the T-L orientation, and L-T orientation respectively (see Fig. 1). FCGR tests were performed at 7 K using a helium flow cryostat and a MTS servohydraulic unit (Model 810) with a built-in fiberscope for direct observation of the crack length; the test procedure has been detailed previously. Within this task it could be determined that the resistance to crack propagation of the aged 316LN steel base is slightly inferior to that of the weldment from the compacted section; this is probably due to the introduction of compressive stresses by the compaction process which oppose the residual tensile stresses in the weld zone.

The aged 316LN steel weld specimens machined from the compacted and bent sections exhibit even lower FCGRs. In addition, these samples show two behavioral regimes; the FCGR during the initial propagation of the fatigue crack (from 0.5 to 4 mm length) is reduced on further penetration (up to 7 mm) into the specimen. This reproducible behavior is attributed to the effect of compression on the propagating crack, resulting in constraints at the crack tip and crack closure effects. The presence of compression stresses at the crack tips appears to be confirmed by the appearance of a „knee" in the load displacement curve obtained during static loading of the specimen containing the 7 mm long crack; this characteristic was not evident in similar tests conducted on the other welded and compacted samples. The FCGR of the aged Incoloy 908 base material is considerably lower (factor of 2 - 3 within the range 20 - 25 MPa√m) than that of the aged 316LN steel base. However, both materials FCGR behavior is comparable at high ΔK regime (~30 MPa√m).

Staff:

A. Nyilas
T. Rusli
H. Baumann

NET 96/433
Definition of a Test Programme for ITER Primary-Wall Module Medium-Scale Mock-up at FIWATKA

Modules in the ITER shield blanket system are subject to large transient thermal loads imposed by the reactor's power cycling operating fashion. Material fatigue of diffusion-bonded material interfaces of copper and stainless steel could be a consequence.

of the module, the aim being a better understanding of the module's working and the creation of a database for defining a FIWATKA test. Fig. 1 displays the module temperature distribution at the end of the burn phase. Critical stresses were observed at midplane first-wall locations shortly after ramp-down and at the poloidal end at the end of the burn phase. Given the general level of stresses found and given the unique design material interfaces in the module, the concern about of material fatigue that is supported by the results is unlikely to be removed completely by design changes. Therefore mock-up testing appears necessary.

A corresponding finite-element analysis of a mock-up shows that important stresses and stress ranges at the poloidal end cannot be reached under current FIWATKA boundary conditions. The results indicate that the assumed constant heating of the mock-up's back region would need to be replaced by cyclic heating to improve the relevance of mock-up conditions .

Literature:

[1] B. Dolensky, S. Gordeev, S. Hermsmeyer, G. Hofmann, M. Kamlah, K. Schleisiek: Definition of a Test Programme for ITER Primary Wall Module Medium-Scale Mock-up at FIWATKA. Interner Bericht (Juni 97)

Staff:

B. Dolensky
S. Gordeev
S. Hermsmeyer
G. Hofmann
M. Kamlah
K. Schleisiek

Fig. 1: Temperature distribution in the ITER shield module at the end of the burn phase

This project was concerned with medium-scale mock-up testing of blanket modules in the FIWATKA facility at FZK, particularly whether mechanical conditions representative of ITER conditions can be simulated. It extended previous work that did not cover the poloidal extension and poloidal ends of the module.

ITER transient temperatures and stresses across the module were analysed using a fully-3d radial-poloidal, 44mm thick, slice

ERB 5004 CT 970009 (NET/96-438)
High Voltage Components and Sensor
Calibration for the ITER TFMC (TF Model Coil)

The aim of the contract is the support of the European industry consortium, AGAN, in the fabrication of the TFMC by providing components which were already developed in the frame of project POLO at FZK. These components are not commercially available and need pretesting at helium temperature. These are radial and axial insulation breaks, instrumentation wire feedthroughs and different types of terminals for high voltage instrumentation cables, which are potential guiding electrodes and warm vacuum tight feedthroughs designed as high voltage tight plugin connectors.

The test facility for the radial insulation breaks is already available. The test facility for axial insulation breaks and feedhtroughs was newly designed and constructed in order to test 8 components in one thermal cycle.

It is expected that the fabrication of the components can start in last quarter of 1997.

The Test Facility for the Axial Insulation Breaks and Instrumentation Wire Feedthroughs

Components which act as a barrier to vacuum have to be tested before they are installed for quality assurance reasons. The most importance test is the leak test under operation conditions. They will be tested at 4 K and the test pressure of 3 MPa after the fifth cycle. The leak rate will be measured at this conditions and should not exceed about 10^{-8} mbarl/s.

For performing these tests a test facility has been constructed in which 8 components can be tested in one thermal cycle. Each component has its own guard vacuum which can be connected to the leak detector. Each component can be pressurized separately by precooled helium gas. The guard vacuum tube with the component in it is immersed in a liquid helium bath. The pressure direction is the same like under original operation conditons. A suitable instrumentation of the facility allows a controlled cooldown. The local temperature gradient has to be less than 40 K across the component. The temperature gradient in time has to remain below 30 K/h.

The 8 guard vacuum tubes are installed in a lid of cryostat (600 mm diameter). Fig. 1 shows the cryostat with its cryogenic supply system and measuring equipment.

The facility was taken into operation and worked well. Presently axial insulation breaks for the TOSKA facility are tested. One thermal test cycle needs about 3 weeks.
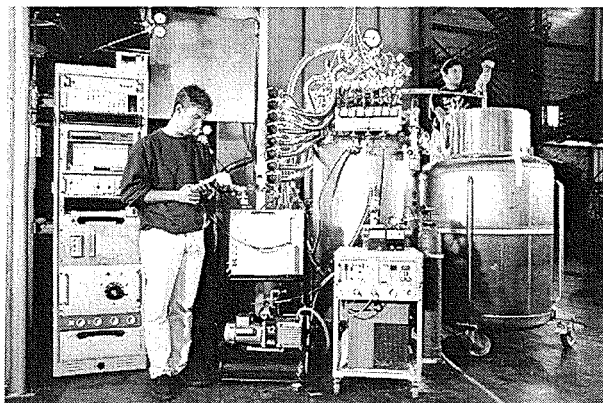
Fig. 1: The cryostat for testing axial insulation breaks and feedthroughs, its cryogenic supply system and the measuring equipment

Staff:

K. Bauer (from 01.10.96)
G. Dittrich
G. Friesinger
H. Kathol (till 31.12.96)
O. Langhans
G. Schleinkofer
A. Ulbricht
A. Völker

ERB 5004 CT 970037 (NET/97-450)
ITER Tritium Plant Engineering Design

Within the frame of the Engineering Design Activity (EDA) of ITER a basic Process Control System concept for the Tritium Plant was defined in Karlsruhe and a detailed cost estimation was carried out. According to the present ITER planning each major process system will be controlled by an independent Automated Control System (ACS). The various ACS will in turn be combined via a central Command Control and Data Acquisition (CODAC) computer system.

According to the concept suggested by FZK the ACS of the Tritium Plant will comprise eleven Distributed Process Units (DPU) and six Display Working Stations (DWS) connected by a redundant fiber optic system bus (SB). The DPU will acquire actual process signals and generate the commands for the control modules of valves, motors, heaters, control loops, etc. Control sequences and interlocks are described and processed with sequential function charts (SFC). Besides the ACS a hardwired safety circuit (SC) is foreseen. The DPU serve as the information data base for the operating Display Work Station (DWS). The DWS constitute the human-machine interface (HMI) and are thus the central instrument of the operator to supervise and control the process. For the development of software for the DPU and the DWS or for modification of the available software a so called Engineering Work Station (EWS) is contemplated. ACS components i.e. DPU, DWS, the EWS and the link to CODAC are connected via the bus system, which transfers all the process signals to the DWS, the operation commands to the DPU and the coordination and interlock signals between the various DPU.

The cost estimation of the ACS for the ITER Tritium Plant is based on relevant data of the systems a) HDT Isotope Separation, b) Tritium Plant Analytical Facilities, c) the Tritium Extraction from an ITER Blanket Module, d) the Atmosphere Detritiation System, and e) the Water Detritiation System as supplied by the ITER Team. Complementary relevant data were obtained from the Tritium Laboratory Karlsruhe (TLK). They include the TLK data from a) the Process Control System, b) the Fuel Storage and Distribution System, and the CAPER concept for the Plasma Exhaust Processing System. In addition many basic concepts and safety devices implemented at the TLK, such as a) the Engineering Work Station, b) the hard wired safety circuit, and c) the use of virtual measurements to compare the condition of diverse sensors were also incorporated into the cost estimation.

For each of the above indicated systems of the Tritium Plant the anticipated analogue and binary I/O signals were estimated and the max. available spares of the system memory and run time were compiled. A total 3821 I/O were considered necessary. In addition the required number of Central Process Units, power supply units, bus I/O interface modules and cabinets were assessed. Recommendations were provided concerning instrumentation and control for the Tritium Plant.

Staff:

K. Borcherding
G. Kopp (Siemens)
R.-D. Penzhorn
T. Vollmer

Long-Term Technology Programme

1. The European Blanket Project (EBP)

The European Blanket Project (EBP) was established in late 1995 and includes three subprojects covering R&D work on:

- a water-cooled lithium lead blanket (WCLL),

- a helium-cooled pebble bed blanket (HCPB), and

- structural materials (SM) for WCLL and HCPB.

At the end of 1996 a reorientation of the long-term blanket and structural materials activities within the EBP was proposed by the Commission and endorsed by the FTSC-P. The revised work programme for 1997/98 covers the period up to the end of the Fourth Framework Programme.

All three subprojects of the EBP utilize a harmonized work breakdown structure, comprising three levels: work packages, tasks, and subtasks. The contributions in this report are on the subtask level. The corresponding work packages and tasks are shown in Table 1 - Table 3.

2 Other Long-Term Technology Activities

Besides the blanket-related tasks FZK contributes to the fields „Materials for DEMO", „Safety and Environment" and „Socio-Economics".

Table 1: WCLL Working Structure *(WP & Task Number Definition)*

(Team Leader: L. Giancarli, Deputy: M. Fütterer)

WP A1 *DEMO Blanket Feasibility & Design* *(C.: L. Giancarli)*	WP A2 *ITER Test Blanket Module Feasibility & Design* *(C.: L. Giancarli)*	WP A3 *ITER Test Blanket Module Fabrication (TBM)* *(C.: M. Fütterer)*	WP A4 *Tritium Control & Permeation Barriers (PB)* *(C.:G. Benamati)*	WP A5 *Tritium Extraction* *(C.: J. Reimann)*
T1 - Segment Design & Analysis	*T1* -Test Blanket Module (TBM) Design & Analysis	*T1* - Double-Wall Tube (DWT) Development & Fabric.	*T1* - Permeation Barriers (PB) Fabrication & Charact.(mat.)	*T1* - Tritium Extraction from Pb-17Li
T2 - External ☒ Circuits & Components	*T2* - TBM Sub-systems (incl.instrum.)	*T2* - DWT Out-of-pile Testing	*T2* - PB Out-of-pile Testing (performances)	*T2* - Tritium Extr. ☒ from Water
T3 - Experiments ☒ Interpretation	*T3* - Interf. ITER & Testing Progr.	*T3* - DWT In-pile Testing	*T3* - PB In-pile ☒ Testing	*T3* - Tritium Extr. ☒ from He (in LL-extractor)
T4 - Maintenance, ☒ Supporting, R.H., W.Disp.	*T4* - Maintenance, Supporting, R.H., W.Disp.	*T4* -TBM Box Fab. Tech. Devel. & Mock-ups	*T4* - PB Self-heal. Evaluation/ Experiments	
		T5 -TBMB Mock- ☒ ups Out-of-pile Testing		
		T6 - TBMB Mock- ups In-pile Testing		
		T7 - Nucl. Qualif. ☒ for Licencing		
		T8 - NDT ☒ Development		
		T9 - Circuit Minor Components & Instrum.		

WP A6 *Demonstration of Blanket Safety* *(C.: G. Marbach)*	WP A7 *Demonstration of Blank. Reliability* *(C.: C. Nardi)*	WP A8 *Pb-17Li Physico-Chem.* *(C.: M. Fütterer)*	WP A9 *Pb-17Li/Water Interactions* *(C.: G. Benamati)*	WP A10 *MHD Effects* *(C.: J. Reimann)*
T1 - Safety Analysis for DEMO	*T1* - Data Base for BlanketSystem	*T1* - Purification ☒ from Corr. & Activ.Products	*T1* - Water Micro- Leaks	*T1* - Theoretical Evaluation of MHD Issues
T2 - Safety Anal. for ITER Test Bl. Module	*T2* - Reliability/ Availability f. TBM System	*T2* - Corr. Product ☒ Redep/Detect. in Magn. Field	*T2* - Water Large- Leaks	*T2* - Experimental Demonstration
		T3 - On-line Li-content Monitoring	*T3* - Definition of Counter- measures	
		T4 - Evaluation of ☒ Produced He Behaviour		

Glossary : WP = Working Package, Project A = WCLL, T = Task, ☒ = Task *not* active in 97-98

Table 2: HCPB Working Structure (WP & Task Number Definition)
(Team Leader: M. Dalle Donne, Deputy: S.Malang)*

WP B1 Demo Blanket Feasibility & Design (C.: K. Schleisiek)	WP B2 ITER Test Module Feasibility & Design (C.: S. Malang)	WP B3 ITER Test Module Feasibility & Fabrication (C.:.G. Dell'Orco)	WP B4 Tritium Control & Requirement for Permeation Barriers (C.: J. Reimann)	WP B5 Tritium Extraction & Helium Purification (C.: J. Reimann)
T1 - Segment Design & Analyses	T1 - Test Module Design & Analyses	T1 - Feasibility & Fabrication	T1 - Modelling of Permeation Losses	T1 - Design of Helium Purification & Tritium Extraction Systems
T2 - Maintenance, Support, Remote Handling, Waste Disposal ⊠	T2 - External Circuits	T2 - Out-of-Pile Tests	T2 - Permeation Tests in Martensitic Structural Material & Incoloy 800	
	T3 - Minor Components & Instrumentation Development ⊠	T3 - In-Pile Tests		

WP B6 Demonstration of Blanket Safety (C.: G. Marbach)	WP B7 Demonstration of Blanket Reliability (C.: C. Nardi)	WP B8 Development of Ceramic Pebbles (C.: N. Roux)	WP B9 Behaviour of Beryllium Pebbles under Irradiati (C.:M.Dalle Donne)**
T1 - Safety Studies for DEMO & ITM	T1 - Data Base for Blanket Systems	T1 - Development of Li_4SiO_4 Pebbles	T1 - Characterization & Optimization of Beryllium Pebbles
T2 - Tritium System Safety Analysis ⊠	T2 - ITM System Reliability	T2 - Development of Li_2ZrO_3 or Li_2TiO_3 Pebbles	T2 - Behaviour of Beryllium Pebbles under Irradiation
		T3 - Reactor Irradiation of Pebbles	

Glossary: WP = Working Package, Project B = HCPB-Blanket, T = Task, C = Coordinator
⊠ = Task not active in 97-98
* After November 1,1997: Team Leader: S.Malang, Deputy: L.Boccaccini
**After November 1,1997: WP-Coordinator: F.Scaffidi-Argentina

Table 3: SM Working Structure (WP & Task Number Definition)
(Team Leader: B. van der Schaaf)

WP SM1: Irradiation Performance (C: vdSchaaf)	WP SM2: RA/FM Characterisat. (C: Tavassoli)	WP SM3: Compatib. in Fusion Environmt. (C: Benamati	WP SM4: Fabrication Qualification (C: LeMarois)	WP SM5: Rules for Design, Fabr.& Inspect. (C: Diegele)	WP SM6: L.A. F/M Steel Qualific.for DEMO (C: Ehrlich)
Task SM1.1 HFR irradiation MANITU/TESEO	Task SM2.1 Short term mech. properties	Task SM3.1 H-effects on ductility	Task SM4.1 Weld cracking & gen. weldability	Task SM5.1 Physical and mechan. data	Task SM6.1 Phenix low & high temp.irradiation
Task SM1.2 HFR irradiation Phase 1A	Task SM2.2 Creep and creep/fatigue	Task SM3.2 H-embrittlement miniatur.specim.	Task SM4.2 Diffusion welding	Task SM5.2 Fracture mechan. concept	Task SM6.2 Effect of ion irrad. on in-beam fatigue
Task SM1.3 HFR irradiation Phase 1B	Task SM2.3 mech. properties of weldments	Task SM3.3 Irrad. effects on H-diffus.&perm.	Task SM4.3 HIP products characterisation	Task SM5.3 Procurement spec.& verification	Task SM6.3 Struct.stab.under heavy ion irrad.
Task SM1.4 He/dpa-effects by Dual Beam		Task SM3.4 (not active)	Task SM4.4 Transition weldmt. qualification	Task SM5.4 (not active)	Task SM6.4 Microstru.charact. by neutr.diffraction
		Task SM3.5 Corrosion in water environmt.	Task SM4.5 Filler metal development	Task SM5.5 (not active)	
		Task SM3.6 Crack initiation in water environmt.		Task SM5.6 Non-destruct. testing	
		Task SM3.7 Crack behav. of irrad.mat.in water			
		Task SM3.8 Compatibility with Pb-17Li			
		Task SM3.9 L M Embrittlement tests			

WP A 2
ITER Test Blanket Module Feasibilty & Design

A 2.1.3
MHD Evaluation and Diffusion Bonding Technique Application

MHD Issues for the ITER TBM Including Impact on T-Permeation

Although the MHD pressure drop is not a feasibility issue in the WCLL design, MHD effects nevertheless lead to new questions to be technically solved.

Therefore the water-cooled liquid metal blanket concepts (WCLL) [1, 2] are considered with regard to their MHD behavior. The comparison is done for DEMO and the ITER test blanket module (TBM) conditions. Therein, first the hydraulic aspects (pressure drop, flow distribution) in the relevant geometries are discussed. In a second step the MHD heat transfer characteristics in basic elements are shown.
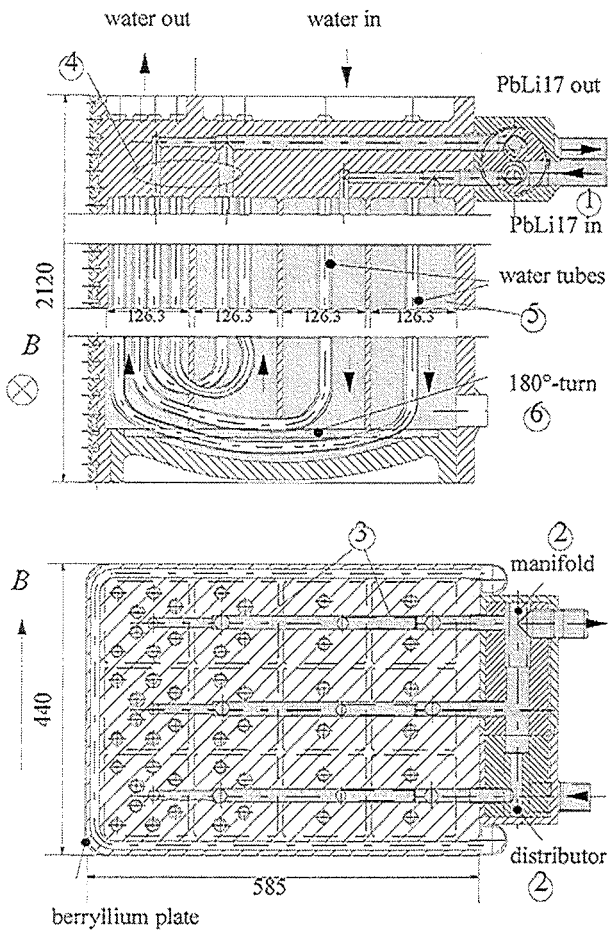
Fig. 1: Sketch of the water-cooled lithium lead blanket concept (WCLL) foreseen for the ITER test module. Top: Side-cut of the module. Bottom: cross-section cut through the top of the blanket.

The numbers denote MHD flowregions: 1. Flow in fringing field. 2. Manifold/ distributor. 3. Subdistributor perpendicular to B. 4. Feeding/ draining pipe flow. 5. Flow in breeding zone. 6. Flow in the U-turn

MHD-hydraulics

Any blanket design is based on the same basic geometric elements of coolant ducts. These are straight ducts of rectangular or circular cross-section, expansions, contractions, etc. as shown in the sketches of table 2. The pressure drop caused by

MHD flows in these elements may be minimized by the use of thin conducting walls or by direct insulations (coatings or ceramics). Thin conducting walls can be achieved by the use of Flow-channel inserts (FCI), where an electrically insulating ceramic sheet is sandwiched by thin steel plates [2]. Since the development of a direct electrical insulation, which persists at fusion conditions, is still an ongoing task we restrict our investigations to electrically conducting duct walls.

The MHD pressure drops in the different blanket designs are calculated for the boundary conditions (flow rates, magnetic field strength) given in table 1. The thermophysical properties of the lead lithium alloy $Pb^{83}Li^{17}$ used in the blanket are taken from [3].

Due to the high magnetic field strength present in the fusion reactor the liquid metal flow is mainly determined by MHD effects. The relative importance of the electromagnetic effects compared to viscous or inertia effects is described by the

Hartmann number: $\quad M = aB\sqrt{\dfrac{\sigma}{\rho v}}$ $\qquad$ (1),

and the

interaction parameter: $\quad N = \left(a\sigma B^2\right) / \left(\rho v_0\right)$ $\qquad$ (2).

Herein, a is half of the ducts height in magnetic field direction, B the magnetic induction, σ the specific electric conductivity, ρ the density and v the kinematic viscosity of the fluid. The average fluid velocity is v_0. The wall conductance ratio c characterizes the relative conductance of the wall with the conductivity σ_W and the thickness t_W compared to the conductance of the fluid domain. c is defined by:

$$ c = \left(\sigma_W\, t_W\right) / \left(\sigma\, a\right). \qquad (3)$$

Table 1: Specifications of the blanket concepts from [1, 2].

	WCLL TBM	WCLL DEMO
flow rate [kg/s]	1.0	8.5
B [Tesla]	5	5
inlet temp. [°C]	290	265
outlet temp. [°C]	315	325

Regarding the MHD pressure losses the following experimentally well validated correlations have been used.

- rectangular ducts

$$ \frac{dp}{dx} = \frac{dx\, p_H}{1 + \dfrac{a}{3b}\dfrac{dx\, p_H}{\left(c_S + M^{-1/2}\right)}} \; ; dx\, p_H = \frac{c_H + M - 1}{c_H + 1} \qquad (4)$$

- circular ducts

$$ \frac{dp}{dx} = \frac{c}{1 + c}. \qquad (5)$$

Herein, the pressure gradient is scaled with the electromagnetic pressure $(a\sigma v_0 B^2)$, while c_H and c_S denote the wall conductance ratios of the walls perpendicular and parallel to the magnetic field. b is the duct width normal to B. The named equations are only valid for a 2D MHD flow. In many parts of the blanket, however, the MHD flow is far of being two-dimensional. In order to identify the MHD problems the different flow regions are marked in figure 1. The different MHD flow regions are:

1. Fringing magnetic fields at the inlet and outlet of the blanket ($v_0 \perp B$).
2. Manifolds/distributors at the blanket header (bends, in which the flow direction changes from parallel to B to perpendicular to B).
3. Subdistributors in the blanket header (flow in bend perpendicular to B.
4. Flow in parallel feeding/ draining ducts.
5. Flow in parallel ducts of the breeding area.
6. U-turn at the bottom of the blanket.

Table 2: Pressure drop of two different blanket concepts, namely the WCLL-ITER [1] and the WCLL-DEMO [2]. The WCLL designs have been calculated without any electrical insulation.

Section of MHD-flow	Geometry	a [m]	L [m]	v_0 [m/s]	M [/] <10⁴	N [/] <10⁴	c [/]	Δp WCLL TBM [Mpa]	Δp WCLL DEMO [MPa]
Fringing field Inlet and Outlet		TBM 0.025 DEMO 0.138	TBM 0.85 DEMO*1 3.04	0.054 [a] 0.001 [b]	0.12 [a] 0.67 [b]	0.024 [a] 7.171 [b]	0.241 [a] 0.039 [b]	0.0461	0.016
Manifold and distributor		TBM 0.025 DEMO 0.138	0.78 [a] 2.08 [b]	0.054 [a] 0.001 [b]	0.24 [a] 1.34 [b]	0.096 [a] 28.68 [b]	0.241 [a] 0.039 [b]	0.1744	0.0155
Subdistributor		TBM 0.012① 0.009② DEMO 0.012	0.74[a]① 0.26[a]② 0.85 [b]	0.078[a]① 0.139[a]② 0.022 [b]	0.12 [a] 0.08 [a] 0.12 [b]	0.032 [a] 0.014 [a] 0.113 [b]	7.03[a]① 9.36[a]② 14.85 [b]	1.06① 0.74②	0.3457
Parallel feeding/ draining ducts		TBM 0.009 DEMO 0.010	0.20 [a] 0.42 [b]	0.139 [a] 0.029 [b]	0.08 [a] 0.10 [b]	0.014 [a] 0.103 [b]	9.36 [a] 17.82 [b]	0.0560	0.2925
Breeding zone down/ upwards.		0.063 [a] 0.080 [b]	TBM 3.64 DEMO 22.00	0.001 [a] 0.003 [b]	0.61 [a] 0.78 [b]	13.09 [a] 5.542 [b]	0.966 [a] 0.761 [b]	0.0313	0.4777
Grid spacer		0.063 [a] 0.080 [b]	TBM 0.12 DEMO 0.20	0.001 [a] 0.003 [b]	0.61 [a] 0.78 [b]	13.09 [a] 5.542 [b]	c remains c_H 7.73 [a] c_H 4.76 [b]	0.0080	0.004
U-turn		0.063 [a] 0.080 [b]	0.49 [a] 0.78 [b]	0.001 [a] 0.003 [b]	0.61 [a] 0.78 [b]	13.09 [a] 5.542 [b]	0.966 [a] 0.761 [b]	0.0051	0.0168
Total pressure drop								2.1209	1.1682
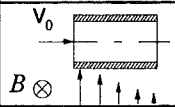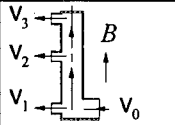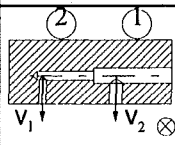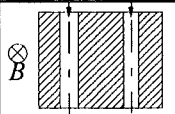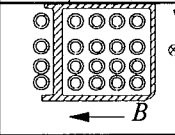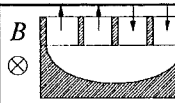
[a] WCLL-TBM;   [b] WCLL-DEMO;   *1Ducts to outer blanket segment;

Most of the MHD flow problems mentioned in the topics 1-6 are three-dimensional MHD flows. However, the degree of three-dimensionality and thus the arising additional 3D pressure drops in the individual problems are significantly different in magnitude.

As long as the ducts cross-section with respect to the magnetic field direction does not change the additional 3D pressure drop can be well assessed. This holds especially for the problems 1, 3 and 6. The 3D pressure drop Δp_{3D} corresponds to an additional longer flow path of two-characteristic length,

$$\Delta p_{3D} = 2 \cdot \left(dp / dx \right) \qquad (6)$$

as long as $N \geq M$, which has been experimentally and numerically proofed by [4].

The flow in manifolds/distributors of the header is much more complex, because the flow changes its direction from parallel to perpendicular to B. By means of asymptotic methods valid for $M \gg 1$ and $N \geq M^{3/2}$ the total pressure drop can be well assessed, see [5, 6]. If $N < M^{3/2}$ a 3D inertial pressure drop $\Delta p_{3D,N}$ has to be added to the asymptotic value of the pressure drop. $\Delta p_{3D,N}$ can be conservatively calculated by:

$$\Delta p_{3D,N} = N^{-1/3}. \qquad (7)$$

A much more critical aspect of these distributors is the distribution of the flow rates between the individual ducts. If the design of the ducts to the subdistributors is identical the subdistributor channels farest away from the feeding pipe have a strongly reduced flow through. Thus, MHD countermeasures in terms of

different channel sizing, aspect ratios, different wall conductivities has to be foreseen in order to guarantee an equal flow rate in each duct.

The flow in the circular feeding and draining ducts (topic 4) can be easily calculated using equations 5 and 6, if the ducts are electrically separated. If the ducts are not electrically separated electric current induced in one duct can enter the neighboring duct. This multi-channel effect (MCE), which is sketched in Figure 2 causes an increased pressure drop. Although MCE's are in terms of the additional pressure drop not a feasibility issue in hybrid concepts, they nevertheless affect significantly the flow distribution between the individual ducts.

The MHD-flow in the breeding area of the blanket may also experience a MCE if no electrical separation is used. In case of MCE we can consider the MHD flow as 2D and then use the pressure drop correlation given in [7]. For the case of two-coupled channels (WCLL-ITM) the dimensionless pressure gradient is given by:

$$\frac{dp}{dx} = \left(1 + c_H + \frac{a}{3b} \cdot \frac{1}{c_S} \right)^{-1}. \qquad (8)$$

In the WCLL for DEMO three channels are coupled leading to a pressure gradient, which is limited by the pressure gradient given in equation 4b. If we consider an electrical separation the pressure drop in the breeding area channels can be calculated using equation 4.

Finally, the MHD flow around the grid spacers will cause also a pressure drop. This additional pressure drop in the spacers is of the same order as in a flow straightener and can be conservatively assessed by relation 6. In the WCLL-TBM there is only

one rather massive spacer, in which the currents induced in the fluid short-circuit. Thus, a MCE in this region can not be avoided and equation 8 has to be used. For the 3D in- outlet flow of the spacers equation 6 will give a rather conservative assessment.

In table 2 the pressure losses in the piping system of each blanket concept are shown. In the calculations conducted for the different WCLL designs electrically conducting walls as stated in [1, 2] are used. The results show that most of the pressure drop occurs in the header of the module. With respect to the MHD pressure drop the actual design of the WCLL-TBM header has a large reduction potential. Although the pressure drop problematics in these concepts is not a feasibility issue table 2 demonstrates that due to the use of two coolant media and the resulting complex header geometry additional MHD problems arise.
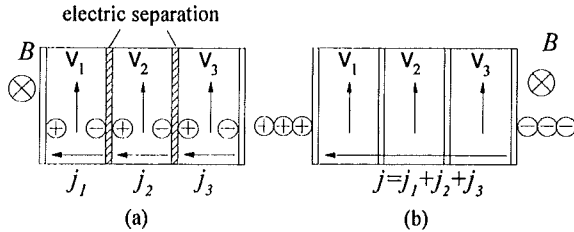
Fig. 2: a.) suppression of multi-channel-effect (MCE) by electrical separation between the ducts 1, 2, 3 (coating or FCI). b.) MCE due to global currents. Currents penetrate in the neighboring ducts leading to increased pressure drop and uneven flow rate in the ducts. For equal pressure drop in each duct 1, 2 and 3 the flow rates will be $v_2 < v_1 = v_3$.

The second main point in the hydraulics is the velocity distribution within the ducts. At high M and N the calculation of the velocity profiles by means of asymptotic models is not too difficult. In figure 3 the velocity distribution between the water cooling tubes in the breeding area is shown. The velocity distribution in 3D- MHD flows (at low N, i.e. if $N < M^{3/2}$) especially at the transition from the breeding zone to the header is hard to predict. An asymptotic approach, which neglects inertia effects, shows that the fluid directly at the first wall will be stagnant.

Figure 3 shows this geometry schematically. The reason for this behavior is that the toroidal fluid motion experiences less electromagnetic forces than the radial motion and thus the toroidal velocity will be much higher. Within this stagnant fluid zone marked black in figure 3 a too high tritium concentration may appear.

MHD-Thermohydraulics

Regarding hybrid concepts the MHD heat transfer is not an important issue, since the liquid metal flow is only required to remove tritium breeded.

At the low velocities considered the MHD heat transfer in these concepts is based on conduction, for which the developed codes predict the temperature distributions quite well [8, 9]. As discussed, stagnant fluid domains at the liquid metal outlet flow may appear near the first wall region due to MHD-effects, see Fig. 3 b. Such a stagnant area may lead to unacceptable high tritium concentrations.

In this first wall region, however, temperature gradients produced by the volumetric heating of the fluid which causes a slow buoyancy driven flow. The magnitude of the velocity depends both on the electromagnetic damping in the fluid and the wall conductance ratio. Using an asymptotic model valid for $M^4 >> Gr$ (Gr ≈ Grashof number), large aspect ratios ($h >> a$, $h >> b$)and small Peclet numbers, which is justified in the WCLL concepts, the velocity distribution can be calculated numerically. Here, the Grashof number is defined by

$$Gr = \frac{\beta g \dot{q} b^4}{\nu 2 \lambda} = \frac{\lambda \beta g \dot{q}_v b^5}{\nu 2 \rho c_p}, \qquad (9)$$

where β is the expansion coefficient, g the gravitation constant, λ the heat conductivity, $\dot{q}$ the heat flux and $\dot{q}_v$ the volumetric heat source due to the neutron flux.
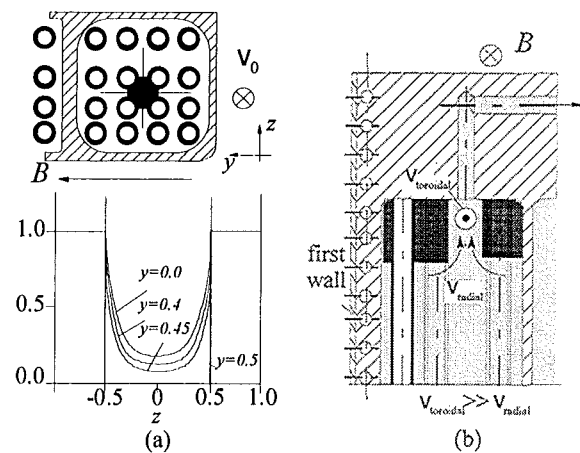
Fig. 3: a.) velocity distribution between the water cooling tubes of the WCLL TBM design at M=6000. b.) Due to MHD effects a stagnant liquid metal zone (marked black) may appear at the top of the blanket module.

The Grashof numbers of the WCLL-TBM attains values of $O(10^{12})$. In case of a well electrically conducting side wall, see fig 4 a, Bühler [10] calculates a dimensionless velocity at the first wall of $O(M^{-1/2})$. The dimensionless velocity profile as a function of y and z for M=1000 and $c \rightarrow \infty$ is shown in figure 4 b. These velocities can be increased by two orders in magnitude using FCI in the breeder region. Although the buoyant velocities are orders of magnitudes lower than the bulk velocity in the WCLL concept they are sufficiently high enough to keep the tritium concentration in an acceptable limit. If we conservatively assume that the diffusive mass transport is of the order of the convective mass transport flow velocities of 10^{-7} m/s are necessary. The calculations shows that such velocities can be achieved by natural convection. However, since the tritium hot spot question is a crucial issue in the hybrid concept an experimental investigation of the fluid motion appearing in magneto-convection has to be performed.
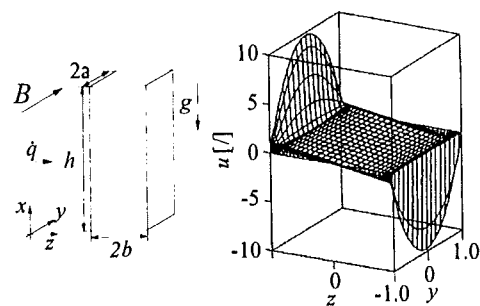
Fig. 4: a.) Sketch of the geometry at the first wall. b.) Calculated dimensionless velocity u scaled by $u = U \sigma B^2 / (\rho \beta g \Delta T)$ as a function of y and z for M=1000 and $c \rightarrow \infty$ from [12].

Design Studies

As a contribution to solve the MHD issues described above some proposals for design modifications have been elaborated. They are related to the flow regions 3 and 4 (see Fig. 1) and lead to a reduction of the MHD pressure loss in this regions, and to an improved arrangement of the draining holes of the breeding zone.

Literature:

[1]   Fütterer, M. et al. 1996 *DMT 96/349 SERMA/LCA/1911.*
[2]   Giancarli 1994 *DMT 94/538 SERMA/LCA/1678.*
[3]   Jauch, U.; Karcher, V.; Schulz, B. *KfK-4144.*
[4]   Reimann, J. et al.1994 2nd Int. Conf. on Energy Transfer in MHD flows. **(2)**, 297-308.
[5]   Reimann, J et al. 1994 2nd Int. Conf. on Energy Transfer in MHD flows. **(2)**, 433-442.
[6]   Stieglitz, R. et al. 1996 *J. Fluid Mech.***(326)**, 91-123.
[7]   Molokov, S. 1993 *Eur. J. Mech.*, **B12**, 769-787.
[8]   Barleon, L. et al. 1997 *FZKA-5927.*
[9]   Bühler, L. 1993 *KfK-5241.*
[10] Bühler, L. 1997 *FZKA-5962.*

Staff:

L. Barleon
R. Stieglitz
S. Gordeev
T. Heider
K. Schleisiek

WP A 3
ITER Test Module Fabrication

A 3.4.2
Adaptation of Diffusion Bonding to TBM Box Fabrication

The "DEMO blanket fabrication scheme" is an alternative fabrication method for the WCLL-TBM. One important fabrication step in this concept is the bending of the plane FW plates including the cooling tubes to form the U-shape TBM box envelope. A small test program has been initiated to demonstrate that the bending process will not lead to cracks, and that the resulting deformations of the FW cooling tubes are tolerable. The bending radius is a test parameter. In the original FW the cooling tubes will be joint to the FW plates by brazing or HIP with an intermediate compliant layer (probably Fe). This technique is still under development, and specimens for bending tests are not yet available. Therefore, in the initial bending tests massive plates with drilled holes will be used. It is expected that the bending characteristics of plates with drilled holes is not significantly different from the behavior of HIP-ped tubes. In contrast, a FW with brazed cooling tube will necessitate dedicated tests.

Staff:

H.J. Fiek, Fa. Kastner
T. Heider
K. Schleisiek

WP A 4
Tritium Control and Permeation Barriers (PB)

A 4.1.2
Fabrication and Characterisation of Permeation Barriers (PB) made by Hot-Dipping

In the water-cooled liquid metal blanket concept the reduction of tritium permeation through the structural material into the cooling water circuit is an important safety and operational issue. The coating materials on the surface of the steel should have a low permeability and/or recombination rate constant. Of these the use of aluminium rich coatings which form Al_2O_3 at their surface appears a very promising solution. Previous permeation tests on hot-dip aluminised and subsequently oxidised MANET yielded a reduction of permeation rate of more than three orders of magnitude [1]. However, in this case the aluminide coating was subjected to an oxidation treatment (950 °C for 30 h in air) which is not compatible to the steel structure.

In the next test series it was decided to keep the temperature for hot-dipping and oxidising below Ac_{1b} temperature of MANET to avoid the repetition of the whole heat-treatment procedure [2]. MANET samples were hot-dip aluminised at 750 °C for 2 min (sample I, II and III) or 5 min (sample IV, V and VI) and oxidised in air at 750 °C for 15 h (sample II and V) or 30 h (sample III and VI). Arrhenius plots of the permeation rate of deuterium through bare and hot-dip aluminised and subsequently oxidised MANET samples are shown in Fig. 1.
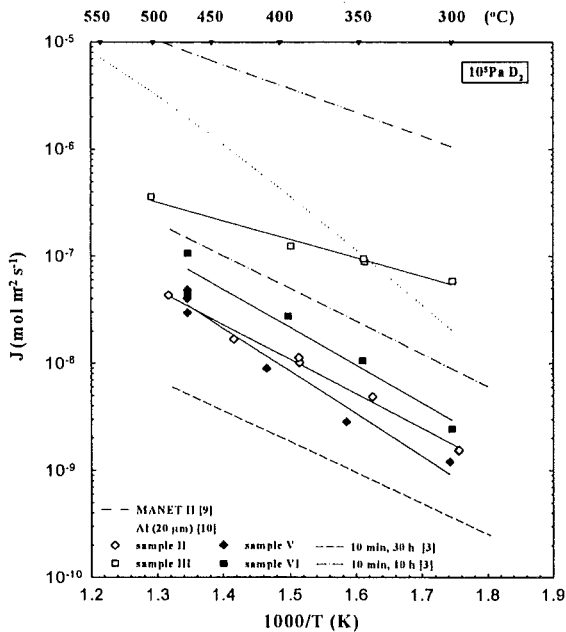
Fig. 1: Arrhenius plot of the permeation rate of deuteriumthrough bare and hot-dip aluminised MANET samples II, II, V and VI.

The similar activation energy for samples II, III, V and VI indicates that the permeation reduction is mainly obtained by an apparent reduction of the substrate area available for permeation rather than a reduction due to having a compact alumina layer at the surface. The measured permeation flux through this type of system will be dominated by permeation through the underlying substrate. However, as the number of cracks and defects will be low the measured permeation rate will be much lower. This means, the development of a smooth surface without cracks and pores is necessary to achieve required permeation reduction factors.

In March 1997, the tritium permeation barrier (TPB) group (members of ENEA, CEA, JRC, FZK) has decided to change the structural material form MANET to F82H-mod. for TPB development. Hence, the Japanese steel F82H-mod. was aluminised by means of hot-dip technique. A comparison of the aluminide layer formed at 700 °C for 30 s immersion time showed that the thickness of the layer on F82H-mod. is with around 26 µm thinner than the layer obtained on MANET (40 µm). For the improvement of the microstructure of the aluminide layer a heat-treatment is necessary. Hence, heat-treatments at different maximum temperatures (700 °C / up to 100 h or 10 75 °C / 0.5 h) were performed to investigate transitions happened.

During high temperature oxidation of the aluminised steels, a complete transformation of the aluminised layer has occurred. In the case of MANET two phases, AlFe and α-Fe(Al), were formed. For F82H-mod. only α-Fe(Al) could be detected. The coating on MANET is double in thickness (250 µm) compared to the coating on F82H-mod. (125 µm). Compared to MANET, the F82H-mod. samples show a smoother surface, no pores in the external layer and only a small porous band between the internal and external layer[3]. Hence, it seems that the permeation reduction factor (PRF) of these F82H-mod. specimens should be better than of the value of previously tested MANET specimens. The cross section of the aluminised and oxidised F82H-mod. sample is shown in Fig. 2.
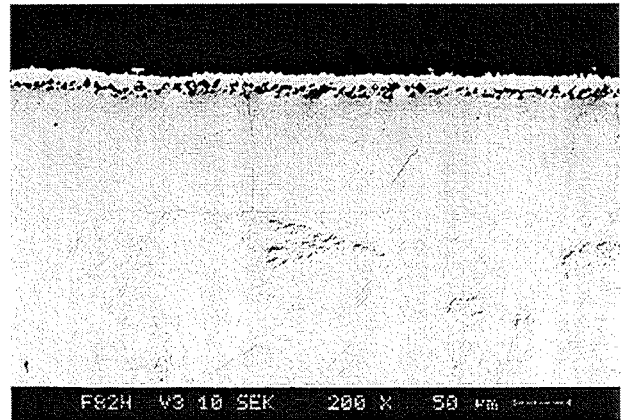
Fig. 2: Cross section of aluminised F82H-mod. samples, heat-treated at 1075 °C for 0.5 h.

Literature:

[1] H. Glasbrenner, A. Perujo, E. Serra, Fusion Techn. 28 (1995) 1159.

[2] E. Serra, H. Glasbrenner, A. Perujo, was presented at the ISFNT-4, Tokyo 1997, Japan.

[3] H. Glasbrenner, J. Konys, K. Stein-Fechner, O. Wedemeyer, will be presented at ICFRM-8 in Sendai, Japan.

Staff:

H. Glasbrenner
J. Konys
K. Stein-Fechner
Z. Voß
O. Wedemeyer

A 4.2.2
Permeation Reduction Factors (PRF) in Gas and Corrosion in Pb17Li

Independently of the blanket concept selected, water cooled liquid metal or solid breeder blanket, the reduction of tritium permeation through fusion reactor structures has to be minimised for safety and economical reasons. For tritium permeation barriers (TPB) development it is necessary to measure the PRF (permeation reduction factor) of the coatings. Hence, a permeation cell was constructed in which hydrogen and deuterium permeation through different materials in the gas phase can be determined.

The permeation of hydrogen through nickel, molybdenum and MANET were already well investigated in the literature. Therefore, first experiments were carried out on these metals for comparison. The permeation was measured for different partial pressures and between 280 °C and 500 °C. The permeabilities obtained for the three materials at 98 mbar are given in Fig. 1. The results are in good agreement with earlier measurements [1].

Literature:

[1] F. Reiter, K.S. Forcey, G. Gervansini, JRC Ispra, EUR 15217 EN report(1993).

[2] E. Serra, A. Perujo, submitted to J. Nucl. Mat.

Staff:

H. Feuerstein
H. Glasbrenner
S. Horn
O. Wedemeyer
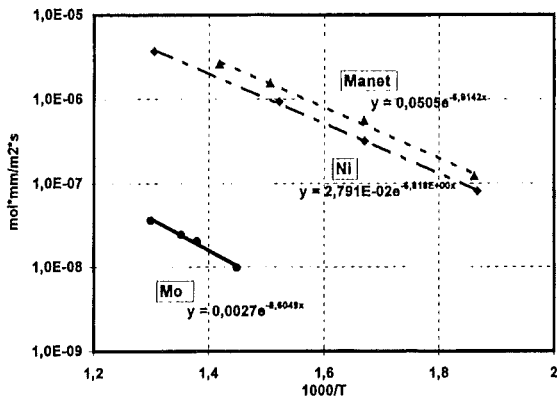
Fig. 1: Permeation of deuterium through different materials at 98 mbar.

Permeation tests through bare MANET discs have been done next. The measurements were carried out with deuterium pressure of 10.4, 98.1 and 1013 mbar. The permeation rates measured are in the same range as mentioned in the literature [2]. The measured curves are given in Fig. 2.
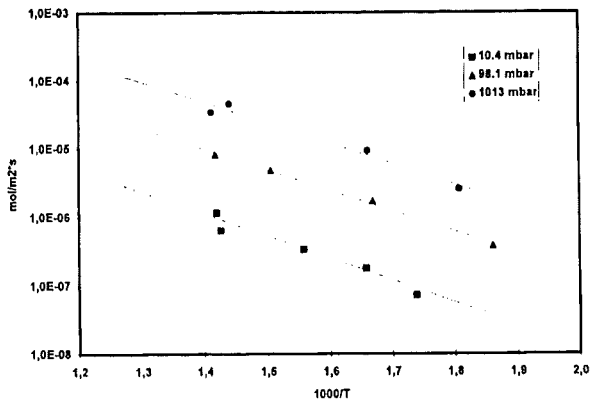
Fig. 2: Permeation of deuterium through bare MANET steel.

A 4.4.1
Permeation Barrier Self-healing in Pb17Li

Experiments in liquid Pb at 600 °C, NaK at 400 °C and Pb-17Li at 400°C were performed with hot-dip aluminised MANET specimens (some of them were subsequently oxidised), as well as a MANET specimen coated with alumina by PVD, and an eloxadized Al-specimen. For details see the following Table 1.

Table 1: Experimental conditions and results

specimen	liquid metal	T (°C)	t (h)	R_i (Ω)	R_e (Ω)
MANET 1*	Pb	650	105	2.0	2.5
MANET 2*	Pb	600	528	4.0	4.4
MANET 3*	Pb	600	168	2.0	2.3
		650	65	1.9	2.3
MANET 3*	Pb+ 2 g PbO	600	77	2.0	4.4
		650	235	3.1	3.5
		600	64	8.2	9.0
		650	259	8.1	8.0
MANET 4*	NaK	400	41	0.6	0.6
PVD 1	Pb + 3 g PbO	600	164	$2.4\ 10^6$	$5.1\ 10^6$
		500	64	$0.3\ 10^6$	$6.5\ 10^6$
		440	18	$3.8\ 10^6$	$0.8\ 10^6$
		650	522	$2.4\ 10^6$	$5.1\ 10^6$
MANET5+	Pb + 3 g PbO	600	373	1.2	2490
		650	103	1451	745
		600	5	1650	2122
MANET6+	Pb + 3 g PbO	600	393	4.9	7.0
MANET7+	Pb + 4 g PbO	600	153	10.4	10.6
MANET8+	NaK	400	25	0.2	0.5
MANET9+	Pb-17Li	400	485	0.5	0.5
Al 1	NaK	400	71	$>10^6$	0.7

* MANET hot-dip aluminised at 800 °C for 10 min; subsequent heat-treated at 550 °C for 2 h

+ MANET hot-dip aluminised at 800 °C for 10 min; oxidised at 950 °C for 30 h

As a measure of the self-healing kinetics, the change of the electrical resistance was used. This quantity should be also relevant for the characterisation of the formation of permeation barriers .

In all experiments with hot-dip MANET specimen, exept one, the initial electrical resistance was in the order of 1 Ω and did not increase remarkably during the experiments. Only in one Pb-experiment, an increase of the initial value of 145 Ω to 2487 Ω after 373 h was observed which corresponds to the formation of an effective electrical insulation.

The initially high resistance of the eloxadized probe broke down during the heat-up phase and did not recover. The PVD covered specimen kept its high resistance during the experiment although significant changes were observed.

Literatur:

H. Glasbrenner, J. Reimann, J. Becker, Z. Voss, „Self-healing tests of iron-aluminides in liquid metals" IEA-Workshop on Experimental Liquid Metal Activities; Paris Sept. 16-18, 1997.

Staff:

J. Becker
H. Glasbrenner
J. Reimann
Z. Voss

WP A 7
Demonstration of Blanket Reliability

A 7.1.3
Contribution to Common Blanket System Data Base

The subtask is closely connected to A 7.2.3 and B 7.1.3. All data used will be taken as basis for the common data base. The use of the same data base for different design options and test module concepts also allows to limit error sources by avoiding differences resulting from various data.

A 7.2.3
TBM System Availability

The availability/unavailability of the WCLL-test blanket module including the Pb-17Li system and the water cooling loops was analysed. A measure for the unavailability is the probability for the system to be unavailable on demand. This occurrence is termed the TOP event. The components and subcomponets failure rates are the data base agreed upon within the fame work of the blanket selection exercise [1], supplemented by a few additional values from the same original reference. For repair and/or exchange of defective components, a time of two to eight weeks is proposed. This must be seen in connection with the entire remote handling concept.

The Pb-17Li system is considered including the He-circuit, which is required for tritium extraction, but the tritium extraction system is left out in the consideration. Due to the low corrosion rate expected in the Pb-17Li system, a cleaning system is not applied. A detailed design of the test module box with the integrated cooling channel structure for the first wall (FW) is not yet available. Various fabrication methods are being discussed. Therefore, this component, is not included in the analysis.

X ...Overall unavailability,   ◆...Pb-17Li system,
▲...H2O-cooling loops,   ■...Test module
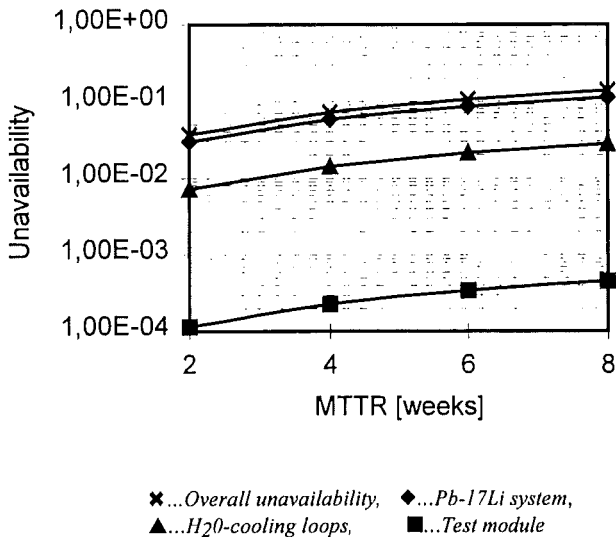
Fig. 1: Unavailability of the WCLL Test Module

From the calculated failure rates of the basic events and components, the unavailabilities have been evaluated. They are presented in Figure 1. The values have been calculated for mean times to repair or exchange ranging from two to eight weeks. The overall unavailability varies between 3.67×10^{-2} and 1.38×10^{-1}. This corresponds to an availability of 96.3 to 86.2%. In Figure 1 the upper curve shows the overall unavailability. The next lower curve shows the contribution of the Pb-17Li system, followed by the curve for the H2O-cooling system. The lowest curve represents only the test module including the pipe system up to the biological shield. The influence of the test module on the overall unavailability is low, it is about 0.3%. The contribution of the Pb-17Li system to the overall result is about 80%, with 78% being contributed by only three basic components, the valves, the pumps and the compressors (see Table 1). Dependent on the MTTR between two and eight weeks the unavailability for the Pb-17Li system is between 3.0×10^{-2} and 1.12×10^{-1}. The unavailability of the H2O-cooling loops contribute about 20%, as shown in Table 1. The unavailability varies between 7.18×10^{-3} and 2.82×10^{-2}.

Table 1: Basic events, calculated failure rates and contribution to the overall results

System	Description, basic event	Fluid	Calculated failure rate [1/h]	Contribution to the overall unavailability [%]
Test module	All components		3.4×10^{-6}	0.30
			$\Sigma = 3.4\times10^{-6}$	$\Sigma = 0.30$
Pb-17Li system	Pipe system, Extraction column	Pb-17Li	7.8×10^{-7}	0.71
	Valves	Pb-17Li	3.0×10^{-5}	26.79
	Pumps	Pb-17Li	2.2×10^{-5}	20.05
He-system	Compressors	He	3.0×10^{-5}	26.79
	Filter	He	2.7×10^{-6}	2.45
	Valves	He	4.0×10^{-6}	3.60
			$\Sigma = 9.0\times10^{-5}$	$\Sigma = 80.40$
H2O-cooling loops	Heat exchangers, Pipes, Bends, Welds	H2O	7.4×10^{-7}	0.66
	Pumps	H2O	2.0×10^{-6}	1.80
	Pressurizer	H2O	2.7×10^{-6}	2.47
	Valves	H2O	1.6×10^{-5}	14.36
			$\Sigma = 1.55\times10^{-5}$	$\Sigma = 19.30$
Overall result			$\Sigma = 1.07\times10^{-4}$	$\Sigma = 100\%$

The impact of a statistical variation of the components unavailability on the overall unavailability has been analysed by a Monte Carlo simulation. Taking the components from Tab. 1 and assuming (pessimistically) an error factor of 10 for each component, the overall error factor will result to about 3.3. This means, the result for 8 weeks repair/down time varies between $U_{0.05} = 3.3\times10^{-2}$ and $U_{0.95} = 3.7\times10^{-1}$ and in case of two weeks repair/down time between $U_{0.05} = 7.7\times10^{-3}$ and $U_{0.95} = 9.5\times10^{-2}$. $U_{0.05}$ and $U_{0.95}$ are the 5% and the 95% confidence limits, respectively. That means that for a lognormal distribution 90 % of all possibilities are within this limits.

Literature:

[1] H. Schnauder, C. Nardi, M. Eid, Comparative availability analysis of the four European DEMO blanket concepts in view of the selection exercise, Fusion Engineering and Design 36 (1997) 343-365

Staff:

H. Schnauder

WP A 8
Pb-17Li Physico-Chemistry

A 8.1
Purification from Corrosion and Activation Products
(former A 3.1.1)
Radiological Important Impurities and Nuclides

During operation of a blanket, Bi, Hg and Tl isotopes are formed from lead by neutron transformations. Their behavior in the eutectic mixture has to be known for the estimation of radiological hazards in case of a Pb-17Li leak.

It was shown before ((1)) that Bi can be removed by a diffusion type cold trap, while the solubility of Tl in the mixture is very high at all temperatures. For the description of the chemistry of an element in solution, the chemical activity is important. It is connected to the concentration by

$$A = \gamma * X,$$

with X the mole fraction. Activity coefficients γ for Tl and Bi in lead and the eutectic mixture were determined by Langmuir evaporation experiments. This method was used before for the determination of chemical activities of Li and Po-210 ((2)). Evaporation rates of the elements from solution were compared with those of the pure elements and calculations.

Fig. 1 shows the results for Bismuth. As expected γ values in Pb-17Li are lower than in lead. The positive slope of the function, however, can not be explained so far.

Fig. 2:   Coefficient of chemical activity of Tl in Pb and Pb-17Li

Literature:

[1] S. Bucké et.al., Fusion Technology 1997 (1996)

[2] H. Feuerstein, et.al., J.Nucl. Materials 191-194 (1992) 288

Staff:

J. Beyer
S. Bucké
H. Feuerstein
L. Hörner
S.Horn

Fig. 1:   Coefficient of chemical activity of Bi in Pb and Pb-17Li

Fig. 2 shows the results for Thallium. The functions have the expected slopes with activation energies of -37 kJ/mol from lead and -28 kJ/mol from the eutectic. The activity coefficients are lower than those of Bi. Obviously, intermetallic compounds with lithium are more stable. Evaporation rates therefore are much lower than expected for ideal solution.

WP A 10
MHD Effects

A 10.1.1 and 10.2.1
Theoretical Evaluation of Natural Convection and Turbulence, Natural Convection Experiments

Introduction

In currently investigated liquid-metal (LM) blankets for fusion reactors the LM - a lithium-lead alloy - serves mainly as breeding material [1]. The externally forced flow required for a continuous circulation of the breeding material is very weak and has typically mean velocities on a scale of a few mm/s. Therefore, buoyant flow may become dominant in the whole blanket influencing heat transfer and the distribution of the concentration of the tritium generated within the liquid metal breeder [2].

Buoyant flow in breeding blankets can be caused by temperature differences within the LM due to volumetric heating and the heat removal through the cooled walls and/or tubes as sketched in Fig. 1. The knowledge of the velocity distribution is important for the evaluation of the heat transfer and is of special interest with respect to the concentration distribution of the tritium generated within the LM.

In order to avoid tritium hot spots in the corner near the first wall a transport velocity of at least 10^{-6} m/s is necessary. sketched in Fig. 1. The knowledge of the velocity distribution is important for the evaluation of the heat transfer and is of special interest with respect to the concentration distribution of the tritium generated within the LM.

In order to avoid tritium hot spots in the corner near the first wall a transport velocity of at least 10^{-6} m/s is necessary.
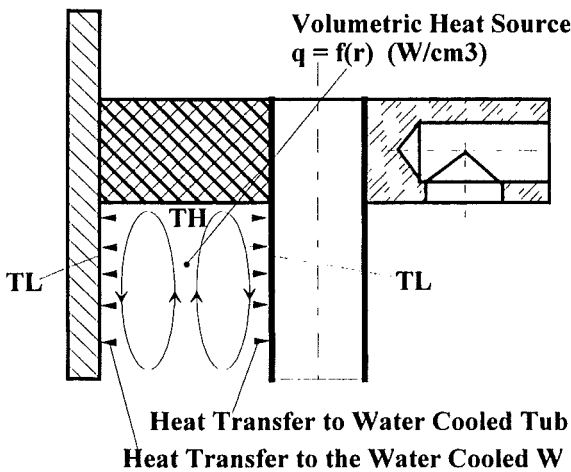
Fig. 1: Natural convection in substructures of the WCLL and the influence on tritium concentration

A second problem sketched in Fig. 2 deals mainly with the possible improvement of the heat transfer from a γ-heated diving wall of the blanket to a row of cooling tubes. Due to the rather low volumetric heating rate at this position this case can be simulated by the heat transfer from a heated to a parallel cooled wall as shown on the right side of Fig.2.

Out of pile experiments on natural convection of volumetric heated LM under MHD-conditions cannot be realized because any electrical heating would interact with the MHD phenomena to be investigated. Therefore it was decided to restrict the experiments to the investigations of the natural convection flow between a heated and a cooled plate. With the experimental verification of numerical results reliable predictions of the flow
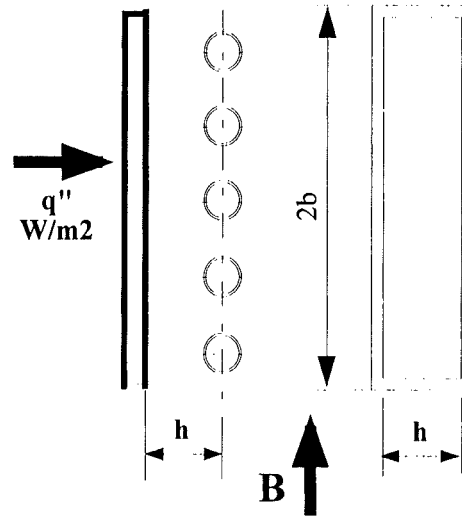
Fig. 2: Heat transfer from a heated wall to a row of cooling tubes

patterns appearing in the blanket can be made.

The experiment

In order to investigate the influence of the size and the direction of a magnetic field, on the behaviour of natural convection three types of experimental arrangements are used: [3]

1. Heat transfer by natural convection in a horizontal flat box with an aspect ratio 2 cm x 20 cm x 40 cm heated from below and cooled on the top wall with a vertical magnetic field vector.

2. The same box horizontally arranged in a horizontal magnetic field and

3. the vertical arranged box in a horizontal magnetic field using a slightly modified cooling system. By this arrangement the conditions of the WCLL blanket are adapted and modelled.

The experiments are conducted in the normal conducting magnet (type 1 experiment) or in the superconducting solenoid magnet (type 2 and 3) of the MEKKA laboratory [3] which allow to measure in magnetic fields of up to 2.1 and 3.5 Tesla respectively.

The Test Section

A cross section through the test apparatus is shown in Fig. 3. The bottom wall (the heated side wall in the type 3 experiment) - a 20 mm thick copper plate - is heated by 20 electrical heater rods embedded and brazed in grooves in order to improve the heat transfer. These heaters allow to operate with an electrical power up to 12 kW corresponding to a heat flux of up to 15 W/cm² and enable Rayleigh-numbers up to 10^5. The top wall (the cooled side wall in the type 3 experiment) - again a copper plate - is cooled and kept at constant temperature of about 100 °C by a boiling pool of water. The other walls are of 1.5 mm stainless steel. To homogenize the boiling heat transfer a particle bed of glass spheres with a diameter of 5 mm is used.

The vapor from the boiling pool is recondensed on water cooled copper tubes integrated in the lid of the test section.

Boiling water pool   Cooling tubes (condens

Thermocouples   Probe   Heater rod
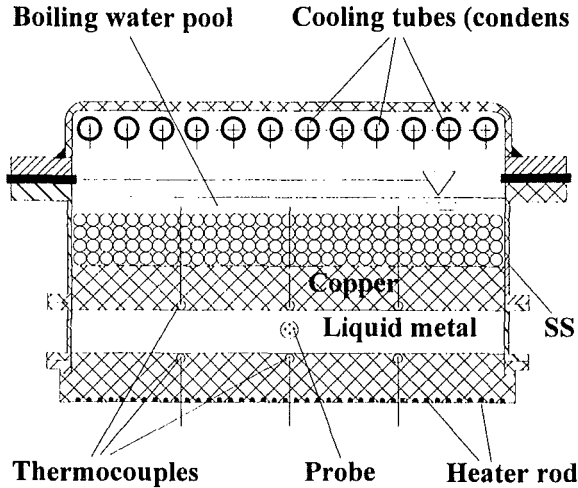
Fig. 3: The test section WUEMAG 1

Five thermocouples in the heated and cooled copper plate are foreseen to measure the temperature difference over the liquid metal layer. Their tips are placed 1 mm from the copper-liquid metal interface. The liquid metal used is the eutectic sodium potassium alloy $Na^{22}K^{78}$. The temperature dependent thermophysical data are taken from the compilation in [3]. Corrections are made for the heat loss from the heated plate to the environment and for the electrical losses in the cold legs of the heater rods. A four pole combined temperature and potential (TEMPO) probe is positioned in the mid between the heated and the cooled plate to measure temperature and velocity (only for higher magnetic field strength) oscillations within the liquid metal.

To perform the type 3 experiments most relevant for blanket design the test section is oriented vertically. In this case the vapor from the boiling water pool is recondensed in a separate cooler.

Theory
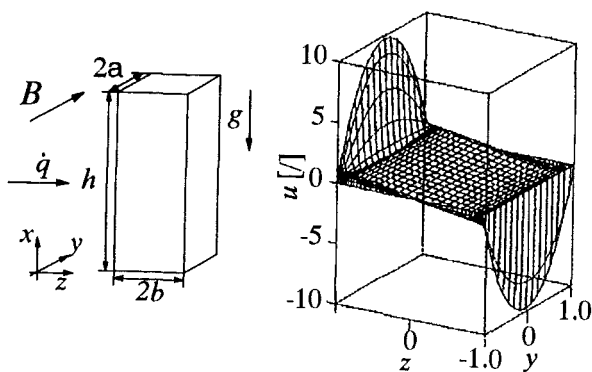
Fig. 4: Buoyancy driven velocity distribution in a perfectly conducting duct with T=z and M=1000.

The buoyancy driven laminar magnetohydrodynamic flow in long vertical channels is investigated [5]. It is assumed that the channels have rectangular cross section with one pair of walls aligned with the strong magnetic field. The walls may have arbitrary electrical conductance. Using asymptotic methods, solutions are derived for general temperature distributions

inside the ducts. Results are shown for different values of the control parameters. One finds the typical subregions for the flow inside the duct, namely the inviscid core, surrounded by viscous Hartmann layers and side layers. The character of the solution inside these regions may deviate from what is expected by a comparison with the classical solutions for pressure driven duct flows. The main difference is that the flow in the core not necessarily exhibits a two-dimensional behavior. Most surprising, however, is the fact, that rather high-velocity jets are observed for the first time even along perfectly conducting side walls as shown in Fig. 4. These jets are able to carry a major part of the flow rate.

Results

First preliminary experimental results are collected from the horizontal arrangement of the flat box with the magnetic field parallel to the gravity. In Fig. 5 the Nusselt-numbers Nu of the heat transfer between the heated bottom plate and the cooled top plate are shown for different Hartmann-numbers M as a function of the Rayleigh-number Ra. Additionally the different critical Rayleigh-numbers are given at which for the different Hartmann-numbers the onset of convection is predicted. Whereas for Rayleigh-numbers above Ra $\geq 5 \cdot 10^3$ the expected reduction of the heat transfer with increased Hartmann-numbers due to the damping of the convection cells is observed the heat transfer below Ra $\leq 5 \cdot 10^3$ shows higher mean values of the Nusselt-number than theoretically predicted for low Hartmann-numbers (M $\leq$ 10). These higher values show strong oscillations with low frequency (about 1/40 Hz) indicating some kind of a periodic instability of the layer of the liquid metal exposed to a strong temperature gradient.

The dimensionless numbers $M = h \cdot B \sqrt{\dfrac{\sigma}{\rho \upsilon}}$,

$Nu = q'' h \cdot \lambda^{-1} \Delta T^{-1}$, $Ra = \alpha \, g \Delta T h^3 \kappa^{-1} v^{-1}$ and $Pr = v/\kappa$ with υ the kinematic viscosity, $\kappa = \lambda / \rho c_p$ the thermal diffusivity, λ the thermal conductivity, ρ the density, c_p the specific heat, σ the electrical conductivity and α the thermal expansion coefficient, ΔT the temperature difference between the heated and the cooled plate are calculated using the thermophysical data of NaK taken from [4] at the mean temperature

$$\overline{T} = \frac{1}{2}\left(T_{Bot} + T_{Top}\right).$$

Literature:

[1] Giancarli, L. et al. (1992), Water-cooled lithium-lead blanket design studies for DEMO reactor, Fusion Technology 21, 2081

[2] Stieglitz, R.; Barleon, L. (1997), MHD aspects and experimental activities in fusion blanket designs, Proc. IEA Intern. Workshop on Liquid Metal Blanket Experimental Activities, Paris, France, Sept. 16-18, 1997

[3] Barleon, L.; Burr, U.; Mack, K. J.; Müller, U. (1997) Natural Convection Phenomena in Magnetic Fields of Liquid Metal Fusion Blankets, Ref. [2]

[4] Barleon, L.; Mack, K. J.; Stieglitz, R. (1996) The MEKKA-facility a flexible tool to investigate MHD-flow phenomena, FZKA-5821

[5] Bühler, L.; (1997) Magneto-convection in long vertical rectangular channels, FZKA-5962

Staff:

L. Barleon   M. Frank
L. Bühler   K. J. Mack
U. Burr   R. Vollmer
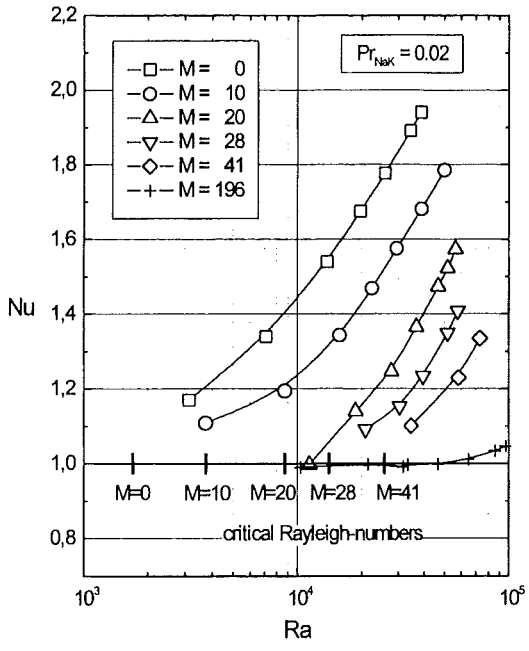
Fig. 5: The measured Nusselt-numbers Nu for different Hartmann-numbers M as a function of the Rayleigh-number

WP B 1
DEMO Blanket Feasibility and Design

B 1.1.1
Segment Design Adaptation to New Specification

The HCPB Demo blanket design is based on a heterogeneous array of alternating beryllium and ceramic pebbles layers arranged in toroidal-radial direction and separated by steel cooling plates [1, 2]. In the previous reference solution, the poloidal height of the breeder and the beryllium pebble bed had been fixed at 11 and 45 mm, respectively, with 8 mm thick cooling plates (60% volume fraction steel). The reference breeder material was Li_4SiO_4 in the form of single size pebbles at a volume fraction of 64% with a Li-6 enrichment of 25 at%.

Extensive neutronics calculations have been performed in 1997 to investigate the breeding performance of the ceramics breeder materials Li_4SiO_4, Li_2ZrO_3 and Li_2TiO_3 (see Table 1) under various conditions in the HCPB demo blanket. Calculations were performed with the MCNP Monte Carlo code [3] and nuclear data from the European Fusion File EFF-1 [4] making use of the 7.5° torus sector model developed previously for the DEMONET configuration [5].

For all of the considered breeder materials the ceramics pebble bed height was varied between 8 and 14 mm while keeping constant the beryllium pebble bed height and the cooling plate thickness. The Li-6 enrichment was varied at different levels with the goal to achieve a global tritium breeding ratio of TBR ≅ 1.13-1.14. This is required to arrive at a final TBR=1.05 when taking into account 10 blanket ports (ΔTBR ≅ 0.06-0.07) and the burn-up effect (ΔTBR ≅ 0.01-0.02). In addition, the effect was analysed of replacing the MANET steel, used as structural material so far, by the low activation (LA) steel EUROFER.

Table 1: Breeder ceramics material data

Material	Composition	Mass density	
		Pebbles [% TD]	Pebble Bed [g/cm³]
Li_4SiO_4	0.96 Li_4SiO_4 0.04 SiO_2	98	1.55
Li_2ZrO_3	0.95 Li_2ZrO_3 0.05 ZrO_2	85	2.06
Li_2TiO_3	0.95 Li_2TiO_3 0.05 TiO_2	90	1.86

The TBR-dependence on the pebble bed height is shown in Fig. 1 for a Li-6 enrichment of 25% when using MANET as structural material. There are no significant changes in the TBR over a wide range of the pebble bed height. In particular, the bed height can be reduced to about 9 mm without affecting the breeding performance too much. Because of the lower Lithium content, there is required, however, a higher Li-6 enrichment of about 50 and 40 at% for Li_2ZrO_3 and Li_2TiO_3, respectively (Table 2).

For Li_4SiO_4 with a Li-6 enrichment of 25 at%, the maximum power density in the ceramics bed amounts to 40, 37 and 35 MW/m³ for a pebble bed height of 9, 10 and 11 mm, respectively. Similar values are obtained for Li_2ZrO_3 and Li_2TiO_3 at a higher Li-6 enrichment, however.

Table 2: TBR comparison at different Li-6 enrichments with MANET as structural material.

Bed height [mm]	Li_4SiO_4	Li_2ZrO_3		Li_2TiO_3	
	25 at%	25 at%	50at%	25at%	40 at%
9	1.12	1.02	1.13	1.05	1.12
10	1.12	1.03	1.13	1.06	1.13
11	1.13	1.04	1.14	1.07	1.14
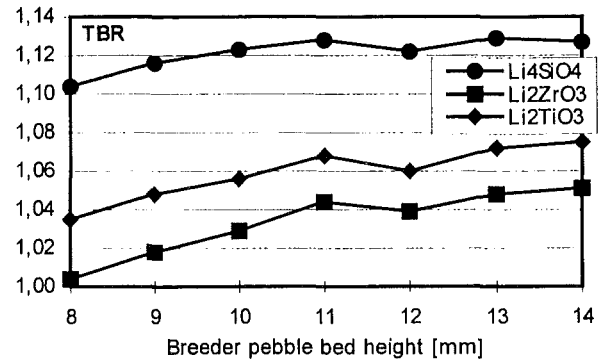
Fig. 1: TBR-dependence on breeder pebble bed height (25 at% Li-6, MANET as structural material).

Replacing MANET by the low activation steel EUROFER (89.125w% Fe, 9.0w% Cr, 0.4w% Mn, 1.1 w% W, 0.07w% Ta and minor constituents) as structural material results in a detrimental effect on the TBR. There is e. g. a reduction from TBR= 1.14 to TBR=1.07 for the variant Li_4SiO_4, 30 at% Li-6, 10 mm pebble bed height. This is due to the highly neutron absorbing Eurofer constituent tungsten. A higher Li-6 enrichment is required to compensate for the resulting TBR-losses since a significant reduction of the tungsten content is not possible without affecting the mechanical stability of the Eurofer steel. In turn, this necessitates a smaller breeder bed height to cope with the higher power density and temperatures in the breeder ceramics. Table 3 gives the results for the finally adopted solutions.

Table 3: TBR and maximum breeder power densities for blanket variants with Eurofer as structural material and 9 mm breeder pebble bed height

	Li_4SiO_4	Li_2ZrO_3	Li_2TiO_3
Li-6 enrichment [at%]	40	75	65
TBR	1.13	1.13	1.14
Maximum power density [MW/m³]	43	41	42

Using the recently improved correlation for the thermal conductivity of the Li_4SiO_4 pebble bed, which yields smaller values than before in the high-temperature range, two-dimensional temperature calculations were repeated for the outboard segment with the MANET structural material, 25 at% Li-6 enrichment and a ceramic layer thickness of 9 mm. The beryllium layer thickness was increased accordingly from 45 to 47 mm in order to maintain the symmetrical arrangement of the cooling plates relative to the cooling channels of the first wall. In parallel, the alternative breeding materials, Li_2ZrO_3 and Li_2TiO_3 pebble beds, were considered. According to the neutron-physical calculations the Li-6 enrichments required for both

breeding materials amounted to 50 and 40 at%, respectively. The power density data varied accordingly. Results are compiled in Table 4 A).

Table 4: Maximum temperatures [°C] of the HCPB DEMO outboard blanket for various breeding materials at a layer thickness of 9 mm and various structural materials

A) Structural material: MANET

T_{max} [°C]	Li_4SiO_4, 25 at% Li-6	Li_4ZrO_3, 50 at% Li-6	Li_2TiO_3, 40 at% Li-6
Steel	515	515	515
Cer	861	977	902
Ber	630	631	632

B) Structural material: T91

T_{max} [°C]	Li_4SiO_4, 40 at% Li-6	Li_4ZrO_3, 75 at% Li-6	Li_2TiO_3, 65 at% Li-6
Steel	502	502	502
Cer	879	971	897
Ber	624	628	627

In a next step, the 9% Cr steel T91 was considered for use as blanket structure material since this steel has similar mechanical properties as expected for EUROFER, and has been qualified for the RCC-MR code. Detailed temperature and stress analyses were carried out. It is evident from the results (see Table 4) that due to the better thermal conductivity of T91 the first wall temperature is smaller by 13 K than that for MANET. As a consequence, the secondary stresses which determine mainly the total stress are reduced. Subsequent stress evaluation according to the RCC-MR design rules has shown that all existing stresses are permissible, although the strength of T91 is smaller than that of MANET.

The results obtained will be taken into account during future design of the DEMO blanket test modules for ITER.

Staff:

U. Fischer
P. Norajitra
K. Schleisiek

Literature:

[1] M. Dalle Donne et al.: Development of the EU Helium-Cooled Pebble Bed Blanket. ISFNT-4, Tokyo, April 1997

[2] M. Dalle Donne et al.: Forschungs- und Entwicklungsarbeiten für das europäische heliumgekühlte „Pebble Bed (HCPB)" Blanket. FZK-Nachrichten, Jg. 29, 1/97.

[3] J. F. Briesmeister (ed.), MCNP - A General Monte Carlo N-Particle Transport Code, Version 4A, LA-12625-M, November 1993

[4] P. Vontobel, A NJOY Generated Neutron Data Library Based on EFF-1 for the Continuous Energy Monte Carlo Code MCNP, PSI-Bericht Nr. 107, September 1991

[5] M. Dalle Donne (Comp.), European DEMO BOT Solid Breeder Blanket, Kernforschungszentrum Karlsruhe, KfK 5429, November 1994

WP B 2
ITER Test Blanket Module Feasiblity and Design

B 2.1.1
TBM Design, Analysis and Integration in ITER

The modification of the DEMO blanket as a consequence of the use of the low activation (LA) material EUROFER entailed likewise a revision of the Test Blanket Modules (TBM) for ITER as compared to the previous concept described in the preliminary DDD [1]. At the same time the new attachment concept of the TBM was taken into account. The related work is described subsequently.

Nuclear Design Analyses

A 9 degree ITER torus sector model with horizontal outboard blanket port, support frame and integrated HCPB blanket test modules (Fig. 1), has been developed previously [1,2]. On the basis of that model, neutronic design analyses were continued for three different TBM variants (Table 1) using the low activation steel EUROFER (89.125 w% Fe, 9.0 w% Cr, 0.4 w% Mn, 1.1 w% W, 0.07 w% Ta and minor constituents) as structural material.
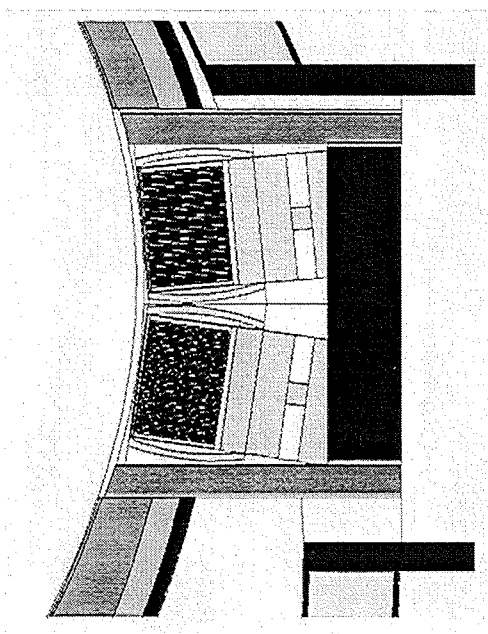
Fig. 1: Horizontal cross-section of the test blanket port with integrated HCPB test blanket modules (MCNP model)

Table 1: Main features of the TBM variants

	TBM-I	TBM-II	TBM-III
Operation phase	BPP	BPP	EPP
Poloidal height of breeder pebble bed	9 mm	15 mm	9 mm
Poloidal height of beryllium pebble bed	47 mm	53 mm	47 mm
Breeder material	Li_4SiO_4	Li_4SiO_4	Li_4SiO_4
Li-6 enrichment	90 at%	90 at%	90 at%
Structural material	EURO-FER	EURO-FER	EURO-FER

Three-dimensional Monte Carlo calculations with the MCNP-code [3] and nuclear cross-section data from the FENDL-1 data library [4] were performed for obtaining the nuclear heat and the

tritium production in the lower TBM as well as the neutron flux spectra for use in subsequent activation calculations. The nuclear power produced at a fusion power level of 1500 MW in the TBM is given in Table 2. In the support steel frame the nuclear power generation amounts to 3.29 and 3.56 MW for the Basic Performance Phase (BPP) and the Extended Performance Phase (EPP), respectively. The local tritium breeding ratio is 0.94, 1.02 and 1.04 for TBM-I, -II and III, respectively.

Table 2: Nuclear power generation [MW] in the HCPB TBM variants

	TBM-I	TBM-II	TBM-III
First wall	0.19	0.19	0.18
Beryllium	0.39	0.38	0.42
Breeder	0.44	0.50	0.48
Structure	0.50	0.47	0.50
Total TBM-I	1.53	1.54	1.58

Three-dimensional activation and afterheat calculations were performed for TBM-I taking into account both MANET and EUROFER as structural material. The afterheat and activity inventory was calculated by making use of an appropriate code system [5] linking the MCNP Monte Carlo code and the FISPACT [6] fusion inventory code. Activation and transmutation cross-section data were taken from the European Activation File EAF-4 [7].

Table 3 shows the afterheat produced in TBM-I after a continuous irradiation of 0.3 years at a neutron wall loading of 1.197 MW/m^2 at the TBM first wall with EUROFER as structural material. For comparison, the table includes the afterheat generation when replacing EUROFER by the martenisic steel MANET. In the support steel frame, being composed of 80% SS-316 and 20% water, the afterheat production amounts to 105 kW at shut-down. Fig. 2 shows the time behaviour for the afterheat of the different materials in TBM-I.

Table 3: Afterheat generation in the HCPB TBM-I.

Time	Total afterheat		
	EUROFER		MANET
	P_{decay} [kW]	P_{decay}/P_{direct}	P_{decay} [kW]
shut-down	29.7	1.94E-02	17.2
1.0 min	17.7	1.15E-02	16.8
1.0 h	12.9	8.44E-03	11.9
1.0 d	2.37	1.55E-03	6.25E-01
1.0 yr	1.85E-01	1.21E-04	1.38E-01
5.0 yr	8.07E-03	5.27E-06	1.57E-02

Thermal and Mechanical Analyses

For the three TBM variants thermal and mechanical analyses have been carried out. In the thermal calculations the improved correlation was used for the thermal conductivity and the heat transfer coefficients of the Li_4SiO_4 pebble bed. Furthermore, the thermophysical and mechanical properties of T91 were used instead of EUROFER (see B 1.1.1).

The maximum power densities obtained from the nuclear calculations are compiled in Table 4.
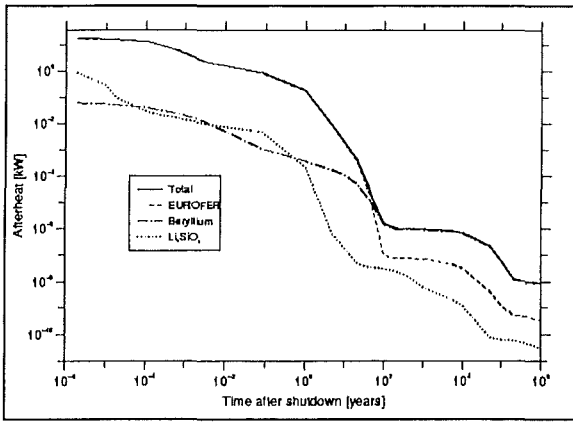
Fig. 2: Total afterheat [kW] in TBM-I as a function of cooling time

Table 6: Calculated maximum and admissible von Mises stresses in the first wall of TBM-I in [MPa] (2D calculations)

State of operation		TBM-I
Normal p_{He} = 8 MPa p_{Bl} = 0.1 MPa	Primary stress	Cooling channel (380 °C) 56 < 267 adm.
	Primary plus secondary stress	Plasma side (494 °C) 332 < 444 adm.
Accident p_{He} = 8 MPa p_{Bl} = 2.5 MPa	Primary stress	Cooling channel (380 °C) 82 < 267 adm.
	Primary plus secondary stress	Plasma side (494 °C) 349 < 444 adm.

Table 4: Maximum power densities in [MW/m^3]

	TBM-I	TBM-II	TBM-III
T91 steel	11	11	10
Li$_4$SiO$_4$ pebble bed	20	16	24
Beryllium pebble bed	5	5	5

The thermohydraulic design calculations of all TBMs have been carried out using the finite element code FIDAP. Thus, heat exchange between the breeding zone and the cooling channels of the first wall could be taken into account implicitly. The helium temperatures determined serve as input data for 2D temperature calculations performed by means of the ABAQUS program. The results for TBM-II are preliminary, as estimated helium temperatures* were used. The calculated temperatures are presented in Table 5.

Table 5: Calculated maximum temperatures (°C) (2D calculations)

	TBM-I	TBM-II*	TBM-III
T91 steel	500	(493)	499
Li$_4$SiO$_4$ pebble bed	581	(835)	632
Beryllium pebble bed	444	(500)	446

Then, 2D stress calculations were performed for the normal state of operation (8 MPa in the cooling channels, 0.1 MPa inside the blanket) as well as for a controlled accident in case of coolant leakage with the pressure inside the blanket being limited to 2.5 MPa, a value which is estimated from a preliminary stress calculation for the caps. Stress evaluation was accomplished on the basis of the S_m and S_t data of the steel T91 in accordance with the RCC-MR design rules. The results obtained for TBM-I are compiled in Table 6. The stresses in TBM-II and TBM-III are in the same range.

Additional 3D calculations with the code ABAQUS have been performed in particular to determine the temperature and stress distribution during power cycling. The FE model is a radial-toroidal slice of TBM-I including six FW channels (see Fig. 3). Transient fluid temperatures as well as averaged cooling-plate temperatures obtained from FIDAP calculations were used as input.

Fig. 3: FE mesh of TBM-I used in the 3D ABAQUS calculations

The result of the transient temperature calculation is presented in Fig. 4. It shows for two power cycles the course of maximum temperatures in the Be coating, FW steel, manifold, Li$_4$SiO$_4$ pebble bed, and beryllium pebble bed. The main information derived from this figure can be summarized as follows:

- The time constant of the plasma-facing front of the box is short in terms of a power cycle, e.g. 25 s after establishing full power the FW has reached 90 % of the temperature rise under steady-state conditions.

- The maximum temperature gradient in the breeder material is 4.5 K/s during ramp-up, and 3.0 K/s during ramp-down.

- The manifold does not reach thermal equilibrium.

Fig. 4: Blanket temperatures during cyclic operation (nominal operation, TBM-I)

In the 3D stress calculations, a generalised plain strain condition was assumed for the nodes on the poloidal model boundaries, i.e. radial-toroidal cross-sections remain plane but may incline. The mechanics of the pebble beds were neglected for the structural calculations. Also, the Young's modulus for the plasma-facing Be layer was diminished thousandfold to account for the sectioning of this layer, making its structural effect negligible. Overall stresses are dominated, by a factor of 10, by secondary thermal stresses and are thus closely linked to the thermal history of the module. A plot of v. Mises stress histories, see Figure 5, puts the maximum stress value at the interface between steel and Be layer, close to the FW corner, at 420 MPa 200 s into the power cycle, thereafter reducing to a stationary value of 410 MPa. Stresses in the side wall are closely linked to the temperature history of the manifold, rising continuously during burn time. However, the stress levels reached are considerably smaller than those in the FW. The maximum quasi-stationary stresses are about 10 % higher than those obtained in the 2D calculations. The three-dimensionality, further the fact that the modelling of structures may have an effect on FW stress, are reasons for these differences. They suggest that the stresses calculated with the 3D model which likewise lie within admissible stresses according to RCC-MC, are more credible. It should be left to a detailed local analysis to determine accurately pattern and values of stresses.

Design Studies

The design of the TBMs including the cap region with the helium inlet and outlet channels was revised according to the actual concept. TBM-I is shown in Fig. 6. In addition to the reference design concept, an alternative solution was elaborated which makes extensive use of diffusion welding techniques for joining of the different parts of the TBM.

TBM Integration in ITER

The design of the Test Blanket Subsystem (TBS) and in particular the plumbing layout is strongly dependent on the adopted remote handling procedures. For the solution with attachment at the vacuum vessel port extension, the arrangement of the TBS inside the port is schematically represented in Fig. 7. The TBMs (1) are contained in a frame (2). This frame will provide a standarized interface with the ITER basic structure and a better shielding capability as well as neutronic and thermal insulation from the basic shielding blanket.

A water cooled Shield (3) is located behind the TBMs and Frame. It will assure neutron protection of the vacuum vessel (VV) and the magnets, and contributes to reduce the neutron load at the VV boundary.

The mechanical interface with the ITER Reactor is provided by the vacuum vessel plug (4). This structure is supported by the vacuum vessel port extension using guide keys.

Fig. 5: V. Mises stress (primary plus secondary) histories during cyclic power operation, TBM-I

Fig. 6: HCPB Test Blanket Module (TBM-I) to be tested in a horizontal ITER test port (dimensions in mm)

(x) indicates mechanical interfaces

1. Test Blanket Modules
2. Frame
3. Shield
4. Vacuum Vessel Plug
5. Plumbing

Fig. 7: Schematic of the Test Blanket Subsystem in the Horizontal Port

The plumbing (5) which extends through the VV closure plate up to the cryostat boundary, is also part of the TBS. Note that all the VV Plug penetrations have rigid connection and do not require vacuum tight flexible connections such as bellows.

This arrangement enables the whole Test Blanket Subsystem (TBMs, frame, shield, VV plug and plumbing) to be a self contained unit that will be installed and removed as a single piece without remote handling operations inside the VV port extension. Indeed this assembly can be completely assembled and tested prior to installation.

The European and the Japanese teams have collaborated in their approach for testing their helium cooled solid breeder test modules. During the BPP the European HCPB Test Blanket Module (EU-TBM) shall occupy the lower half of the test port allocated to the helium cooled blankets, the other half being occupied by the Japanese module (JA-TBM). Fig. 8 shows a vertical section of the ITER horizontal port with the EU-TBM.

The TBM is contained in an insulating frame, so that the thermal conditions on the side wall of the TBM need not be identical to the conditions of the shielding blanket. Although the nominal temperature of the test blankets may be in the neighborhood of 300°C to 500°C, the frame is cooled to approximately 150°C. Basic parameters of the frame cooling are similar to the ITER shielding blanket modules. The frame will also contribute to the neutron shielding of the vacuum vessel and the magnets.

There is a gap allowance of 50 mm around the perimeter of the frame to account for the differential motion between the back plate and the VV during operational and off-normal conditions. The wall thickness of the frame has been chosen so that it allows a suitable TBM size and at the same time a good neutron shielding capability. The external frame dimensions adjacent to the regular shielding blanket modules are 1.5 m wide by 2.5 m high, with a wall thickness of 175 mm. In the region outside the back plate there is a step increase in the wall thickness to 305 mm; this allows a better shielding capability at the side walls and shielding from the neutron streaming through the gap between Frame and ITER shielding blanket system.

The first wall of the Frame follows approximately the FW contour of the adjacent shield blankets modules, but it is recessed from it by 60 mm.
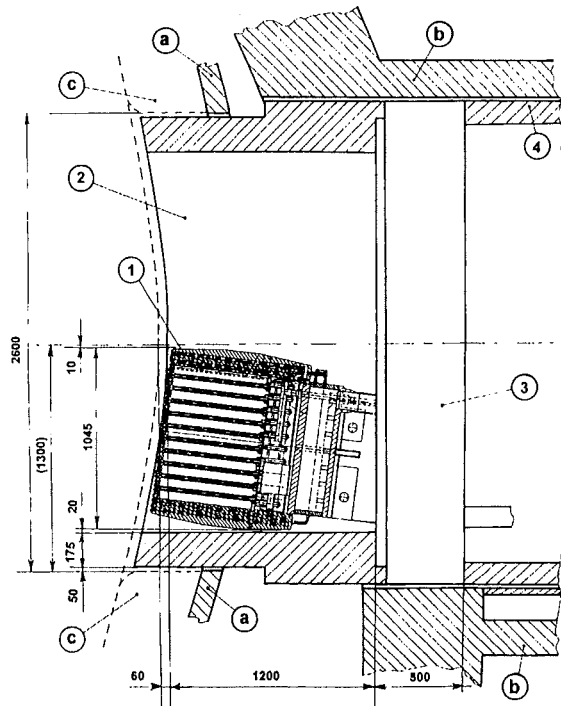
1. Test Blanket Module   a. Back Plate
2. Frame   b. Vacuum Vessel
3. Shield   c. Shield Blanket
4. Vacuum Vessel Plug

Fig. 8: Vertical cross section of the ITER Horizontal Port with the European HCPB-TBM

Taking into account 20 mm gap between TBMs and frame and between EU- and JA-TBM, the maximum dimensions of each TBM is 1045 mm high and 1110 mm wide. The maximum radial dimension (from the frame FW to the shield, measured at the middle port plane) necessary for the EU-TBM is about 1.2 m. It is dictated by the radial dimension of the EU-TBM that reproduces at full-scale a portion of the European HCPB DEMO blanket. The first wall of the TBM is planar, without curvature, but it conforms as closely as possible to the first wall of the adjacent shield blankets modules. The deviation from the ITER first wall contour is in the range of 60-75 mm.

Additional shielding will be provided by the water-cooled shield. This is a 500mm-thick structure, which also provides the attachment points for the frame and the TBMs.

Helium Cooling System

The helium cooling system of the HCPB TBM has been designed to the extent needed for safety analysis (section B6.1.1) and for demonstration that it can be accommodated in the space allocated by ITER. The cooling system includes the primary helium heat removal loops with all components, and the pressure control subsystem. Two separate primary heat removal loops of 2 x 50 % heat capacity are foreseen to assure decay heat removal in case of a failure in one loop. The secondary cooling loop with the ultimate heat sink is part of the ITER cooling system providing water flow at low temperature. Another interface to the cooling system are the connections to the helium purification system which takes a bypass flow of 0.1 % of the main mass flow rate. The cooling system will be housed in the wedge-shaped pit outside of the cryostat at the level of the test module. The thermal-hydraulic design parameters are summarised in Table 7.

Table 7: Nominal Design Data of the Helium Cooling System (TBM-I)

Total heat to be removed (MW)	1.9
Primary coolant	helium
Number of loops	2
Temperature at TBM inlet/outlet (°C)	250/350
Pressure (MPa)	8
Mass flow rate, both loops (kg/s)	3.7
Total pressure loss (MPa)	0.36
Helium inventory, both loops (kg)	15
Typical tritium inventory (g)	10^{-3}
Secondary coolant	water
Temperature at HX inlet/outlet (°C)	35/75
Pressure (MPa)	0.5
Mass flow rate, both loops (kg/s)	11.4

Fig. 9: Helium cooling system flow diagram

Main components in each loop are the heat exchanger, circulator, electrical heater, dust filter, and pipework (see flow diagram Fig. 9). The total helium mass inventory in one loop amounts to 7.5 kg and the overall pressure loss is about 0.36 MPa, half of which occurring in the test module proper. The heat exchanger is assumed to be a straight tube bundle heat exchanger, or alternatively consisting of U-tubes, with high pressure helium flowing inside the tubes. The design specification for the circulator is as follows: temperature 300 °C, pressure 9.6 MPa, mass flow rate 1.9 kg/s at a pumping head of 0.36 MPa at 80 % of maximum speed and at 250 °C inlet temperature, speed variation max/min of at least 4. The electrical heater with a power of 100 kW which is installed in a bypass to the heat exchanger is needed for baking the test module first wall at 240 °C and for heating the whole cooling system. A filter unit is installed in the hot leg of the main loop, accumulating residual dust and particles from fabrication, and erosion particles down to a size of typically 10^{-6} m. For the main pipework an outer diameter of 101.6 mm and a wall thickness of 6.3 mm have been chosen. This results in flow velocities of between 40 and 50 m/s. The total pipe length sums up to 48 m per loop. The number of valves in the main loops has been kept at a minimum to avoid inadvertent closure which would mean loss of heat sink. All of the piping and components in the primary cooling system will be constructed of austenitic steel.

The pressure control subsystem is needed for evacuation, helium supply, pressure control, and overpressure protection. The components are conventional and of relatively small size.

Activation of cooling system components is expected to be generally low allowing controlled personnel access. Remote handling is envisaged for connection and disconnection of the test module by the aid of a transporter. The large components require lifting equipment with a load capacity of about 2 tons.

The following system control scheme is proposed for pulsed operation: The principal objective is to keep the test module inlet temperature at 250 °C. The secondary cooling water inlet temperature is kept at 35 °C, the circulator is operated at rated speed, the electrical heaters are turned off, and flow partition through the HX and heater bypass is controlled as to maintain the inlet temperature close to 250 °C. During longer shutdown periods decay heat removal is achieved at reduced circulator speed, or by natural convection.
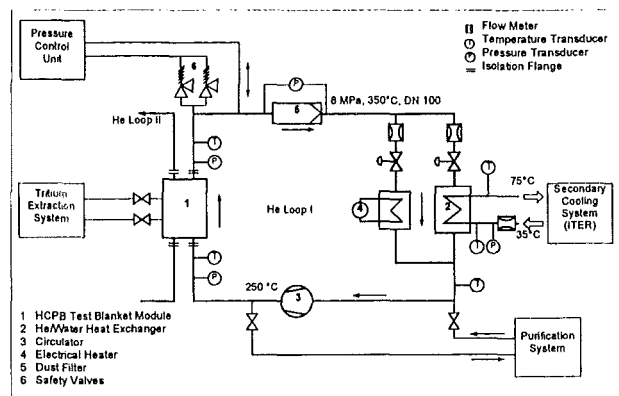
Literature:

[1] M. Dalle Donne, L. V. Boccaccini (Comp.): European Helium Cooled Pebble Bed (HCPB) Test Blanket, ITER Design Description Document, Status 1.12.1996, Forschungszentrum Karlsruhe, Wissenschaftliche Berichte FZKA 5891, April 1997.

[2] U. Fischer, M. Dalle Donne: Three-dimensional Neutronics Analysis of the European HCPB Blanket Test Module in ITER, 4th Int. Symp. on Fusion Nuclear Technology, Tokyo, Japan, April 6 - 11, 1997.

[3] J. F. Briesmeister (ed.): MCNP - A General Monte Carlo N-Particle Transport Code, Version 4A, LA-12625-M, November 1993

[4] FENDL/MC-1.0 - Library of Continuous Energy Cross-Sections in ACE Format, Summary Documentation by A. B. Pashchenko, H. Wienke and S. Ganesan, IAEA-NDS-169, Rev. 3, November 1995

[5] H. Tsige-Tamirat: Three-dimensional Activation Analyses for Demo Type Fusion Reactor Blankets, Proc. of the 19th Symp. on Fusion Technology, Lisbon, Portugal, 16-20 Sept. 1996, Vol. 2, p.1559-1562, Elsevier 1997

[6] R. A. Forrest , J.-Ch. Sublet: FISPACT 4 User Manual, UKAEA FUS 287, July 1995.

[7] J. Kopecky, D. Nierop: The European Activation File EAF-4, Report ECN-C-95-072, December 1995.

Staff:

L. Boccaccini
M. Dalle Donne
U. Fischer
S. Gordeev
St. Hermsmeyer
K. Kleefeldt
T. Lechler
M. Lenartz
P. Norajitra
G. Reimann
K. Schleisiek
I. Schmuck
H. Tsige-Tamirat

B 2.2.1   TBM Ancillary, Equipment Design

The external circuits of an ITER Test Blanket Module comprise a Cooling System, a Tritium Extraction System, and a Coolant Purification System. The present contribution reports about the design work carried out for the two latter systems.

1. Tritium Extraction System

The extraction of tritium from the blanket is achieved with the help of a helium purge gas containing up to 0.1 % H_2; the added hydrogen facilitates the tritium release by isotopic exchange. The tasks of the Tritium Extraction System are:

• Removal of tritium produced in the blanket test module,

• Separation and intermediate storage of the two main chemical forms of tritium, i.e. HTO and HT,

• Purification and conditioning of the purge gas.

The main design data of the Tritium Extraction System are summarized in Table 1. A flow diagram is shown in Fig. 1. The instrumentation for process control, e.g. sensors for temperature, pressure, flow rate, etc., are not included in the figure. The mode of operation shown is the extraction mode where the cold trap and the first molecular sieve bed are in operation.

Process Description:

At the beginning of the loop, there are 5 valves (V1...V5) which are used to enable a safe isolation of the loop from the test blanket module. This is especially important in the case of a pressure increase in the TBM caused by a leakage in the

cooling system.

Table 1: Main design data of the Tritium Extraction System

Helium mass flow	0.85 g/sec
Swamping ratio	He: H_2 = 1000
Tritium production rate	0.15 g / day
Partial pressures [a]	
p (H_2)	110 Pa
p (HT + HTO)	0.3 Pa[b]
p (H_2O)	≈ 0.2 Pa[b]
Extraction rates	
H_2	18.4 mole/day
HT	≈ 0.04 mole/day
H_2O / HTO	≈ 1 g/day
Extraction efficiency	≥95 %

[a]   Average values at test module outlet

[b]   About 80 % of HTO is assumed to be converted to HT + H_2O by isotopic exchange; no HTO / H_2O is assumed to be reduced by the steel walls

Front-end components of the loop are a cooler to reduce the temperature of the incoming gas to room temperature and a filter cartridge to remove particulate material which might be carried out from the blanket zone. Downstream of the filter, there is a bypass line leading to the compressor (No. 8) which is

1 Cooler
2 Filter
3a/3b Tritium Monitor
4 Cold Trap
5 Recuperator
6a/6b Low Temp. Adsorber
7 Heater
8 Compresor
9 HeliumMakeup Unit
10 Water Collector
11/13/17 Blower
12 Relief Tank
14 Diffusor
15 Getter Bed
16 Helium Buffer Vessel
ES Evacuation System
▷◁ open Valves
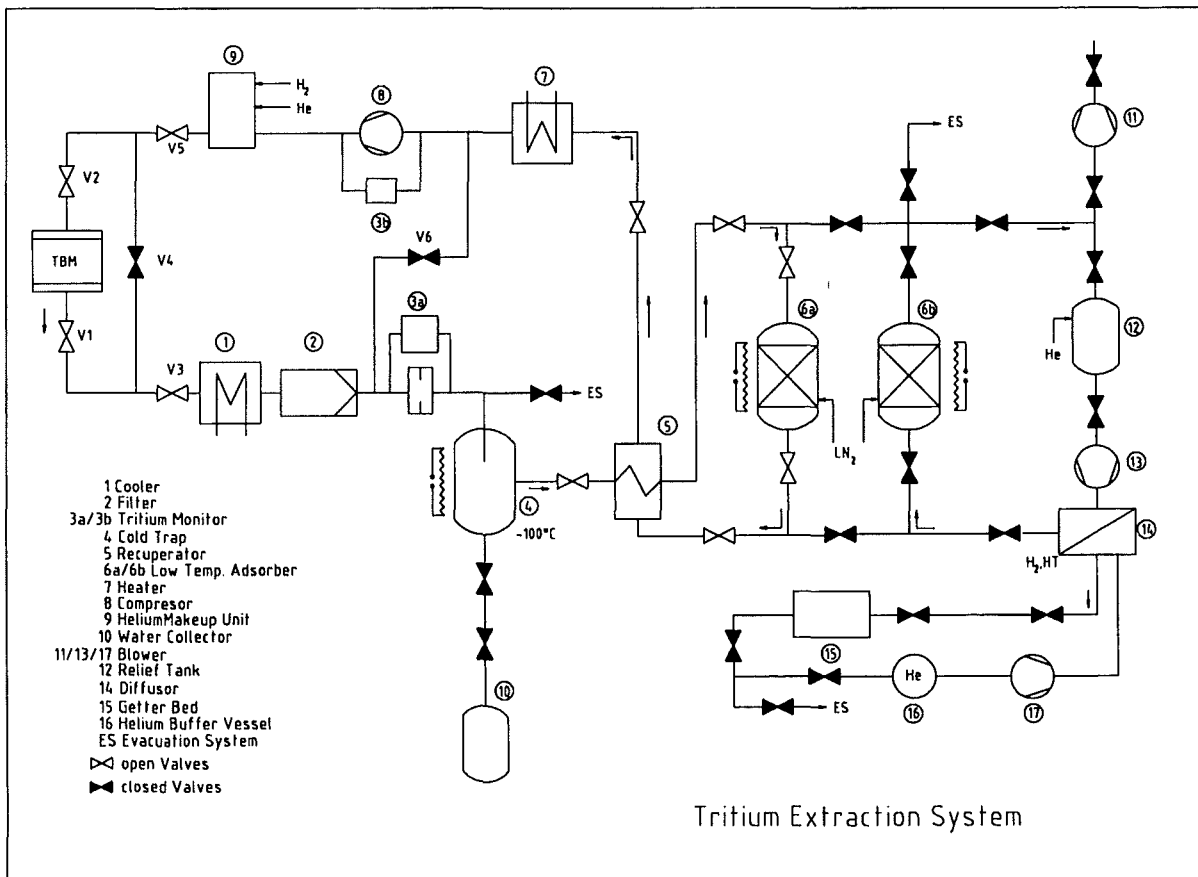▶◀ closed Valves

Tritium Extraction System

Fig. 1. Flow diagram of the Tritium Extraction System

foreseen for initial scavenging of the TBM.

An ionization chamber (No. 3a) to measure the tritium activity is installed in a bypass to the main gas stream; an orifice or a throttle valve provide the required small gas flow through the ionization chamber. The Q_2O content (Q = H, T) of the gas is frozen out in the cold trap (No. 4) operated at $\leq$ -100°C. The residual Q_2O concentration at the outlet is < 0.015 vpm.

The purge gas is further cooled down by a recuperative heat exchanger (No. 5) and then passed through an adsorber bed (No. 6a) operated at liquid nitrogen (LN_2) temperature. The bed is filled with 5A zeolite pellets which adsorb molecular hydrogen as well as gaseous impurities and residual moisture. The bed contains filters on the down-stream and upstream side to prevent particulate material from being transferred during loading or unloading operations. In addition, the bed is equipped with an electrical heater. The second bed provides additional adsorption capacity.

The clean gas leaving the adsorber bed is first warmed up in the heat exchanger (No. 5) mentioned above and then by an electrical heater (No. 7). The next components are the purge gas blower (No. 8) coming in contact only with clean gas at room temperature, and the helium make-up unit (No. 9) where hydrogen is added to provide a He : H_2 swamping ratio of 1000 for the gas reentering the test blanket module. In addition, this component is used for the first fill-up of the loop with helium.

Ancillary Installations

The main tasks of the ancillary installations is to facilitate the transfer of the extracted tritium from the purge gas system to the Water Detritiation System (WDS) and to the Isotope Separation System, respectively.

The first aim is reached by liquefying the ice of the cold trap and by draining the water into a mobile container (No. 10) which is later on transferred to the WDS.

The second task is accomplished by warming up the low temperature adsorber beds to about -150°C. The desorbing gas (i.e. the hydrogen isotopes and some coadsorbed helium) is circulated through a palladium diffuser, which allows to separate the hydrogen isotopes from helium and to store them in an uranium getter bed (No. 15) installed at the secondary side of the diffuser.

Analytical Tools

The processes of tritium extraction and purge gas purification are controlled by continuous measurement of the tritium concentration at several points of the gas loop and by taking gas samples for chemical analysis.

a) Ionization chambers are used at the following points:

- upstream of the cold trap (component No. 3a, see Fig. 1);

- downstream of the cold trap; after removal of HTO, the HT concentration is determined and - as the total activity is known - also the HT/HTO ratio;

- downstream of the heater (No. 7) to control the integral tritium removal efficiency of the loop (ionization chamber No. 3b);

- upstream of the relief tank (No. 12) to control the removal of the hydrogen isotopes by the Pd/Ag diffuser and the tritium concentration of the gas sent to the

Waste Gas System at the end of the adsorber unloading / regeneration process.

b) A gas chromatograph (GC) is used to measure the gas composition upstream of the helium make-up unit. A small gas transfer pump is used to transport gas samples to the GC where they are quantitatively analyzed with respect to Q_2, N_2, CO, etc. Additional gas samples taken from other points of the TES can be analyzed with the same GC. Hydrogen concentrations in the range of 1000 vpm, however, are preferably determined by specific hydrogen detectors as mentioned below.

c) Two specific hydrogen detectors to control the hydrogen concentration are used at the inlet of the cold trap and at the outlet of the helium make-up unit.

A moisture detector which would be very difficult to operate at Q_2O concentrations less than 1 ppm appears not to be necessarry since the corresponding information can be obtained from the amount of water collected in the cold trap and / or from the results of the measurements carried out with the ionization chambers.

Space Requirements

It is intended to install the Tritium Extraction System in the Tritium Building of the ITER plant. The space requirement is about 16m² which includes 2 gloveboxes which are needed as secondary containments for radiological safety reasons. Additional space of about 30 m² is needed for a control station, for electrical cabinets, and for the working area of the operator.

The size of supply and diposal facilities have not been estimated as most of these facilities will be shared with other subsystems in the Tritium Building.

Table 2 gives a summary of the common facilities needed for the operation of the Tritium Extraction System.

Table 2: Supply and Disposal Facilities needed for the Operation of the Tritium Extraction System

Type of Facility
Central Evacuation System
Supply Facilities for – Gases (He, H_2, Pressurized Air) – Liquid Nitrogen – Cooling Water – Electrical Power (including emergency power and uninterruptible power)
Waste Gas and Waste Disposal System
Water Detritiation System
Radiological Safety Systems

2. Coolant Purification System

The design of the Purification System and its principle of operation has been described in [1, 2]. Within the work performed for the ITER Design Description Document (DDD) for the European Helium Cooled Pebble Bed Test Blanket, the

design was extended by describing the technical specifications of the following loop components:

- Particle Filter,
- Tritium Monitors,
- Cold Trap,
- Recuperator,
- Low Temperature Adsorber Bed,
- Compressor,
- Helium Make-up Unit,
- Water Collector,
- Relief Tank,
- Blower,
- Diffuser,
- Getter Beds,

and several ancillary components, e.g. Cooler, Heater, Helium Buffer Vessel, LN_2 Supply Tank, Gaschromatograph, and Glove Boxes.

This information will be available in the corresponding DDD Report which will be issued within the next months.

Literature:

[1] Nuclear Fusion Project Annual Report of the Assossiation Forschungszentrum Karlsruhe / Euratom, October 1995 - September 1996, FZKA 5858, January 1997, p. 123 ff

[2] European Helium Cooled Pebble Bed (HPBC) Test Blanket, ITER Design Description Document, Status 1.12.1996, Compiled by M. F. Dalle Donne and L.V. Boccaccini, FZKA 5891, April 1997

Staff:

H. Albrecht
E. Hutter

WP B 3
ITER Test Blanket Module Fabrication

B 3.1.1
Development of Fabrication Methods and Manufacturing of Mock-ups

Introduction

The design of the European Helium-Cooled Pebble Bed (HCPB) blanket (see subtasks B 1.1.1 and B 2.1.1) makes it necessary to investigate, develop and qualify fabrication and inspection techniques which enable the manufacturing and assembly of the DEMO blanket segments and in particular the test blanket module to be tested in ITER. The work of the past year was concentrated on the following four fabrication steps [1].

- Diffusion welding of first wall (FW) sections and cooling plates, in particular with milled grooves to produce plates with integrated cooling channels.

- Bending of the diffusion welded FW plates to obtain a section of the U-shaped segment box.

- Electron beam (EB) welding of cooling plates with headers.

- Welding of the cooling plates to the FW at the inside of the segment box.

- Ultrasonic (US) inspection of EB welded double seams.

The results of these investigations are described subsequently.

Diffusion Welding of FW and Cooling Plates

The diffusion welding experiments on plates with internal cooling channel structures performed in a vacuum facility under axial mechanical pressure have produced excellent results. Strength in the joining zone roughly corresponds to that of the base metal. Because of the uniform quality of the vacuum and the monitoring of deformation during the welding process, the vacuum systems offer optimum preconditions. However, no parts with blanket-related dimensions can as yet be welded.

For this reason, tests are now being carried out in cooperation with the company of Seilstorfer, Haag-Winden, to find out whether sufficiently good welded joints can be produced also in hot isostatic presses (HIP), because such plants exist in the appropriate size. Before the halves of the specimen plates are introduced into the HIP facility they are fitted with pressure plates of TZM on both sides for protection of the channel structures and then enclosed in a thin blanket of sheet metal. The interior of the package is evacuated and sealed gastight.

Some first HIP experiments on structures of the first wall and of the cooling plates did not produce acceptable results despite the use of the same welding parameters (pressure, temperature, time) as had been employed in the mechanical press. For the second series of experiments, the surfaces to be joined of the specimens were first fine-ground and then prepared in a special cleaning and pickling process. Moreover, shortly before loading into the HIP facility the specimens were run through an extensive baking program under a vacuum. Except for some defects in the edge zones, some preliminary US inspections seem to indicate good bonding. Destructive post-welding examinations still need to be carried out.

Besides these special tests, a more general test program was initiated in the FZK facility HIP 3000 to find out the optimum HIP conditions. Parameters like HIP pressure and temperature, dwell time and surface treatment are investigated. To determine the quality of the joint a test program is carried out including

tensile, bending and impact test, and metallographical examinations. To facilitate the manufacturing process the joints are evacuated and sealed by EB welding in a single step. Post-weld heat treatment is carried out after the HIP process inside the HIP facility.

Bending of FW Plates

To complete the previous investigations an additional test series has been carried out with the bending radius of 75 mm (with filling material and without sandwich plate) and with a bending radius of 50 mm in order to explore the bending limits of the material [2].

For the 75 mm bending radius no surface cracks could be detected, but the real bending radius was between 55 and 70 mm, i.e. the stability of the plate is not sufficient to follow the bending punch.

Looking at the tests with 50 mm bending radius a successful bending with and without filling material is only feasible with the support of a sandwich plate. The reduction of the channel height with and without filling material increased to a value of 10.8 % and 18.6 %, respectively. Bending without sandwich plate and with filling material leads to a crack in the elongated plane because of the instability of the plate and a sharp bending radius (much smaller than 50 mm).

In the next step plates will be bent with an addition to the wall thickness corresponding to the height of the ribs needed for the welding of the cooling plates. The manufacturing of these ribs as an integral part of the FW is considered as an attractive alternative to the manufacturing of the ribs by weld build-up.

EB welding of Cooling Plates with Headers

The HCPB blanket is equipped with a large number of cooling plates. Each plate is welded to one header. Four variants of manufacturing processes for these components have been considered. One way of manufacturing the components is by joining the two parts by EB welding (Fig. 1). Welding tests are necessary because of the complicated geometry with the depth of the weld changing several times over the entire welding length, in accordance with the number of cooling channels, from 2 mm in the channel area to approx. 6 mm at the webs which are 2 mm wide.

In cooperation with the Schweißtechnische Lehr- und Versuchsanstalt (SLV), Halle, a suitable EB welding technique was developed. Welding of the MANET samples was performed from both sides. The web areas were approached under NC operation first and welded so as to overlap in the center, and then the parts were joined over the whole length to a depth of 2 mm. Welding has been completed. The post-welding examinations show that the logitudinal welds are without flaws. The webs are welded on 70 % of their cross section; a further improvement can be reached by applying the puls welding technique.

One of the test specimen was submitted to pressure of 50 MPa in the cooling channels without failure.

Welding of Cooling Plates to the FW Box

The cooling plates separating the ceramic and the beryllium pebble beds have to be joined to the bent FW box by TIG welding.

In a first test program the welding process and the US testing methods have been applied with very good results [4]. Flawless welds showing very small distortions have been achieved without preheating. Following thermal treatment of the

specimens, the tests have been evaluated by metallographic examination of the welded zone, and by strengh measurement in bending tests and tensile tests. These tests have shown that the strength is approximately the same as that of the base material. The US weld inspection is able to detect relatively small flaws, i.e. slots with a depth of 0.5 mm, a width of 0.2 mm and a length of 5 mm as well as holes with a diameter of 1 mm.

HEADER

SURFACE TO BE EB-WELDED

EB
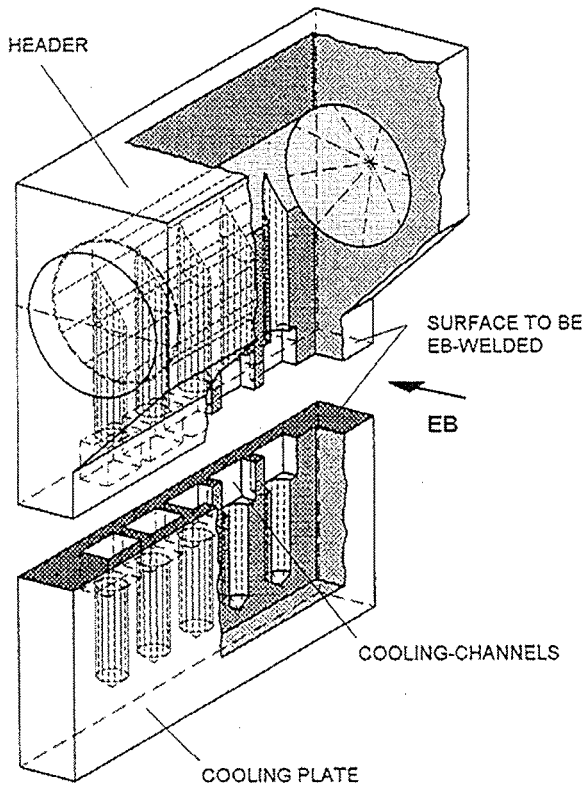
COOLING-CHANNELS

COOLING PLATE

Fig. 1: Sample for EB welding of cooling plate with header

In a second test one complete cooling panel (without cooling channels) has been welded into a stiff U-shaped frame comparable with the FW to expose the weld to realistic load conditions.

Another aspect is the possibility of overhead welding of this joint. First results exhibit that overhead welding can be carried out with the same parameters used for downhand welding. The results of these tests are important for the handling of the module during assembling.

A first handling concept has been worked out with the result that most of the components needed for the assembly are available, and the missing ones can be developed with a limited amount of work [5].

US Inspection of EB Welded Double Seams

The experiments about the US inspection of EB-welded double seams with an intermediate channel for monitoring purposes were performed to learn about the sensitivity of the inspection method and find possibilities to determine defect sizes.

Another series of US inspections run at Siemens KWU used the VS70-4MHz probe by Krautkrämer and, for very small defects,

a specially developed Siemens 60 SET 5.5 MHz probe, which provided high axial and lateral resolution. Surface defects (cracks) to 0.2 mm depth were detected; the limit of detection of volume defects (porosities) was a diameter of 0.5 mm. Defect sizes were assessed through evaluations of the dynamics of back reflection or, with defects smaller than approx. 2 mm down to some 0.5 mm, by comparison with the evaluation curves determined on test specimens of the same type (geometry and material).

The results of US examinations allow welds to be subjected to probablistic analysis and evaluation with respect to uncertainties inherent in US inspections [6]. The inspection technique can be used with blanket components in situ, provided preceeding inspections of identical test specimens were run to determine the shape reflections due to the specific geometry of the component, and provided also that the welds are easily accessible.

Literature:

[1] T. Heider, K. Schleisiek, G. Reimann, Ch. Dellis and E. Rigal: Development of Manufacturing Processes for the ITER HCPB Blanket Test Module. ISFNT-4, Tokyo/Japan, April 97.

[2] G. Haufler, A. Schwager: Biegen von Platten aus MANET II mit integrierten Kühlkanälen. KE/FGU Stuttgart, 1-TB-249/96, (1996).

[3] G. Sobisch: Abschlußbericht zu Elektronenstrahl-Schweiß-versuchen mit dem Werkstoff 1.4914 (Platinen-Musterteile) an Blanketsegmenten für Fusionsreaktoren. Schweißtech-nische Lehr- und Versuchsanstalt Halle GmbH (Okt. 1997)

[4] R. Girardier, H. Lüscher: Schweiss- und Prüfversuche zur Ermittlung der optimalen Parameter. Sulzer Innotec, VTW TB 96.006, (December 1996)

[5] C. Dippold: Handhabungskonzept zum Einschweißen der Kühlplatten in die Erste Wand. Siemens / KWU, NW-A/96/54, (December 1996).

[6] K. Gemmer-Berkbilek: Arbeitsprogramm zur quantitativen Bestimmung von Schweißfehlern in EB-Doppelschweiß-nähten mittels Ultraschall-Teil B „Quantitativer Testfehler-nachweis". Siemens / KWU, Erlangen, KWU NW-P3/96/058 (1997).

Staff:

J. Heger
T. Heider
O. Jacobi
T. Lechler
G. Reimann
H. Riesch-Oppermann
R. Ruprecht
L. Schäfer
L. Schmidt
K. Schleisiek
P. Weimar

B 3.2.1
HEBLO Tests and Construction of Test Sections for HEBLO and HEFUS-3

For completion of the second HEBLO experiment with a mixed pebble bed, two-dimensional transient temperature calculations were carried out using the ABAQUS program. The temperatures calculated for the first test phase at 1 MPa piston load are in good agreement with the measured values (Figure 1).

1 Helium gas inlet
2 Measured temperature at the center of the pebble bed
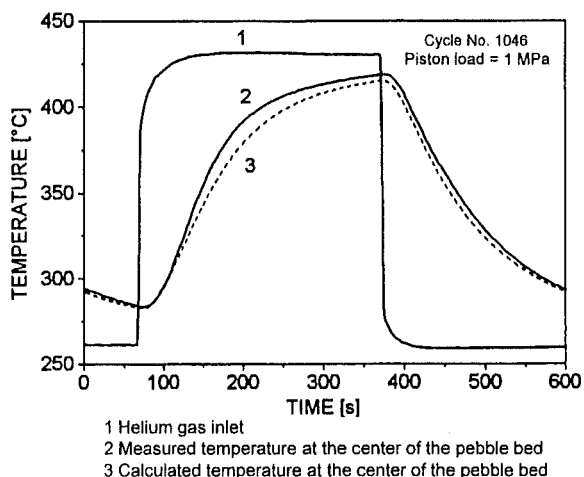3 Calculated temperature at the center of the pebble bed

Fig. 1: Calculated transient temperature profile (broken curve) during a cycle of the second HEBLO experiment

The test section applied for the third experiment at the HEBLO facility of IMF III represents a section of the first wall with a cooling plate and separate pebble beds of Be and Li_4SiO_4 pebbles according to the HCPB concept for the DEMO reactor and the DEMO test module in ITER. For the simulation of the internal heat sources, high-performance heating plates are fixed to the beds and the first wall.

The test insert is enclosed by a containment designed for an internal pressure of 80 bar. This containment has already been subjected to preliminary inspection by the TÜV.

On the basis of the IMF III designs, detailed drawings of the test facility were set up by a construction firm. In March 1997, the FZK central workshop was charged with the manufacture and assembly of two test inserts and a containment. The diffusion weldings required for the first wall and cooling plate components of the test section were performed successfully by KE Stuttgart.

An external firm has been charged with the construction of a special box on the FZK premises. Here, the pebble beds can be filled into the test section under controlled conditions and tight welding of the test section is accomplished.

For experimental simulation of the internal and external heat sources in the blanket, heating plates have been developed and optimized in preliminary tests. According to the concept selected, two resistance heating loops (conductor material NiCr 8020 with 4.5 Ohm/m, external diameter 2 mm) arranged in grooves shall be applied. The transition from the heating section to 4 mm thick cold conductors is located on the heating plate. To improve heat transfer, the grooves of the heating plate are filled with a nickel base brazing. This heating plate design was tested successfully at a surface power of about 30 W/cm² up to 900°C.

Costs have been estimated for the construction of an identical test section with containment for operation in the HEFUS-3 helium circuit of ENEA at Brasimone, Italy.

Staff:

M. Dalle Donne
K. Müller
P. Norajitra
D. Piel
G. Reimann
R. Ruprecht

B 3.3.4
## Help in the Detail Design of an In-pile Test Module

Within the European Blanket Program SCK/CEN Mol and ECN/IAM Petten carried out feasibility and cost studies on an HCPB Blanket Submodule Irradiation Test in the BR2 at Mol and the HFR at Petten, respectively. Forschungszentrum Karlsruhe supported this work by the definition of the objectives of this test, the elaboration of a conceptual design of the blanket submodule (see Fig. 1), a preliminary thermohydraulic analysis, and a comparative assessment of the concepts developed for both reactors.

The main conclusion from the assessment can be summarized as follows:

- Each reactor / concept has advantages and drawbacks; this requires careful trade-off.

- Main advantage of the BR 2 ist the large test space which allows the realisation of Be pebble beds of sufficient size, the inclusion of a FW, and of design provisions to obtain the desired mechanical behaviour of the submodule (e.g. stiffness, constraint).

- Main advantage of the HFR is the higher burn-up rate leading in combination with the larger availability of the reactor to significantly lower irradiation times.

- A general problem in both reactors is the selection of the power densities in the different materials: for steel and beryllium the power density is given by the Gamma flux and, hence, by the core position; the ratio of power densities in steel to those in beryllium is in general larger than in fusion plants.

- The power density in the ceramic material can to a certain degree be adjusted by the Li-6 enrichment, however this influences the burn-up rate as well. An adequate power density in the beryllium and the structural material in combination with a sufficiently high burn-up rate will lead to rather high power densities in the ceramic breeder material.

- The realisation of ITER-typical power cycles by cycling of the reactor power is probably not acceptable for the reactor operation. Furthermore, the shift between neutron and Gamma flux could affect the test result. A movable shield influences mainly the neutron flux, i.e. the power density in the ceramic material. The power density in the steel and beryllium will not be significantly reduced. Hence, the removal of the test section from the irradiation position seems to be the most attractive solution.

- The cost will be a decisive factor.

Staff:

M. Dalle Donne
S. Gordeev
St. Hermsmeyer
K. Schleisiek
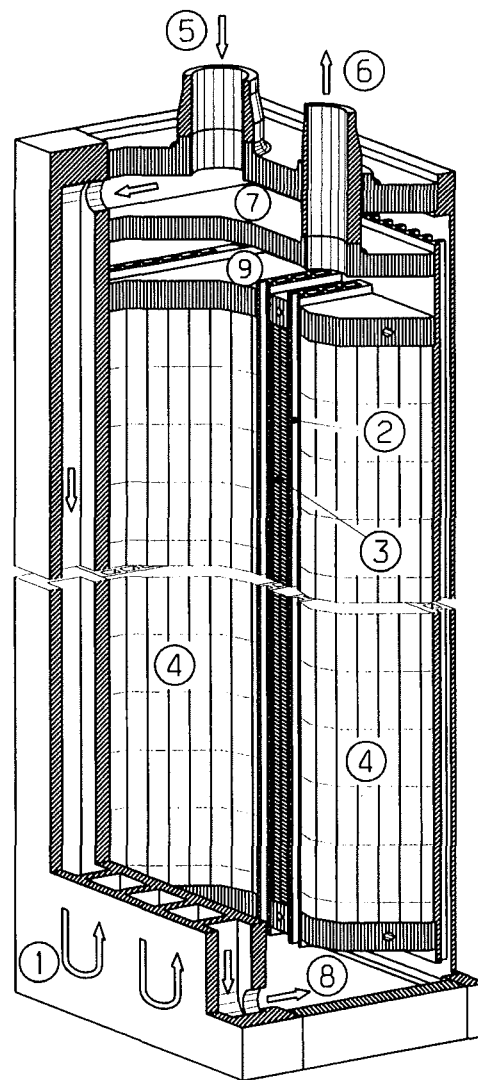
① First Wall
② Cooling Plate
③ Ceramic Breeder Pebble Bed
④ Beryllium Pebble Bed
⑤ Helium In
⑥ Helium Out
⑦ Inlet Header
⑧ Intermediate Header
⑨ Outlet Header

Fig. 1: Conceptual design of a HCPB blanket submodule for irradiation in the BR2

WP B 4
Tritium Control and Requirement for Permeation Barriers

B 4.1.1
Calculation of Tritium Permeation Losses from First Wall and Purge Gas System

Due to a number of technological properties and, first of all, to a low atomic number, beryllium will be used as plasma facing material in the ITER fusion reactor. Tritium control, including both the permeation through and inventory in the beryllium, is of great importance for the safety of the device. Experimental data have shown that, under ITER-like plasma conditions, the plasma facing surfaces of the beryllium develop high porosity (bubbles) and saturate, leading to a strong uptake of tritium and deuterium ions almost independent of the incident flux. At fluxes typical of ITER, surface erosion of beryllium should be also taken into account.

A computational model has been used with the computer code TMAP4 to reproduce the available experimental data concerning hydrogen ion implantation in beryllium. The obtained results refer to the first wall of the European Helium Cooled Pebble Bed Blanket (HCPB) Test Blanket Module (TBM-I) [1].

Tritium may get to the ambient by:

- injection from the plasma into the First Wall and then through permeation to the helium main coolant system;

- permeation from the tritium purging system through the pebble bed containing walls to the helium main coolant system;

- permeation from the helium main coolant system through the walls of the steam generators to the steam turbine cycle.

The permeation from the first wall is of great importance as it represents a great source of tritium contamination [2,3]. The presence of a protective layer of beryllium can strongly modify both permeation and inventory.

Fig. 1 shows a poloidal section of the Blanket Test Module with the local temperature distribution. Some main characteristics of this first wall design are briefly here put together:

- pulsed operation incident flux equal to $1.x10^{20}$ ions/m²xs with 1000 s pulses and 1200 s plasma dwell time;

- a 5 mm thick protective layer of beryllium for a first wall of MANET , a martensitic steel (10-11% Cr, 0.6% Mo, 0.65% Ni, 0,25% V and 0.15% Nb), initially foreseen for the DEMO reactor;

- a neutron load of 0.5 MW/m²;

- a maximal temperature in the first wall of 782 K.

Hydrogen plasma interactions with beryllium surfaces

A first approach to the topic of the tritium permeation through beryllium as plasma facing material for an ITER-like device was made in Ref. [2]. There it was assumed a low porosity (pitting) inside the beryllium during ion implantation. In comparison with the case of a recombination-limited model, the pits result in a reduction of permeation by more than a factor of three and an increase in the time delay to breakthrough by a similar amount [2,3]. This modelling technique involves the creation of a fictitious volume between the disturbed surface layer where the pitting occurs and the relatively undisturbed beryllium matrix

[4,5]. It resulted in a permeation of about 9 mg/d for the total FW surface of the Test Module of 1.2 m².

A good number of experiments [6-9] have shown a high release rate at the plasma facing surface of beryllium, caused by open porosity in the near-surface area. This suggests that retention and permeation through beryllium are controlled by mechanisms other than normal diffusion and surface recombination.

When hydrogen is deposited in Be by implantation, the hydrogen collects in bubbles, eventually growing to form interconnected porosities opening to the surface. Once such porosities open, there is virtually no more uptake of hydrogen. Implanting ions very quickly find a free surface where they recombine and return to the plasma. Damage caused by the incident ions is not confined to the implantation zone but extends several micrometers deeper, propagated apparently by the diffusion and agglomeration of defects. Most hydrogen in ion-implanted Be resides in bubbles and exists in the molecular form. A smaller amount is combined with vacancies and impurity inclusions such as oxides. Another interesting experimental observation is that gas pressure in the bubbles is almost equal to the yield strength of the material. Under the here considered plasma conditions, it appears that when the implantation layer has become saturated, essentially all of the implanting flux returns to the upstream face through the cracks and open porosity that develops. Hence the relative independence on implantation flux [10].

Moreover, under ITER-like plasma conditions beryllium erosion should be taken into account in any dynamic modelling of the process.

Computational method and results

The one-dimensional computer code TMAP4 [11] has been used for computations referring to the TBM-I design.

The 5mm thick coating layer of beryllium was modelled as three segments in series, Fig. 2. The first 50 nm thick segment represents the implantation region, i.e. where the bubbles are. It was assumed that they are as a trap concentration of 8% and a trapping energy of 2.2 eV, i.e. the formation enthalpy for diatomic hydrogen molecules. Experimental data [6,7] observed molecular hydrogen saturation already at 6.5%.

A second region, 1 μm thick, represents a zone of damaged beryllium influenced by the bubbles, characterised by a 0.1% trap at 0.95 eV. In the remaining part of undisturbed beryllium the traps concentration amounts to 0.06% at 0.95 eV trapping energy.

Bubbles generated by hydrogen implanting into beryllium agglomerate and move to grain boundaries where they coalesce to form surface-connected porosity. This results in a saturation effect that limits the entry of further hydrogen into the beryllium. Once porosity develops, the driving potential for diffusion to the bulk is the gas pressure in the bubbles, which is temperature dependent. Bubble pressure at the saturation reaches approximately the value of the material yield strength, given by:

$$S_y = \frac{355 \; MPa}{1 + 0.0012T + (T/950)}$$

To accommodate the saturation effects on the plasma side of beryllium, the recombination coefficient has been modified, thus allowing a recombination-like boundary condition in the TMAP4 input file.
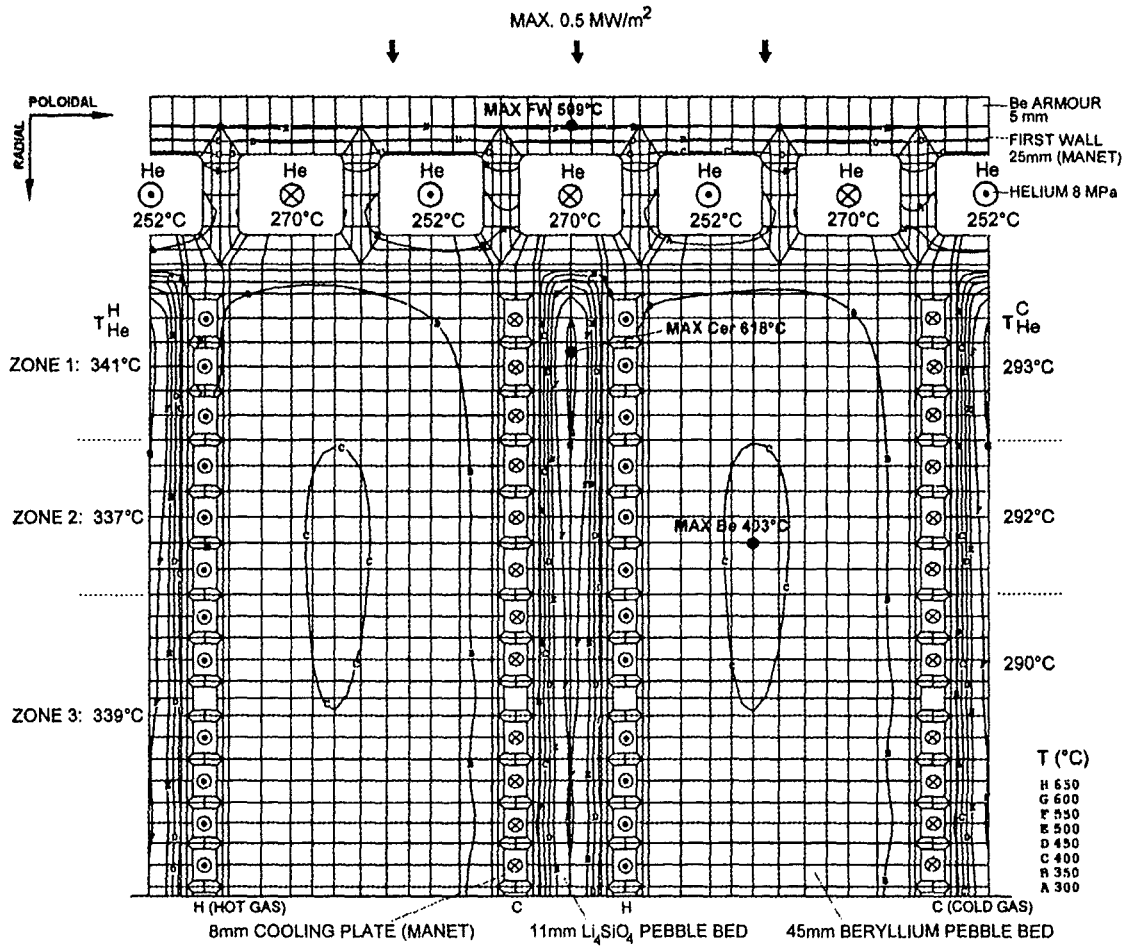
Fig. 1: Temperature distribution in TBM-I
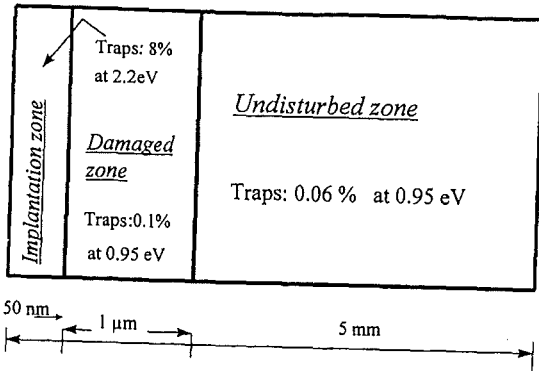
Fig. 2: Structural assumed in modelling beryllium layer

The resulting equation for K_r, which grows exponentially when the surface concentration reaches the saturation level, is:

$$K_r = \left[3.4E - 29 \exp\left(\frac{-0.28eV}{kT}\right) \right] x \left[1 + \exp\left(\frac{20n_0}{n_{sat}} - 1\right) \right] + \frac{u}{1+n_0} \quad \left[\frac{m^4}{s} \right]$$

The first term in brackets is the Hsu-Andrew-Causey value [10], the second one accomplishes the exponential growth where n_{sat} is the concentration saturation value and n_0 the surface mobile

concentration; the third one finally takes into account the loss of hydrogen due to surface erosion.

The term n_{sat} has been defined in two ways. The first one as product of the solubility and the square root of the material's yield strength, where for solubility the Shapolov-Dukel'ski value [9] has been used:

$$S = 2.176E + 22 \exp(-0.17eV/kT) \quad [at/m^3 Pa^{1/2}]$$

A better interpolation of available experimental data [6-8] is given by the following dimensionally inconsistent expression:

$$n_{sat} = \frac{S_y^{1/2}}{D} (\phi\partial)^{2/3}$$

where S_y is the yield strength in MPa, ϕ is the ion flux to the surface in ion/m^{2}s and δ is the implantation depth in m.

For diffusivity D Abramov's „extra-grade" value has been used for the first segment; the „high-grade" value for the rest of beryllium [12].

Erosion due to sputtering results in a diffusion in a moving coordinate system. The diffusion equation used for atom flux J_i through the matrix of beryllium is:

$$J_i = -D\left(\nabla n_i + \frac{n_i Q^*}{kT^2} \nabla T \right)$$

where D is the diffusivity, n_i the concentration of atoms, k is Boltzmann's constant, T is the temperature and the second term in parentheses accounts for the Soret effect [13], i.e. the mass transport due to a temperature gradient, characterised by the heat of transport Q^*. Neglecting Q^* for beryllium, we can use the relation:

$$\frac{DQ^*}{kT^2} \nabla T = u$$

where u is the face erosion velocity assumed equal to:

$$u = \frac{\phi \eta}{N}$$

being η the sputter coefficient (taken as 3×10^{-3}) and N the lattice concentration, Fig. 3.
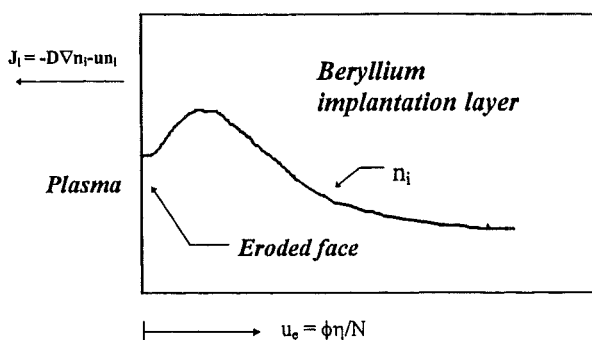

Fig. 3: Modelling of surface erosion in TMAP4

Erosion was included only in the damaged zone. The reduction of the beryllium thickness, leading to a lower inventory and higher permeation, was accounted for by an iterative procedure.

Total operational time was given as 6×10^6 seconds, i.e. about 70 days. For the assumed first wall surface of 1.2 m^2 and the whole operating period, a permeation of about 0.007 g has been obtained. This very low permeation is not appreciably influenced by the use, instead of MANET, of a ferritic steel like T91.

Permeation from the purge flow system

The major contribution to the permeation is represented by the tritium coming from the lithium orthosilicate beds (Li_4SiO_4), as the permeation from the beryllium bed is negligible.

The procedure illustrated in [2,3] has been also applied to the TBM-I design [1]. The smaller tritium production and the lower wall temperatures in comparison to the DEMO design lead, for a total permeating surface of 10 m^2, to a tritium permeation of about 0.3 mg/d.

Conclusion

With a coating layer of beryllium, the permeation through the first wall is strongly reduced, so that it can be neglected. As far as the permeation is concerned, the choice of the steel to be used together with beryllium does not play an important role.

What remains to be modelled is the influence of carbon on the retention and permeation of beryllium-clad surfaces. There are no many data available about how much of the carbon that will be sputtered from high-heat-flux surfaces in the divertor will be

transported to the main plasma chamber and end up on the first wall, where carbon film build-up should not be a problem.

The hydrogen implantation in the first wall seems in any case to be significant at depths, that result in development of the described open porosity.

Literature:

[1]   FZKA 5891, Design Description Document, HCPB Test Blanket, Dec. 1996.

[2]   L. Berardinucci, M. Dalle Donne, Proc. of 19th SOFT, Lisbon, Portugal, Sept. 16-20, (1996) 1427-1430.

[3]   FZKA 5858, Nuclear Fusion Project, Annual Report, Jan. 1997

[4]   D.F. Holland, G.R. Longhurst, Fus.Tech. 8 (1985) 2067-2073.

[5]   R.A. Anderl et al., INEL, IEEE (1986), 644-649

[6]   M.I. Guseva, A. Yu. Birukov, V.M. Gureev, L.S. Daneljan et al., J. Nucl. Mat., 233-235, (1996) 681-687.

[7]   V.N. Chernikov, V.Kh. Alimov, A.P. Zakharov et al., J. Nucl. Mat., 233-237, (1996) 860-864.

[8]   A.A. Haasz and J.W. Davis, Proc. 12th Int. Conf. On Plasma Surface Interactions in Contr. Fusion Devices, St. Raphael (1996).

[9]   V.I. Shapovalov and Yu.M. Dukel'ski, Russian Metallurgy, 5, (1984) 201-203

[10] R.A. Causey, K.L. Wilson, Journal of Nuclear Materials, 212-215, (1994) 1436-1442

[11] G.R. Longhurst et al., TMAP4 User's Manual, INEL, EGG-FSP-10315 (1992).

[12] E. Abramov et al., CFFTP-G-9013, Canadian Fusion Technology Project, Mississauga, Ont., Canada (May 1990).

[13] G.R. Longhurst et al., J.Nucl.Mat., 131 (1985) 61-69.

Staff:

L. Berardinucci

B 4.2.1
Manufactoring of Test Section for Tritium Permeation Experiments

Tritium permeation from the helium coolant through the steam generator must be restricted to very small values. The essential measure to achieve this is the addition of H_2 and H_2O to the coolant.

During the report period the test facility was modfied by the installation of an open gas system (Argon flow with a defined H_2 addition and saturating the gas mixture in an oxalic acid humidifier, kept at temperatures below 0°C). First experiments with INCOLOY 800 specimens showed drastic reductions in the permeation rate, as shown in more detail in the JRC/Ispra contribution on Substask B 4.2.2.

Staff:

A.Perujo (JRC/Ispra)
J.Reimann (FZK)

WP B 5
Tritium Extraction and Helium Purification

B 5.1.1
Design of Helium Purification and Tritium Extraction Systems

The gases to be processed in the Helium Purification System and the Tritium Extraction System of an ITER HCPB Test Blanket Module (TBM) are characterized by the following conditions:

- Relatively large helium gas flow rates,

- Hydrogen concentrations of 10 - 1000 ppm,

- Tritium concentrations of $\leq$ 3 ppm, with two main chemical forms of tritium, i.e. HT and HTO,

- Concentrations of impurities and activation products in the range of $\leq$ 5 ppm.

Although these extreme conditions have been considered in the process selection for tritium extraction and helium purification, it is necessarry to demonstrate the feasibility of the main process steps in a technical scale.

For this aim, a small Pilot Plant is being designed to be operated in the FZK Tritium Laboratory. The objectives of the investigations to be carried out with this facility are:

a) to test and to improve the design of the main components, i.e.

 • Cold trap for H_2O / HTO removal at $\leq$ -100°C

 • Molecular sieve bed for removal of H_2 / HT and impurities at -195 °C

 • Precious metal reactor for H_2 / HT oxidation;

b) to develop methods for process control;

c) to test and improve procedures for quantitative measurement of very small residual concentrations of hydrogen, water vapor, and impurities in the presence of tritium and activation products.

The process parameters of the Pilot Plant are shown in Table 1 in comparison with those forseen for the ITER HCPB Test Blanket Module (TBM). A flow sheet of the FZK facility is shown in Fig. 1.

A modular design principle has been chosen to allow a stepwise installation and to carry out tests with single components as well as integral tests with all components. Four modules are foreseen for the following tasks:

Modul 1: Main gas loop including gas supply, buffer vessel, circulator, equipment for quantitative gas analysis and tritium activity measurement at the loop inlet

Modul 2: Oxidizer unit and analytic instruments to measure residual (excess) oxygen and humidity

Modul 3: Cold trap, humidity sensor, tritium monitor

Modul 4: Molecular sieve bed, analytic instruments to measure all residual gas components, tritium monitor.

Table 1: Comparison of Process Parameters

	ITER TBM	Pilot Plant
Purge Gas System:		
Gas flow rate (Nm³/h)	17	3 - 5
Pressure (MPa)	0.1	0.1
Partial pressures (Pa)		
p (H_2)	100	20 - 100
p (HT+HTO)	0.3	0.1 - 0.5
p (H_2O)	$\approx$ 0.2	0.1 - 5
Coolant Purification System:		
Gas flow rate (Nm³/h)	37	3 - 5
Pressure (MPa)	8	0.1
Partial Pressures (Pa)		
p (H_2)	62	20 - 100
p (HT)	0.5	0.1 - 0.5
p (H_2O + HTO)	35	10 - 50
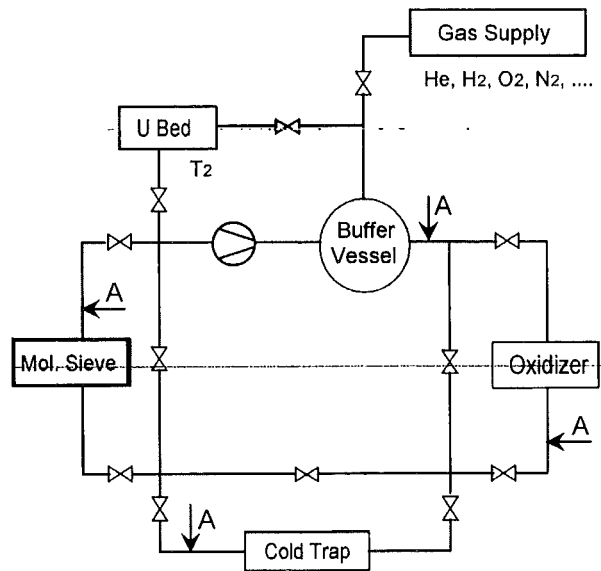
A = Points for Gas Analysis and Activity Measurement

Fig. 1: Flow sheet of the Pilot Plant

The gas supply includes an evacuation system for the entire loop, gas cylinders for He, H_2, O_2, N_2, and mass flow controllers for each type of gas. Tritium is supplied from an uranium getter bed. Humidity will be produced and added to the gas in the oxidizer unit; if this unit is not available at the beginning of the test series, a moisture generator will be added to the gas supply system described above.

It is important that the gas composition at the outlet of the buffer vessel remains constant during an experiment because otherwise it would be very difficult to study the time dependent behavior of the main loop components.

Staff:

H. Albrecht
E. Hutter

WP B 6
Demonstration of Blanket Safety

B 6.1.1
Safety Approach for TBM and DEMO

The safety considerations of the helium cooled pebble bed (HCPB) blanket focused on the accidental safety aspects of the test blanket module (TBM) to be tested in a horizontal port of ITER. The effort was on four points: (1) Identification of causes and accident description, (2) thermal-hydraulic transient analysis during postulated accidents with the system code RELAP5/Mod3.1 and Mod3.2, (3) one-dimensional long term decay heat transport to the vacuum vessel and in-vessel components, and (4) bounding estimates for potential chemical Be/air and Be/steam reactions in the TBM pebble beds. The analysis is based on the neutronics calculations for the TBM and on the helium cooling system layout, both described in section B2.1.1. A summary to the four points is given below.

Identification of causes

Two reference events associated with the HCPB TBM system were found to be the most demanding occurrences with respect to the potential release of radioactive material (in particular tritium) into the ITER containment, i.e., an in-vessel TBM coolant leak and an ex-vessel TBM coolant leak. These two Primary Initiating Events (PIE) need to be considered in different variants or in combination with a set of postulated aggravating occurrences that could be triggered by the PIE. The following event sequences were defined to be studied in detail for the final Design Description Document (DDD) for ITER, considering cases 1a and 2a as the reference initiating events and the cases 1b, 1c, 1d, and 2b, 2c, 2d, respectively, as parameter studies thereof.

1. Large in-vessel TBM coolant leak

    a) First Wall (FW) failure as primary initiating event (PIE)

    b) PIE plus pebble bed Be/steam chemical reaction

    c) Large leak inside module

    d) Small leak inside module

2. Large ex-vessel TBM coolant leak

    a) Main pipe failure in the pit as PIE

    b) PIE plus subsequent failure of FW

    c) PIE plus large leak inside module

    d) PIE plus subsequent failure of FW when reaching a surface temperature of 1150 °C

Thermal-hydraulics analysis with RELAP

The performance of the TBM during normal operation and accidents was investigated in two phases. The first phase of the studies was based on an earlier version of the helium cooling system layout [1] which was originally supposed to be located in the tritium building [2], leading to large components and coolant inventory. Later in the development ITER requested to relocate the cooling system to the wedge-shaped pit close to the cryostat. This implied a number of modifications in the layout, affecting almost all safety relevant data of the helium cooling system, while keeping the basic concept unchanged. Hence, a second phase of thermal-hydraulic analyses was performed for the revised system.

In the first phase four accident families were studied in a parameter analysis: (a) loss of flow accidents (LOFA), (b) loss of coolant accidents (LOCA), (c) leak inside test module accident (LEAK), and (d) loss of heat sink (LOHS). In addition,

the performance during normal pulsed operation was studied. The following conclusions were drawn from this screening analysis which, in essence, apply to the revised system as well. (Analyses for the second phase with regard to the accident sequences identified above are still in progress.)

Steady state and pulsed operation: Due to the strong radial gradient in heat generation in the TBM, adjustment of the helium mass flow rates in individual channels of the cooling plates is necessary to achieve equal helium temperatures at the outlet. The analysis showed, that the adjustment can be accomplished by orifices at the inlets to the cooling channels. However, very small orifice openings are needed in part which are susceptible to plugging and could lead to local overheating. The analysis of the test module during pulsed ITER operation revealed, that the TBM temperatures can follow the power cycles with acceptable delay. No heat-up of the TBM takes place with increasing numbers of cycles. Hence, the chosen temperature control scheme by division of the helium flow on the heat exchanger (HX) and on a bypass was found to be effective.

Loss of flow accidents: A loss of power supply to the circulators without plasma shutdown will lead to failure of the FW within about 30 s. The maximum temperature excursions in the TBM in cases with normal plasma shutdown, i.e. ramp-down within 100 s, would also be above the acceptable margins. However, they show a strong dependence on the shutdown delay time and on the circulators moments of inertia as illustrated in Fig. 1. Short delay times (up to 3 s) and large circulator moments of inertia are effective means to minimise temperature overshoots. The long term heat removal is assured by the natural circulation if the water conditions on the secondary side remain unchanged. Even at a geodetic level difference between the TBM and the HX of 0.5 m the natural circulation is sufficient to provide for decay heat removal. A total loss of flow in both TBM cooling loops due to inadvertent valve closures would lead to an unlimited temperature increase in the TBM calling for fast shutdown to prevent failure of the FW within the first 100 s. After the shutdown has occurred, the time span for other countermeasures extends to 4 - 8 h.
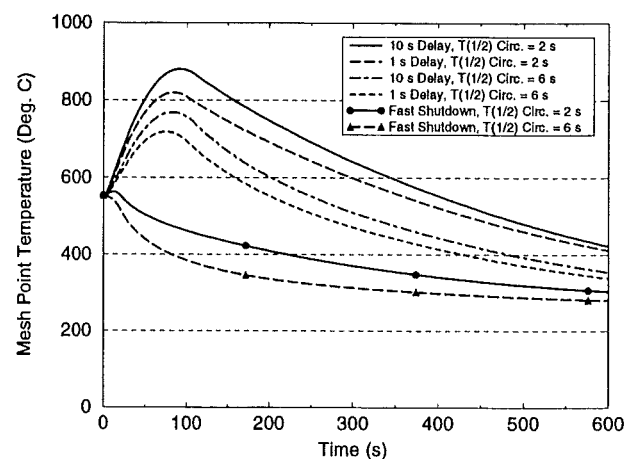
Fig. 1: Temperature evolution in FW after a LOFA in both loops at various shutdown parameters

Loss of coolant accidents: The simultaneous double-sided break of the hot-leg pipes in both TBM cooling loops leads to depressurization of the cooling circuits within about 2 s. The sudden expansion of the coolant leads to intense cooling of the structure, which involves the risk of cracks. An in-vessel loss of coolant will cause plasma termination and pressurisation of the vacuum vessel. However, the equilibrium pressure after drain of both cooling loops is two magnitudes below the design pressure of the vacuum vessel. The decay heat of the TBM can

be rejected by forced circulation in one of the cooling loops even at the low equilibrium pressure level of 20 kPa.

Leak inside test module accidents: A leak inside the test module from the cooling channels into the pebble beds leads to a moderate pressure decrease in the cooling system and pressure build-up in the tritium extraction system. Continuous power load on the TBM in conjunction with the reduced helium throughput in the circuits causes a structural temperature rise in the TBM until a new steady state temperature profile has developed. The temperature rise in the FW will be of the order of 60 °C with the old cooling system layout. Meanwhile it has been decided to provide for fast isolation of the tritium extraction system and for pressure relief for the TBM box, the consequences of which need to be determined.

Loss of heat sink accidents: A total loss of the heat sink will lead to an unlimited heat-up of the TBM and its auxiliary systems. Without plasma shutdown failure of the FW is expected to occur within the first 600 s. With plasma shutdown it will take several hours until the critical FW temperature is reached. A total loss of flow on the secondary side will lead to heat-up and evaporation of the secondary cooling water. Yet, the heat sink remains available at an elevated temperature level as long as the evaporation process takes place which lasts for many hours. Even in case of combined loss of flow on the secondary side and a loss of circulator power on the primary side the natural circulation flow is strong enough for decay heat removal. The decay heat generation is not intense enough to evaporate considerable quantities of water in the HX.

Passive decay heat dissipation

A frequently discussed problem in blanket safety is the question, whether in case of a complete loss of convection cooling in the TBM (or in the blanket in general) the decay heat can be dissipated by thermal conduction and radiation to an ultimate heat sink at tolerable temperature levels. To analyse this problem, a 1D heat transport model for the TBM has been set up. It represents a radial unit cell cylinder cut out of the TBM from the FW all the way through the breeding zone, manifold region, support structure, up to and including the 0.48 m thick radial shield. The model includes thermal conduction, radiation across elements with high void fractions, and radiation from the bounding surfaces at both ends to the environment. The material data assigned to each node are lumped values for material mixtures, i.e., the specific heat is derived as the mass-weighted mean, and the thermal conductivity is taken as the volume-weighted mean pertaining to each node.

Fig. 2 shows as example the decay heat driven temperature evolution in the 22 nodes over a period of 12 days after a large in-vessel coolant leak accident (case 1a). The temperature in the front nodes peak at a few hours after the accident, reaching a quasi equilibrium state after two days. The following stable phase is dominated by the heat, the TBM receives at the plasma facing surface from the tokamak FW which is assumed to be at 400 °C. As soon as this temperature is reduced to 200 °C (which was arbitrarily assumed to occur after 10 days) the TBM temperatures decay further. This example teaches four results: (1) The temperature overshoot during passive decay heat removal is moderate (<80 K) and lasts for a few hours only. (2) The temperature in the breeding zone, where the beryllium pebble beds are prone to chemical reactions, stay essentially below 400 °C. (3) The actual temperature evolution is, besides the decay heat, strongly influenced by the boundary conditions. (4) For the HCPB TBM under ITER specific boundary conditions passive decay heat removal can be demonstrated.
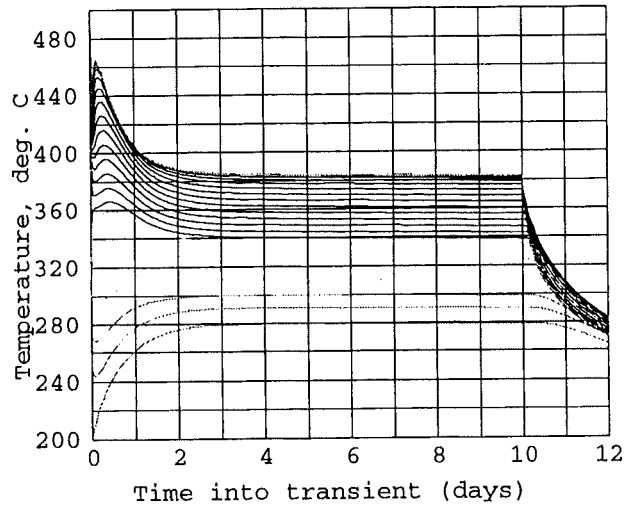

Fig. 2: Decay heat driven temperature evolution in the TBM after LOCA (1D model with 22 radial nodes from FW (top curves) to shield (bottom curves))

Chemical reaction of beryllium pebbles

The accident scenarios 1b and 2b entail steam or air, respectively, entrainment into the beryllium pebble beds which expose a large surface to the reactant of typically 8 m² per kg of beryllium. Therefore bounding estimates have been performed on the potential heat and hydrogen production in the TBM based on reaction rates specified in the safety analysis data list (SADL-2) of ITER. An extremely pessimistic assumption has been adopted: There is unlimited access of steam or air to the entire TBM beryllium pebbles (450 kg) which are at a uniform temperature. The resulting hydrogen production rates in case of a Be/steam reaction, and the chemical heat for a Be/steam and Be/air reaction are plotted as function of the reciprocal absolute temperature in Fig. 3. For comparison, the decay heat range of the TBM in the time span of 1 hour to 1 day after shutdown is indicated.
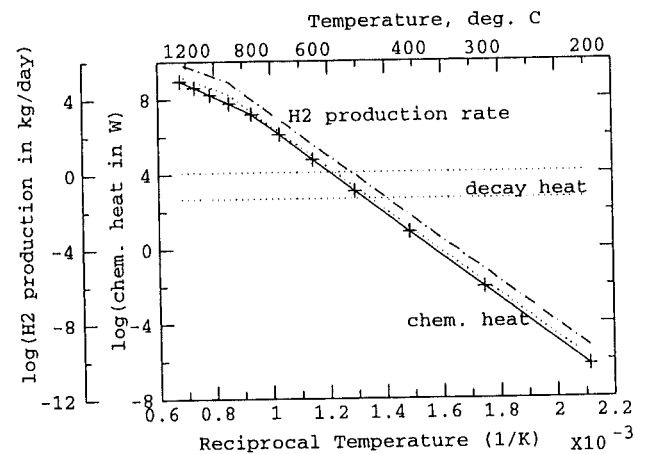
Fig. 3: Chemical reaction rates of TBM beryllium pebbles (solid: heat for Be/air, dotted: heat for Be/steam, dashed-dotted: Hydrogen for Be/steam, horizontal band: TMB decay heat

The following results are obtained. The temperature limit for the beryllium pebbles to become safety relevant in terms of heat and hydrogen generation in case of steam or air ingress is about 500 °C. At this temperature the hydrogen production rate from a Be/steam reaction would be of the order of 1 kg per day. The chemical heat would amount to about 1.2 kW for Be/air and

1.8 kW for Be/steam reaction. This is of the order of 20 % of the total decay heat the TBM produces a few hours after shutdown (when the maximum temperature in the TBM will be reached during passive decay heat dissipation as shown above). The beryllium burn rate at 500 °C would be less than 1 % of the initial inventory per day. At a more realistic temperature level of less than 400 °C instead of 500 °C all reaction rates would be reduced by at least two orders of magnitude and, hence, become uncritical.

Literature:

[1] K. Gabel, K. Kleefeldt: Thermal-hydraulic analysis of the helium cooled pebble bed test blanket module for ITER during normal operation and accidents, FZK report to be published.

[2] M. Dalle Donne, L. V. Boccaccini et al.: European helium cooled pebble bed (HCPB) test blanket, FZKA 5891.

Staff:

K. Gabel
K. Kleefeldt

WP B 7
Demonstration of Blanket Reliability

B 7.1.3
Contribution to Common Blanket System Data Base

This Subtask is connected with the Subtasks B 7.2.2 and A 7.1.3. All data used there will be taken as basis for the common data base. Availability analysis is subjected to large uncertainties. They are due to the facts that system design is still in progress and the data base is insufficient. In general, however, it must be pointed out that the data base will remain a problem, especially when prototype components are concerned and high reliability is required. The use of the same data base for different design options and test module concepts also allows to limit error sources by avoiding differences resulting from various data.

The results of a testing programme on EB welding and non-destructive evaluation of a specific EB weld in the First Wall led to the conclusion that a flaw size of about 0.5 mm can be detected [1] and that this sensitivity should also be possible for other welds of comparable size while an exact sizing of flaws is more difficult to obtain. Additional investigations based on TIG welding [2] support that a 50% detection probability of flaws with a size of 0.5 mm seems to be appropriate. Scatter in non-detection probability may reflect more or less difficult testing situations.

Together with results of a previous study which showed that residual stresses play a negligible role after welding, but may influence hot cracking during the welding process [3], these findings can be used to assess the reliability of welds based on non-detection-probability of flaws and the flaw size distribution together with the design stresses of the component. Results may supplement the database which is currently being used for availability predictions.

Literature:

[1] K. Gemmer-Berkbilek, Arbeitsprogramm zur quantitativen Bestimmung von Schweissfehlern in EB-Doppelschweiss-naehten mittels Ultraschall - Teil B "Quantitativer Testfehler-nachweis", SIEMENS Report No. KWU NW-P3/96/058, 1997.

[2] R. Girardier, H. Lüscher, FZ Karlsruhe-DEMO-Fusionsreaktor Schweiss- und Prüfversuche zur Ermittlung der optimalen Parameter, SULZER INNOTEC Report No. VTW TB 96.006, 1997.

[3] L. Cizelj, H. Riesch-Oppermann, Stresses in the First Wall of a Dual-Coolant Liquid-Metal Breeder Blanket During Electron-Beam Welding, Fusion Technology 32 (1997), 14-22.

Staff:

H. Schnauder
H. Riesch-Oppermann

B 7.2.2
TBM System Availability

The availability/unavailability had been investigated for the HCPB ITER Test Blanket Module (TBM) including the supply pipes and the He-cooling loops. The fault tree methodology was applied. It comprises the definition of the system, break down of the system into components (e.g., pipes, blowers, valves, heat exchanger, etc.) and subcomponents (e.g. welds of different types, bends, tube sections, etc.) defining the TOP event and designing the related fault tree, assigning failure rates to components and subcomponents, estimating repair or replacement times for components, and finally computing the unavailability, that is the occurrence probability of the TOP event. The TOP event is defined as the case, that the system under considerations is unavailable (in the sense that the plant must be shut down) on demand. The most critical point in the analysis are the failure rates and the mean time to repair (MTTR). The data base established during the blanket selection exercise has been adopted [1]. A repair of the TBM system in the vacuum vessel is not envisaged. For repair and/or exchange of a defective component, a time of two to eight weeks is proposed. This time must be seen in connection with the entire remote handling concept. At the moment, it is difficult to asses appropriate values for the MTTR. Therefore the results are given in parametric form as a function of the MTTR. By an additional Monte Carlo simulation the impact of a statistical variation of the components overall unavailability has been analysed.

The basis for the unavailability analysis is the HCPB-TBM as described under Task B 2.1.1. Design modifications performed since the last annual report are taken into account. The principal configuration consisting of blanket box, cooling plates, pebble beds, manifolds, the He-cooling loops and the purge gas system up to the tritium recovery system (TRS) and the coolant purification system (CPS). TRS and CPS are excluded in the analysis. They are placed in the tritium building away from the pit behind the ITM, which lets expect a similar low unavailability as obtained for DEMO.

■...*Test module without FW,* ▲...*Test module incl. FW,*
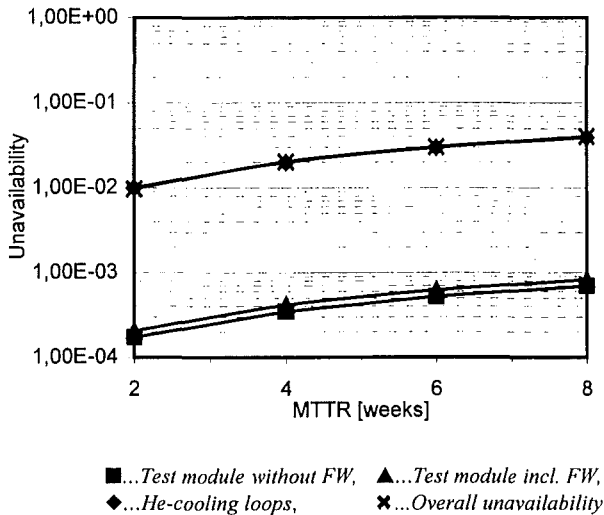◆...*He-cooling loops,* ✖...*Overall unavailability*

Fig.1: Unavailability of the HCPB ITER Test Blanket Module (TBM)

The results are given in Fig. 1. The lowest curve shows the test module without the FW part, while the next higher curve includes the FW. The unavailability of the He-cooling loops dominate the overall unavailability. Dependent on the MTTR the unavailability for the He-cooling loops varies between 1.0×10^{-2} and 3.9×10^{-2}, whilst the overall unavailability varies between 1.02×10^{-2} and 4.0×10^{-2}. This equals an availability between 99

and 96%. The unavailability of the test module is nearly two orders of magnitude lower than that of for the He-cooling loops. The calculated failure rates and the contribution to the overall unavailability the test module including He-cooling loops are given in Tab. 1.

Table 1: Calculated failure rates for the main components and percentage of the overall unavailability of the test module including the He-cooling loops

Description	Calculated component failure rate [1/h]	Percentage of the overall unavailability [%]
Test module	6.2×10^{-7}	2
Pipes, Bends, Heat exchangers, Welds	6.1×10^{-7}	2
Valves	4.0×10^{-6}	13
Circulators	2.0×10^{-5}	65
Dust-filter	5.6×10^{-6}	18
Total	3.1×10^{-5}	100

This table contains also the calculated failure rates. The individual contribution to the overall unavailability is valid for all MTTR considered. The highest influence on the overall unavailability comes from the circulators (65%), the next lower from the dust-filter (18%) and from the valves (13%). Compared to the He-cooling loops, the contribution of the test module of 2% can almost be neglected.

The impact of a statistical variation of the components unavailability on the overall unavailability has been analysed by a Monte Carlo simulation. Taking the components from Tab. 1, and assuming (pessimistically) an error factor of 10 for each component, yields to an overall error factor of about 4.4. This means, the result of 8 weeks repair/down time varies between $U_{0.05} = 6.0 \times 10^{-3}$ and $U_{0.95} = 1.2 \times 10^{-1}$ and in case of two weeks repair/down time between $U_{0.05} = 1.5 \times 10^{-3}$ and $U_{0.95} = 3.1 \times 10^{-2}$. $U_{0.05}$ and $U_{0.95}$ are the 5% and the 95% confidence limits, respectively. That means 90% of all possibilities that in a lognormal distribution are within these limits.

Literature:

[1] H. Schnauder, C. Nardi, M. Eid, Comparative availability analysis of the four European DEMO blanket concepts in view of the selection exercise, Fusion Engineering and Design 36 (1997) 343-365

Staff:

H. Schnauder

WP B 8
Development of Ceramic Pebbles

B 8.1.1
Development of Li_4SiO_4 Pebbles

The reference breeding material for the Helium Cooled Pebble Bed (HCPB) blanket are slightly overstoichiometric lithium orthosilicate (Li_4SiO_4 + 2.2wt% SiO_2) pebbles, which are fabricated by the firm Schott Glaswerke by melting and spraying with a gas jet. The pebbles are placed in the blanket in the gap between two cooling plates, and helium flows through the bed carrying away the produced tritium. To have an high filling it is necessary to have pebbles smaller than 1 mm, however, to avoid too large pressure drops in the helium purge flow the pebbles should not be too small. The chosen diameter range is 0.25-0.63 mm.

In the optimization of the Li_4SiO_4 pebble fabrication a small quantity of TeO_2 has been added to the overstoichiometric lithium orthosilicate. On the basis of first tests in air at room temperature it was expected that this would improve the thermomechanical behaviour of the pebbles quite considerably: a higher crush strength at room temperature and a lower scattering band in this property has been obtained (see also B 8.3.1). In order to release the stresses caused by the fast cooling during the spraying operation the pebbles had to be annealed before being used, and the optimization of the annealing operation has been performed by the firm Schott. As result an annealing at a temperature slightly lower than 1000 °C has been adopted. Fig. 1 shows a picture of the pebbles obtained by scanning electron microscopy.
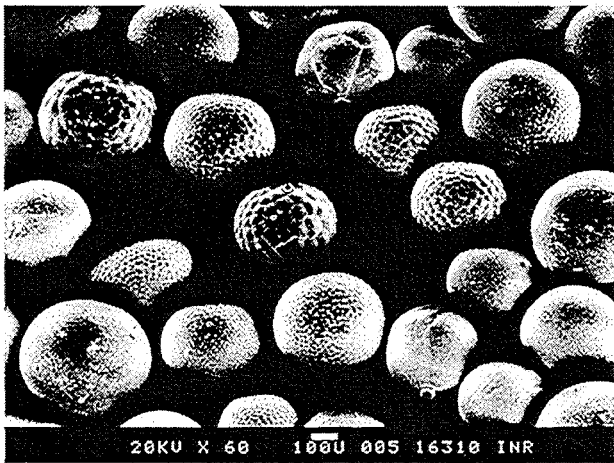

Fig. 1: Li_4SiO_4 pebbles with tellurium

Phase studies on SiO_2 and TeO_2 doped Li_4SiO_4

The overstoichiometric lithium orthosilicate pebbles with TeO_2 have been analyzed with X-ray diffraction and X-ray microanalysis to study the phases present in the material before and after the annealing at temperature slightly lower than 1000 °C.

The tellurium concentration in not annealed pebbles was constant across the radius. After annealing a three-phase microstructure was observed with $Li_4(Te)SiO_4$ and $Li_2(Te)SiO_3$ with 1.8 and 3.2 wt% TeO_2 respectively, both having reduced unit cell volumes compared to undoped Li_4SiO_4 and Li_2SiO_3. X-ray diffraction of the third phase gave indication of the formation of Li_2TeO_3 , however quantitative X-ray microanalysis was not possible.

In order to explore the pseudo-ternary Li_2O - SiO_2 -TeO_2 system the isothermal section at 700 °C under inert atmosphere was

established. A three-phase field Li_4SiO_4 - Li_2SiO_3 - Li_2TeO_3 exists. The latter phase crystallises in a monoclinic structure and melts at 725 °C. DTA (Differential Thermal Analysis) results on the pseudo-binary Li_4SiO_4 - TeO_2 section reveal a maximum solubility of 1.6 wt% TeO_2 in Li_4SiO_4. In case of higher TeO_2 quantities a three-phase field is formed Li_4SiO_4 - Li_2SiO_3 - Li_2TeO_3. Isothermal annealing of these phases at 700°C and 960°C under inert atmosphere produced an abundant tellurium metal sublimate of black colour, whereas in air a white lithium tellurate (VI) sublimate in less amounts was observed.

Thermomechanical behaviour of Li_4SiO_4 pebble beds

Tests under blanket-relevant conditions have shown that long time high temperature annealing (600 °C - 800 °C) in helium atmosphere produces evaporation of relatively high portions of the tellurium content. Therefore it has been decided to go back to the previous solution without tellurium. There is a large data base for this material, and rather recent long term annealing tests showed a very similar behaviour of the two materials (with and without tellurium) in regard to room temperature crush loads as well the scattering band. Furthermore there are indications that the strength of a single pebble at room temperature is not really representative for the behaviour of a pebble bed at blanket temperatures. Therefore tests were initiated where the deformation of a typical pebble bed under constant temperature/constant pressure is measured. There are indications that the mechanical load on the breeder pebbles is reduced: a) at lower temperature by some relocation of pebbles under pressure, and b) at higher temperatures by some plastic deformations in the hotter middle zone of the breeder bed. These results have to be confirmed by further tests over a larger range of parameters, but it seems that the strength of the pebbles without tellurium will be high enough for the realistic loads. The other advantages obtained with tellurium [a small increase of the thermal shock resistance (from 68 to 70 °C/s), a small decrease of the pressure drop in the purge gas flow caused by the breaking of some pebbles during thermal cycle operation (from 0.15 to 0.125 bar), the probable decrease of the total ceramic tritium inventory from the value of 30 g for the case with Li_4SiO_4 + 2.2wt% SiO_2] are not considered essential.
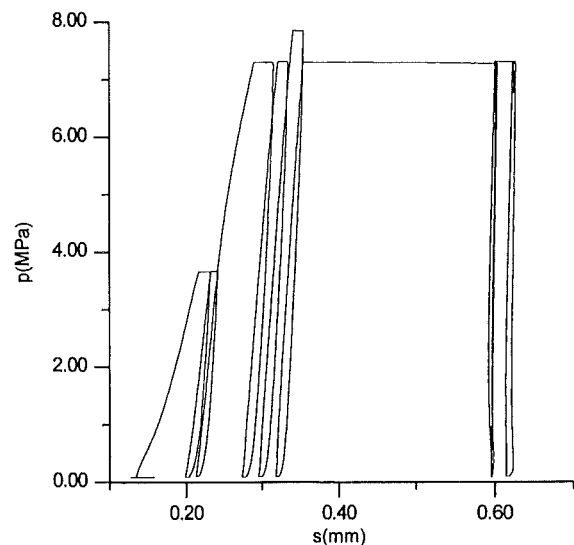

Fig. 2: Experiment at 760°C, pebble bed heigth 13.2 mm

The thermomechanical behaviour of Li_4SiO_4 pebble beds was investigated at pressures up to 8 MPa and temperatures up to 850°C. The pebble beds were axially loaded in cylindrical

containers and the axial deformation was measured. At ambient temperature T_a, additional experiments were performed with glass spheres with a similar diameter distribution.

At T_a, the characteristic pressure-deformation-curves and Young's modulus are very similar for both granular materials. At T=760 °C, the Li_4SiO_4 pebble bed exhibits a time dependent consolidation behaviour connected with an increasing stiffness of the bed. No remarkable plastic deformation of the individual particles was observed after the end of the experiment. Fig. 2 shows the initial mechanical cycling of the bed, the bed deformation during constant load over a time period of about 70 hours, and the final mechanical cycling. At 850°C and 7.5 MPa, the pebbles deform significantly and a partial sintering occurs.

Measurement of the thermal conductivity of a Li_4SiO_4 pebble bed

For the design of the blanket data on the effective thermal conductivity of the lithium orthosilicate bed are required. Fig. 3 shows schematically the experimental apparatus to measure the heat transfer parameters of the bed.
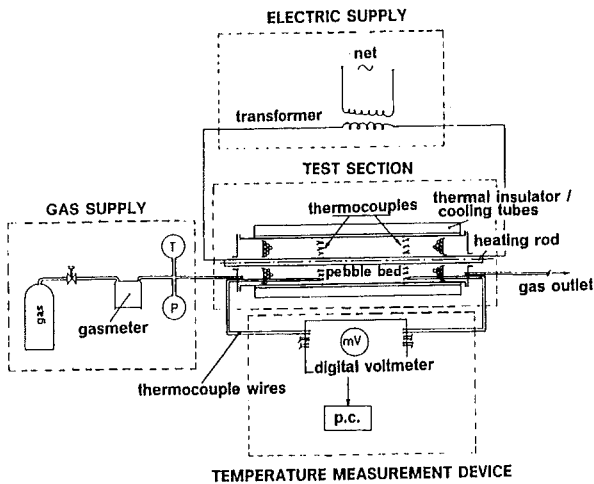
Fig. 3: Experimental apparatus to mesure the heat transfer parameters of a pebble bed

The inner cylinder contains an electrically heated rod. Helium flows in the axial direction through the bed . The radial distribution of the temperature in the bed is measured either in one or in two axial positions in the central part of the test section, where the axial temperature gradients are negligible in comparison with the radial ones, by means of banks of 32 thermocouples placed at various radii at four different azimuthal angles. For the present experiments only one bank of 32 thermocouples placed at the middle axial position of the test section was used. Furthermore the temperatures on the inner and the outer cylinder surface are measured by thermocouples placed into the walls. The temperature level of the bed has been varied by varying the heating power in the inner road.The heat transfer measurements were performed with helium flowing at very low velocity, so that the heat transfer parameters are not affected by helium convection.

Fig. 4 shows the measured effective thermal conductivity of the bed of Li_4SiO_4 pebble bed versus the bed average temperature and at various pressures of the flowing helium. The agreement with the Schlünder correlation is quite good. The thermal conductivity is practically independent from the helium pressure. There is no Smoluchowski effect for helium pressure higher than 1 bar. A linear equation is used to correlate the thermal conductivity data.

Fig. 4: Bed thermal conductivity as function of temperature

Staff:

M. Dalle Donne
A. Goraieb
R. Huber
E. Kaiser
K. Kleykamp
D. Knebel
W. Laumer
S. Müller
G. Piazza
J. Reimann
H. Ziegler

B 8.3.1
Contribution to the PIE of Li$_4$SiO$_4$ Pebbles Irradiated in the HFR Petten
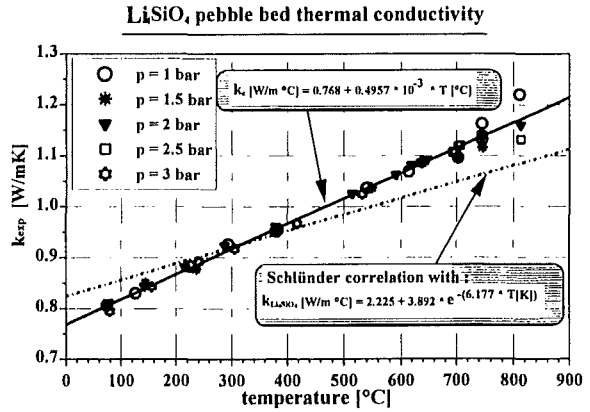
A bed of orthosilicate pebbles and two mixed beds of orthosilicate and beryllium pebbles have been irradiated in the HFR Petten test EXOTIC-7 to a lithium burnup between 6 and 18 %. A quite extensive post-irradiation examination (PIE) program has been performed for both types of pebbles. A final report is in preparation. PIE includes studies of the microstructure (optical and scanning electron microscopy, x-ray analysis), of the mechanical behaviour and of the tritium release characteristics. Important results of EXOTIC-7 PIE for the orthosilicate pebbles are [1, 2]:

- tritium inventory at end of irradiation (burnup 6 %) consistent with EXOTIC-6 inpile data (maximum burnup 3 %),

- pebbles essentially intact after irradiation.

EXOTIC-7 PIE results concerning X-ray analysis of selected samples and compressive strenth of Li$_4$SiO$_4$ pebbles are discussed below.

June 1997 EXOTIC-8 was started with two FZK capsules containing orthosilicate pebbles with a small addition of TeO$_2$. Out-of-pile annealing tests indicated that the TeO$_2$ improves considerably the tritium release. Unfortunately it turned out that these pebbles are not suited as breeder material because the Te is released at higher temperatures. Therefore preparations are underway to replace the material in one of the EXOTIC-8 FZK capsules by the earlier reference material (Li$_4$SiO$_4$ + 2.2 wt% SiO$_2$).

EXOTIC-7, X-ray microanalysis

Post-irradiation studies by X-ray microanalysis were made on selected samples of the MANET steel lined capsule 28.2 of the EXOTIC-7 experiment. A mixture of Be pebbles and SiO$_2$ doped Li$_4$SiO$_4$ pebbles with about 52 % ^{6}Li enrichment had been irradiated in the HFR up to 18 % burn-up. A Li/Si decrease occurs due to Li fission which results in increasing amounts of Li$_2$SiO$_3$ in the Li$_4$SiO$_4$ pebbles. Furthermore, oxygen is released by the fission process and oxidises the surface of the Be pebbles to BeO. Direct BeO-Li$_2$SiO$_3$ contact results in the formation of Li$_2$BeSiO$_4$. The predominant Li$_2$O vapour species above solid Li$_4$SiO$_4$/Li$_2$SiO$_3$ is transported to the colder, inner liner surface and recondensates as stratified Li$_2$O and Li$_8$SiO$_6$ layers. The chemical reactions between the MANET steel liner and the breeder materials play a minor role.

EXOTIC-7, Compressive strength of Li$_4$SiO$_4$ pebbles

Three FZK capsules were irradiated in EXOTIC-7 (Table 1).

Table 1: EXOTIC-7, FZK capsules

Capsule	Material	Lithium burnup (%)	Diameter of Li$_4$SiO$_4$ Pebbles (mm)	Diameter of Be Pebbles (mm)
26.2 (M)	Li$_4$SiO$_4$+Be	13	0.1 to 0.2	0.1 to 0.2 +2.0
28.1	Li$_4$SiO$_4$	6	0.1 to 0.2	0.1 to 0.2
28.2 (M)	Li$_4$SiO$_4$+Be	18	0.1 to 0.2	0.1 to 0.2 +2.0

(M) = mixed beds

In Table 2 compressive strength data at room temperature of Li$_4$SiO$_4$ pebbles irradiated in EXOTIC-7 are compared with that of unirradiated pebbles.

Table 2: Compressive strength of irradiated (EXOTIC-7) and unirradiated Li$_4$SiO$_4$-pebbles

Capsule	Lithium burnup (%)	Compressive Strength (Gpa)	
		unirrad.	ilrrad.
26.2	13	4.64	4.82
28.1	6	4.64	4.92
28.2	18	4.64	4.87

The compressive strength of the irradiated, high burnup pebbles from EXOTIC-7 is essentially the same as that of the unirradiated pebbles. In addition, the data are also in reasonable agreement with those from previous irradiations [3] (Table 3).

First optimization tests at room temperature in air indicated that the addition of small amounts of TeO$_2$ to Li$_4$SiO$_4$ would improve the mechanical stability of the pebbles due to an increased surface tension of the molten phase [4]. Unfortunately, this could not be confirmed experimentally after heat treatment under realistic conditions (reducing atmosphere, high temperature). After heat treatment for 90 h at 1000 °C under Helium the compressive strength of unirradiated Li$_4$SiO$_4$ + 2 wt% TeO$_2$ pebbles decreased to ~ 3.5 GPa. These values are in the same range as those of the pebbles without TeO$_2$ (Table 2 and 3).Therefore, the reference material for the further HCPB blanket development is Li$_4$SiO$_4$ + 2,2 wt% SiO$_2$ (without TeO$_2$).

Literature:

[1] M. Dalle Donne, F. Scaffidi-Argentina, H. Werle, FZK-Nachrichten, Jahrg. 29, 1/97, p. 61.

[2] F. Scaffidi-Argentina, H. Werle, "Tritium Release from EXOTIC-7 Orthosilicate Pebbles: Effect of Burnup and Contact with Beryllium during Irradiation", Sixth Int. Workshop on Ceramic Breeder Blanket Interactions (CBBI-6), Mito, Oct. 22 - 24, 1997.

[3] P. Weimar, H. Steiner, H. Zimmermann, L. Dörr, 18th SOFT, Karlsruhe, 1994

[4] M. Dalle Donne et al., 19th SOFT, Lisbon (1996) and Nuclear Fusion Annual Project Report of the Association FZK/EURATOM (1996), P. 109

Staff:

M. Dalle Donne
E. Damm
H.D. Gottschalg
H. Häfner
E. Kaiser
H. Kleykamp
D. Knebel
B. Neufang
R. Pejsa
O. Romer
F. Scaffidi-Argentina
H. Steiner
A. Wacker
G. Weih
P. Weimar
F. Weiser
H. Werle
H. Ziegler

Table 3: Compressive strength of Li_4SiO_4 pebbles at room temperature after irradiation to different Li burnups

Irradiation	Material	Pebble Dia. (mm)	Burnup (%)	Load (N)	Compressive Strength (GPa)
ELIMA 2	Li_4SiO_4	0.5	0.3	7.2	3.5
DELICE 3	Li_4SiO_4	0.5	1.0	5.2	3.1
ALICE 3	$Li_4SiO_4+2.2\%SiO_2$	0.5	3.0	5.7	3.2
ALICE 3	$Li_4SiO_4+2.2\%SiO_2+1\%Al_2O_3$	0.5	3.0	7.3	3.5
EXOTIC 6	Li_4SiO_4	0.5	3.0	12.7	4.2
EXOTIC 7	$Li_4SiO_4+2.2\% SiO_2$	0.1-0.2	18.0	1.87	4.9

WP B 9
Behaviour of Beryllium Pebbles under Irradiation

B 9.1.1
Characterization and Optimization of Beryllium Pebbles

For the Helium Cooled Pebble Bed (HCPB) Blanket the neutron multiplier consists of a mixed bed of about 2 and 0.1-0.2 mm diameter beryllium pebbles. The main structure of the pebble bed is given by the larger pebbles with a packing factor of 63.3%. In the space between them are placed the smaller beryllium pebbles with a packing factor of 17.5%.

Both kinds of pebbles are fabricated by melting, however, for the larger ones a relatively inexpensive intermediate product of the beryllium fabrication route (Brush-Wellmann Company) has been chosen [1].

Because of their poorly defined production conditions, the 2 mm Be pebbles are usually characterized by a large scatter in the microstructural and mechanical data. Therefore, a relatively large number of both unirradiated and irradiated pebbles were analyzed in order to get representative data necessary for characterizing the material as far as possible before its use in a nuclear fusion environment.

Microstructural Analysis

The bigger unirradiated beryllium pebbles usually show a relatively large number of indentations on their external surface. This is probably due to the fact that during the fabrication process very hot (or still partially molten) beryllium pebbles come in contact with cold and already solidified ones. With optical microscopy, a quite strong variation of coarse pores was observed. Some pebbles show big voids which seemed to be generated during the cooling phase of the fabrication process. Relatively often a coarse porosity with a pore size of 0.1-0.2 mm has been observed. On the other hand, most of the pebbles reveal a very small micro-porosity usually oriented along the crystal axis showing a very fine dendritic or cellular structure. Fig. 1 shows a typical porosity distribution in the 2 mm beryllium pebbles.

In general, it has been observed that the porosity of small pebbles is always smaller than that of the bigger ones, which clearly confirms that coarse porosity is generated during the cooling phase of the fabrication process. Furthermore, a large number of pebbles presents, near the external surface, a dense region the depth of which usually reaches 0.2-0.3 mm.

The metallographic structure of both smaller and bigger pebbles shows the presence of large grains, in some cases as large as the pebble diameter [2].

From the chemical point of view, insoluble impurities have been usually observed on the grain boundaries, while iron and chrome are almost exclusively present in solid solution in the beryllium-matrix. The concentration of the main impurities is shown in Tabs. 1 and 2 for the 2 mm and the 0.1-0.2 mm diameter pebbles respectively.

Mechanical Properties

Microhardness measurements were performed in the microsections prepared by metallographic techniques. On the basis of hardness levels, techniques were developed to record the tendencies of irradiation-induced changes in the mechanical properties, i.e. plasticity and elasticity. The hardness measurements were initially conducted with a holding time of 5 s. Afterwards, the same position was subjected to pressure once again, but with a holding time of 60 s. The increase in area, expressed in percent, produced by the second impression was used as a benchmark for the subsequent evaluation of the plastic deformation of the material. The permanent deformation of the hardness impression is in fact a consequence of both plastic and elastic deformation fractions. The concave dishing of the sides of the impression square is a measure of the elastic reset forces, comparable to the compression limit of the material. The unit of measurement used was the percentage difference in areas between the impression calculated from diagonals of the impression and the real impression as determined by microscopy analysis.
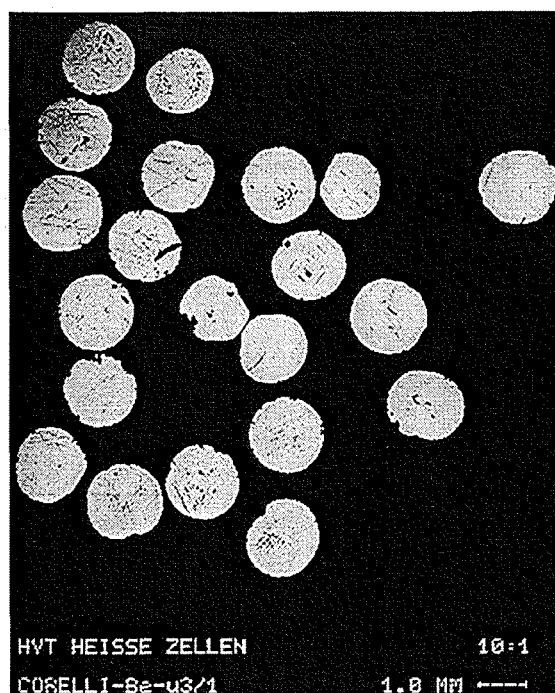

Fig. 1: Porosity distribution in 2 mm pebbles

Table 1: Main impurity concentrations in the 2 mm pebbles (data in wt%).

BeO	F	C	Mg	Fe
0.078	0.0585	0.05	0.16	0.073
Al	Si	Zr	U	Cr
0.025	0.0205	0.0125	0.007	0.015

Table 2: Main impurity concentrations in the 0.1-0.2 mm pebbles (data in wt%).

BeO	F	C	Mg	Fe
0.34	___	0.07	< 0.01	0.09

Al	Si	Zr	U	Cr
0.04	0.03	___	___	___

Although the applied load was always the same all over the sample, in some cases different microhardness impression shapes have been obtained. This was due to the different orientation of the beryllium grains, what causes an anisotropic behavior of the material itself. Because of this fact the pebbles were characterized by a quite large scatter in the mechanical data. Therefore, a very large number of pebbles was analyzed to be able to get statistically representative data.

The mechanical properties of the pebbles from the "Beryllium" experiment [3] did not significantly change during irradiation: only an increase of less than 5% of their elastic behavior and a decrease of less than 10% of their plastic behavior has been observed after irradiation. On the contrary, pebbles from EXOTIC-7 [4] show an increase up to about 30% of their elastic behavior range and a decrease up to about 50% of their plastic behavior range after irradiation. The decrease of the plasticity is much more evident in the smaller pebbles due to the fact that the implantation depth of tritium coming from ceramics ($\approx$40-50μm) is of the same order of magnitude as the pebble radius ($\approx$100-200 μm), which results in a higher implantantion efficiency than in the case of the larger Be pebbles.

Literature:

[1] M. Dalle Donne, et al., European DEMO BOT Solid Breeder Blanket, Bericht 5429, Kernforschungszentrum Karlsruhe, November 1994.

[2] M. Dalle Donne, et al., Metallographic Investigation and Mechanical Behavior of Beryllium Pebbles at Room Temperature, Proc. of the 19th Symposium on Fusion Technology, Lisbon, September 16-20, 1996. Fusion Technology 1996, p. 1487-1490.

[3] R. Conrad and R. May, Project D282.01, Beryllium, Final Irradiation Report, Report HFR/95/4262, Petten, May, 1995.

[4] R. Conrad, R. May, "EXOTIC-7, Irradiation Progress Report No. 11", Technical Memorandum HFR/95/4196, JRC Petten, April 1995.

Staff:

M. Dalle Donne
E. Kaiser
H. Kleykamp
O. Romer
F. Scaffidi-Argentina
H. Werle

B 9.2.1
Behavior of Beryllium Pebbles under Irradiation

1. Optical microscopy

The EXOTIC-7 [1] as well as the "Beryllium" [2] experiments carried out in the HFR reactor in Petten are considered as the most detailed and significant tests for investigating the beryllium pebble response under neutron irradiation. The beryllium irradiated in both the EXOTIC-7 and the "Beryllium" experiments consists of a mix of about 2 mm and 0.08-0.18 mm diameter beryllium pebbles. However, while in EXOTIC-7 the beryllium pebbles were - during irradiation - in contact with Li_4SiO_4-pebbles, in the "Beryllium" experiment mainly pure beryllium pebble beds were irradiated.

For some post-irradiation examinations (PIE) the components of the EXOTIC-7 mixed beds had to be separated. The 2 mm diameter Be pebbles were separated from the small (0.1-0.2 mm) Li_4SiO_4 and Be pebbles by sieving. The small Li_4SiO_4 and Be pebbles were separated by a wet procedure using an organic liquid with a density in-between that of the Li_4SiO_4 and Be pebbles.
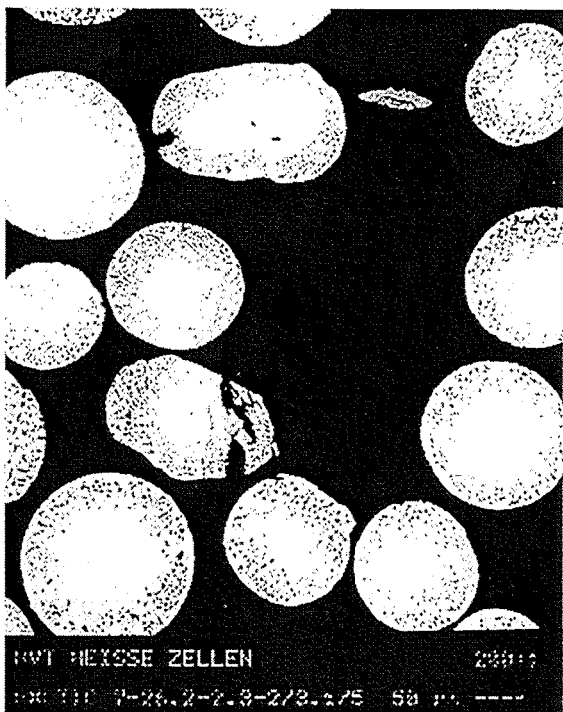

Fig. 1: New porosity due to the contact between Be and ceramics.

Because of the relatively low irradiation temperatures in both EXOTIC-7 and "Beryllium" experiments (T_{irr}=410-550 °C), no remarkable thermally induced changes in the beryllium structure (macroscopic and microscopic) have been observed after the neutron irradiation except the almost complete disappearance of the porosity fraction in the range 230-300 μm. However, although the fast neutron fluence was almost the same in both experiments ($\Phi\approx1.3\cdot10^{21}$ cm^{-2}; $E_n>$ 1 MeV), the beryllium pebbles from EXOTIC-7 showed strong irradiation induced structural changes. In particular a new type of porosity was observed in a boundary layer of the pebbles not deeper than 40-50 μm. The new pores are of an oblong shape, are oriented along the crystals and have diameters of up to 2 μm as shown in Fig. 1. This new porosity is essentially due to the contact between beryllium and Li_4SiO_4 during irradiation.

Etching the microsections reveals a polygonization pattern consisting of bundles of oblong lines, mostly aligned in the same direction as shown in Fig. 2.

Polygonization is the first step in subgrain formation, and is initiated by an array of step dislocations towards small-angle grain boundaries. At higher temperatures, this gives rise to rounded subgrain shapes, which already existed in the structure of the unirradiated pebbles. Along with the line structures of polygonization, etching causes a dense network of etching pits. A striking phenomenon are narrow strips of approx. 2 μm width on both sides of the grain boundaries, which remain free from etching attack. This phenomenon is almost identical to that observed in the UO_2 fuel elements of fission reactors with the only difference that, in case of beryllium, instead of the fission product gases, helium precipitated from the Be (n, 2n) 2 He reaction is present.

Fig. 2: Poligonization patterns in the pebbles.

2. Tritium release

In general the beryllium specimens irradiated in the "Beryllium" experiments show that the release from 0.7 mm diameter pieces from the large pebbles is faster than that from the whole pebbles ("particle size" effect), but a further decrease of the particle size to ≤0.5 mm diameter indicated no further release improvement. However, release from the small pebbles was faster than that from 0.7 mm diameter pieces from the large pebbles.

With reference to EXOTIC-7, release of all investigated Be samples (Be 2 mm, Be 2 mm broken, Be 0.1-0.2 mm) from the mixed beds (Be + Li_4SiO_4) of capsules 28.2 and 26.2-1 is very similar. In agreement with previous studies [3,4] the release starts at about 500-550 °C and achieves a maximum at about 700 -750°C.

The total release of the large Be pebbles (Be 2 mm) is slightly larger ($\approx$ 6•10^{10} Bq/g) than that from Li_4SiO_4 from the same capsules, while that of the small Be pebbles (Be 0.1-0.2 mm) is

about a factor 30 larger ($\approx 1 \bullet 10^{12}$ Bq/g). According to previous studies [4] it is expected that, if Be is in direct contact with ceramics during irradiation, a fraction of the 2.74 MeV tritons produced in the Li_4SiO_4 is implanted in a surface layer of beryllium (depth $\approx$ 40 μm). This leads to an additional inventory which is usually several times larger than that directly produced by the neutrons reacting in the beryllium. Tritium generation data in Be for both EXOTIC-7 capsules 26.2-1 and 28.2 are not yet available. However, with reference to calculations for the "Beryllium" experiment [4] one can estimate a ratio He-production/T-production of a about 45. Based on the He-production in Be for the HFR reactor of about 3440 appm per 10^{22} n/cm^2 ($E_n \geq$ 1 MeV) [5], the total He produced at the end of the EXOTIC-7 experiment, (fast fluence $1.2 \bullet 10^{21}$ cm^{-2}) should be 450 appm (for both capsules 26.2-1 and 28.2). This leads to a specific tritium production in Be of $1.3 \bullet 10^9$ Bq/g, in reasonable agreement with a value of 2×10^9 Bq/g based on tritium production vs. fast fluence graph [6]. In any case, the neutron-generated tritium in Be is about a factor 50 lower than the released tritium from the larger Be pebbles and about a factor 700 lower than that from the smaller Be pebbles, assuming no release during the irradiation. This high tritium inventory in both the large and small Be pebbles from EXOTIC-7 capsules 26.2-1 and 28.2 can be only due to implantation from ceramics. Furthermore, the total release from the small Be pebbles is about a factor 15 larger than from the bigger ones. This is probably due to the fact that in the small Be pebbles the implantation depth of tritium coming from ceramics ($\approx$ 40 μm) is of the same order of magnitude as the pebbles radius ($\approx$ 50 - 100 μm), which results in a higher implantation efficiency than in the case of larger Be pebbles.

Literature:

[1] R. Conrad, R. May, "EXOTIC-7, Irradiation Progress Report No. 11", Technical Memorandum HFR/95/4196, JRC Petten, April 1995.

[2] Conrad and R. May, Project D282.01, Beryllium, Final Irradiation Report, Report HFR/95/4262, Petten, May, 1995.

[3] F. Scaffidi-Argentina and H. Werle, Tritium Release from Neutron Irradiated Beryllium: Kinetics, Long-Time Annealing and Effect of Crack Formation, Proceedings of the Second IEA International Workshop on Beryllium Technology for Fusion, Jackson Lake Lodge, 1995, p. 235-248.

[4] H. Werle, Tritium Release of Beryllium Pebbles from Neutron-Irradiated Pure Beryllium and Mixed Li_4SiO_4/ Beryllium Beds, Proc. Fifth Int. Workshop on Ceramic Breeder Interactions (CBBI-5), Rome, Sept. 1997, p. 181-187.

[5] M. Küchle, Material Data Base for the NET Test Blanket Design Studies, KfK Internal Report, Kernforschungszentrum Karlsruhe, February 1990.

[6] H. Werle, Release of Neutron-Generated Tritium from Beryllium, Internal Report INR-1906, Kernforschungszentrum Karlsruhe, October 1994.

Staff:

E. Damm
M. Dalle Donne
D. Knebel
F. Scaffidi-Argentina
H. Werle
H. Ziegler

SM 1.2.1, SM 1.3.1
MANITU Irradiation Program

1. Introduction

The MANITU irradiation and impact-toughness testing programme on promising low-activation ferritic/martensitic steels has been completed, and impact test data are now available for an array of irradiation parameters covering doses of 0.2/0.8/2.4 dpa and temperatures of 250/300/350/400/450°C. Particular emphasis was to be laid on the further evolution of the impact properties with increasing dose at the different irradiation temperatures, and on the behaviour of the different alloys in comparison to each other, especially at the critical lower irradiation temperatures. The previous investigation had shown for irradiation parameters of 250°C/0.8 dpa that the US-heat, referenced as 'ORNL', had yielded the lowest ductile-to-brittle transition temperatures (DBTT), although its chromium content, distinctly above that of the Japanese F82H and not far from various FZK-alloys, would have suggested a different behaviour. In the course of the current work, besides the evolution of dose dependency, there was a great deal of curiosity on our side to look into other factors which might have had an influence on fracture toughness deterioration.

2. Experimental

The Charpy specimens have been produced parallel to the rolling direction (l-t) of the material plates and according to the European standard for subsize specimens. The same type has already been used in our previous investigations to enable a direct comparison of the results. For the same reason, all tests have been carried out with the same instrumented facility which is installed in the Hot Cells. The test and evaluation procedure was also identical as in our previous investigations.

For each experiment the force-vs.-deflection curve was recorded and the impact energy was determined by integration. As usual this quantity was drawn against the test temperature and from this the characteristic values upper shelf energy (USE) and ductile-to-brittle transition temperature (DBTT, i.e. temperature at USE/2) were derived.

The irradiations of the MANITU programme were all carried out in the HFR, Petten. The target values of 0.2, 0.8, and 2.4 dpa were reached at least within ±20% depending on the core position of the specimens. The irradiation temperatures of 250, 300, 350, 400, and 450°C were maintained within ±5% by a proper balance between n,γ-heating and compartment cooling with different He-Ne mixtures.

A minimum of 5 specimens for each material, dose level, and irradiation temperature ensured a sufficient number of measurement points in order to connect and group them to curves with the irradiation temperature as abscissa and the materials and dose levels as parameter.

3. Results and Interpretation

The results have been drawn up in figure 1. It can be seen that for a given irradiation temperature DBTT is shifted from the „unirradiated" value, which is also indicated, to higher temperatures with increasing dose, a few exceptions being thought to be attributed to statistical scatter rather than to

systematic effects. A comparison of the different materials repeats what has already been noticed previously, namely that the more advanced alloys with respect to a decrease in Cr content and a reduction in long-term activation show improvements both of the absolute values of DBTT and their impairment by the irradiation. As demonstrated by figure 2, USE shows a more or less complementary behaviour, i.e. the higher the dose the lower is USE, especially when the irradiation temperature was low. Dynamic yield, derived from measurements at 100°C, has also been evaluated, but the results are not given in this paper because of space limitations.

To allow for a better quantitative comparison of the irradiation behaviour for the different materials, dose dependency of DBTT has been drawn up for one of the more critical, i.e. lower, irradiation temperatures. DBTT-shift (ΔDBTT), rather than absolute DBTT, has been chosen in order to eliminate the differences introduced by the different Cr contents. As demonstrated by figure 3, ΔDBTT behaves very similarly for all steels, but with quite different slopes.

Starting from some suspicion about the influence of helium on impact toughness, and from complementary investigations with He-implanted Charpy V specimens, the boron contents were brought in relationship to the slopes. The result was quite evident: The higher the boron concentration, the steeper the slopes were. But all curves showed the same tendency to saturate at rather low doses. Indeed is boron, with its 20 % of the isotope ^{10}B, one of the strongest thermal neutron absorbers which shows a burn-up effect already at very moderate neutron fluences and is thereby transformed to stable helium and ^{7}Li.

The burn-up constant τ, defined here as the dose D in dpa, necessary to decrease the initial ^{10}B-content down to a fraction of 1/e (i.e. ca. 37%), was derived from the neutronic calculations of HFR-Petten to be 0.34 dpa for the spectral conditions of this irradiation. A burn-up of 99.3 %, corresponding to 5-times the burn-up constant, is reached after ca. 1.6 dpa which is in the range of the dose when saturation for irradiation hardening was found for MANET-I. For a comparison with the measured embrittlement behaviour the ^{10}B-to-He transformation curve has also been drawn into Fig. 3. It lies at hand to attribute the He-content originating form boron, to the evolution of ΔDBTT for the different steels. Fig. 3 has consequently been analysed applying the growth function N(He) = $N_0(^{10}B)*(1-exp(D/\tau))$ to the different curves. Under the assumption that ΔDBTT is proportional to N(He), and neglecting effects such as He bubble growth and size, this equation can be brought into the linearised form: $ln(1-\Delta DBTT/\Delta DBTT_{max})$ = -D/τ, from which $\Delta DBTT_{max}$ can be derived for the different materials by a fit to the common slope being -1/τ. The values are given in Table 1 together with the corresponding He-levels resulting from complete ^{10}B transmutation. Indeed the ratio of ΔDBTT over He in atomic ppm (appm) is more or less the same for all materials measured, and amounts to approximately 2-3 K per appm He.

This is a significant effect that apparently overrides all other factors, but leaves a few questions open which shall now be discussed. One is a DBTT-shift that had been previously measured for MANET-I to be ca. 260 K at doses of 5 dpa and above. A reasonable explanation is that displacement damage induced hardening as such also has an effect which shows up at increased doses and is not likely to saturate as supposed

Table 1: Extrapolated DBTT-shift and helium content after complete ^{10}B burn-up

	MANET-I	MANET-II	OPTIFER-Ia	OPTIFER-II	F82H std.	ORNL
ΔDBTT$_{max}$	210 K	190 K	115 K	120 K	60 K	45 K
max. He	85 appm	70 appm	60 appm	60 appm	<20 appm	<10 appm

earlier. Another point is that a much lower DBTT-shift amounting to only about 45 K was found for specimens after He in-depth implantation of about 300 appm by means of a high-energy cyclotron in a parallel investigation. Certainly, the way how the helium is introduced in the material plays a decisive role, and it is generally accepted that the distribution of boron in steel is quite inhomogeneous. The third question is raised by the recovery effect of property deterioration at increased irradiation temperatures. Explanations for this behaviour are proposed in, but further investigations will be needed.

A critical aspect of the influence of helium on DBTT arises, if one translates our results to fusion reactor conditions where about 10 appm helium have been calculated to be generated per dpa by the (n,α)-reaction of fast neutrons with iron. This is a non-saturating source, and tremendous DBTT-shifts could be extrapolated if one takes a target value of at least 100 dpa for structural materials into account. Fortunately the effects of helium homogeneity and recovery phenomena at higher temperatures, as discussed above, create a more relieved situation with respect to impact properties deterioration.

4. Conclusions

The dose dependency of impact properties for different advanced ferritic/martensitic alloys at low irradiation temperatures has been uncovered to be in the low-dose range mainly an effect of helium generated by different levels of boron, the ^{10}B isotope of which is burnt up with nearly the same characteristic time constant as DBTT increases towards saturation. At higher irradiation temperatures the DBTT-shift is significantly lower. In addition, a more homogeneous distribution of He in the matrix shows a smaller effect on DBTT. These findings are of utmost importance for fusion since in a fusion reactor environment there will be an inexhaustible source for helium from fast neutron reactions with iron. Validation tests to proof and further quantify our results are indispensable. As long as no powerful fusion or accelerator-based neutron source is available, also a continuation of high-energy helium implantation tests by means of an available cyclotron should seriously be reconsidered.

Literature:

[1] M. Rieth, B. Dafferner, Low Temperature Embrittlement Behaviour of Different Ferritic/Martensitic Alloys for Fusion Applications, J. Nucl. Mat. 233-237 (1996) 229-232.

[2] M. Rieth, B. Dafferner, H.D. Röhrig, Charpy Impact Properties of Different Low Activation Alloys for Fusion Applications After Neutron Irradiation, J. Nucl. Mat. 233-237 (1996) 351-355.

[3] M. Rieth, B. Dafferner, W. Kunisch, H. Ries, O. Romer, Bestrahlungsprogramm MANITU: Ergebnisse der Kerb-schlagbiegeversuche mit den bis 0,2 dpa bestrahlten Werk-stoffen, FZKA 5750, April 1997.

[3] M. Rieth, B. Dafferner, Der Einsatz des Störgrößen-kompensationsverfahrens bei der vollautomatischen dyna-mischen Werkstoffprüfung, Roell-Amsler Automatisierungs-tag, 24.04.1997, Ettlingen.

[5] M. Rieth, B. Dafferner, O. Ernst, Vollautomatisches Pendelschlagwerk und Auswertesoftware zur Bestimmung der werkstoffrelevanten Kenngrößen, Amsler Symposium '97, 17.-18. Juni 1997, Gottmadingen.

Staff:

J. Aktaa
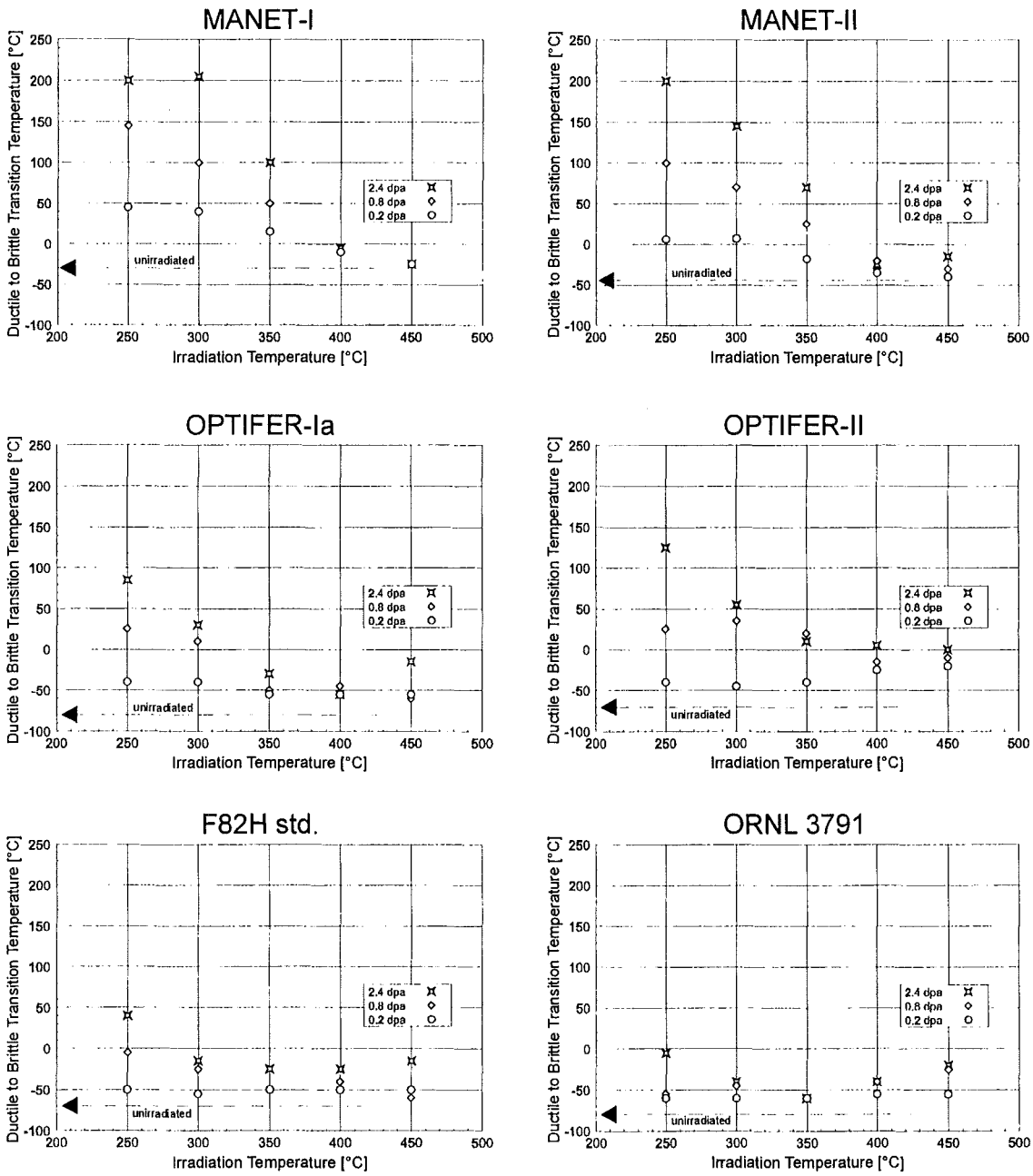B. Dafferner
W. Kunisch
H. Ries
M. Rieth
O. Romer

Fig. 1: Ductile-to-brittle transition temperature vs. irradiation temperature (parameter: irradiation dose)
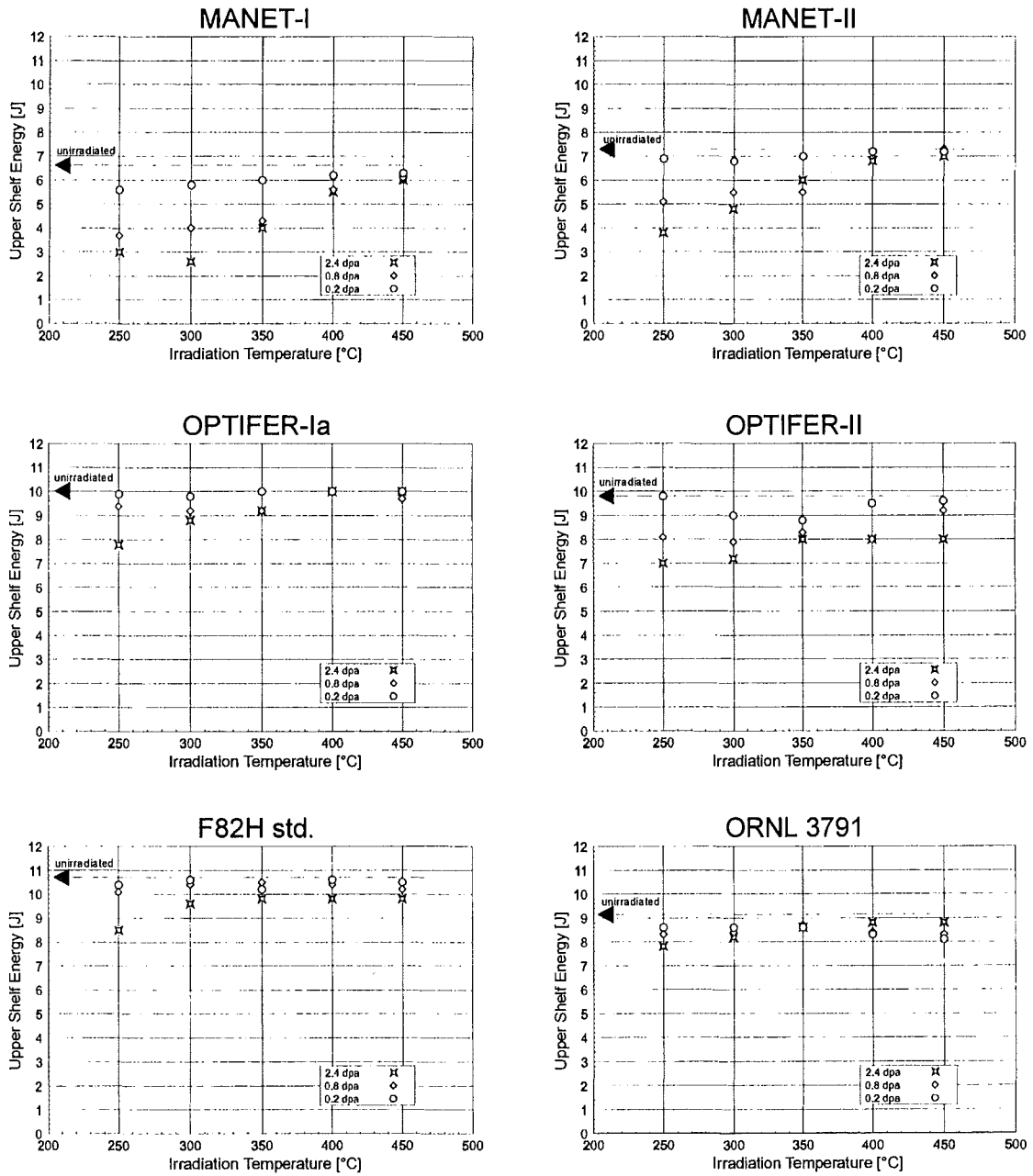
Fig. 2: Upper shelf energy vs. irradiation temperature (parameter: irradiation dose)
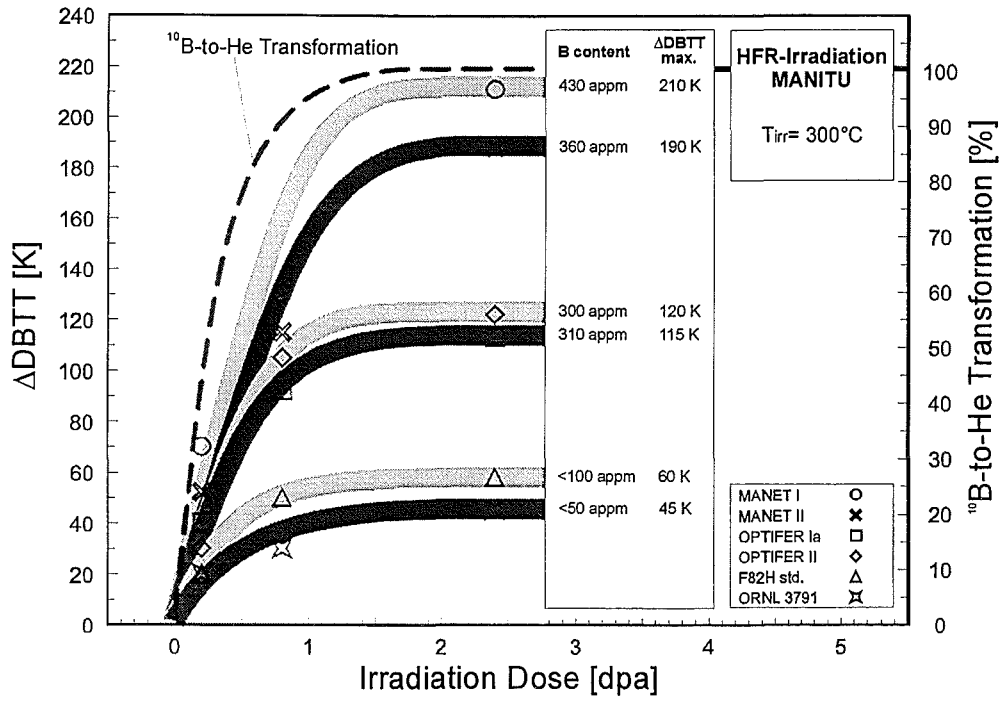
Fig. 3: Irradiation induced shifts of ductile-to-brittle transition temperature and ¹⁰B-to-He transformation vs. irradiation dose (parameter: materials)

SM 1.4.1, SM 6.2.2
Effects of Radiation Hardening and He in LAM / Fatigue Properties under Irradiation

The Dual Beam Facility of FZK, where α-particles (≤104 MeV) and protons (≤40 MeV) are focused onto a target, was developed as a research tool for materials within the European Fusion Technology Program. This high energy dual beam technique allows the simulation of fusion neutrons by systematic variation of hydrogen, helium, and damage production in thick metal and ceramic specimens as well as the simulation of Tokamak relevant thermal and mechanical loads in proposed plasma facing materials. In the present program the investigations include:

Comparison of the conventional steels with reduced activation steels for tensile and charpy properties, especially helium and dpa effects as well as microstructural stability (WP SM 1.4.1), and

Effects of irradiation on fatigue properties for reduced activation steels including crack morphology investigations (WP SM 6.2.2).

In the following the activities done within the reporting period are summarized.

1. Tensile Properties of the Ferritic/Martensitic Steels MANET and F82H-mod after Helium Implantation

Whether or not helium generated by inelastically scattered fusion neutrons will influence the strength and ductility properties at lower irradiation temperatures, is a matter of concern and subject to ongoing discussions. Therefore, changes in the tensile properties of the conventional type 10Cr-2CrMoVNb steel MANET-1 and the reduced activation type 8Cr-2WVTa steel F82H-mod after implantation of 500 appm Helium at 0.3dpa between 60 and 420 °C are investigated.

Sheet tensile specimens with a reduced gauge volume of 7.0mm x 2.0mm x 0.20mm were produced from foils following the reference heat treatment and were homogeneously irradiated in purified helium atmosphere at the Dual Beam Facility of FZK, using a degraded 104 MeV alpha-particle beam. The helium and damage rates were 2.5-3.0x10^{-3} appmHe/s and 1.4-1.8x10^{-6} dpa/s, respectively. That is, special emphasis was put on fairly low production rates. All implanted specimens were tensile-tested at the irradiation temperature in vacuum with a constant strain rate of 5x10^{-4}/s.

In agreement with results on standard specimen geometries it was found that in the unirradiated condition both yield and tensile strength of the MANET-1 steel are about 150MPa above the related values of the F82H-mod steel, except between 270 and 350 °C, where a plateau region was observed on MANET-1 samples. This plateau was accompanied with a minimum in total elongation and with pronounced serrated yielding, indicating dynamic strain aging. After irradiation a strength increase has been observed in both steels that decreases continuously from 60 to 350 °C and diminishes rapidly above about 400 °C. At 60 °C e.g., this irradiation induced hardening amounts to 265 MPa in MANET-1 but only 115 MPa in F82H-mod specimens (Fig. 1).

For the helium implanted specimens the hardening ratio between F82H-mod and MANET-1 is about 0.44±0.09 within a wide temperature region. By analyzing various strengthening contributions it can be shown that the dominant hardening contribution stems from dislocation loop formation or irradiation enhanced precipitation. Helium only tends to stabilize these effects. However, a significant reduction in the uniform elongation between 65 and 35% has been observed between

60 and 200 °C in both steels, whereas the ductility remains only slightly affected by the helium implantation at 250 °C and above. It is remarkable that in contrast to MANET-1 specimens that showed a pronounced dynamic strain aging (DSA) related to a ductility drop from 3 to 0.3% after helium implantation between 270 and 350 °C, no DSA was observed in unirradiated and helium implanted F82H-mod specimens.
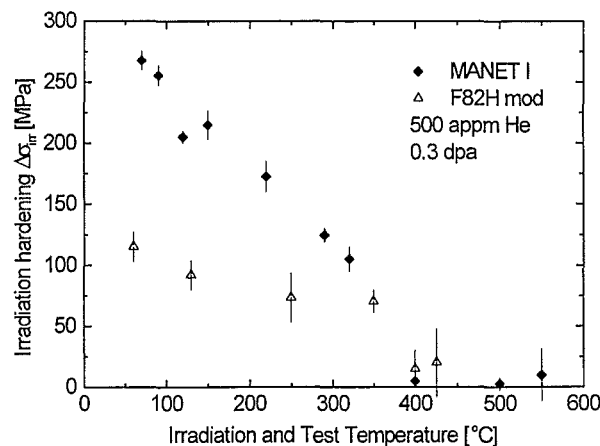

Fig. 1: Temperature dependency of the Irradiation induced hardening; comparison between conventional type (MANET 1) and reduced activation type (F82H mod) steels.

2. Influence of Helium on Impact Properties of Reduced-Activation Ferritic/Martensitic Cr-Steels

Moving towards the development of low-activation 8-9Cr-2WVTa steels, some encouraging results have become available meanwhile on the critical issue of low temperature irradiation induced hardening and embrittlement. However, whether helium generated by inelastic (n,α)-processes will have a significant effect on impact properties, such as the ductile to brittle transition temperature (DBTT), is hardly understood in the literature and subject of ongoing discussions. The demonstration of a direct relationship between helium and embrittlement based on fast or mixed spectrum fission reactors is very difficult because such simulation techniques require an alloying with B-10 or Ni-59 for the helium production. To make matters worse, fission neutron induced helium might not be homogeneously distributed but associated to precipitates enriched with B or Ni. This work describes changes in the Charpy impact properties of the reduced activation type 8Cr-2WVTa steel F82H-mod after homogeneous implantation of 300 appm Helium at 250 °C. The results are compared with investigations on neutron irradiated specimens and explained within the frame of an analytical model.

Instrumented charpy impact bending tests have been performed using an evaluation system for sub-size specimens according to the European standard (3 x 4 x 27 mm^3). The impact properties were characterized by the upper shelf energy (USE), the DBTT as well as the irradiation induced shifts of these values (ΔDBTT and ΔUSE). The cyclotron irradiation took place at the Dual Beam Facility of FZK, using a degraded 104 MeV alpha-particle beam. The helium implantation rate was 6-10x10^{-4} appm/s and the associated displacement damage 0.22 dpa. For comparison, mixed spectrum neutron irradiations at the HFR Petten have been performed on F82H specimens and OPTIFER-Ia specimens,

that had been alloyed with 40 appm B and irradiated to the same dpa level at the same temperature.
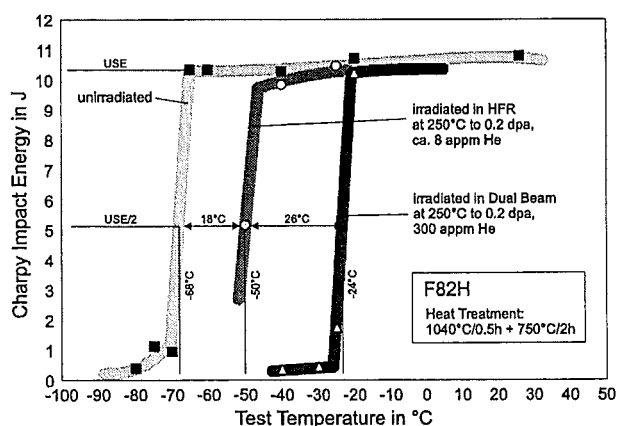

Fig. 2: Effect of helium and dpa damage on the transition temperature in the reduced activation steel F82H mod.

After neutron irradiation the F82H steel shows a DBTT of -50 °C and a ΔDBTT of 18 °C, whereas the 300 appm helium implanted F82H steel has significantly higher DBTT and ΔDBTT values of -26 °C and 42 °C, respectively (Fig. 2). This is a direct proof that under dynamic loading conditions and at lower irradiation temperatures, where the mean free diffusion path of helium atoms is small, helium contributes sensitively to the embrittlement of ferritic/martensitic steels. The conclusion is also supported by a B-doped steel of similar composition (OPTIFER-Ia) that showed a ΔDBTT shift of 44 °C after neutron exposure to 0.21 dpa at 250 °C. During the reporting period, a model has been outlined which describes the impact properties taking into account features of the helium bubble morphology as well as precipitates and irradiation induced defects.

3. Fatigue Behavior and Development of Microcracks in F82H after Helium implantation at 200-250 °C

Among other criteria, the materials for the first wall should be optimized with regard to the nuclear inventory. In this work, strain controlled fatigue experiments have been performed on F82H. Continuous push-pull cycling has been applied with a strain range between $\Delta\varepsilon_{total}$=0,4 % and $\Delta\varepsilon_{total}$=0,9 %. The cycle ratio was R=-1. A first wall relevant temperature range between T=200°C and T=250°C was chosen. The tested hollow specimens have a square cross-section optimized by elastic-plastic FE calculations for irradiation and fatigue experiments at the Dual-Beam facility of the Forschungszentrum Karlsruhe. Prior to fatigue some of the specimens were irradiated with a degraded 104 MeV α-particle-beam, in order to get a homogeneous implantation of 400 appm helium in the gauge volume. The fatigue experiments were performed in air.

In the fatigue tests, the unirradiated specimens follow a typical lifetime distribution in accordance with the Coffin-Manson law. All irradiated specimens show a significant irradiation induced hardening and a strong loss of plasticity. At higher strain ranges ($\Delta\varepsilon_{total}$=0,9 %), the lifetime of the irradiated specimen is distinctly reduced. At lower strain ranges ($\Delta\varepsilon_{total}$=0,5 %), the lifetime after irradiation lies at the upper limit of the scatter band of unirradiated specimens. During the fatigue tests the polished surfaces of the specimens were observed by the aid of a special long-distance microscope. The interest was focused on the formation and development of microcracks. The very small cracks have

been classified by their length, orientation, density of occurence and coalescence. In dependency of the test conditions (strain range, irradiation hardening), the crack patterns show different properties concerning the mentioned criteria. The behaviour of the cracks is strongly influenced by the microstructure of the material. Rows of small secondary precipitates of type $M_{23}C_6$ can act as local, internal sites of crack initiation or encourage crack growth in the direction of the precipitation alignment. The formation of cracks seems to be driven by two different forces: Some cracks originate from intrusions and extrusions. They are caused by plasticity and their inclination to the load axis is about 45°. Other cracks occur at the rows of precipitates. They are more sensitive to normal stresses and their inclination to the load axis lies between 45° and 90°. If normal stresses are high enough, the contribution of cracks that are oriented to higher angels, increases. This is the case for fatigue tests with high strain rates and after irradiation hardening. Here the lifetime is reduced by the fast development of cracks along internal surfaces. At low strain rates and after irradiation the stresses - although there is an irradiation induced hardening - are not high enough to favour crack formation at the rows of precipitates. But the reduction of the plasticity slows down the development of in- and extrusions as crack initiating sites and the lifetime of the specimens may even be longer than in the unirradiated case.

Literature:

[1] J. Bertsch, R. Lindau, A. Möslang, Journ. Nucl. Mater. 233-237 (1996) 276.

[2] E. Daum, J. Bertsch, A. Möslang, Journ. Nucl. Mater. 233-237 (1996) 959.

[3] R. Lindau and A. Möslang, Journ. Nucl. Mater 233-237 (1996) 1294.

[4] J. Bertsch, Mikroskopische Untersuchungen der Bildung von Ermüdungsrissen an zwei ferritisch-martensitischen Stählen im unbestrahlten und vorbestrahlten Zustand, FZKA report 5984, Sept. 1997.

[5] E. Daum, H.D. Röhrig, Impurity concentrations of niobium and molybdenum in the Japanese steel F82H-mod by activation analysis, Journ. Nucl. Mater., July 1997, in press.

[6] R. Lindau, E. Materna-Morris, A. Möslang, D. Preininger, M. Rieth, H.D. Röhrig, Influence of Helium on Impact Properties of Reduced-Activation Ferritic-Martensitic Cr-Steels, ICFRM-8, Oct. 26 - 31, 1997, Sendai, Japan

Staff:

S. Baumgärtner
G. Bürkle
E. Daum
R. Lindau
A. Möslang
D. Preininger

SM 2.1.4, SM 5.3.2
Mechanical Properties & Microstructure of Reduced Activation Ferritic/Martensitic Steels (RAF)

Material Development

Material Characterization of the Steel F82H-mod.:

In the frame of the European Technology Program the steel F82H-mod. was investigated and characterized by mechanical tests and microstructural investigations. The associated European laboratories performed a quality assurance program and homogeneity tests on all delivered F82H-mod. plates. The material of this steel in the as-received state shows a homogeneous microstructure and well balanced mechanical properties over the whole batch.

Belonging to this European Program the creep properties of the steel F82H-mod. are determined. The creep and creep rupture tests in the temperature range 450°C - 700°C are completed with a rupture time up to 15.000 hours, not including still running long-term tests. Fig. 1 shows the results as a stress vs. rupture time diagram for the material in the as-received condition of 1.040°C 38 min + 750°C 1 h. These data are in a good agreement with the results of the other European laboratories (next page).
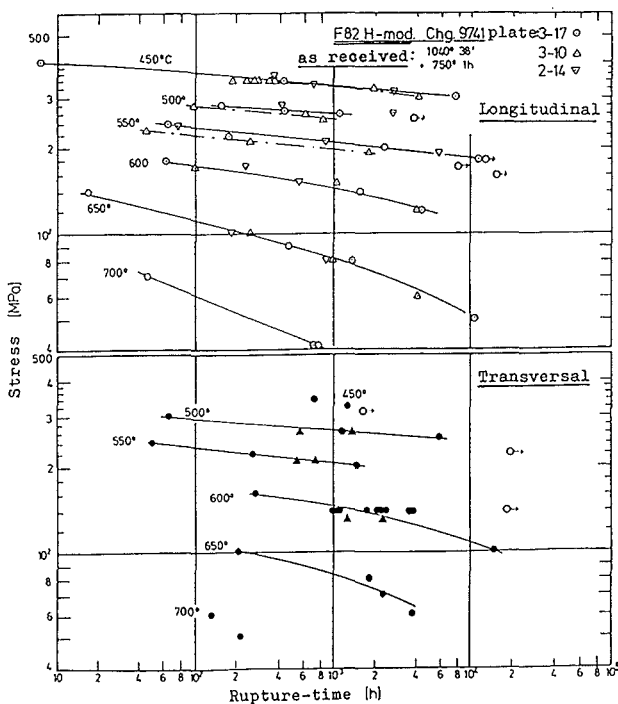
Fig. 1: The stress to rupture time diagram of F82H-mod.

In the present the program of selective measures concerns the aging behavior of the steel F82H-mod.. The aging heat treatments are designed for 5.000 h at 550°C and 600°C (after 1040°C 0.5 h + 750°C 2h), as up to 10.000h at 600°C (after 950°C 0.5 h + 750°C 2h).

The first results are the short time tests. The tensile properties were not changed after aging at 550°C 5.000 h and 600°C 5.000 h, respectively (Fig. 2).

Supplementary creep tests are running in order to study the influence of aging treatments, the influence of a lower hardening

temperature (950°C, 1.000°C) and the influence of a temperature transient of 875°C before the creep test at 500°C.
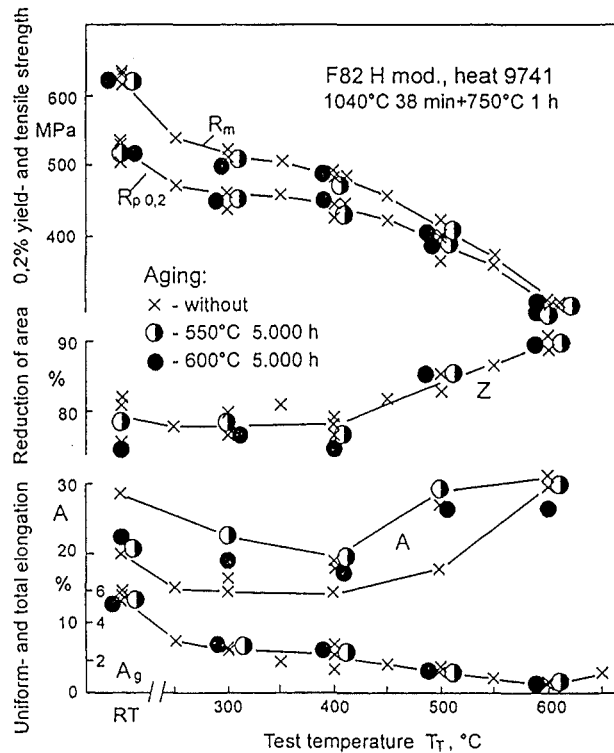
Fig. 2: Tensile properties after aging in dependence of the test temperature of the steel F82H-mod.

Fig. 3 shows the present status of the aging program after impact tests of F82H-mod.. The tendency of an increase in DBTT due to aging is recognizable, but much stronger after the further heat treatment of 950°C 0.5 h + 750°C 2 h with an aging at 600°C 10.000 h.
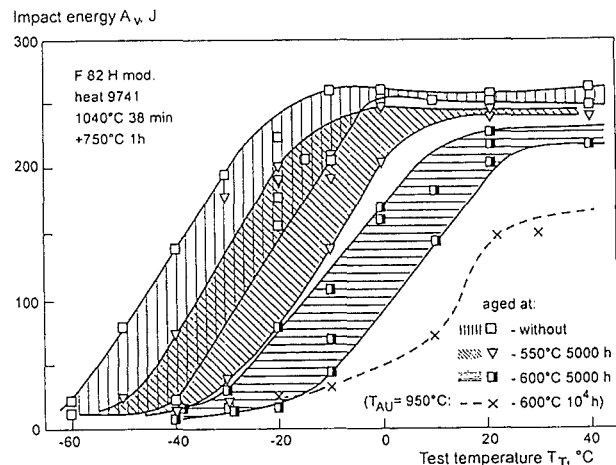
Fig. 3: Impact energy of the steel F82H-mod. In dependence of the test temperature

One reason for this behavior can be the formation of the chromium carbides, which depends on the mobility of carbon and chromium. The concentration in weight percent could be determined by chemical extractions. In the as received state the F82H-mod. has 1.8 w.t.% carbides and after the further heat treatment of 950°C 0.5 h + 750°C 1 h with an aging at 600°C 10.000 h the carbide content was 2.9 wt.%.

Of further interest was to show the microstructural development after an isothermal heat treatment (after austenitizing of 1040°C 15 min). The cooling was interrupted at 500°C (Fig. 4) like a warm bath hardening. The hardness and the microstructure was investigated after 500°C 5 h, 24 h, 100 h, 500 h, 2.000 h, 5.000 h and 10.000h. The hardness has a stable value between 393 and 400HV30. No remarkable change was found in the microstructure. The typical rod- or plate-like precipitates (M_2X) of this temperature was found in all samples with the same concentration and the high dislocation density (Fig. 5).

Fig. 4: Isothermal heat treatment after austenitization

Fig. 5: M_2X-Phase in the F82-H-mod. after isothermal heat treatment of 500°C 10.000h

Alloy Development OPTIFER:

The 2nd series of the OPTIFER alloys were limited to a W-variation (batch 735, 736) and a W-free batch with Ge (batch 734) and both B-free. The hardening and annealing behavior correspond to the batch from the 1st series (batch 664 up to 668). The charact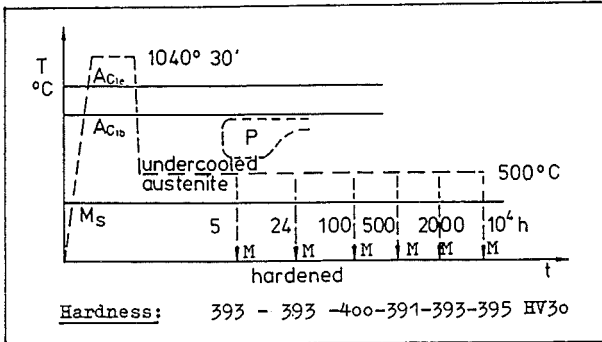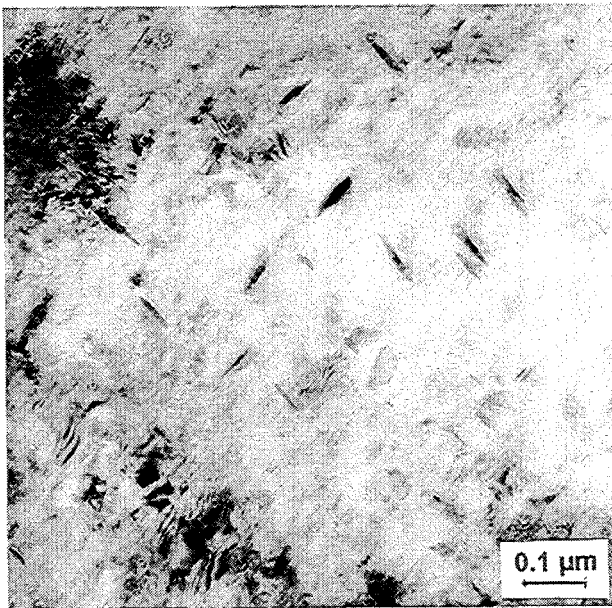erization investigations (tensile-, Charpy- and creep tests) will be performed in the heat treatment with the reduced hardening temperature of 950°C instead of 1.075 °C. The CCT-diagrams of these variations show a small drop of the transformation points (A_{c1b}, A_{c1e}, M_s, M_f) for the austenitizing

temperature 950°C and a small shift of the pearlite range to higher cooling rates.

The results of impact and tensile tests should never be considered separately, since optimizing gains are in most cases countercurrent. Therefore in Fig. 6 the 0.2%-yield strength at 500°C, representing high-temperature strength, and the transition temperature DBTT representing impact toughness are plotted in dependence of austenitizing T_{AU} and annealing temperature T_{AN}. The best combination of low transition temperature of impact energy and a high value of yield strength are desired. The values are granted in the center of the diagram. It shows the data in between the required limits.
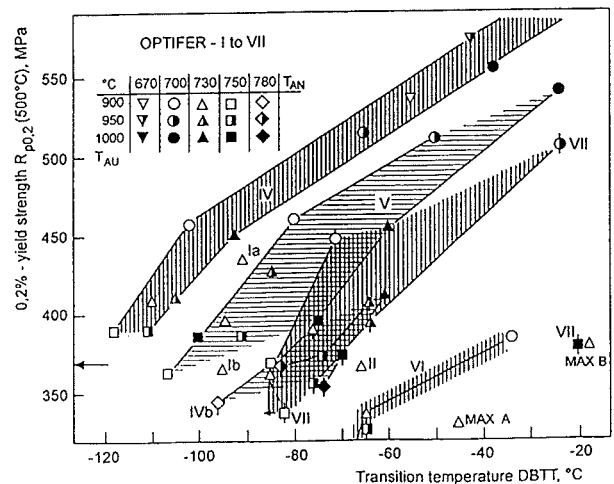
Fig. 6: 0.2%-yield strength and DBTT LAA-alloys in dependence of the austenitizing and annealing temperature

Assessment of the EUROPEAN LAA-Development

Results of the Milestone Meeting September 1997:

In the frame of the European Technology Program a series of ferritic/martensitic developmental alloys, like OPTIFER, OPTIMAX, BATMAN and F82H-mod. the composition of which had been optimized towards low long-term activation, was investigated in different European laboratories and compared with conventional 9-12%CrMoVNb steels. Reviews of the present status of art were made on several occasions as written summaries and assessments [5] and at the Second Milestone Meeting of the Associated laboratories of Europe [9].

The scope of the Second Milestone Meeting was to present the data on the commonly investigated IEA alloy F82H-mod., to report on the progress of LA-alloys development in the different European laboratories and to compare the properties of the conventional 9-12%CrMoVNb steels with the new 7-10%CrWVTa alloys. Also first results of low-dose irradiation experiments in the HFR-reactor Petten, the Dual-Beam Facility/Karlsruhe and PIREX-experiments/Villingen were expected in order to understand the effect of irradiation on the low-temperature hardening and embrittlement and the shift in ductile-to-brittle transition temperature in these materials.

It could be shown that by these chemical modifications neither the physical metallurgy nor the transformation behavior was changed markedly; Table 1 and Fig. 7. Tensile-, creep-rupture- and fatigue properties are somewhat reduced, whereas fracture toughness and impact data are far superior to conventional materials (Fig.8, 9). This is an important advantage, especially if the expected detrimental effect of neutron irradiation on the

Material (steel name)	Transformation Temperatures				Critical cooling-rate for pearlite	Reference
	Ac_{1b} °C	Ac_{1e} °C	M_s °C	M_f °C		
MANET-II 6 heats	775-780	890-900	340-357	155-161	< 0,2°/min	FZKA 5607, 9/95, Schirra
Steel 91 3 heats	810-820	870-885	385-400	100-120	3-4°/min	"
F82H-mod. heat 9741	835	915	425	220	1°/min	"
OPTIFER-Ia heat 664	820	900	418	222	< 4°/min	"
OPTIFER-II heat 668	825	920	395	172	2,5°/min	"
BATMAN heat 1953	837	911	440	230	0,7°/min	G. Filacchioni Notice 1.8.96
BATMAN heat 1955	843	913	430	215	0,7°/min	"
LA 13 Ta	821	925	325	n.d.	1,25°/min	NT-SRMA 96-2173 Alamo et al.
LA 12 TaLC	820	940	405	n.d.	1,5°/min	"

Table 1: Compilation of transformation data and critical cooling rates for perlite formation in conventional and LA-ferritic/martensitic steels
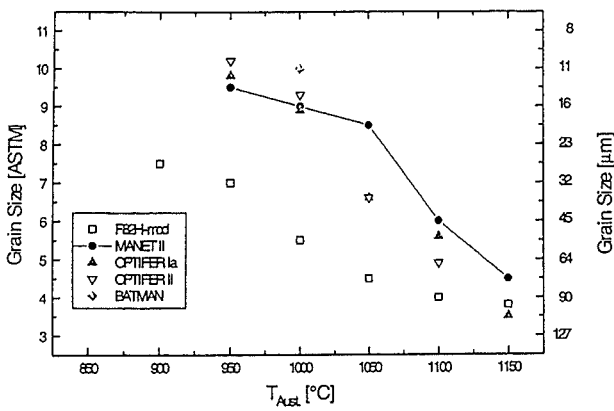

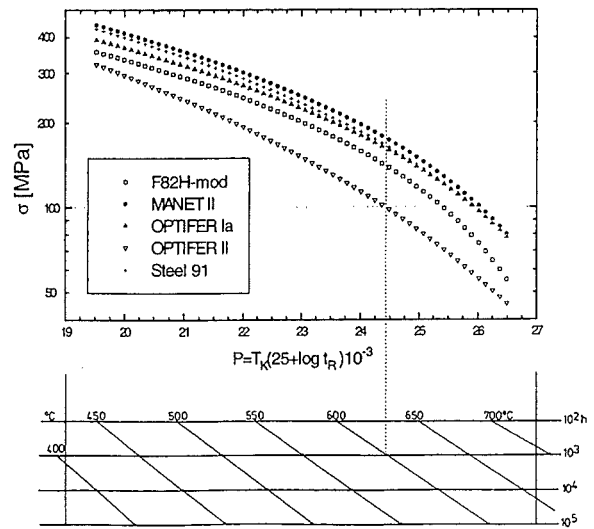Fig. 7: Comparison of grain size vs. hardening temperature

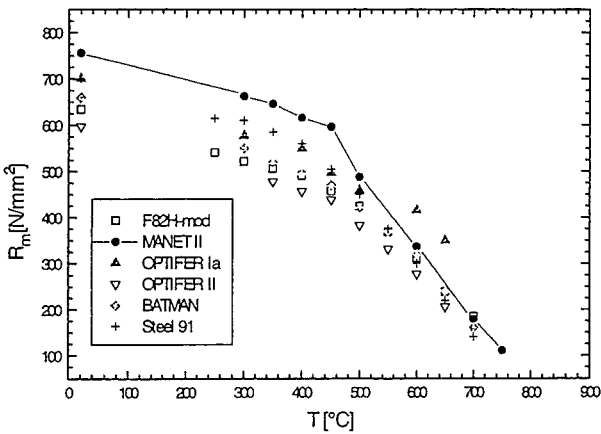Fig. 9: Comparison of Larson-Miller plots for rupture time

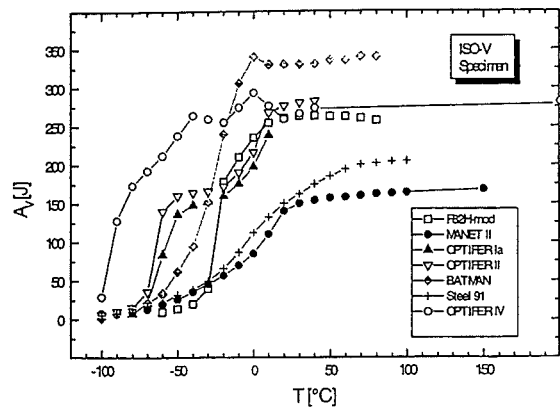Fig. 8: Comparison of the ultimate tensile strength

Fig. 10: Comparison of test temperature vs. absorbed energy

	Min wt%	Max wt%	Target	Remarks
Chromium	8.50	9.50	9.0	• minimum of DBTT around 9% Cr (unirradiated, irradiated) • better corrosion behaviour (cf. F82H)
Tantalum	0.05	0.09		• stabilizes grain size, 600-800 ppm sufficient • improves DBTT and strength, higher contents no advantage
Tungsten	1.0	1.2	1.1	• minimum of DBTT around 1.2% W (as-tempered, after ageing) • upper shelf energy less affected after long-term ageing • tensile strength proportional to W-content, • ductility inversely proportional to W-content, 1% W good compromise • creep strength of OPTIFER (~1% W) not worse than F82H (2% W) • T-breeding rate (TBR) higher for lower W-contents
Boron		0.001	ALAP*)	• no addition, He - embrittlement

*) ALAP = as low as possible

Table 2:   Justification for the content of certain alloying elements (*) ALAP = as low as possible)

latter properties is taken into account. First results of low-fluence irradiation indicate that the new alloys are less prone to irradiation-induced DBTT shifts.

A positive experience can also be reported about the overall performance of an alloy (F82H-mod.) which had been produced as a 5 ton batch with present steel-making technology. Homogeneity tests have provided very reproducible properties and it could also be shown that by a proper selection of the ingot material a reasonably low concentration of undesired elements can be achieved, like Nb, which controls the long-term activation.

The overall conclusion was that the development of ferritic/martensitic alloys with reduced long-term activation has made good progress. It is expected that up to the end of present screening phase (1998) a „Primary Candidate Alloy" for this material group can be specified.

SM 5.3.2
Specification of an alloy EUROFER 97:

A technical specification for the supply of a weldable reduced activation ferritic martensitic steel of the 9 CrWTaV type has been elaborated under the leadership of FZK in cooperation with different European laboratories (CEA, ECN, FZK) and under supervision of a technical EU-Coordinator. This product specification contains the technical rules for the manufacturing of such a ferritic/martensitic steel named EUROFER 97 to be used for components within the European Blanket Project (EPB) of the European Fusion Program and covers the different product forms plates, tubing, bars, forging and filler wire. The major goals for the procurement of such a large-scale heat are as follows:

•   Gaining experience in producing a high-purity steel in an near-industrial scale, and to what extent can the experience made with developmental alloys be transferred to large scale metallurgical processes.

•   Gaining experience in the fabrication of semi-finished products by means of traditional manufacturing processes like rolling, forging and drawing, as well as by means of advanced technologies like powder-metallurgy with respect to process-related parameters and whether e.g. pre-determined mechanical and microstructural properties can be achieved.

•   Gaining technological experience in manufacturing a ½ scale mock-up of a blanket module with respect to

workability , weldability , HIPPING, and other production-related properties.

Besides this, a characterization program shall determine the relevant mechanical and metallurgical properties of the material.

The chemical composition of EUROFER 97 had been fixed after an intense discussion of the critical elements with respect to the desired mechanical and radiological properties utilizing the data obtained from experiments made with F82H mod., OPTIFER and other developmental RAF-Alloys. The chosen contents of some important elements and their impact on certain properties are given and discussed in Table 2.

The technical and commercial implementation is being carried out by the NET-Team. At present a call for tender for the supply of 3.5 tons semi-finished products (plates, forging, filler wire and tubes) has been put out Europe-wide. The tenders are now in the technical evaluation phase so that the delivery of the semi-finished products will not take place before summer 1998.

Literature:

[1]   H. Finkler, M. Schirra: Transformation behaviour of high temperature martensitic steels with 8-14% Cr. Steel Research 67 (1996) No.8.

[2]   L. Schäfer, M. Schirra, R. Lindau: Mechanical properties of the LA martensitic chromium steel F82H mod.. 19th Symp. on Fusion Techn., Lisboa, Sept. 1996, Portugal.

[3]   M. Schirra, K. Ehrlich: Mechanische Eigenschaften von niedrigaktivierenden martensitischen Stählen (Typ OPTIFER) . 19. VDEh-Veranstaltung, Düsseldorf, 29.11.96.

[4]   K. Ehrlich: Die Entwicklung niedrigaktivierender ferritisch-martensitischer Stähle für Fusionsreaktoren. FZK-Nachrichten, Jahrg. 29 1/97.

[5]   K. Ehrlich, D.R. Harries, A. Möslang (Edit.): Characterization and Assessment of Ferritic-Martensitic Steels. FZKA 5626, February 1997.

[6]   M. Schirra, A. Falkenstein, S. Heger: Das Zeitstand-festigkeits- und Kriechverhalten des Stahles F82H mod., (internal report) PKF 077, March 1977.

[7]   S. Heger, M. Schirra: Zusammenstellung von Kriechkurven - F82H mod., (internal report) PKF 082, April 1977.

[8] K. Ehrlich: Werkstoffentwicklung für die Kernfusion. Eingeladener Vortrag, Universität Karlsruhe, Mai 1997.

[9] E. Daum, K. Ehrlich, M. Schirra: Proc. of Second Milestone Meeting: Development of ferritic martensitic steels. FZKA 5848, June 1997.

[10] E. Camus, N. Wanderka, S. Weizel, E. Materna-Morris and H. Wollenberger: Cr redistribution in thermally aged and irradiated ferritic-martensitic steels. Proc. of 44th Internat. Field Emission Symp., July 7-11, 1997, Tsukuba, Japan.

[11] K. Ehrlich: Werkstoffentwicklung für die Kernfusion. Eingeladener Vortrag, Max-Planck-Institut für Plasmaphysik, Garching, August 1997.

[12] M. Schirra, E. Materna-Morris: Änderung in der chemischen Zusammensetzung von OPTIFER-Versuchslegierungen auf der Basis von 10-12% Cr-Stählen und deren Konsequenz auf die physikalisch-mechanischen Eigenschaften. Metallographie-Tagung '97, 10. - 12. September 1997, Karlsruhe.

Staff:

E. Daum
K. Ehrlich
A. Falkenstein
P. Graf
S. Heger
R. Lindau
E. Materna-Morris
L. Schäfer
M. Schirra
H. Zimmermann

SM 2.2.1
Fatigue and Creep Properties of Base Material F82H mod. and OPTIFER IV

1. Introduction

Structural components of a DEMO-blanket are subjected during service to alternating thermal and mechanical stresses as a consequence of the pulsed reactor operation. Of particular concern is the fatigue endurance of ferrite-martensite steels like MANET II and Reduced Activity Ferrite-martensite (RAF) steels like the Japanese steel F82H mod. and the German steel OPTIFER IV under cyclic strains and stresses produced by these temperature changes. In order to design such structures, operating under combined mechanical and thermal cycling, fatigue life has to be examined in isothermal fatigue tests for materials data generation and in thermal fatigue for verification of design codes.

In this report measured isothermal mechanical and thermal low-cycle fatigue data of the RAF steels F82H mod. and OPTIFER IV are compared to those of MANET II ferrite-martensite steel.

2. Experiments

The F82H mod. samples are tested in the tempered as received condition (Normalizing: 1040°C and tempering: 750°C) and the OPTIFER IV samples in case of isothermal, total strain control low cycle fatigue (LCF) in the tempered condition (Normalizing: 1075°C and tempering: 750°C) and in case of thermal fatigue control (TCF) in hot forged condition. The ferrite-martensite MANET II samples had been deformed after the three-step reference annealing e.g. [1].

Cylindrical samples of MANET II, F82H mod. and OPTIFER IV, respectively - solid in case of LCF and hollow in case of TCF - have been used for the experiments. Both materials have been tested in air under LCF- and under TCF-conditions, respectively.

The LCF tests have been performed with computer-controlled MTS servohydraulic testing machines operating in strain controlled push-pull mode. Triangle wave forms are applied with constant strain rates of 3×10^{-3} 1/s in case of LCF tests. More detailed informations about the test procedure are received from [2].

For the LCF experiments, solid specimens of 77 mm length and of 8.8 mm diameter in the cylindrical gauge length of the specimen have been use, where 21 mm is the initial gauge length of the axial extensometer.

The TCF test rig consists of a stiff load frame for mechanical clamping of the sample, which is directly heated by the digitally controlled ohmic heating device. Cylindrical specimens are used with similar outer dimensions as the above mentioned solid specimens, but with a wall thickness of 0.4 mm. Variable strain rates are applied at TCF test mode, due to the constant heating rate of 5.8 K/s and variable temperature changes.

With respect to extensometry a TCF test includes complications to strain measurement not normally encountered with isothermal LCF tests. Since both temperature and mechanical strain cycling are taking place, mechanical strain is available only after subtraction of the thermal strain from the net strain.

3. Results

A comparison of isothermal fatigue behavior between MANET and both RAF steels shows at a temperature of 450°C with a total strain range of 1 % a nearly identical number of cycles to failure. A different result can bee seen at the total strain range

level of 0.6 % for both RAF steels. For smaller strain ranges, the isothermal fatigue lifetime of the examined RAF steel F82H mod. is significantly worse than that of the MANET steels.
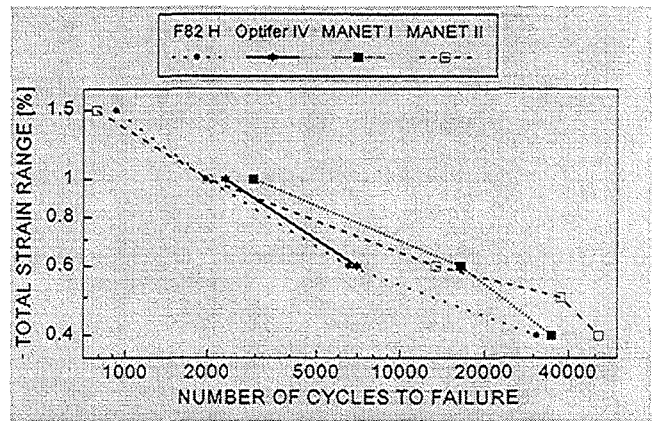
Fig. 1: Comparison of isothermal fatigue behavior between MANET steels and the RAF-steels F82H mod. and OPTIFER IV

Fig. 2: Comparison of total mechanical strain range of thermal fatigue behavior between F82H mod., OPTIFER IV and MANET II.

The comparison of thermal fatigue behavior between F82H mod., OPTIFER IV and MANET II in respect to total strain range vs. number of cycles to failure is depicted in Fig. 2, where the tempered F82H mod. shows at a temperature change of 200 to 600°C e.g. at increasing total mechanical strain ranges a drastic reduction in number of cycles to failure of about one order of magnitude compared to MANET II. In comparison, the hot forged OPTIFER IV under the same test conditions reacts at decreasing total mechanical strain ranges with a slight increase in number of cycles to failure. It should be mentioned that OPTIFER IV regularly will be applied in the tempered condition. Therefore the comparison has to be taken as a preliminary result.

The comparison of thermally fatigued samples of the three materials in respect to plastic mechanical strain range results for the tempered F82H mod. samples in much higher, and for the hot forged OPTIFER IV in slightly lower values than for MANET II. This is shown in Fig. 3. But the behavior still follows qualitatively a MANSON-COFFIN relationship.

The third comparison of thermally fatigued samples of the three materials is made in respect to total stress range, and results for the tempered F82H mod. samples in much lower, and for the hot forged OPTIFER IV in slightly higher values than for MANET II. This is shown in Fig. 4

4. Thermal fatigue round robin (TFRR)

Sample distribution for the four participants of TFRR, which are ENEA, Italy, ENSTIM, France, JRC, Netherlands and FZK, Germany, each with their specific sample shape, from F82H mod. (28mm plate), perpendicular to the rolling direction, had been done by FZK end of February 1997.

Thermal fatigue and thermomechanical fatigue tests will be performed in air atmospere with heating and cooling rates of 5 K/s. The temperature range is defined to 200°C - 600°C. Mechanical clamping of the sample in case of thermal fatigue should be performed at the low temperature (200°C) of the cycle. A total mechanical strain value in out-of-phase thermomechanical fatigue experiments should also be chosen to 0.4%.

Two thermal fatigue experiments have been performed at FZK, but the other partners did not run the experiments up to now, mainly due to funding restrictions.

Literature:

[1] C. Petersen, R. Schmitt and D. Garnier, Journal of Nuclear Materials, 233 - 237 (1996) 285 - 288

[2] A. F. Armas, I. Alvarez-Armas, M. Avalos, C. Petersen and R. Schmitt, Proceedings of 19th SOFT, Lisbon, Portugal 16. - 20. Sept. 1996, Eds.: C. Varandas and F. Serra, Vol. 2 (1997) 1359 - 1362.

Staff:

J. Aktaa
M. Klotz
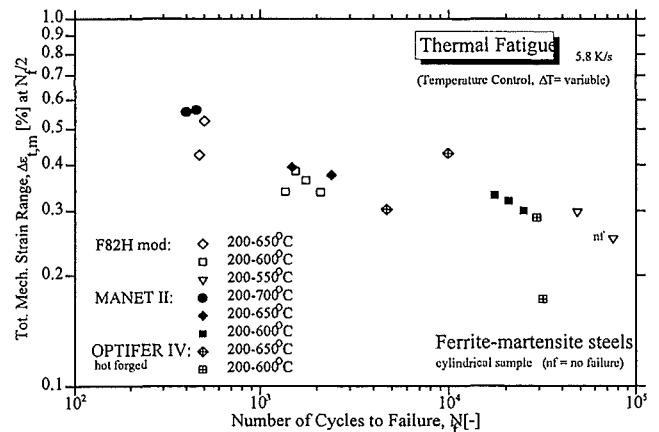C. Petersen
M. Pfeifenroth
D. Rodrian
R. Schmitt
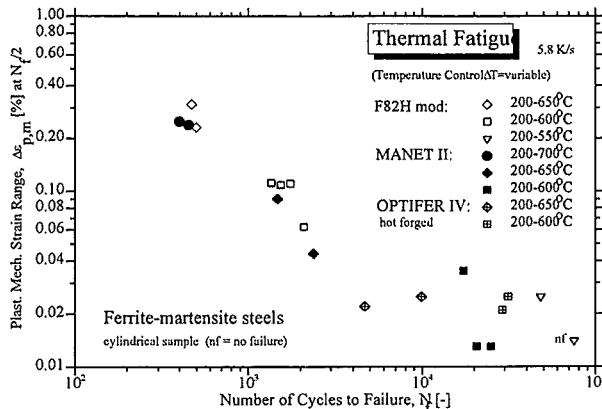
Fig. 3: Comparison of plastic mechanical strain range of thermal fatigue behavior between F82H mod., OPTIFER IV and MANET II.
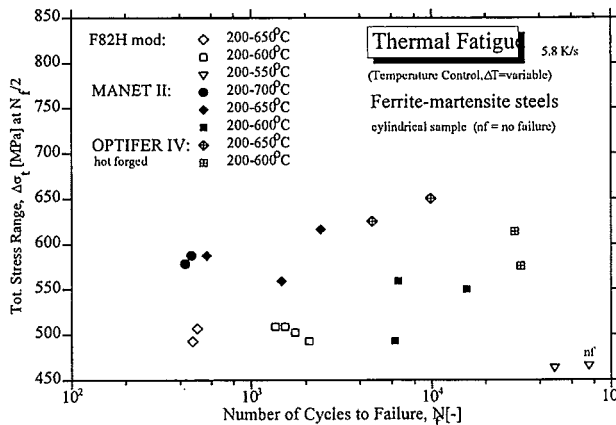
Fig. 4: Comparison of total stress range of thermal fatigue behavior between F82H mod., OPTIFER IV and MANET II.

SM 3.8.1
Corrosion of RAF/M Steel in Liquid Pb-Li

The test loop PICOLO is used for corrosion measurements in flowing Pb-17Li. Corrosion behaviour of MANET-I in PICOLO has been already investigated at 500 °C and 550 °C [1, 2]. Concerning these previous results, MANET-I can be treated as reference material and is now again under investigation. Additional to MANET two other RAF steels are in the test series: F82H-mod. and Optifer IV-a.

The chromium content of the steels to be tested varies between 7.7 % in F82H-mod., 8.5 % in Optifer IV-a and 10.6 % in MANET-I. The grain size of the three steels differs as well. After austenisation the grain size of Optifer IV-a is around 10 µm for T = 900 °C, of MANET-I 32 µm for T = 1075 °C and of F82H-mod. about 50 µm for 1040 °C [3]. It is expected that the chromium content and / or the grain size could have an influence on the corrosion behaviour.

The exposure temperature in PICOLO loop is 480 °C and the flow velocity of Pb-17Li is 0.3 m / s. The test series has now reached an exposure time of > 4000 h. Specimens exposed for 1000, 2000 and 3000 h are under analytical investigation. At the end of this year, the experiment will be finished.

Literature:

[1] H.U. Borgstedt, H.D. Röhrig, J. Nucl. Mater., 179 - 181 (1991) 596.

[2] H.U. Borgstedt, G. Frees, M. Grundmann, Z. Peric, Fusion Engng. and Design, 14 (1991) 329.

[3] E. Daum, K. Ehrlich, M. Schirra, FZKA 5484, 1997.

Staff:

H. Glasbrenner
K. Stein-Fechner
Z. Voß

SM 4.2.1
Weldability Tests (Diffusion Welding)

Fusion reactors require walls with internal cooling channels that are not straight and, hence, cannot be integrated into the ready-built wall. A suitable construction method of such walls is to cut the halved cooling channels into two steel plates in a mirror-inverted manner and to join both plates by diffusion welding to a wall with internal cooling channels. The properties of the welds of MANET-II steel are controlled in tensile, bending and impact bending tests. Here, all test methods shall be compared.

Figure 1 shows the stress-strain diagrams of the tensile tests at T_p = RT. It is evident from this and an analogous representation at a test temperature of T_p = 250°C that the stress-strain curves are identical, except for material-related scatterings. Variable quality of the diffusion welds is reflected by the curves breaking off after various strains. It is not reflected, however, by the small shift of some curves towards higher or lower stresses. Similar results are obtained by the bending tests at T_p = RT and at T_p = 250°C, and by the instrumented impact bending tests.

Fig. 1: Stress-strain diagram from tensile tests of specimens with different quality of the diffusion welds

Several material parameters can be obtained from the force-displacement diagrams. However, only few of them may be used as parameters for the quality of a diffusion weld. In case of extremely bad welds, fracture takes place in the elastic range already. Here, quality could be described by the strength achieved or the force. In case of welds with fractur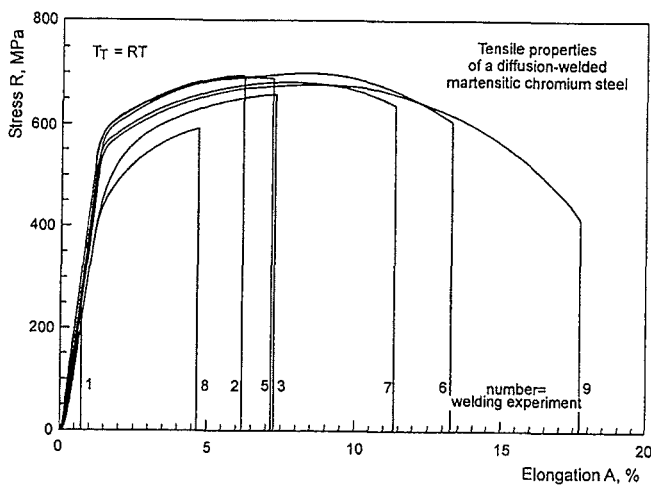es in the range between the elasticity limit and the force maximum, both the strength and the ductility can be applied. In case of good welds, the fracture of which takes place beyond the force maximum, only ductility of the specimen can be used to characterize the quality of the welds as all specimens have the same strength. To compare specimens with the fracture occurring along the entire force-displacement curve except for the elastic range, only ductility may be used as a quality parameter of the weld. This may probably apply to most cases in practice. To find out which test method is most appropriate to determine the quality of the weld, the ductilities measured in the tensile, bending and impact bending tests are compared.

Total elongation as obtained in the tensile test and bending of the bending test are compared in Fig. 2. At both test temperatures a good correlation of both material parameters can be observed. In case of good welds, both test methods are equally suitable, in case of bad welds, however, total elongation from the tensile test is the more sensitive parameter. This is reflected by the increased slope of the correlation curve at the beginning. The correlations of the ductility as obtained from the

tensile and bending test with that of impact bending test are acceptable, but not very significant due to the relatively small number of impact bending tests.
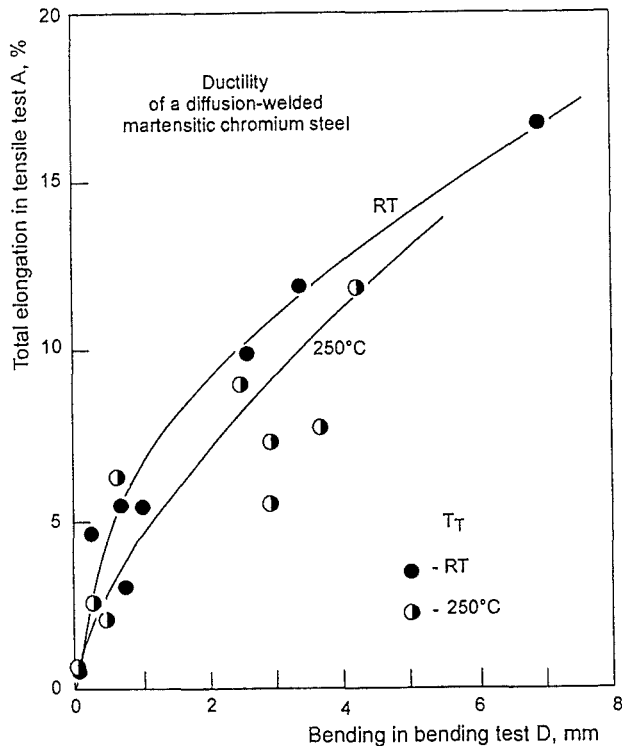
Fig. 2: Correlation of total elongation in tensile tests and bending in bending tests

It may certainly be advantageous to include other less relevant material parameters for ductility. For example, information on the strength may be useful, even though it is hardly indicative, as high strengths can easily be achieved for bad welds, while the good and very good welds unfortunately have the same strength. If it is disadvantageous to work with several and possibly "contradictory" material parameters (e.g. ductility and strength), a parameter based on two combined material characteristics may be of more practical use. This applies to the product of ductility and strength, which may be understood as toughness. The results are very similar to Fig. 2. The impact bending test seems to respond to certain welding parameters (state of the welding surfaces) in a different way than the tensile and bending tests. Therefore, only some correlations were found with the data set available. This response makes it a necessary complement of the tensile test, provided that the component load to be simulated may also be of a sudden nature.

Figure 3 shows the strength, ductility and toughness measured in the tensile, bending and impact bending tests as a function of a pre-forming parameter. The measured values are related to the basic material and, hence, vary between zero and one. All material parameters are improved with an increasing pre-forming parameter. Good strength values are reached at low pre-forming already. In contrast to this, pre-forming must be high to obtain a good ductility and impact bending strength.

Literature:

[1] L. Schäfer: Mechanische Eigenschaften von Diffusions-schweißverbindungen des Stahles MANET-II. Jahrestagung Kerntechnik '97, Aachen, KTG u. Deutsches Atomforum e.V., Tagungsberichte, INFORUM-Verl., Bonn (1997) 546 – 549.

Staff:

L. Schäfer
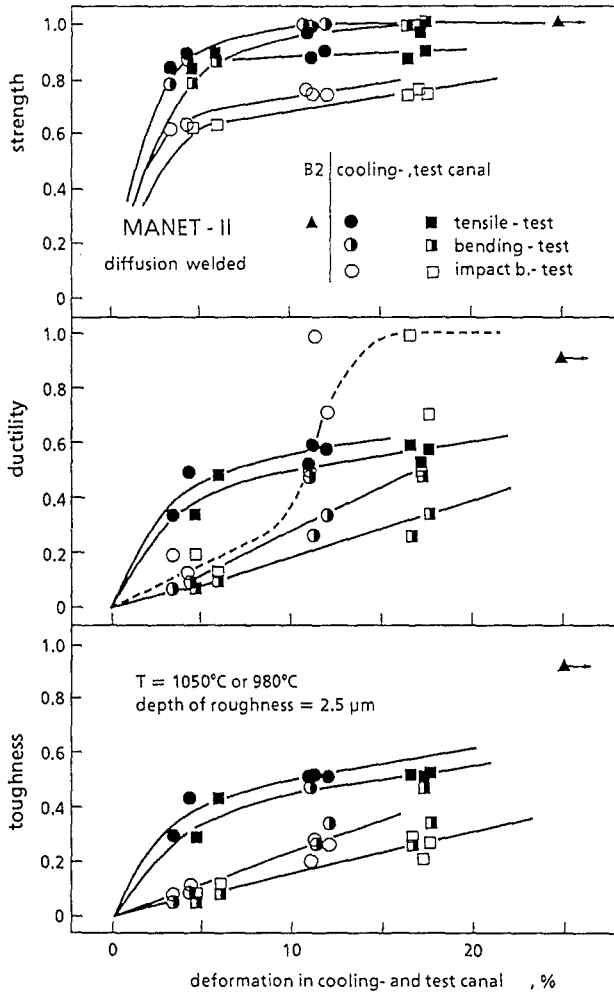
Fig. 3: Strength, ductility and toughness measured in tensile, bending and impact bending tests as a function of a pre-forming parameter

SM 5.1.1
Evaluation of Lifetime Predicting Models

The objective of this task is

- to define needs for material properties to be used in design codes for DEMO blankets and for DEMO related blanket test modules to be tested in ITER, and,

- to evaluate lifetime predicting constitutive models.

In a first step, a general type of visco-plastic material models has been implemented into the finite element (FE) code ABAQUS using the UMAT (user supplied material model) subroutine. The constitutive relations are based on the theory of finite deformation and use temperature-dependent material parameters. The theory also includes the capability to model viscous (time - dependent) processes like thermal and irradiation creep. In a second step, the constitutive equations were enhanced, including now a scalar variable, which accounts for damage processes like void nucleation and void growth.

Thereafter a tool for identification of material parameters from uniaxial experiments has been developed. The procedure uses neural networks.

The next step will be the determination of material parameters from available data of mechanical tests (e.g. from F82Hmod).

Staff:

E. Diegele
G. Rizzi

SM 5.2.1
Fracture Mechanics Studies

A fracture mechanics approach based on the physical description of fracture initiation sites in an elasto-plastic stress field is applied to describe the ductile-to-brittle transition behaviour of low activation ferritic-martensitic steels. Special emphasis is put on the description of size effects due to different stressed volumes of specimens (statistical size effect) and due to different stress fields of small specimens (mechanical size effect). It is felt that this approach has inherent capability of dealing with both effects, and that the material parameters obtained can be used in considerations related to design code developments.

During the last year, it was decided to choose the F82H-mod structural steel as reference material because of its standard heat treatment condition and the ensuing homogeneity of the database.

Progress was made in different fields:

1. Material stress-strain law

Due to the lack of material data it was necessary to perform tension tests on unnotched round bars in the required temperature interval of −150 °C up to ambient temperature. The obtained true stress-logarithmic strain curves were used to obtain a strain hardening relation. A Ramberg-Osgood elasto-plastic material law was obtained with a hardening exponent of N = 14 and temperature dependent values of the 0.2 % yield stress which were in good agreement with previously obtained results, if available.

2. Design of notched tensile specimens geometry

The obtained material law was used for an elasto-plastic stress analysis of notched tensile specimens with different notch radii and varying outer and inner diameter. This was done in order to ensure pronounced differences in the stress field of the various specimen geometries and also in order to ensure that the maximum stresses are not located at the notch root but in the specimen interior. Finally, values of 10 (5) mm were chosen for the outer (inner) diameter of the specimens and notch radii of 1, 2, and 5 mm were selected. Fig. 1 shows the axial stress distribution of the 1 mm notched specimen for three different temperatures.
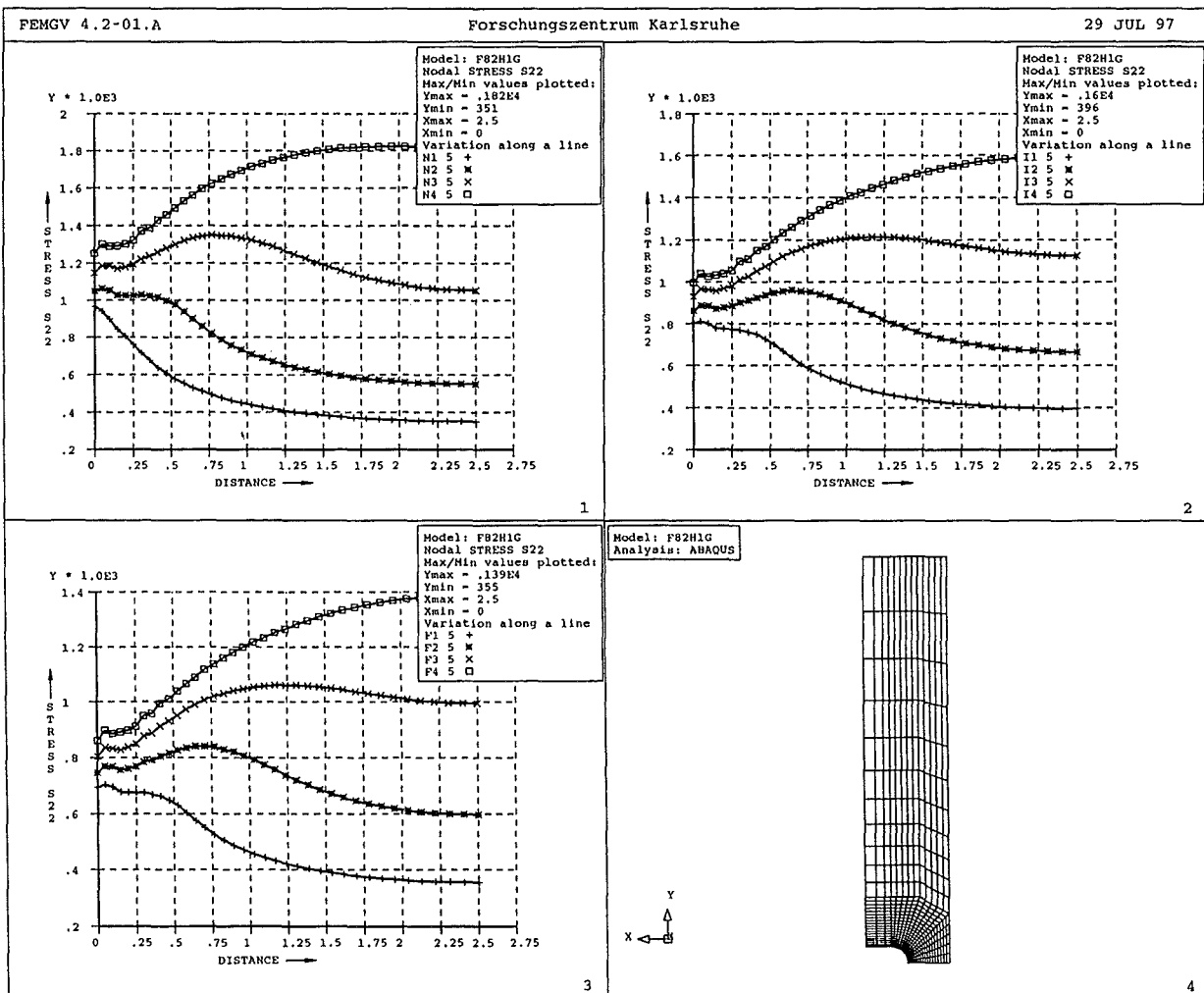
Fig. 1: Axial stress distribution of 1 mm notched specimen at (1) −150 °C, (2) − 75 °C and (3) ambient temperature. Stress variations are shown along a line starting from the notch root and extending to the centre of the specimen. The four increasing load levels of each graph result from identical displacement boundary conditions.

3. Standardization of parameter identification

Standardization of local approach fracture criteria is currently in progress under the auspices of the European Structural Integrity Society (ESIS). A statistical estimation procedure for the parameters of the Weibull stress at brittle fracture was contributed by FZK to the Draft ESIS Document (ESIS P6-94D (4.). A numerical post-processor for the calculation of the Weibull stress at brittle fracture from the results of a Finite Element stress analysis (ABAQUS) is about to be completed.

4. Notched tensile tests

After selection and manufacturing of the different specimen geometries, it will be possible to obtain first results within the next few months. This includes the numerical analysis of the experiments as well as the fracture surface analysis, which will be part of a comprehensive study on fracture initiation sites and fracture modes in the transition regime.

Staff:

J. Aktaa
E. Diegele
M. Klotz
C. Petersen
H. Riesch-Oppermann
G. Rizzi

Neutron Source

ERB 5004 CT 960062 (NET/96-420)
Conceptual Design of Lithium Target and of the Experimental Test Assembly of the D-Li Neutron Source (Phase 2)

The International Fusion Materials Irradiation Facility (IFMIF) project was started in 1994 under sponsorship of the International Energy Agency (IEA). The international design team formed to conduct the Conceptual Design Activity (CDA) phase of IFMIF completed a conceptual design and initial cost estimate for all major IFMIF systems and facilities in December 1996. After agreeing on the outcome of the CDA, both the IEA and the FTSC-P approved the proposal for an IFMIF Conceptual Design Evaluation (CDE) phase (1997-1998).

The need to develop a structural material that can withstand the high-energy neutron flux environment expected for the first wall and blanket regions of deuterium-tritium (D-T) fusion reactors is recognized as one of the key challenges remaining in the program aimed at producing commercial fusion power. IFMIF's mission is (i) to provide a neutron source with an energy spectrum simulating that of fusion neutrons at sufficient intensity and irradiation volume to test samples of candidate materials up to about full lifetime of anticipated use in a fusion DEMO reactor in a reasonably short operation time, and (ii) to calibrate data generated from fission reactors and particle accelerators. Initial studies have indicated that a volume of about 0.5 L is required in a region producing a flux equivalent to 2 MW/m^2 (0.9 x 10^{18} n/m^2-s) or greater. The design concept consists of a deuteron accelerator producing particle energies in the range of 30 to 40 MeV. The deuterons interact with a flowing liquid lithium target (D-Li) producing high energy neutrons with a peaked flux around 14 MeV. The resulting high energy neutrons will interact with a set of test assemblies located immediately behind the Li-Target. Designs for the four major technical subsystems

- Accelerator System
- Lithium Target System
- Test Facility System, and
- Conventional Facilities

have been developed in parallel and harmonized in three design integration workshops during the CDA phase. During the reporting period it has become obvious that also in future advanced neutronics calculations are urgently needed both for technical design and for the evaluation of IFMIF from the users' point of view. Within the present CDE phase, the FZK activities will concentrate on key engineering development items of the Test Facility System as well as on an optimization of the suitability of IFMIF for the fusion materials community in terms of irradiation parameters, specimen geometries and test matrixes. For the CDE phase, the international coordination of the „Users' requirements" and the „Test Facilities Systems" is organized by two FZK members. In July 1997, the first IFMIF CDE technical workshop on the Test Facilities was held at FKA with specialists from Europe, Japan and America. The main objectives of this meeting were (i) to review the baseline design concept of the former Conceptual Design Activity (CDA) period, (ii) to present the recent progress made in the design and neutronics fields and to discuss the consequences, (iii) to establish and harmonize major R&D activities following international guidelines specified for the present CDE phase. In the following, the FZK activities of the reporting period are summarized.

1. Neutronics

Neutronics work has been continued in the fields of nuclear data and code development as well as detailed design analyses for the IFMIF high flux test region. At the end of the IFMIF CDA, comprehensive calculational results for neutron transport and engineering responses were existing for the high flux test region (i.e., the volume in which a displacement damage rate of 20 dpa/y, full-power-ear or more in iron can be obtained) as well as for both the He cooled and the NaK cooled high flux test modules as designed in the CDA, loaded with steel samples. Additional, a more detailed analysis of the displacement damage was performed for the IFMIF high flux test region and other irradiation facilities. These results have been documented [1 - 6]. They constitute a major improvement over the previous approximate results.

1.1 Intermediate Energy Neutron Cross Section Evaluation

The evaluation work in co-operation with the Institute of Nuclear Power Engineering (INPE), Obninsk, Russian Federation, to provide evaluated nuclear data up to 50 MeV has been continued [7]. The already evaluated neutron cross-section data files for V-51 and Cr-52 have been completed to include photon production data and spectra of secondary particles and recoil nuclei. In addition, a complete new data file has been prepared for O-16. As a result of the co-operation with INPE Obninsk, complete evaluated nuclear data files in ENDF-6 format are at present available for the nuclides V-51, Cr-52, Fe-56, O-16, and incomplete data files (without photon production data) for C-12, Na-23, Si-28, and K-39. As an example, Fig. 1 shows the Fe-56 recoil energy spectra due to elastic collisions of neutrons of various energies.
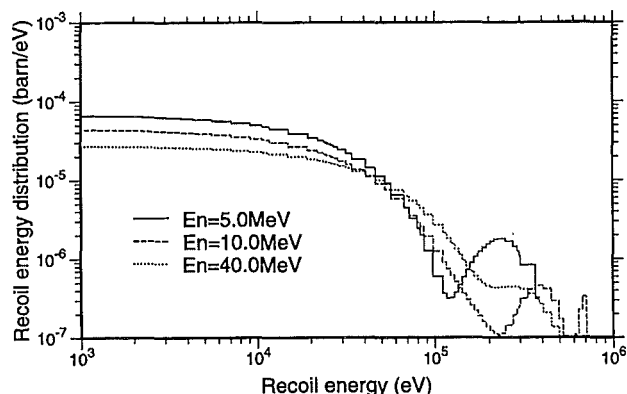
Fig. 1: Recoil energy spectra of Fe-56 due to elastic collisions at different neutron incidence energies.

New high energy neutron cross-section evaluations up to 150 MeV have been also prepared and released for a number of nuclides relevant to IFMIF by the Los Alamos National Laboratory (LANL), USA. In addition, a new working group for intermediate-energy cross-section data has been established within the JEFF (Joint Evaluated File for Fusion and Fission) project of the OECD nuclear data evaluation activity with the objective to arrive at a closer co-operation and organisation for the evaluation of cross-section data above 20 MeV. In that framework, ECN Petten have contributed their high energy evaluations (up to 150 MeV) for Fe-54, Fe -56, Ni-58 and Ni-60, and FZK/INPE have released the data files for Fe-56, V-51 and Cr-52. It was decided, furthermore, to extend the upper energy limit to 150 MeV for all future evaluations.

In addition to the data for neutron transport and responses considered so far, an evaluation programme was started, again

in co-operation with INPE Obninsk, to provide the activation and transmutation cross sections which are needed for IFMIF activation calculations. Transmutation and activation cross-section data files so far have been prepared, again on the basis of standard ENDF-6 format rules, for the stable and major unstable isotopes of Fe, Cr, W and Ta up to 150 MeV. Below 20 MeV, the cross-section data were adopted from the latest version of the European Activation File EAF-97.

1.2 Cross Section Data Processing

Processed nuclear data files have been generated with NJOY/ACER for use with the MCNP Monte Carlo code for all of the prepared data evaluations. Kerma factors and dpa cross sections, needed for nuclear heating and damage calculations respectively, are available only for the nuclides with completely evaluated files, i. e. V-51, Cr-52 and Fe-56. In the case of O-16, a processing error occured, resolution of which is pending. In addition, the high energy data files of LANL, based on the same ENDF-6 format options as the FZK/INPE evaluations, were processed with NJOY/ACER and are therefore available for MCNP based neutronics calculations for IFMIF. These include the nuclides ^{54,56,57,58}Fe, ^{12}C, ^{2}H, ^{16}O, ^{27}Al, ^{40}Ca, ^{206,207,208}Pb and ^{182,183,184,186}W.

The new activation and transmutation cross-section files up to 150 MeV were prepared according to ENDF-6 format rules using the option MT=5 with LAW=0 file on MF=6. This has the advantage that, while the total excitation function is given on file 3 as a regular cross-section dependent on the neutron incidence energy, the individual product yields are stored separately for each reaction product on file MF=6 using the LAW=0 option. As the reaction products are specified by Z,A identifiers and not by MT-numbers, there are no restrictions to the number of activation and transmutation reactions that can be handled. This is vital in view of the multitude of reaction channels existing at higher energies. The activation codes and their associated data processing codes require development work, however, for utilizing this type of cross section data.

1.3 Neutron Source Model

The Monte Carlo Deuteron Light nucleus [McDeLi] routine and the analytical INS-code were used to characterise the high flux test region of IFMIF as described in section 1.4. In the process of this characterisation, the uncertainty of the Li(d,n) reaction neutron yield, (0.064± 0.009) neutrons per incident deuteron, was shown to result in a large uncertainty in the available high flux volume, which is (550±180) ml (uncollided calculation), as shown in Fig. 2.

In an attempt to better understand and eliminate this neutron yield uncertainty, the McDeLi routine is being modified to include new reaction components in both the very high and very low energy regions. The engineering responses (see below) are not expected to be altered by the improved source model, but the uncertainty is expected to be reduced. New experimental measurements of the total neutron yield are also needed to help reduce this uncertainty.

Therefore, preparations were started for an experiment at the Karlsruher Isochron-Zyklotron, in which a lithium target of 21 mm thickness will be exposed to a 40 MeV deuteron beam. The neutron spectrum and the absolute yield will be measured by activation foil dosimetry in cooperation with JAERI, Japan. It is attempted to also measure the Be-7 production and tritium production.
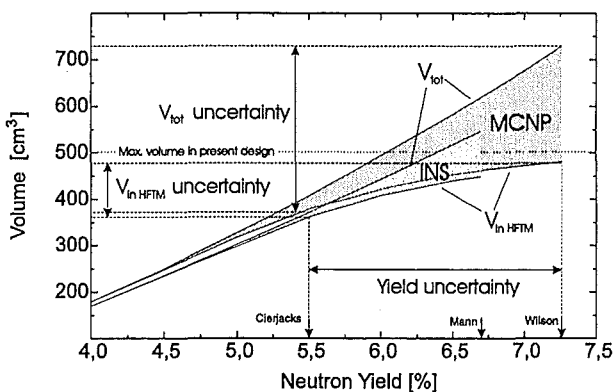
Fig. 2: Uncollided calculations of the irradiation volume with ≥20 dpa/full-power-year in Fe as a function of the total neutron yield. 'INS' and 'MCNP' refer to two different calculation codes.

1.4 Transport and Responses Calculations for the Test Cell and Comparison with Fusion Reactors

Results for the high flux region have been extensively documented in Ref.[1]. An example is shown in Fig. 3.
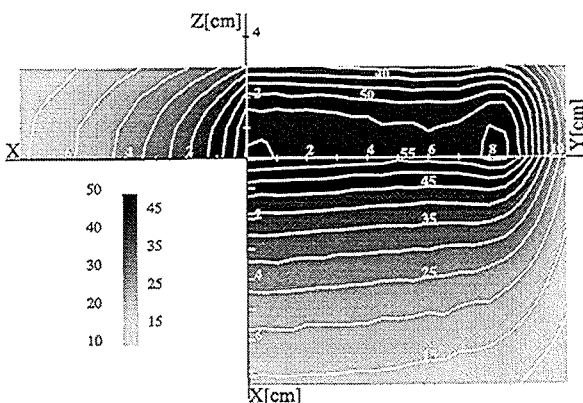
Fig. 3: Damage rate contours in dpa/full-power-year in the three symmetry planes of the high flux test region.

The results in general can be summarized as follows:

* The comparisons with fusion reactor calculations show that the IFMIF high flux test region is very well suited to meaningful material tests within fusion development programmes (see Table 1).

* The expectation that the high energy tail of the neutron spectrum, which constitutes the main difference from a fusion reactor spectrum, strongly enhances certain responses, notably the gas production and the displacement damage, is confirmed.

* The original neutronics specifications for the high flux test region can be met in most cases, the main exception being the neutron flux gradient.

* By redesigning the high flux test modules, the utilization of the available ≥20 dpa/full-power-year test volume can be greatly improved. Such a redesign can also mitigate the flux

gradient effects by allowing for suitable orientations of the samples.

Transport and response calculations for the medium, low and very low flux regions of the test cell have been taken up.

Table 1: Displacement damage and gas production rates in the first wall of ITER and DEMO and in IFMIF.

	Damage prod. [DPA/FPY]	He-prod. [appm/ FPY]	H-prod. [appm/ FPY]	He/DPA [appm/ DPA]	H/DPA [appm/ DPA]
ITER	20	230	891	11.5	45
DEMO	17	180	709	10.6	42
IFMIF midplane	57	553	2145	9.6	37.4
IFMIF averaged	37	339	1320	9.2	35.8

1.5 Qualification of the Displacement Damage for IFMIF and a Comparison with other Irradiation Facilities

In order to demonstrate the quality of IFMIF irradiations a more detailed analysis of the displacement damage on the basis of PKA-spectra has been performed and compared to other irradiation facilities. The results are documented in [3, 6] and shown in Fig. 4. IFMIF lies close by DEMO.
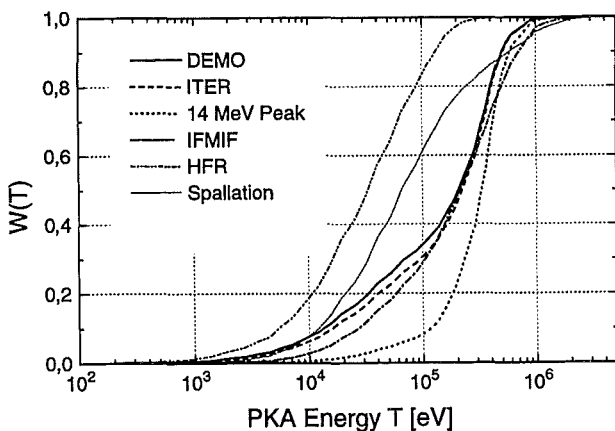
Fig. 4: W(T) functions for IFMIF and other irradiation facilities. W(T) describes the fraction of damage energy produced by PKA's as a function of their kinetic energy.

Literature:

[1] E. Daum et al.: Neutronics of the High Flux Test Region of the International Fusion Materials Irradiation Facility (IFMIF), report FZKA-5868 (1997).

[2] P. Wilson et al.: accepted for publication at ANS Topical Mtg. on Accelerator applications and in Fusion Technology.

[3] E. Daum, P.P.H. Wilson, K. Ehrlich, U. Fischer, Characterization of the Irradiation Parameters in the IFMIF High Flux Test Region, accepted at the ICFRM-8 conference and in JNM.

[4] E. Daum, P.P.H. Wilson, A. Möslang, Characterization of the Volume for High Dose Irradiations with IFMIF, accepted at the ICFRM-8 conference and in JNM.

[5] Daum, A. Möslang, M. Sokcic-Kostic, Collection of IFMIF Neutronic Calculations for Test Modules with NaK and He Cooled High Flux Test Cells, Internal Report, IMF 036, FZK, (1997).

[6] Daum, Qualifizierung der Verlagerungsschädigung in [56]Fe in Bezug auf ITER/DEMO für verschiedene Neutronenbestrahlungseinrichtungen, Internal Report, IMF 037, FZK, (1997).

[7] Yu..A. Korovin et al.: Evaluation and test of nuclear data for investigation of neutron transport, radiation damage and processes of activation and transmutation in materials irradiated by intermediate and high energy particles, Proc. Int Conf. on Nuclear data for Science and Technology, Trieste, 19-23 May 1997 (to appear).

Staff:

E. Daum
U. Fischer
U. von Möllendorff
M. Sokcic-Kostic
P.P.H. Wilson
D. Woll

2. Test Facilities Engineering

In spite of the fact that the bulk of devices specified for the Test Facilities can be designed and fabricated with today's technology, various development efforts are necessary to establish a facility which combines overall structural integrity, high reliability, feasible and tested remote maintenance operations, and advanced safety standards. The development program identified for the Test Facilities Engineering has been established basically at the end of the Conceptual Design Activity (CDA) phase and can be subdivided into the three categories (i) development and engineering design of prototypical components, and (ii) fabrication and testing of key devices that cannot rely on existing experience. Significant progress could be achieved at FZK during the second year of the CDA phase and in the early stage of the CDE phase with respect to hardware design and specification.

2.1 Test Cell Design

The FZK design of the IFMIF Test Cell is shown in Fig. 5 as elevation view. To significantly increase flexibility and redundancy, two nearly identically equipped test cells side by side are foreseen. In the test cell, the two 40 MeV deuteron beams with 2x125 mA beam current strike a single flowing lithium jet with a 20 degree impinging angle producing neutrons mainly in the forward direction. The IFMIF test cell contains (1) two vertically oriented test assemblies, referred to as Vertical Test Assemblies (VTAs) 1 and 2, which support the test modules used for long-term irradiation of specimens in the high and medium flux regions, (2) an array of tubes, referred to as Vertical Irradiation Tubes (VITs), used for inserting test capsules in the low and very low flux regions, (3) a vacuum liner that encloses the test modules and also accommodates the lithium target, which is the source of the high-energy neutrons, (4) a neutron shielding system that is gas-cooled to prevent overheating of the concrete, (5) the test cell removable cover, which can be removed with a universal robot system to gain access to the entire test cell, and (6) a seal plate for providing a vacuum seal (10^{-1} Pa) between the removable VTAs and the removable cover. Each of the test assemblies incorporates a

Fig. 5: Elevation view of the complete test cell arrangement (dimensions in mm). Design version with a stainless steel heat shield.

set of test specimens, the primary cooling system for these specimens, and sensors used to monitor and control the irradiation environment. Various design changes have been made by FZK that are described in more detail in Ref. [8]

Directly above both test cells, the access cell houses the equipment for all remote handling manipulations in either test cell. The present design concept implies that all irradiated specimens and materials of interest, after disassembly, will be investigated in suitable PIE facilities.

2.2 High Flux Test Assembly VTA1

Providing a test module for specimen temperatures up to about 1000 °C is one of the most challenging design requirements for the IFMIF Test Facilities. The successful development of a He-cooled test module would provide for any material a broad temperature window as well as flexible and very safe operating conditions.

Since the end of the CDA phase, the initial design of the helium gas cooled high flux test module was improved significantly. The gas coolant ducts are now an integrated part of the test apparatus to increase the coolant efficiency and the overall mechanical stability. Another activity during the early CDA phase was to perform improved hydraulic calculations of the helium pressure drop (PD) in the helium cooled high flux Vertical Test Assembly (VTA1). Because this calculation has

given a too high PD of greater than 0.8 bar in that reference design, form and dimension of the helium pipes were optimized and changed from circular form with a diameter of 30 mm to a rectangular form of about 50 mm side length. Also the shape of the rigs in helium flow direction was changed resulting in a lower hydraulic resistance. These updates of the reference design are shown in Figs. 6 and 7. The helium is now streaming from the bottom of the rigs upwards, it flows along both sides of the test modules (better cooling efficiency) and the rigs are opened on top and bottom to guarantee similar helium pressure inside and outside the rig walls. Another important feature is that all rigs can be disassembled and re-assembled individually.

Another design guideline was to minimize the volume and thus the heat deposition of the structural materials. In order to achieve a high mechanical integrity of all individual components, it is foreseen presently to use as structural material (e.g. specimen capsules, rigs, test module) the same type as for the specimens proper.

2.3 Medium Flux Test Assembly VTA2

Because the CDA reference design considered in the medium flux position one VTA equipped with one test module, it would only be possible to perform one type of test in this flux regime at the same time. In order to increase the efficiency of the available irradiation volume and the flexibility in the test matrixes, a design concept has been developed in the early

stage of the CDE phase by FZK that allows the simultaneous irradiation of two independent test modules in this flux region. Therefore, in the current reference design concept the vertical test assembly VTA2 of the medium flux region is equipped with two individual test modules: (i) a module for in-situ creep-fatigue experiments housing a miniaturized universal testing machine for simultaneous testing of three independent push-pull fatigue specimens, and (ii) a module for in-situ tritium release experiments on various ceramic breeder materials. Instead of ceramic breeders, this module can also be equipped with any PIE specimens.
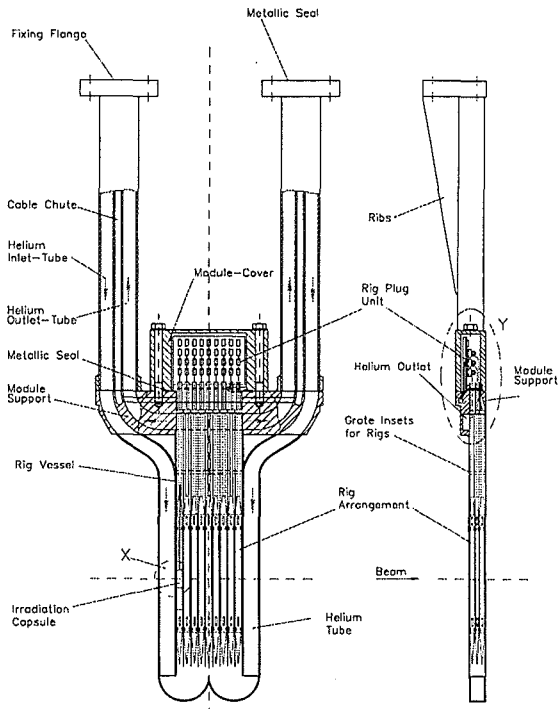

Fig. 6: Design configuration for the helium gas cooled high flux test module with vertical rigs housin encapsulated specimens.

The present reference design for VTA2 shown in Fig. 8 has been mainly guided by the requirements to effectively use the available volume of 6 L and to allow the simultaneous irradiation of both in-situ test modules.

2.4 Post Irradiation Examination PIE Facilities

The present design concept implies that all irradiated specimens and materials of interest will be investigated in suitable Post-Irradiation Examination (PIE) Facilities on IFMIF site. These facilities consist of :

- the Conventional Hot Cell Laboratory, an array of testing equipment in one single Hot Cell for mechanical testing of conventional, nontritiated high level radioactive specimens,

- Shielded Glove Box Laboratory for microstructural analyses of small or low dose nontritiated metals and nonmetals,

- the Tritium Laboratory for the investigation of tritium contaminated or tritium containing specimens and components.

Based on long-term experience from already existing hot cells, FZK has proivded for IFMIF modular type designs for completely instrumented conventional hot cells and glove box laboratories. Finally in the reporting period FZK has developed a layout for the related ventilation and exhaust systems.
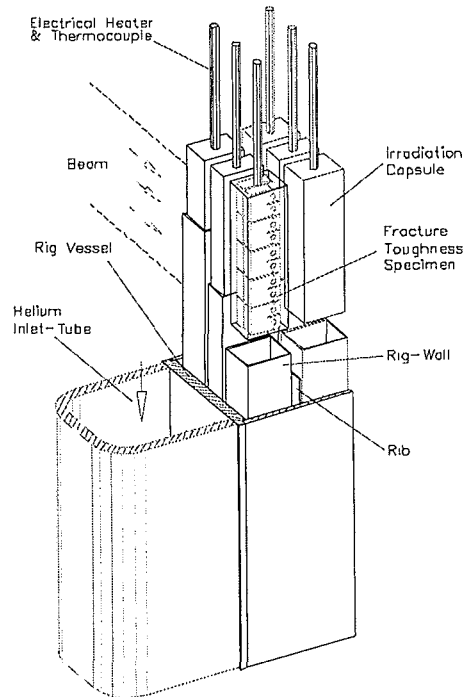
Fig. 7: Section view of the helium gas cooled high flux test module

Literature:

[8] A. Möslang and R. Lindau (eds.), proceedings of the IEA Technical workshop on the IFMIF Test Facilities, July 7-9, Karlsruhe, FZKA report 5993 (1997).

[9] K. Ehrlich and A. Möslang, „IFMIF- An International Fusion Materials Irradiation Facility"; Proc: 5th European conf. on accelerators in applied research and technology; August 26-30 1997, Eindhoven (to appear).

[10] K. Ehrlich and A. Möslang, „IFMIF: User requirements and Test Cell design"; Proc.: Annual Meeting on Nuclear Technology, May 13-15 1997, Aachen; p. 550.

[11] A. Möslang: FZK/IMF I activities for the conceptual design of the IFMIF test facilities; Internal report 1997.

[12] A. Möslang : Cost Estimate IFMIF test facilities; Internal report 1997.

Staff:

G. Bürkle
E. Daum
K. Ehrlich
R. Lindau
A. Möslang
G. Schmitz

Fig. 8: Test modules for (i) in situ tritium release experiments and (ii) in situ creep-fatigue tests on three independent speciments
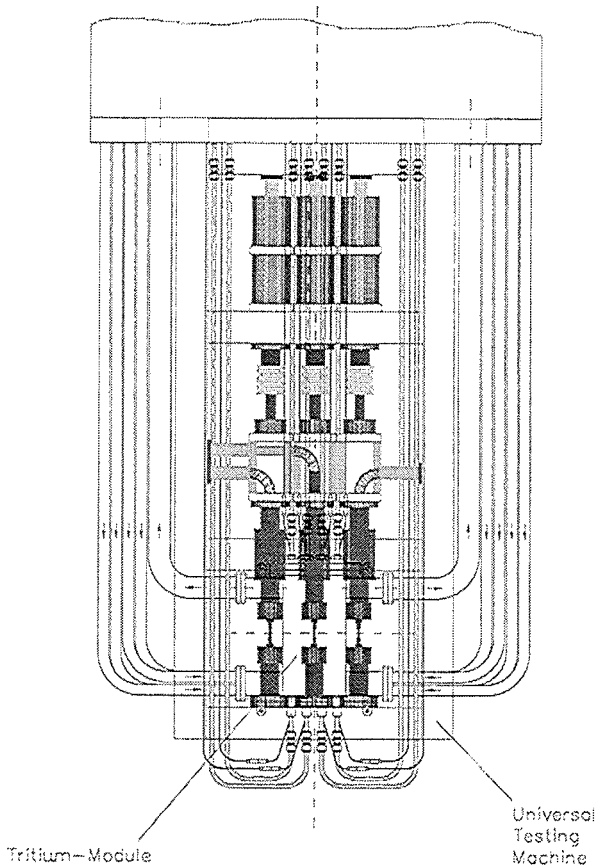
3. Target System

An analysis of deuteron energy deposition and thermal hydraulic response of the liquid lithium target has successfully been performed with the FIDAP code. To our knowledge this is one of the very few studies which includes a consistent simulation of the turbulent flow in both the target nozzle and the jet itself with application to all major target configurations: a) curved backwall, b) flat (straight) backwall and c) free jet.

From the computational point of view, the simulation of the full size problem is prohibitively expensive. Therefore, a significant simplification was introduced by dividing the problem into three parts: 1) Hydraulic analysis of turbulent flow in the target nozzle; 2) Thermal hydraulic analysis of the lithium jet with incident deuteron beam and, 3) Assessment of the free surface effects on the jet flow.

A good nozzle design should provide a relatively uniform velocity profile at the outlet with a low turbulence and thin boundary layer. Our simulation of the flow through the target nozzle was not intended for the optimization of the nozzle design. To this purpose the recommended approach is to start with some empirically obtained design (for example, the asymmetric FMIT design which was also experimentally validated) and iteratively improve it both by water mock-up and numerical simulation.

In our study we wanted to describe realistically enough the lithium flow in the target nozzle in order to investigate the influence of the jet inlet velocity and turbulence field profiles on the thermal hydraulic response of the lithium jet. Without detailed information the FMIT design is difficult to reproduce

rigorously. Hence, as target nozzle we assumed a 2-D symmetric Shima type reducer [13] which has the advantage of an analytical shape description. Recent studies performed at the JAERI water loop test facility have demonstrated that a double-reducer nozzle of Shima type successfully provided a stable jet flow with a uniform velocity distribution [13].

The transversal component of the velocity at the nozzle outlet and the level of turbulent kinetic energy are important parameters related to the mechanical stability of the jet.

Figure 9 (left) gives the contour maps of the transversal component of the velocity at the nozzle outlet for an average inlet velocity of 5 m/s. Our simulation predicts a relatively fast decay of this component of the velocity from more than 7.5 m/s in the region with the strongest curvature to around 2 cm/s at the outlet plane on a flow path of about 3 channel widths. On the right of the Figure 9 we show the contour maps of the turbulent kinetic energy for the same initial conditions. One can notice the correlation between the two pictures. The strong acceleration region displayed by the transversal component of the velocity seems to be the main source of turbulence. The transport of turbulent kinetic energy in both radial and axial directions is also clearly revealed. Obviously, the nozzle boundary layer acts as an additional source of turbulence.

The thermal response of the lithium jet was calculated by solving the heat conduction equation together with the turbulence hydrodynamics equations for the 2-D discretized jet with inlet conditions obtained in the previous step of the nozzle hydraulic simulation.

Typical temperature distributions for all three target concepts are shown in Figure 10. One first observation is that the temperature profiles are practically not dependent on the target concept. As expected they retain the deuteron energy deposition pattern. The maximum temperature on the free surface is about 290 °C and is located at the lower edge of the beam footprint. The temperature peak inside the jet is roughly located at the same depth as the Bragg's peak and about 3 cm below the beam centerline. The boiling margins in the jet and at the free surface and the vaporization rates have been calculated using the local pressure distribution and the measured temperature dependence of the lithium saturation pressure [14, 15].

Although we used a different fluid-flow simulation code and a different lithium properties data set, most of our results for the reference IFMIF target are consistent with those of the IFMIF partner groups. Thus, the surface vaporisation proved to be relatively small for the beam and jet parameters studied. The free surface at the lower edge of the deuteron beam has been identified as the most critical area for boiling. For relatively low pressures in the vacuum chamber (lower than $p=10^{-3}$ Pa) one can note that the boiling margin at the free surface (for example $\Delta T_b \approx 7$ °C for $p=10^{-4}$ Pa) is the limiting issue of the lithium target design.

The boiling margin inside the jet seems to be strongly sensitive to the target concepts. In case of the curved backwall concept, due to the centrifugal force inside the jet the pressure increases quasi-linearly from the reaction chamber pressure until $p \approx 1.3 \cdot 10^4$ Pa near the back-wall such that boiling inside the jet is strongly prevented. For other concepts like the straight back-wall which allows limited internal pressure inside the jet or like the free jet target which allows no internal pressure, boiling can be prevented only at the expense of a significant increase of average jet velocity and consequently increased lithium inventory. In addition, previous investigations in the frame of the FMIT project and very recently at the JAERI water loop test facility have demonstrated the hydraulic stability of the curved back-wall target concept. In conclusion, it seems that the curved
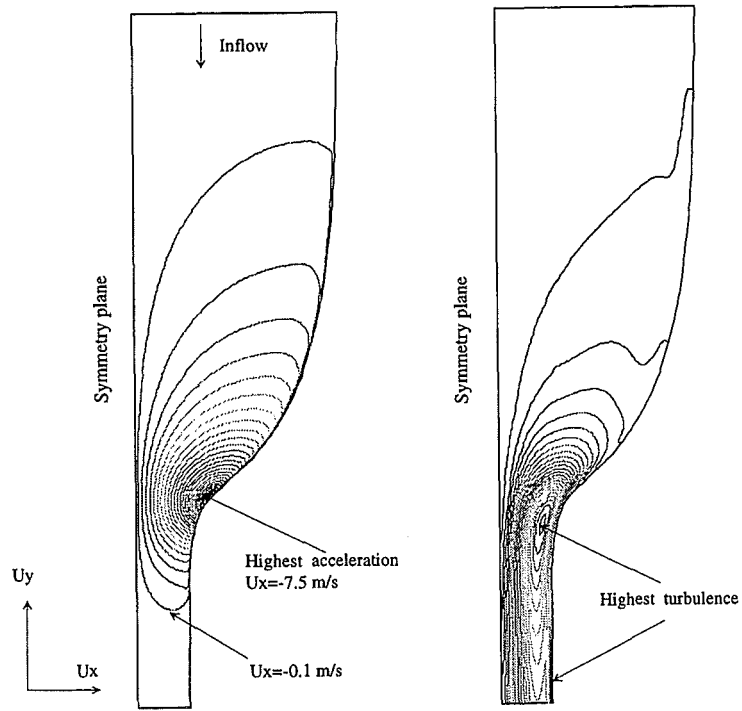
Fig. 9: Contour maps of the x component of the velocity (left) and the contour maps of the turbulent kinetic energy (right). Inlet boundary comditions: fully developed flow with average velocity of 5 m/s.
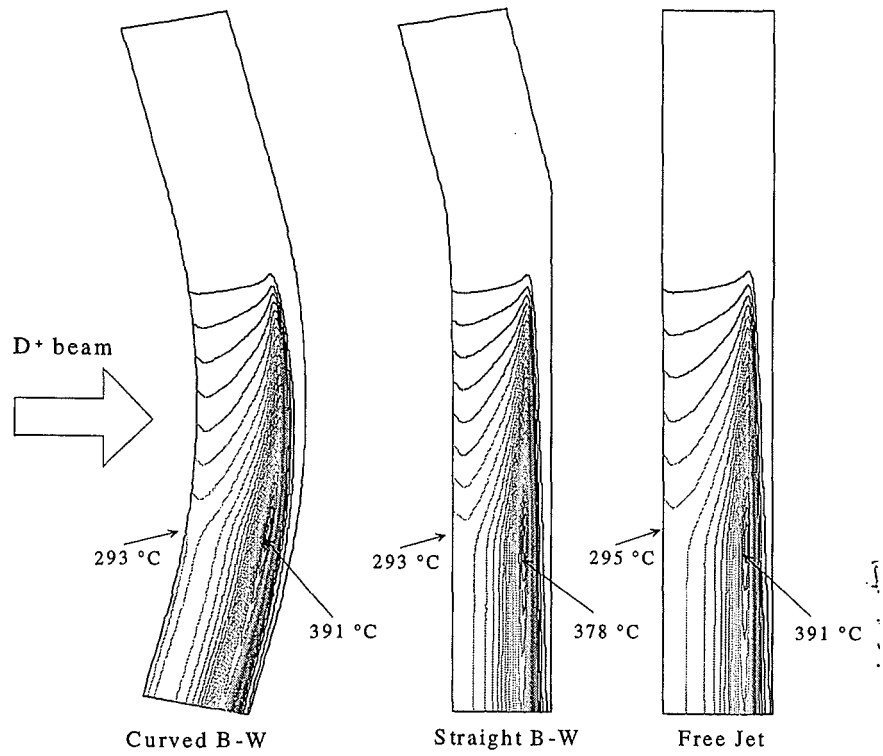

Fig. 10: Temperature distribution contour maps for the three target concpets. Jet average velocity U=17.4 m/s, Inlet temperature T=250°C.

back-wall target concept should be preferred in the initial phase of operation.

The impact of the amount of vaporized lithium, its deposition and its interaction with the incident deuteron beam need further analysis. In this respect we proposed the use of a Monte Carlo Direct Simulation code for modeling of mass and heat transport in the lithium target reaction chamber and in the target-accelerator interface.

We can conclude that the results obtained in this study corroborated with other investigations have confirmed the physical feasibility of the IFMIF target in the reference curved back-wall configuration.

The models and methodology developed in this study could be used, with adequate modifications, for the investigation of other liquid metallic targets exposed to intense energy beam like: tokamak divertor cooled with liquid lithium, spallation target for intense neutron sources, fusion reactor liquid blankets, etc.

Literature:

[13]   Nakamura,H., Itoh,K. and Kukita,Y., Water Experiment of High-Speed, Free-Surface, Plane Jet Along Concave Wall, submitted to NURETH-8 (8th International Topical Meeting on Nuclear Reactor Thermal-Hydraulics, to be held at Kyoto on Sept. 30 to Oct. 4, (1997)

[14]   W. Schütz, I. Tiseanu, Thermal Hydraulic Analysis of IFMIF Lithium Target including Free Surface and Nozzle, Jahrestagung Kerntechnik '97, Aachen, 13.-15.Mai 1997

[15]   I. Tiseanu, W. Schütz, Thermal Hydraulic Analysis of IFMIF Lithium Target with Incident Deuteron Beam, FZKA-Report 5978, in print

Staff:

I. Tiseanu
W. Schütz

Nuclear Data Base

The development of a nuclear data base is an integral part of the Long-Term Fusion Technology Programme. In the framework of this programme, FZK contributes to the development and qualification of the European Fusion File (EFF), the European Activation File (EAF) and the International Fusion Evaluated Nuclear Data Library (FENDL).

FENDL- 2 Nuclear Data Library

The FENDL-1 nuclear data library has been developed in international effort initiated and co-ordinated by the IAEA/NDS. FENDL-1 currently serves as well qualified reference data library for design calculations in the ITER project. An improved file version FENDL-2 was elaborated over the past two years on the basis of new data evaluations from the EFF, JENDL-FF (Japan), ENDF/B-VI (USA) and BROND-2 (RF) data files. The candidate evaluations were subjected to an extensive testing and benchmarking against integral experiments [1, 2] making use of coupled neutron-photon transport calculations with the Monte Carlo code MCNP, the discrete ordinates ONEDANT and the nodal transport code NGSN/1D.

The experiments analysed in the course of the FENDL-2 selection procedure cover a wide range of fusion-relevant materials. In particular, 14 MeV neutron transmission experiments on rectangular iron and beryllium slabs, and on spherical iron, beryllium, aluminium, silicon and molybdenum shells with measurements of neutron leakage spectra were analysed. In general, the analysed new EFF and JENDL-FF data evaluations show better agreement with integral experiments than do the existing FENDL-1 data. In particular this is true for iron, aluminium, silicon and zirconium.

Based on the benchmark testing results and a careful review of the submitted cross-section evaluations, the selection shown inTtable 1 was adopted for the new FENDL-2 evaluations [3, 4]. Currently working libraries are being produced for use in deterministic (multigroup data) and probabilistic (continuous energy cross-section data) transport calculations. After completion, the FENDL-2 data library is supposed to replace its predecessor as reference nuclear data library for fusion applications, in particular with regard to reactor design analyses.

Table 1: New data evaluations included in FENDL-2.

JENDL-FF	^{9}Be, ^{12}C, ^{14}N, ^{16}O, ^{51}V, ^{nat}Zr, ^{93}Nb, ^{nat}Mo, ^{nat}W
EFF-3	^{27}Al, ^{56}Fe
ENDF/B-VI	^{28,29,30}Si
BROND-2	^{2}H, ^{nat}Sn

EFF- Nuclear Data Library

In the framework of the EFF project, benchmark analyses are being performed as part of the quality assurance procedure for the EFF-2 and -3 data evaluations.

Benchmark analyses for EFF-2 , -3 data

A comprehensive programme of benchmark analyses has been conducted for the EFF data evaluations of Be, Si, Fe, Mo, Cr (EFF-2) and Al, Fe, and V (EFF-3) in conjunction with the integral data tests performed for the FENDL-2 selection. This included comparisons with corresponding nuclear cross-sections from the JENDL-FF and the FENDL-1 data files and tests against integral experiments. Main results were presented

in a contribution to the Int. Conf. on Nuclear Data for Science and Technology [1]. A comprehensive documentation with detailed results in numerical and graphical form is given in Ref. [2].

EFF-3 ^{56}Fe data analyses

Special attention was given to detailed analyses of the EFF-3 ^{56}Fe data. This evaluation shows advanced, unique features and was selected for that reason for FENDL-2. In particular, the EFF-3 ^{56}Fe evaluation includes a detailed and accurate description of the neutron total and inelastic cross-sections in the unresolved energy range above 0.85 MeV up to about 10 MeV based on ultra-high resolution cross-section measurements performed at IRMM Geel [5]. The focus of the ^{56}Fe data test analyses was on the application of the data in MCNP based calculations for an iron slab experiment performed previously within the EFF-project at TU Dresden [6]. That experiment is typical for a fusion reactor shielding problem with pure iron and suitable for testing of iron cross-section data. Measurements of neutron and photon spectra leaking the 30 cm thick iron slab were provided in the experiment.

In the MCNP-calculations a full 3d-model, developed previously by TUD, of the experimental set-up was used including the neutron generator, collimator and the experimental hall. An anisotropic source distribution function was added to the model at FZK. In addition, two-dimensional sensitivity and uncertainty calculations were performed using the SUSD/TWODANT code package and covariance data processed from the EFF-2 and -3 data files [7, 8].

A comparison plot is shown in Fig. 1 for the neutron spectra, C/E (calculation over experiment) data are given for integrated neutron and photon fluxes in Fig. 2 and Table 2, respectively. It is concluded that there is generally good agreement with the measured neutron spectra within the experimental uncertainty for all of the state-of-the-art data files (EFF-2, -3, FENDL-1, JENDL-FF) and a clear improvement over obsolete data evaluations like EFF-1. The photon flux, however, in general is underestimated. With regard to EFF-3, there are two severe problems: one is the underestimation of the neutron spectrum in the energy range 5 - 10 MeV, the other one is the largely overestimated photon flux. Both problems are being investigated currently in great detail. Most likely they are caused by improper data representations on the file and subsequent processing errors.

Table 2: C/E (Calculation/Experiment) data for integrated photon flux spectra in the TUD iron slab experiment TUD iron slab experiment.

Energy range [MeV]	TUD experiment	C/E		
		EFF-3	EFF-2	FENDL-1
0.4 - 1.0	$(1.07 \pm 0.05) \cdot 10^{-6}$	1.17	0.87	0.82
1.0 - 8.0	$(1.15 \pm 0.04) \cdot 10^{-8}$	1.21	0.77	0.70
E > 0.4	$(2.22 \pm 0.10) \cdot 10^{-6}$	1.19	0.81	0.76

With regard to the data uncertainties, the SUSD/TWODANT-calculations have shown a clear improvement of EFF-3 over the EFF-2 data. This is especially true with regard to the

uncertainties of the neutron fluxes in the different energy ranges (Table 3). In the uncertainties of the total flux (E>0.1 MeV), there is involved a strong compensation of the uncertainties originating from elastic and inelastic neutron scattering. Note that the given uncertainties are solely due to uncertainties in the excitation functions. Uncertainties coming from secondary energy and angle distributions are not yet included.

Table 3: Uncertainties of calculated neutron fluxes in the TUD iron slab experiment due to cross-section (excitation functions) uncertainties.

Energy range	Uncertainty [%]	
[MeV]	EFF-3	EFF-2
0.1 - 1.0	3.25	5.03
1.0 - 5.0	2.01	9.17
5.0 - 1.0	10.5	22.1
E > 10.0	13.9	45.2
E > 0.1	2.81	4.21

Pre-analyses for a breeder blanket mock-up experiment.

A nuclear breeder blanket mock-up experiment is planned to be performed at the Frascati Neutron Generator (FNG) with the objective to validate the nuclear performance of the ITER breeding blanket [9]. For preparing the experimental set-up, calculational pre-analyses were started in 1996 on the basis of the ITER breeding blanket reference design. In 1997, the pre-analyses were continued to investigate various material configurations and the effect of different data evaluations on the tritium production and heating rate distribution in the ceramics breeder layers. Three-dimensional MCNP-calculations were performed for that purpose using a full 3d-model of the breeder blanket mock-up assembly with the mock-up support, the experimental hall and the FNG neutron source. The radial build of the mock-up replicates the ITER inboard breeder blanket build (two 1 cm thick breeder layers embedded between large beryllium blocks with a total blanket thickness of 25 cm).

The results indicate that the breeder blanket can be represented in the experiment by cylindrical slabs (Be/ceramics/steel) with a radius of no more than 25 cm if surrounded by a suitable reflector like steel or aluminium and the nuclear measurements being performed in a central channel of 5 cm diameter. Tritium production and nuclear heating in the ceramics layer differ by 10% at maximum when comparing different data evaluations (EFF-1, -2, FENDL and JENDL-FF). The beryllium data are the main cause of this differences.

Literature:

[1] Y. Wu, U. Fischer, Integral Data Tests of the FENDL-1, EFF-2, EFF-3 and JENDL-FF Fusion Nuclear Data Libraries, Int. Conf. on Nuclear Data for Science and Technology (NDST-97), May 19-24, 1997, Trieste, Italy

[2] Y. Wu, U. Fischer, Integral Data Tests of the FENDL-1, EFF-2, EFF-3 and JENDL-FF Fusion Nuclear Data Libraries Forschungszentrum Karlsruhe, Wissenschaftliche Berichte FZKA-5953, to be published.

[3] A. B. Pashchenko, Summary Report of the IAEA Consultants' Meeting on Selection of Basic Evaluations for the FENDL-2 Library, Karlsruhe, June 24-28, 1996, INDC(NDS)-356, September 1996.

[4] M. Herman, A. B. Pashchenko, Report on IAEA Advisory Group Meeting on Extension and Improvement of the FENDL Library for Fusion Applications (FENDL-2), Vienna, March 3-7, 1997, INDC(NDS)-373, July 1997.

[5] K. Berthold et al., Proc. Int. Conf. on Nuclear Data for Science and Technology, Gatlinburg, USA, May 9-15, 1994, p. 589.

[6] H. Freiesleben et al., Experimental Results of an Iron Slab Benchmark, Technische Universität Drseden, TUD-PHY-94/2, Februar 1995.

[7] U. Fischer, H. Freiesleben et al., Improved Cross-section Data for Fe-56 and Application to an Integral Fusion Neutronics Experiment, Int. Conf. on Nuclear Data for Science and Technology (NDST-97), May 19-24, 1997, Trieste, Italy

[8] U. Fischer, H. Tsige-Tamirat, Y. Wu, Sensitivity and Uncertainty Analysis of the TUD Iron Benchmark Experiment, EFF-Doc-589, Fusion Data & Neutronics Monitoring Meeting (EFF/EAF-projects), NEA Data Bank, Paris, June 19-20, 1997.

[9] Nuclear Fusion Project, Annual Report of the Association Forschungszentrum Karlsruhe/EURATOM, comp. by G. Kast, FZKA 5858, EUR 17512EN, page 158.

Staff:

U. Fischer
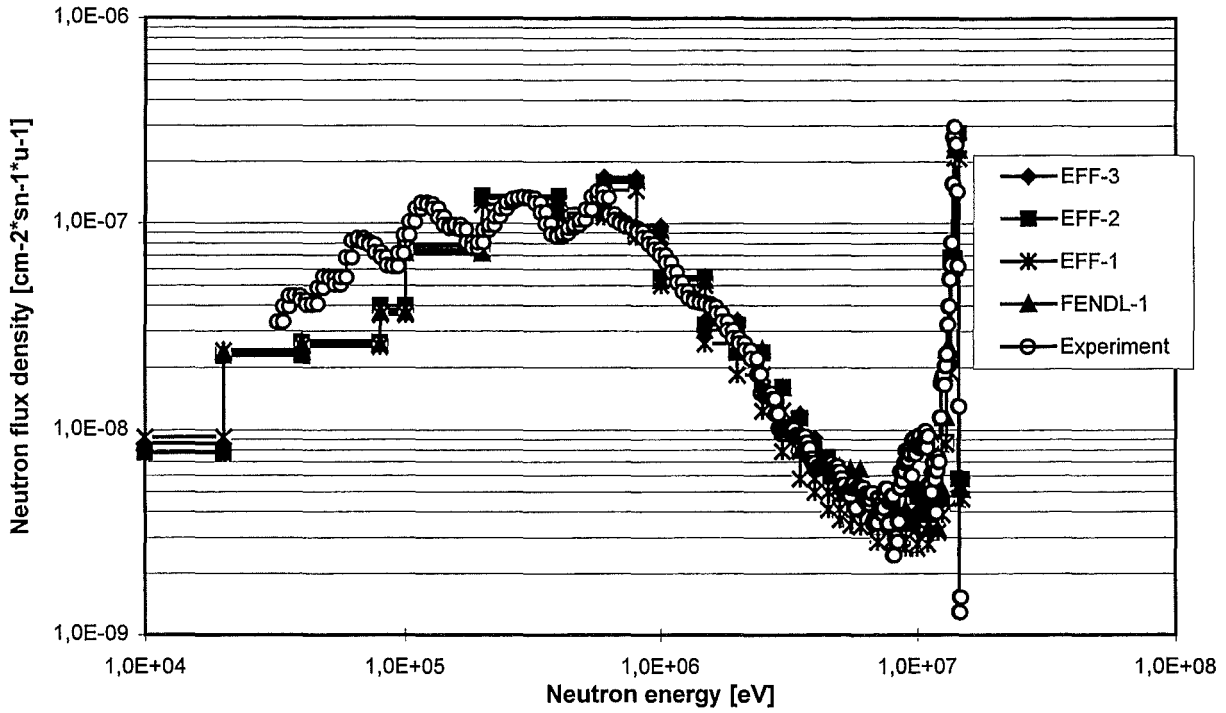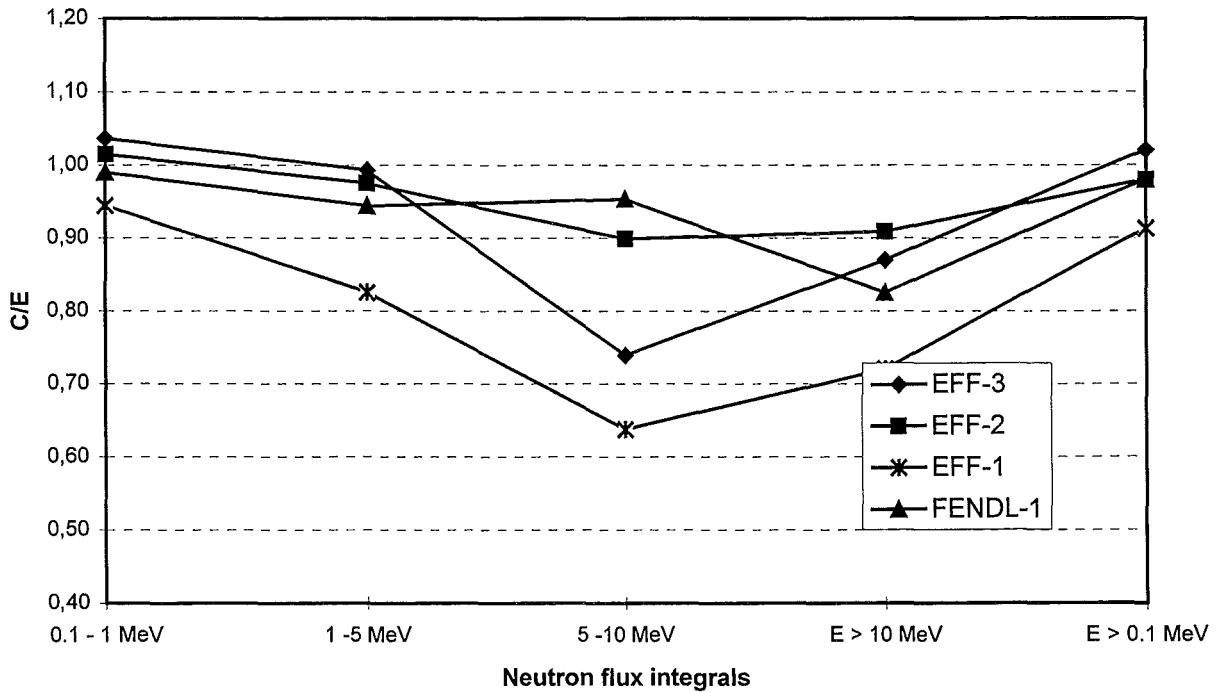H. Tsige-Tamirat
E. Wiegner
Y. Wu

Fig. 1: Comparison of neutron flux spectra in TUD iron slab experiment

Fig. 2: C/E (Calculation/Experiment) - comparison for neutron flux integrals in the TUD iron slab experiment

Activation Library

Safety analyses of reactor designs such as ITER and DEMO require among others a reliable data base for neutron-induced radioactivity. A joint effort of integral experiments has been started to validate the European Activation System (EASY). EASY consists of the inventory code FISPACT [1] developed at Culham and of the European Activation File EAF [2] originally compiled at Petten. Samples of two steels, MANET-2 and SS316, were activated in a 14-MeV neutron field and subsequently measured for γ activity by TU Dresden. Similar experiments on a sample from the same MANET-2 batch and on F82H-mod steel were performed with an intense white fast-neutron field ranging up to 20 MeV at Karlsruhe [3].

1. 14 MeV irradiations by TU Dresden

The 14 MeV irradiations were carried out at the high-intense neutron generator SNEG-13 [4] at Sergiev Posad in collaboration with the Russian Research Centre 'Kurchatov Institute' Moscow and the Coordination Centre 'Atomsafety'. The samples had dimensions of 10 mm x 10 mm and a thickness of less than 1 mm resulting in a mass of about 1 g. The 14 MeV neutron flux was monitored by $^{93}Nb(n,2n)$ activation with a thin Nb foil attached to the steel samples. In about 30 hours of irradiation time neutron fluences in the order of 10^{14} neutrons/cm^2 were applied. A possible background component of thermal and intermediate neutrons was checked by $^{197}Au(n,g)$ and by $^{115}In(n,()$ activation using thin foils.

Gamma spectra were taken from the irradiated samples several times during cooling with conventional Ge(Li)-spectrometers. Gamma activities identified by energy and half-life were used to calculate the nuclide activities with gamma yield data from EASY.

Activities of the following nuclides with half-life greater than 1 day were measured and calculated for the same cooling times: ^{48}Sc, ^{51}Cr, ^{54}Mn, ^{59}Fe, ^{57}Co, ^{58}Co, ^{60}Co, ^{57}Ni, ^{89}Zr, ^{92m}Nb, ^{95}Nb and ^{99}Mo. ^{60}Co has the largest half-life, 5.3 years.

The sums of all activities identified are plotted in Fig. 1 as function of the cooling time. They represent 90% of the total activity of gamma emitters at 1day, 99% at 1 month and 99.9% at 1 year cooling. As they are normalized to equal sample mass and neutron fluence the activation behaviour of the two materials can be directly compared. The expected low activation profile of MANET-2 is observed. In both cases the calculation underestimates the measured values. The dominating radionuclide for cooling times up to 1 month is ^{51}Cr which contributes about 80% to the activity of MANET-2 and 50 ~ 60% to the SS316 activity. At 1 year cooling time to a similar extent ^{54}Mn is dominating in MANET-2 (^{57}Co in the second place) and ^{57}Co in SS316 (^{54}Mn in the second place).

The pathways for the production of these dominating activities and of the other identified radionuclides are further investigated.

The experiments are extended in 1997/98 to the low-activation steel F82H-mod and to vanadium alloys.

Staff:

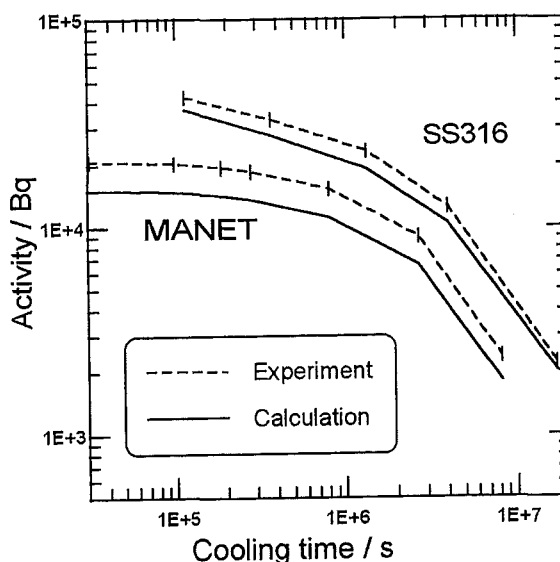H. Freiesleben
D. Richter
K. Seidel
S. Unholzer

Fig. 1: Measured (dashed line) and calculated (solid line) activity of 14-MeV irradiated SS316 and MANET versus cooling time for a sample mass of 1.0 g and a neutron fluence of 1.0×10^{14} neutrons/cm^2.

2. White-spectrum irradiations by FZK

The EASY calculations for the Karlsruhe experiments on MANET-2 and F82H-mod steels [3] were refined by using the actual, measured spectrum of the d+Be neutron source. This spectrum was obtained by activation foil dosimetry in collaboration with JAERI, Tokai-mura, Japan [6]. Since the measurement was performed on the same Be target as the F82H-mod irradiation, the absolute neutron yield was also obtained, so that C/E ratios for F82H-mod can now be given as absolute values without normalization. The flux on the sample was 1.6×10^{11} neutrons/cm^2/s.

The γ activity of the samples was measured repeatedly after different cooling times using a 150 cm^3 high-purity germanium detector with a personal-computer based multichannel analyzer. An energy range of either 0 - 2 or 0 - 4 MeV was resolved into 4096 channels.

The source spectrum was obtained from the measured dosimetry reaction rates by an unfolding calculation. The a-priori guess spectrum required as input to the unfolding procedure was obtained by Monte-Carlo calculations using the MCNP-4A code [6] together with the M^{C}DELI neutron source routine [7]. These calculations also served for scaling the result from the 5x5mm^2 dosimetry foils to the 10x10mm^2 steel samples, in view of the pronounced anisotropy of the neutron source. The unfolded and scaled spectrum is shown in Fig. 2, together with a typical spectrum of the DEMO reactor for comparison. The γ ray spectra were analyzed automatically, using the same commercial software system (ORTEC 'Gamma-Vision') which also serves for data acquisition and calibrations. Some erroneous nuclide assignments were found, that could be clarified by observing the decay of spectral lines between subsequent measurements.

Table 1 gives the results for F82H-mod in the form of calcu-lation/experiment ratios at two different cooling times. Table 2 gives the results for MANET-2, also at two cooling times. The tables contain all radionuclides found experimentally with reasonable confidence, with the exceptions: (1) nuclides erroneously assigned to γ lines by the analysis software, as indicated by a time decay not fitting the known half-life, (2) Sc-48 and V-48, which decay to the same daughter nuclide so that

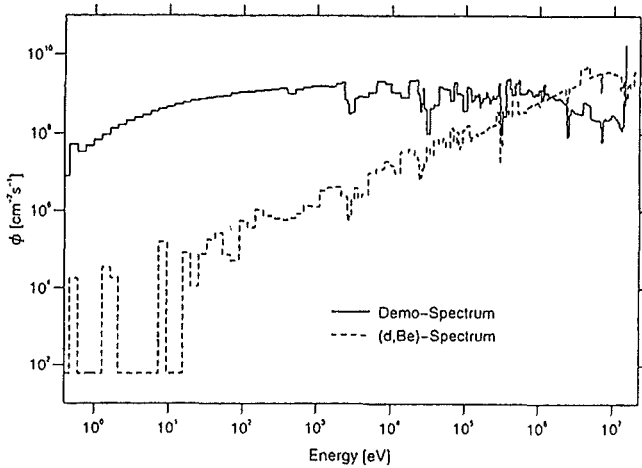their more important γ lines are identical, (3) nuclides above A=150.

Fig. 2: Neutron spectra of d+Be source and of DEMO (neutrons per group, cm² and second)

Table 1: Calculation/experiment ratios C/E for F82H-mod from Karlsruhe experiment

Nucl.	$T_{1/2}$	T_c = 181 h		T_c = 1263 h	
		f_a %	C/E	f_a %	C/E
Cr-51	28d	53.3	1.19	29.2	1.10
Mn-52	5.6d	*	0.06	**	--[a]
Mn-54	312d	18.1	1.05	27.7	1.02
Fe-59	44d	0.03	0.85	0.02	0.79
Co-56	77d	*	0.02	0.0004	0.02
Co58	71d	0.22	1.02	0.25	0.96
Co-60	5.3a	*	0.85	0.0008	0.77
Ni-57	36h	*	1.12	**	--[b]
Zr-89	78h	*	0.16	**	--[a]
Nb-92m	10d	0.01	3.10	0.001	--[a]
Mo-99	66h	0.005	0.98	**	--[a]

$T_{1/2}$: Half-life
T_c: Cooling time
f_a: Fraction of total sample activity at T_c
*   < 0.02%
**   < 0.0008%
[a]   below exptl. Threshold

[b]   not given by FISPACT

Each of the omitted nuclides is ≤1% of the sample activity at the cooling times considered, with the possible exception of activation products around A=180 from the 2% W content of F82H-mod. These may be more important and are seen in the γ spectra. However, their clean analysis requires additional work because of low and partially duplicate γ line energies. For any nuclide in Tab. 1 and 2 that constitutes ≥0.1% of the sample activity at the respective cooling time, C/E is between 0.96 and 1.19 for F82H-mod, and between 0.68 and 1.28 for MANET-2. We conclude from this that the EAF-4.1 library is reasonably well suited to predict the induced activity in these steels, at least for the range of cooling times considered here.

Table 2: Calculation/experiment ratios C/E for MANET-2 from Karlsruhe experiment, normalized toMn-54

Nucl.	$T_{1/2}$	T_c = 87 h		T_c = 676 h	
		f_a %	$(C/E)_{norm}$	f_a %	$(C/E)_{norm}$
Cr-51	28d	53.5	1.02	47.4	1.28
Mn-52	5.6d	*	0.06	**	--[a]
Mn-54	312d	13.4	(1.00)	20.7	(1.00)
Fe-59	44d	*	0.68	0.03	0.70
Co-56	77d	*	1.00	0.01	0.35
Co-57	272d	0.4	0.72	0.06	0.87
Co58	71d	5.2	0.98	6.7	0.82
Co-60	5.3a	*	0.52	0.02	0.13
Zr-89	78h	0.2	1.08	**	--[a]
Zr-95	64d	*	0.41	0.008	--[a]
Nb-92m	10d	2.7	1.22	0.8	1.25
Nb-95m	87h	0.05	1.02	**	--[a]
Mo-99	66h	3.9	0.68	0.01	--[a]

$T_{1/2}$: Half-life
T_c: Cooling time
f_a: Fraction of total sample activity at T_c
*   < 0.3%
**   < 0.008%
[a]   below exptl. threshold

The longest lived nuclide detected in the present analyses is Co-60, which is known to dominate the activity of steels at cooling times of about 10 to 100 years. In Tab. 1 and 2, the C/E for Co-60 are below unity and decrease with increasing cooling time. This indicates a possible systematic experimental error, caused by a Co-60 calibration source stored with insufficient shielding near the spectrometer, which may have introduced a varying Co-60 background in the different measurements. The steel samples will be remeasured under cleaner conditions for this important nuclide.

Literature:

[1] R. A. Forrest and J-Ch. Sublet, FISPACT-4 - user manual, Report UKAEA FUS 287, Culham (1994).

[2] J. Kopecky and D. Nierop, The European Activation File EAF-4, Report ECN-C-- 95-072, Petten (1995).

[3] U. von Möllendorff, H. Giese and H. Tsige-Tamirat, in: 'Fusion Technology 1996' (eds. C. Varandas and F. Serra), Elsevier, 1997, Vol. 2, p. 1603-1606.

[4] V. D. Kovalchuk et al., Neutron generator SNEG-13; neutron and photon field characteristics, Report IAE-5589/8, Russian Research Centre "Kurchatov Institute", Moscow (1992).

[5] F. Maekawa, to be published

[6] J. F. Briesmeister (ed.), report LA-12625-M, 1993

[7] P.P.H. Wilson and U. Fischer, in: 'Fusion Technology 1996' (eds. C. Varandas and F. Serra), Elsevier, 1997, Vol. 2, p. 1599-1602.

Staff:

H. Giese
U. von Möllendorff
H. Tsige-Tamirat
P. Wilson

SEAFP 2 Long Term Safety Program

Task 1:   Energies, Inventories and Hazards

Subtask 5:   Magnetic Energies and Hazards

For subtask 5 two reports have been prepared. The first compiles the stored energy of the magnet system of a fusion plant. The second determines the accident sequences to be analyzed.

It was found that the cold magnet structures can absorb 440 GJ and the liquid Helium coolant can absorb 427 GJ to reach ambient temperatures. The electromagnetic energy stored in the magnets is 170 GJ for the TF system and a value between 20 GJ and 50 GJ for the PF system, depending on the time in a burn cycle.

Cryogenic accidents need heat transfer and have large time constants to become effective. The stored magnetic energy, however, has small time constants and needs more detailed investigations. Typical failures for magnet accidents are: Control failure, false switching and loss of insulation. Typical consequences are: Excessive mechanical loads and thermal loads possibly leading to arcs and/or conductor melting.

The accident sequences to be analyzed were determined by a comparison of sequences that have already been analyzed under SEAFP1[1] and those presently under investigation for ITER[2]. It was found that for SEAFP2 four accident sequences have to be investigated.:

1) Local quench without discharge for TF and CS

2) Dump of a shorted coil or double pancake that can transform into an arc.

3) Dump of a coil with a short/arc at the bus bar for TF and CS.

4) air ingress into cryostat.

The analysis will be performed under Ttask 2.2.

Literature:

[1] J .Raeder et al.: Safety and environmental assessment of Fusion Power (SEAFP). EURFUBRU XII-217/95

[2] N. Mitchell et al.: Super conducting Magnet System Safety Assessment. ITER Detailed Design Document (1.1-App.G)

Staff:

R. Meyder

SEAL 1.3 Beryllium Behaviour under Irradiation

Since beryllium is considered as one of the best neutron multiplier materials in the blanket of the next generation fusion reactors, several studies have been started to evaluate its behaviour under irradiation during both operating and accidental conditions. In general, the produced tritium can diffuse through the lattice and/or be captured by structural traps (i.e. intragranular helium bubbles, closed porosity, grain boundaries, etc.). If tritium is trapped in a helium-filled bubble, it follows the fate of the bubble and will be released only if the bubble is vented into an open porosity network, through which the gas can escape with effectively no activation energy. On the other hand, recent theoretical studies, as well as practical experience, indicate that the presence of a surface oxide can be a very important factor controlling tritium retention in the Be. The beryllium in blanket modules is inevitably oxidised to some extent during construction, and oxide can be located both at the grain boundaries and on the external surface of the specimen.

The external oxide layer could thicken slowly as the result of gettering of air leaks or water desorption over the operating lifetime. Furthermore, in an accident scenario, sudden ingress of air could cause rapid oxidation of the beryllium, accompanied by a temperature rise: clearly in this case the oxide layer would play an important role in determining the amount of tritium released during the accident.

The ANFIBE code developed at the Forschungszentrum Karlsruhe is a sophisticated computer code for calculating both swelling and tritium release under simultaneous irradiation and heating. The tritium release from beryllium during irradiation has been successfully predicted in a large range of experimental conditions (i.e. temperatures, tritium production rates, etc.) but in all cases the surface oxide layer was thin and not varying. However, to apply the code to accident scenarios, or to look at the effect of air leaks, it is essential to take into account the effect of the surface oxide layer on tritium egress. It is essential that experiments are performed on the appropriate type(s) of beryllium, under experimental conditions which are both well-controlled and realistic of those expected in real scenarios.

At JRC Ispra, an apparatus has been commissioned which allows the tritium release from irradiated beryllium to be accurately measured in a wide range of temperature, pressure and carrier gas composition. It can also be used to oxidize tritium samples in-situ.

Experimental procedure

The experimental procedure is first to measure tritium release during a series of temperature steps at 100 °C intervals from the irradiation temperature up to 900 °C, into inert carrier gas. Tritium release is monitored continuously. The gas chosen for the "inert" carrier gas is He+0.1% H_2, which is the carrier gas foreseen for the blanket. A small addition of hydrogen is essential for swamping the tritium through to the detectors. Next, the experiment is repeated, using an identical specimen, in an oxidizing environment, humid air, dry air or humid helium. 0.1% hydrogen will also be added to these environments, since some hydrogen would also be present in practice, and it helps isotopes swamping. The results will be used:

- To validate the ANFIBE code (for inert gas environment).

- To develop an empirical formula for predicting the release of tritium from Be caused by an air or water leak.

- To evaluate how accidents or leaks could affect subsequent tritium release from the blanket.

- To check that tritium release from bulk Be is negligible under first wall accident conditions.

Staff:

M. Dalle Donne
Scaffidi-Argentina

Socio-economic Research on Fusion (SERF)

Contribution 1997

The report "Fusion Programme Evaluation 1996-Findings and Recommendations" of the "Fusion Evaluation Board" states:

"The Board considers that at the present stage of fusion development there is a need to complement the existing knowledge bases with a new track, that of socio-economic research of fusion (SERF). Such research calls for a multi-disciplinary approach, bringing together researchers in the physical sciences, engineering and the economic, social and environmental sciences."

The director of the Fusion Programme of DG 12 therefore invited experts to participate in the "Working Group on SERF". Representatives of the members of the EUR Associations on fusion took up the invitation.

This working group prepared a proposal for the description of SERF in 1997-1998.

The proposal was approved by the FTSC-P in March 1997 and the proposed contributions of the Associations were accepted at the June meeting of the FTSC-I.

The programme consists of the following macro-tasks:

SE 0: Long term scenari

E 1:   Production costs

E 2:   External costs and benefits

S 1:   Fusion as a large technical system

S 2:   Fusion and public opinion

FZK with the Institute for Technology Assessment and System Analysis (ITAS) is involved in work on macro-task S1 together with, Prof. L. Ingelstam, Linköping University, Department of Technology and Social Change, Sweden und Mr. I. Cook, UKEA Fusion, Culham Science Centre, UK

Within the scope of macro-task S 1, our activity will consist of:

– Highlighting the issue of the relationships between technological structures and social processes during the development of complex systems (fusion);

– The description and analysis of the psychological and social impacts of fusion;

– The structure and course of societal conflicts during the introduction of fusion;

– Identification of the actors involved and their strategies and examination of the potentials for consensus and disagreement;

– Development of proposals for the social and cultural integration of fusion technology into the existing energy supply system.

The 1. technical workshop on SERF was held in Garching October 8 - 10, 1997.

Staff:

G. Bechmann
E. Lessmann
M. Rader

Appendix I: Table of ITER / NET Contracts

Theme	Contract No.	
ITER Magnets and TFMC Stress Analysis	ERB 5000 CT 950064	NET/95-384
Transient Voltage Behaviour for the ITER TF Coil	ERB 5004 CT 960050	NET/96-405
Characterization of Jacket Materials	ERB 5004 CT 960053	NET/96-408
Conceptual Design of the Lithium Target and of the Experimental Test Assembly of the D-Li Neutron Source (Phase 2)	ERB 5004 CT 960062	NET/96-420
Definition of a Test Programme of ITER Primary Wall Module Medium Scale Mock up at FIWATKA		NET/96-433
High Voltage Components and Sensor Calibration for the ITER TFMC	ERB 5004 CT 970009	NET/96-438
ITER Tritium Plant Engineering Design	ERB 5004 CT 970037	NET/97-450

Appendix II: FZK Departments Contributing to the Fusion Project

FZK Department	FZK Institut/Abteilung	Director	Ext.
Institute for Materials Research	Institut für Material- und Festkörperforschung (IMF)	I. Prof. Dr. K.-H. Zum Gahr	3897
		II. Prof. Dr. D. Munz	4815
		III. Prof. Dr. H. Haußelt	2518
Institute for Neutron Physics and Reactor Engineering	Institut für Neutronenphysik und Reaktortechnik (INR)	Prof. Dr. G. Keßler	2440
Institute for Applied Thermo- and Fluiddynamik	Institut für Angewandte Thermo- und Fluiddynamik (IATF)	Prof. Dr. U. Müller	3450
Institute for Reactor Safety	Institut für Reaktorsicherheit (IRS)	Prof. Dr. D. Cacuci	2550
Central Engineering Department	Hauptabteilung Ingenieurtechnik (HIT)	Dr. H. Rininsland	3000
Institute for Technical Physics	Institut für Technische Physik (ITP)	Prof. Dr. P. Komarek	3500
Central Experimental Engineering Department	Hauptabteilung Versuchstechnik (HVT)	Dr. K. Schubert	3114
- Hot Cells	- Heiße Zellen (HVT-HZ)	Dr. W. Nägele	3650
- Tritium Laboratory Karlsruhe	- Tritiumlabor Karlsruhe (TLK)	Dr. R.D. Penzhorn	3239
Central Department for Real-time Data Processing and Electronics	Hauptabteilung Prozeßdatenverarbeitung und Elektronik	Prof. Dr. H. Gemmeke	5635

Contributing:

Institute for Nuclear and Particle Physics, Technical University Dresden	Institut für Kern- und Teilchenphysik der Technischen Universität Dresden	Prof. Dr. H. Freiesleben	0351/463.5461

Appendix III: Fusion Project Management Staff

Head of the Research Unit	Dr. J.E. Vetter	ext. 5460 e-mail: joerg.vetter@pkf.fzk.de
Secretariate:	Fr. I. Sickinger	ext. 5461 e-mail: ingeborg.sickinger@pkf.fzk.de
	Fr. I. Pleli	ext. 5466 e-mail: ingrid.pleli@pkf.fzk.de
	Fr. V. Lallemand	ext. 5466 e-mail: vera.lallemand@pkf.fzk.de
Project Budgets, Administration, Documentation	BW. G. Kast	ext. 5462 e-mail: guenter.kast@pkf.fzk.de
Studies, ITER / NET Contracts, Superconducting Magnets, Gyrotron Development	Dr. J.E. Vetter	ext. 5460 e-mail: joerg.vetter@pkf.fzk.de
Tritium Technology Structural Materials	Dr. H.D. Röhrig	ext. 5463 e-mail: roehrig@pkf.fzk.de
Blanket Technology	DI. A. Fiege	ext. 5465 e-mail: albert.fiege@pkf.fzk.de

Address: Forschungszentrum Karlsruhe GmbH
Nuclear Fusion Project Management

Post Office Box 3640, D - 76021 Karlsruhe / Germany

Telephone No: 07247-82- Extensions .....

Telefax No: 02747-82-5467

Telex No: 17 724 716

world wide web: http://w3.fzk.de/pkf